Experimental biomechanics of vertebral fractures

Nicola Brandolini

Submitted in accordance with the requirements for the degree of

Doctor of Philosophy

The University of Leeds

School of Mechanical Engineering

November 2015

The candidate confirms that the work submitted is his own, except where work which has formed part of jointly authored publications has been included. The contribution of the candidate and the other authors to this work has been explicitly indicated below. The candidate confirms that appropriate credit has been given within the thesis where reference has been made to the work of others.

Sections of work from chapters 2 to 5 were published as jointly authored conference and journal publications. The candidate was the lead author in all conference and journal publications regarding burst fracture creation [1] and biomechanics of the surgical treatment, where he performed all laboratory work, analysis and final write-up. Work on *in situ* testing was part of a collaboration formed with Dr. N. R. Roberts and Dr. C. Whyne (University of Toronto), for the development of a finite element model of multiple myeloma infiltrated spine. It was responsibility of the candidate to develop the test protocol and provide experimental data, whilst Dr. N. R. Roberts developed the numerical simulation based on such data. Substantial parts describing this work were taken from the publication authored by Dr. N. R. Roberts [2].

Prof. R. M. Hall and Prof. N. Kapur had supervisory roles and contributed towards the final review of all work.

“Considerate la vostra semenza:

fatti non foste a viver come bruti,

ma per seguir virtute e conoscenza.”

“Consider well the seed that gave you birth:

you were not made to live as brutes,

but to follow virtue and knowledge.”

Dante Alighieri

Divina Commedia ‘Inferno’, Canto XXVI.

Acknowledgments

I would like to thank my supervisors Prof. Richard Hall and Prof. Nik Kapur for the opportunity and guidance throughout this PhD. Thanks are extended to Mr. Jake Timothy for providing valuable clinical insight, and Mr. Jil Rabaud for his help in sourcing materials for kyphoplasty.

This work was funded by the European Union within the project SPINEFX-ITN under the FP7 Marie Curie Action (grant agreement number PITN-GA-2009-238690-SPINEFX) and the University of Leeds.

I am grateful to all the friends and colleagues within the Institute of Medical and Biological Engineering, in particular Dr. Antony Bou Francis and Dr. Nicholas Roberts for the helpful discussions and constructive criticism. Additional thanks go to Dr. Sami Tarsuslugil for his research advice and assistance, and Dr. David Keeling for his patient help with LabVIEW coding.

Finally, I am grateful to my family for their support and understanding, I want to dedicate this work to them. The greatest acknowledgement for anything I have achieved will always go to my wife, Benedetta Emiliani. Hold my hand, and I will never be afraid.

Abstract

Vertebral fractures are a severe cause of morbidity and disability. In particular, burst fractures are a common traumatic injury presenting neurological impairment in 47 % of cases. However, diagnosis and planning of the treatment is challenging as the injury originates in highly dynamic conditions. Short-segment pedicle instrumentation (SSPI) in combination with kyphoplasty (SSPI–KP) has been used to provide additional stabilisation of the fracture. However, there is a lack of understanding about the effectiveness SSPI–KP.

The aim of this study was to follow the fracture pathway, from onset to the outcome of surgical treatment. The first part focused on the phenomena underlying fracture creation and the dynamics of interpedicular widening (IPW). Although associated with neurological deficit, no previous study has shown how IPW evolves at fracture initiation. Subsequently the performance of treatment was assessed to evaluate how KP can improve SSPI to a simulated early follow-up.

Burst fractures were induced in 12 human three-adjacent-vertebrae segments. Following fracture investigation, SSPI and SSPI–KP were performed, and samples underwent fatigue loading. Image processing of high-resolution CT scans was performed to assess anatomical changes at consecutive experimental stages on the treated and adjacent vertebrae.

Experiments proved that IPW reaches a maximum at fracture onset and then decreases to the value measured clinically. SSPI–KP marginally improved stability of the treated spine, whilst providing a significant restoration of the endplate geometry. Vertebral body underwent significant changes in height and endplate curvature throughout the fracture pathway.

This study provided further insight on the biomechanics of vertebral fractures and the findings can be used to improve and/or develop novel treatments as well as validate numerical models for retrospective assessment of the injury. In addition, outcomes from the collaboration work on the development of a computational simulation may help better understand cancer related vertebral fractures.

Contents

Abbreviations

ALL	Anterior longitudinal ligament
AP	Antero-posterior
BMD	Bone mineral density
BW	Body weight
CaP	Calcium phosphate
CSA	Cross sectional area
CT	Computed tomography
DAQ	Data acquisition
EZ	Elastic zone
FE	Finite element
FR	Fragment retropulsion
HR-pQCT	High Resolution peripheral quantitative CT
IBT	Inflatable balloon tamp
IPW	Interpedicular widening
KP	Kyphoplasty
LF	Laminar fracture
LSPI	Long-segment pedicle instrumentation
LVDT	Linear variable displacement transformer
MRI	Magnetic resonance imaging
MSE	Mean squared error
NZ	Neutral zone
PBS	Phosphate buffered saline
PLL	Posterior longitudinal ligament
PMMA	Poly (methyl methacrylate)
ROM	Range of motion
r_s	Spearman rank correlation coefficient
SCO	Spinal canal occlusion
SSPI	Short-segment pedicle instrumentation
SSPI - KP	SSPI performed in combination with KP
Tb.Sp	Trabecular spacing
Tb.Th	Trabecular thickness

Parameters defined in 2.2.2

HE	High energy group
LE	Low energy group
SCA	Spinal canal CSA

CSA_{min}	Minimum CSA of the vertebral body
IPW_{CT}	IPW calculated from HR-pQCT scans
IPW_{max}	Maximum IPW measured dynamically
IPW_{res}	Residual IPW measured dynamically
SCO_{CT}	SCO calculated from HR-pQCT scans
SCO_{clin}	SCO calculated using the clinical method
SCO_{max}	Maximum SCO measured dynamically
SCO_{res}	Residual SCO measured dynamically

Parameters defined in 2.2.3

BIV	Inflation volume of the IBT
CV	Volume of cement injected
$Stiff^{Fall}$	Stiffness calculated over the falling edge of the sine waveform
$Stiff_{in}^{Fall}$	$Stiff^{Fall}$ calculated at the beginning of the test
$Stiff_{fin}^{Rise}$	$Stiff^{Fall}$ calculated at the end of the test
$Stiff^{Rise}$	Stiffness calculated over the rising edge of the sine waveform
$Stiff_{in}^{Rise}$	$Stiff^{Rise}$ calculated at the beginning of the test
$Stiff_{fin}^{Rise}$	$Stiff^{Rise}$ calculated at the end of the test
MaxStrain_mean	Maximum mean value between the two strain gauges
MaxStrain_p2p	Maximum peak to peak value between the two strain gauges
$MaxStrain\_mean_{in}$	MaxStrain_mean calculated at the beginning of the test
$MaxStrain\_p2p_{in}$	MaxStrain_p2p calculated at the beginning of the test
$MaxStrain\_mean_{fin}$	MaxStrain_mean calculated at the end of the test
$MaxStrain\_p2p_{fin}$	MaxStrain_p2p calculated at the end of the test
Disp_mean	Mean value of the axial displacement of the actuator
Disp_p2p	Peak to peak value of the axial displacement of the actuator
$Disp\_mean_{in}$	Disp_mean calculated at the beginning of the test
$Disp\_mean_{fin}$	Disp_mean calculated at the end of the test
$Disp\_p2p_{in}$	Disp_p2p calculated at the beginning of the test
$Disp\_p2p_{fin}$	Disp_p2p calculated at the end of the test
Post_mean	Mean value of the displacement from the posterior LVDT
Post_p2p	Peak to peak value of the displacement from the posterior LVDT
$Post\_mean_{in}$	Post_mean calculated at the beginning of the test
$Post\_mean_{fin}$	Post_mean calculated at the end of the test
$Post\_p2p_{in}$	Post_p2p calculated at the beginning of the test
$Post\_p2p_{fin}$	Post_p2p calculated at the end of the test

Ant_mean	Mean value of the displacement from the anterior LVDT
Ant_p2p	Peak to peak value of the displacement from the anterior LVDT
Ant_mean$_{in}$	Ant_mean calculated at the beginning of the test
Ant_mean$_{fin}$	Ant_mean calculated at the end of the test
Ant_p2p$_{in}$	Ant_p2p calculated at the beginning of the test
Ant_p2p$_{fin}$	Ant_p2p calculated at the end of the test

Figures

Tables

Chapter 1: Introduction

Vertebral fractures are a severe cause of morbidity and disability as well as a significant burden for healthcare systems. However, the biomechanics underlying fracture onset and success of its treatment raises research questions which are still far from being answered. A vertebral fracture is a medical condition arising from the loss of continuity in the bony structure, therefore affecting the physiological biomechanics and/or homeostasis of the spine [3]. The cause of the fracture may be either pathological or traumatic.

The main pathological conditions are osteoporosis and cancer, whose metabolic alterations result in bone weakening [4, 5]. Osteoporosis has been estimated to afflict up to 30 % of post-menopausal women [6] causing about 1.4 million new vertebral fractures every year [7]. Metastatic infiltration, primary spinal tumours and multiple myeloma (MM) usually induce gross osteolytic lesions, leading to painful vertebral fractures and severe back pain [8, 9]. In fact, 70 % of cancer patients show presence of spinal metastasis [10] whilst bone mass loss and destruction is found in more than 70 % of MM patients [11]. Those figures become even more alarming when considering that patients with malignant infiltration have a median survival rate of 10 months [12], rarely exceeding two years [10]. Understanding the mechanics of those fractures is then fundamental to develop effective treatments, also considering the little time available to mend the life quality of patients (metastatic infiltration may occur at a terminal stage of the cancer).

Spinal traumatic fractures are present in more than 20 % of trauma cases [13] and they occur when the spine undergoes accidental high-energy loading conditions, hence exceeding its own strength. The vertebral bone fracture may also be associated with distraction and/or disruption of the ligamentous structures [14, 15]. The complexity of trauma biomechanics lies in the fact that it is an abrupt dynamic event and the resultant fracture depends on the posture of the spine at the time of the event occurrence [16]. Moreover, traumatic vertebral fractures are inherently a major cause for spinal cord injuries and related disability/mortality: clinical reports show a 7 % first-year mortality rate when paraplegia is associated with vertebral fractures [17]. The majority of spinal traumas arise from motor vehicle accidents (~66 %) and fall from heights (~13 %) [13], which are events where the main force component is axial. Compression fractures indeed account for about 66 % of all spinal fractures with a 14 % incidence of neurological deficit [18]. Burst fractures are a sub-type of compression fractures, and they account for about 30 % of all spinal injuries [18] whilst approximately 47 % of cases present with a degree of neurological deficit at the time of admission [15]. The main features of the fracture are the spinal canal occlusion (SCO), comminution of the endplates and interpedicular widening (IPW). However, the major limitation in the diagnostics of burst fractures is that the neurological injury occurs at the fracture onset. Although SCO has been usually considered the main factor responsible for the neurological injury [19-21] it appears not to fully explain its extent [15, 22], most likely because the fracture onset is a dynamic abrupt event. On the other hand, clinical studies have shown an association between IPW and neurological deficit [23]. Although several *in vitro* studies have focused on the dynamics of SCO [24-28], there is a lack in the literature about more comprehensive investigations on burst fractures involving also IPW.

The strategy of treatment of spinal burst fractures is a widely debated surgical topic [29]. When there is no neurological deficit and the fracture is stable, conservative treatment (i.e. use of brace, cast) is undertaken with satisfactory results [30, 31]. Alternatively, surgical intervention is performed, especially when there is more need for correction and stabilisation of the fractured vertebra [32]. Short-segment pedicle instrumentation (SSPI) is a technique where screws are inserted above and below the fractured vertebra and have been shown to be a reliable choice for burst fractures treatment [33]. However, several studies reported a loss of correction over time probably caused by lack of anterior support [34, 35]. To overcome such mechanical issues, kyphoplasty (KP), a minimally invasive augmentation technique, has been exploited in combination with SSPI (i.e. SSPI – KP). Several clinical studies embraced this approach obtaining successful follow-up results [36-40]. Nonetheless, SSPI – KP is not free from concerns as the extent of the biomechanical improvement is not exactly clear.

This work focused on a set of specific research questions within the field of vertebral fractures. As far as trauma is concerned, this thesis aimed at the characterisation of spinal burst fractures, from their onset to the investigation of the performance of their treatment (i.e. SSPI – KP versus SSPI). With regard to pathological fractures, experimental tools and data were provided to allow the development and validation of a numerical model of MM infiltrated vertebrae.

1.1 Functional anatomy and biomechanics of the human spine

The human spine is an articulated multi-segment structure responsible for bearing the loads acting on the upper body as well as allowing its physiological range of motion (ROM) (Figure 1-1). In addition, the physical protection of the spinal cord depends on the integrity of the whole structure [41]. The spine is composed of 24 articulated vertebrae: seven cervical, twelve thoracic and five lumbar, therefore dividing the spine into three main regions. There are four main curvatures on the sagittal plane of the spine: the cervical, thoracic, lumbar and sacral curve. The thoracic region presents a kyphosis that ranges from 18° to 51° whilst the lumbar region lordosis ranges from 42° to 74° [42]. The first cervical vertebra (also called the atlas) is jointed with the skull, whilst the last lumbar vertebra (L5) is jointed with the sacrum. The sacrum is fused with the coccyx and is located posteriorly within the pelvis. This is the most caudal region of the spine and made of nine fused vertebrae. Each vertebra is articulated with its adjacent one through an intervertebral disc and a pair of facet joints. In addition, thoracic vertebrae present an additional joint, the costovertebral joint, where the ribs articulate. The additional stiffness provided by the rib cage increases strength and energy-absorbing capability in traumatic events [41]. Several muscle groups and ligaments run along the spine, exerting a complex set of forces and moments to achieve motion as well as cooperate with the other spinal structure to provide stability. Spinal stability is indeed a fundamental concept in spinal biomechanics which White et al. defines as “the ability of the spine under physiological loads to limit patterns of displacement in order not to damage or irritate the spinal cord and nerve roots and to prevent incapacitating deformity or pain caused by structural changes” [41].

A detailed description of each functional component of the spine is provided below.

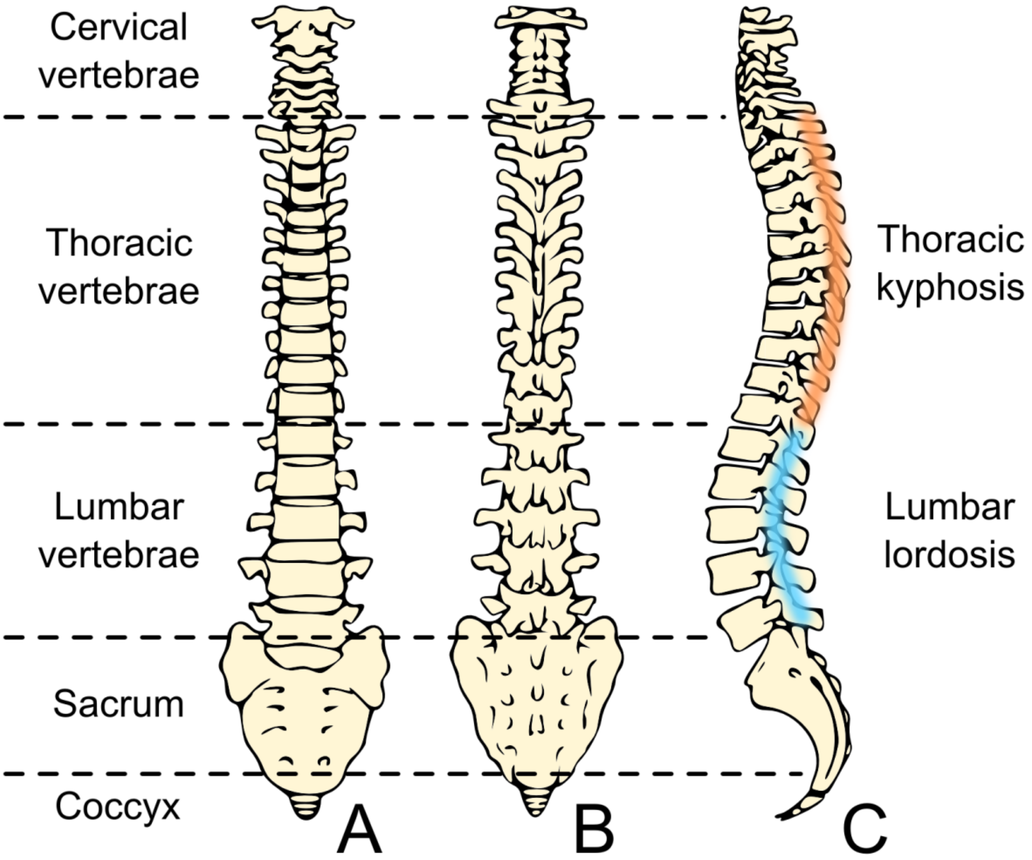

Figure 1-1: The human spine. A: frontal view; B: posterior view; C: sagittal view.

1.1.1 The vertebra

The vertebra is a bone consisting of two main anatomical regions: vertebral body and neural arch. The neural arch originates at the end of the pedicles, which protrude from the postero-lateral surface of the upper part of the vertebral body. The hollow region confined within the posterior wall of the vertebral body, the pedicles and the neural arch is the vertebral foramen, which encloses the spinal cord [41]. The posterior processes (transverse and spinous) are bony structures emerging from the neural arch and are site of insertion of numerous muscle and ligaments (Figure 1-2). The vertebral body can be roughly approximated to an elliptical cylinder, principally composed by trabecular bone, surrounded by a shell of cortical bone. The strength of the vertebral body has been typically associated with its bone mineral density (BMD) and overall geometry [43, 44]. However, these two factors alone have been shown not to be enough to fully describe the mechanical properties of the vertebra. The resultant structural behaviour is in fact the result of a complex interaction between the quality of the tissue and the architecture in which the bone is organised [45, 46]. It has been shown that the combination of BMD, micro-architecture and its heterogeneity can explain up to 86 % of variability in vertebral failure load whilst BMD alone can explain only up to 44 % [47]. The trabecular bone core is a network of rod and plate shaped struts [48, 49] which has been estimated to bear 76 to 89 % of the total load [50]. The thickness (Tb.Th) and spacing (Tb.Sp) of the trabecular network have been measured by several authors using micro computed tomography (micro CT) and some indicative dimensions are reported below in Table 1-1. It is possible to note how measurements of micro-architecture vary among studies due to age and bone quality [48].

Table 1-1: Trabecular thickness (Tb.Th) and spacing (Tb.Sp) for the vertebral body (mean ± standard deviation).

	Wegrzyn et al., 2011 [51]	Roux et al., 2010 [52]	Fields at al., 2009 [46]	Lochmuller et al., 2008 [53]	Hulme et al., 2007 [54]
Tb.Th	0.31±0.04	0.24±0.44	0.16±0.02	0.15±0.02	0.22±0.02
Tb.Sp	1.34±0.33	-	0.98±0.11	0.96±0.18	1.11±0.11

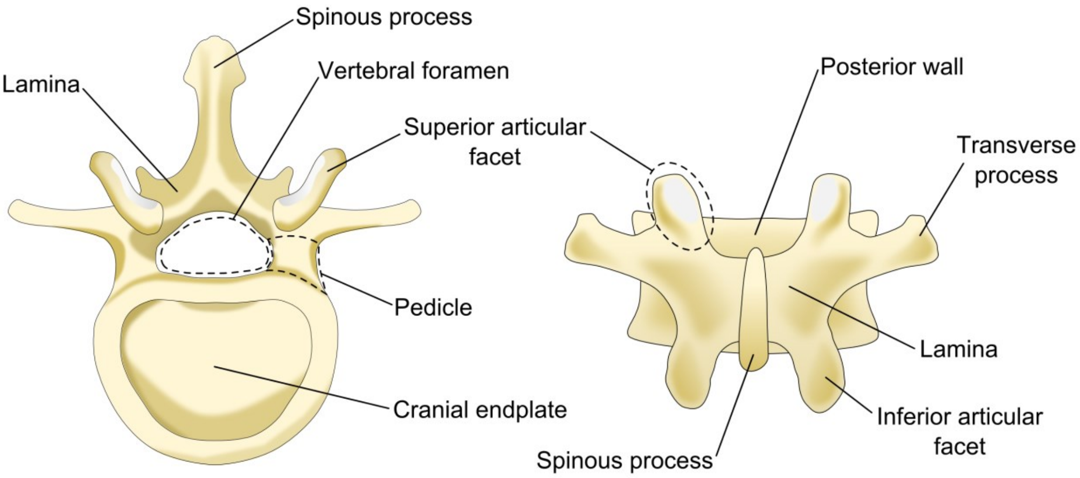

Figure 1-2: General anatomy of the vertebra.

The trabeculae within the vertebral body are organized according to load paths [55] and micro-scale finite element (FE) modelling suggests that the majority of the load is transmitted through parallel columns of vertically oriented trabeculae [56]. Furthermore, the trabecular structure extends from the vertebral body into the posterior elements through the pedicles following typical pathways, both on the sagittal and transverse plane (Figure 1-3), to counteract the forces and deformations to which the posterior processes undergo [57]. The geometry of the pedicles also varies significantly along the cranio-caudal direction, with a peculiar transition at the thoracolumbar junction (Figure 1-4). The thoracolumbar junction is an anatomical region spanning T11 to L1, where the thoracic spine joints the lumbar spine. The average cross sectional area (CSA) of the pedicle ranges from ~32 to ~65 mm^2 in the thoracic vertebra and from ~83 to ~160 mm^2 in the lumbar [58, 59]. In addition, the micro-structural properties of trabecular bone within the pedicle are different to those of the vertebral body. Trabeculae within the pedicles are more numerous, plate-like, and tend to be more densely packed, with a mean Tb.Th and Tb.Sp of 0.20 ± 0.04 and 0.93 ± 0.12, respectively [60].

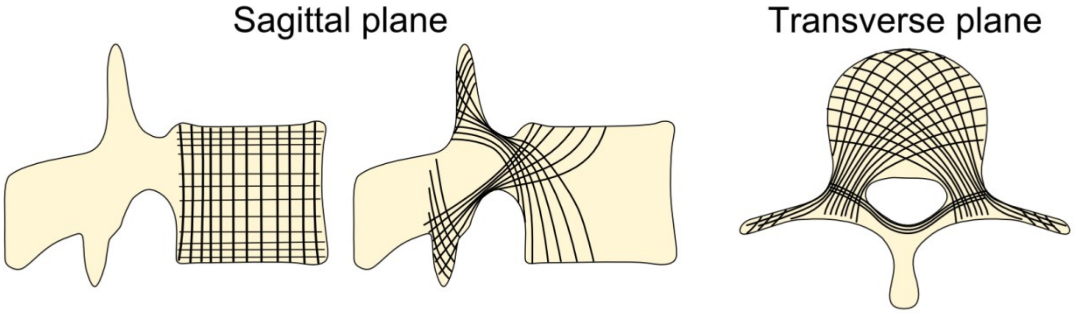

Figure 1-3: Principal orientations of the trabecular architecture in the vertebra. Adapted from [57].

The endplates are the most cranial and caudal surfaces of the vertebral body and represent the transition region between the vertebral body and the intervertebral disc. The thickness of the endplate ranges from 0.25 to 0.52 mm, with the cranial endplate being usually slightly thinner than the caudal one [61]. The thickness of the cortical shell ranges from 0.38 to 0.60 mm anteriorly and from 0.18 to 0.26 mm posteriorly [61]. Direct histological measurements have shown that the endplates and the cortical shell have a similar morphology, both appearing to be more of a thin, irregular porous layer of fused trabeculae rather than compact cortical bone, as that present in long bones [61]. However, the actual contribution of the cortical shell to vertebral strength is still unclear [52].

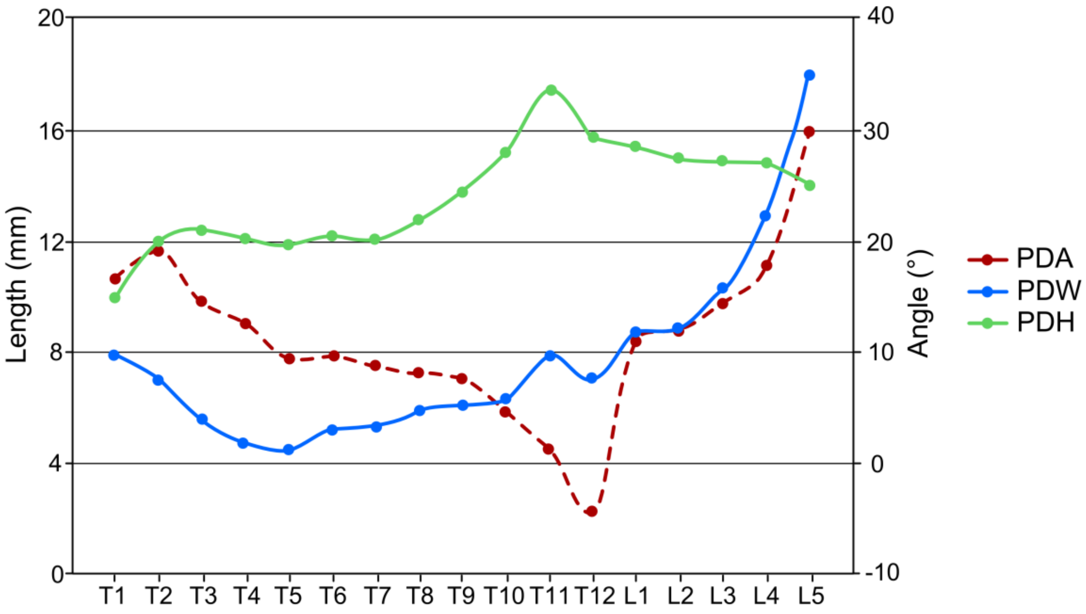

Figure 1-4: Anatomical variation of the pedicles across levels. PDA: pedicle angle on the transverse plane; PDW: pedicle width; PDH: pedicle height. Data from [62].

Although the overall anatomy of the vertebrae in the different regions remains the same, the actual bony features adapt to the functional changes along the spine, with the vertebral body being optimised to bear axial loads [63]. In fact, the size and mass of the vertebra, as well as the endplate area, increase downwards to withstand the increase in compressive forces [41] (Figure 1-5). The shape of the vertebral foramen also significantly changes along the spine, becoming more elliptical in the lumbar spine. This is mostly related to an increase of the spinal canal width (SCW), which can also be considered equivalent the interpedicular space distance (Figure 1-6).

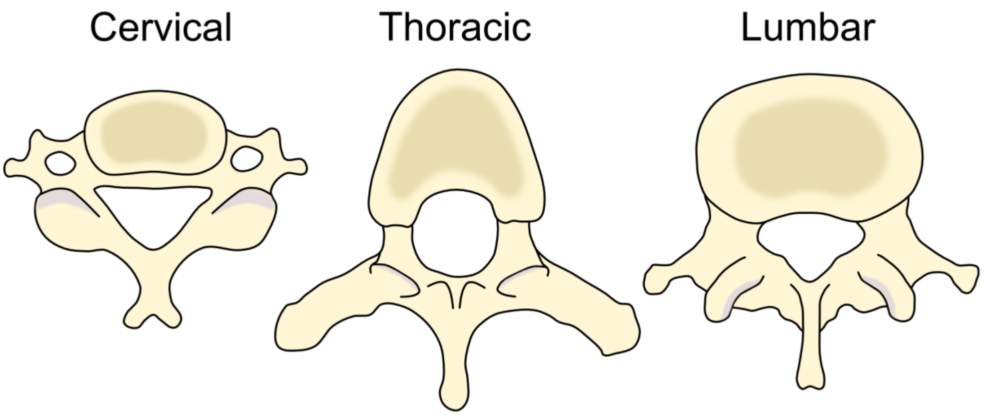

Figure 1-5: Gross anatomical differences amongst cervical, thoracic and lumbar vertebrae.

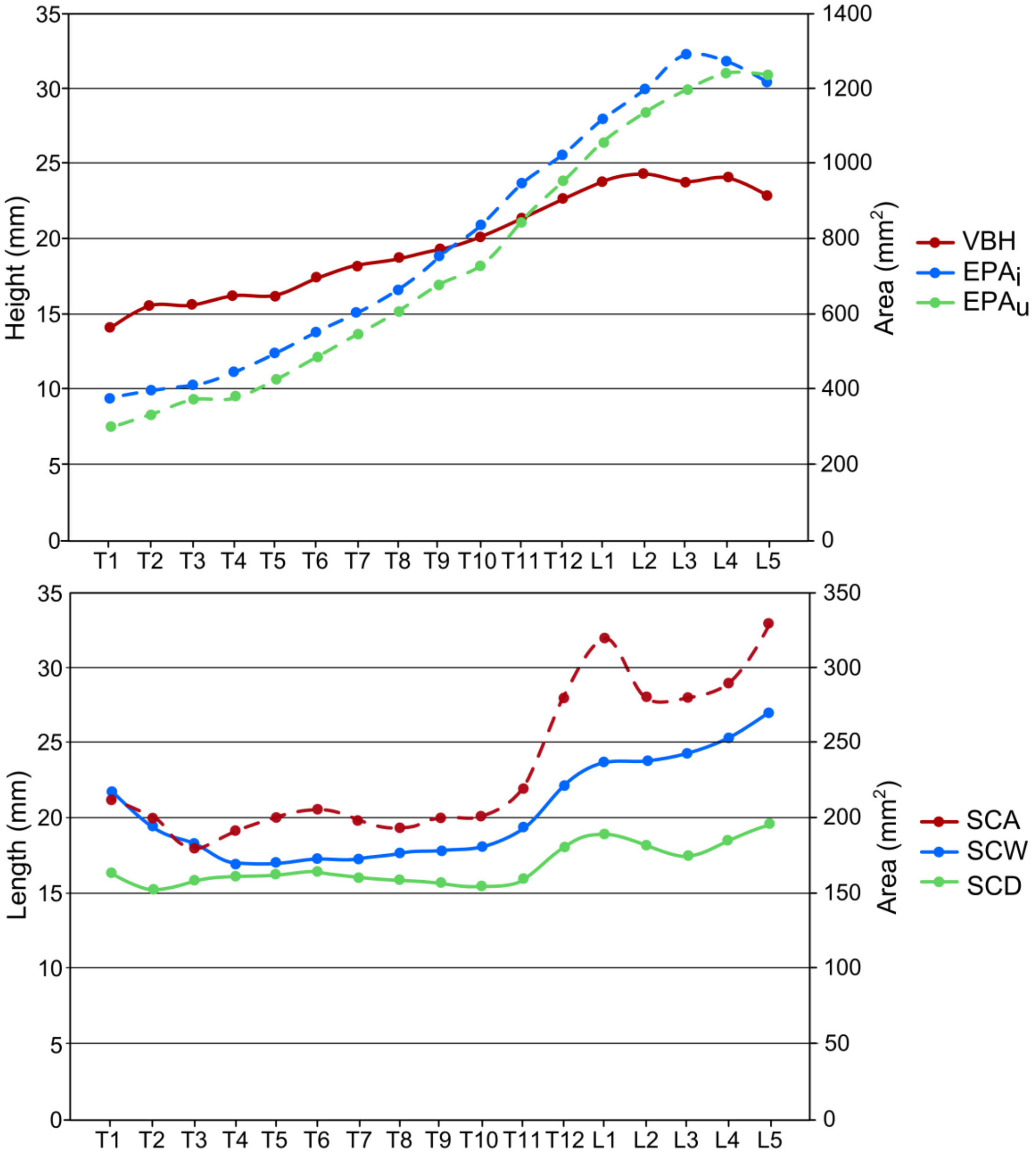

Figure 1-6: Anatomical variation of the vertebra across levels. VBH: vertebral body height; EPA: endplate area (EPA_i and EPA_u stand for inferior and upper endplate, respectively); SCA: spinal canal area; SCW: spinal canal width; SCD; spinal canal depth. Data from [58, 59].

1.1.2 The intervertebral disc

Each vertebral body articulates with the adjacent one through an avascular soft tissue called intervertebral disc. The intervertebral disc is limited superiorly and inferiorly by the endplate (often considered as part of the intervertebral disc too [64]) and is divided in two main regions: the nucleus pulposus and the annulus fibrosus (Figure 1-7). The nucleus pulposus is located centrally and composed of a loose network of fibres within a mucoprotein gel which has a water content ranging from 70 - 90 % [41]. An additional ~0.8 mm thick layer of hyaline cartilage separates the bony endplate and the nucleus. Such layer is called cartilaginous endplate and is responsible for the exchange of nutrients from the blood vessels within the vertebra to the nucleus [65]. The nucleus is confined radially within the annulus fibrosus which is organised in 15 to 25 concentric layers called lamellae. The main component of each lamella is collagen, arranged in thick fibers running parallel to each other and anchored to the endplate [64]. The fibers are oriented at about 60° to the vertical axis and they run in opposite direction to each adjacent lamella (i.e. there is a 120° angle between fibers in adjacent lamellae) [41]. When loaded, the nucleus generates a hydrostatic pressure towards the annulus and the endplates [66]. Such pressure makes the endplate deflect [67] whilst the annulus bulges, hence putting the collagen fibers in tension. In fact, a 500 N compressive load induces a 0.7 mm bulge which results in the fibers undergoing a 2.7 % strain [68].

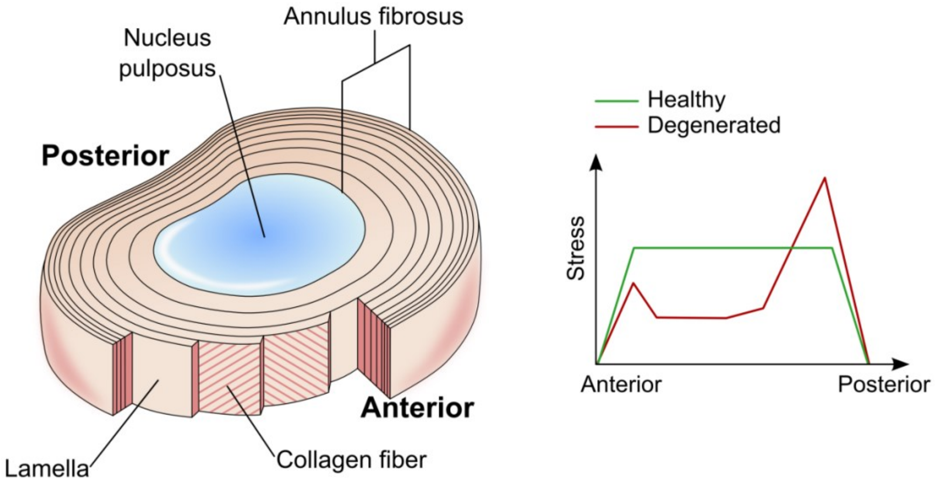

Figure 1-7: The intervertebral disc: anatomy and schematic stress profiles within the disc. Adapted from Adams et al. [66].

1.1.3 The facet joints

The facet joints (or zygapophysial joints) are two synovial joints located between the neural arches of each pair of adjacent vertebrae. The facet is a bony process that originates laterally on the neural arch; each vertebra has two superior and inferior facets. A layer of hyaline cartilage (~1 mm thick) is present onto the mating surface of each facet to allow articular motion with minimum friction. The synovium and ligamentous capsule extend from the superior and inferior margin of the joint providing, respectively, lubrication for the cartilage and mechanical reaction against separation of the joint [69] (Figure 1-8). [70][70][71]

The shape of the facet is what actually dictates the kinematics of the joint and therefore that of the functional spinal unit [41]. The facets of the thoracic spine have a flat geometry whilst in the lumbar spine they have significantly curved mating surfaces to constrain axial rotation [41]. In the thoracic region the articular surface has a typical inclination of approximately 20° with the transverse plane and 60° with the sagittal. Conversely, in the lumbar region, the facet surface becomes almost orthogonal to the transverse plane whilst their orientation increases in the caudal direction up to ~50° (i.e. the facets splay) [41].

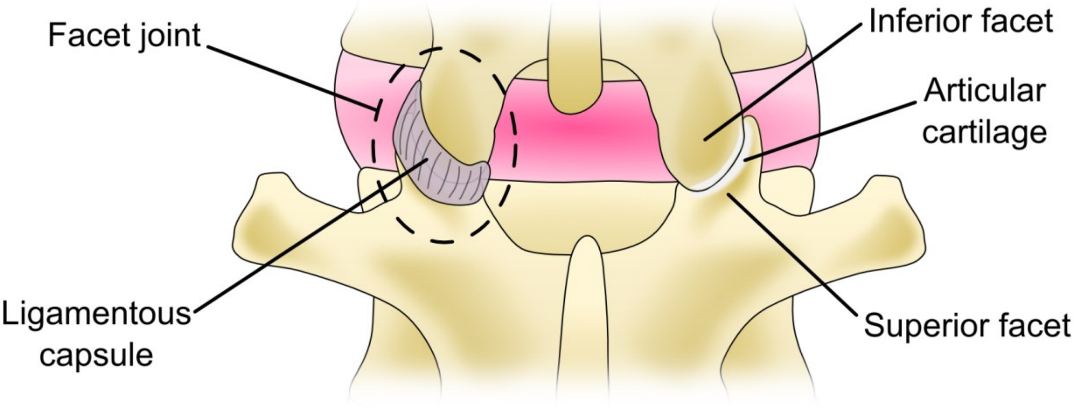

Figure 1-8: The facet joints.

1.1.4 Spinal ligaments and musculature

The spine is surrounded by a complex ligamentous structure that runs along it (Figure 1-9). Ligaments are mainly made of collagen and elastin fibers arranged in fascicles to provide uniaxial resistance. Furthermore, ligaments can respond only to tensile forces as they buckle in compression. This behaviour is due to the fibrous nature of the tissue itself. At low strains the elastin takes on the majority of the load as the collagen fibers are still crimped. Although being highly linear, the stiffness of the elastin is significantly lower than that of collagen. As the strain increases the collagen fibers uncrimp providing the actual stiffness required to withstand significant loads. Mechanical testing reflects this behaviour. There is an initial tract with low stiffness (neutral zone, NZ), followed by a higher stiffness tract (elastic zone, EZ). NZ and EZ are the physiological working regions. Exceeding EZ injuries the ligament (plastic zone) and may results in its failure [41]. Ligaments provide a passive component of stabilisation by restricting motion of the vertebrae, therefore also protecting the spinal cord [72]. They have a fundamental role in traumatic events to provide quick reaction forces against deviation from the physiological posture [41].

There are two main longitudinal ligaments running down the whole spine which have insertions on the surface of the vertebral body and disc: the anterior longitudinal ligament (ALL) and the posterior longitudinal ligament (PLL). ALL provides stability mainly in extension as it covers the anterior aspects of the spine. Conversely, the PLL stabilises mainly in flexion since it runs between the posterior wall and the spinal cord. The deposition of the fibers can originate from one vertebra and then span several levels whilst bulging of the disc contributes to their pre-tensioning [41]. This complex arrangement allows exerting the reaction force over several consecutive joints [57].

The posterior processes are connected via a set of multiple ligaments. The ligamentum flavum bridges the laminae of adjacent vertebrae and is located posteriorly to the spinal cord. This ligament is designed not to buckle (in physiological conditions) and recoil promptly in extension to avoid spinal cord impingement. Thus, the fibers of the ligamentum flavum are pre-tensioned also in the neutral position, whilst linearity of the response at low strains is given by the high content of elastin [41]. The interspinous ligament appears as a band connecting the superior ridge of the spinous process to the inferior of the adjacent one and is connected anteriorly to the ligamentum flavum. The fibers appear not to be organised as in other ligaments, thus the resistance provided in flexion is inferior [57]. The supraspinous ligament lies on the mid line of the most posterior aspect of the spinous process and bridges the interspinous spaces. The structure of the ligament is ambiguous as the deep layer is made up of tendinous fibres originating from the adjacent muscles [57].

The spinal musculature is the only active component of the spine and their function is to contribute to stabilisation and produce movements [41]. The aim of the muscles is to counteract the external loads through the modification of the shape of the spine [69]. From a functional point of view, the muscles can be generalised into four categories: superficial and deep flexors; superficial and deep extensors. Superficial muscles are usually longer, spanning several levels, and their activation controls gross movements. On the other hand, deep muscles are usually shorter and closer to the vertebral rotation axes and thus can act directly on the position of the vertebrae [72]. Preserving muscle integrity in surgery is paramount since dissection or excessive retraction of the tissue may lead to subsequent pain or disability [73].

1.1.5 Neurological structures

The neural structures (nerves) that originate from the spine deliver the neural signals from the central nervous system to the rest of the body. The spinal cord is a tubular shaped nervous tissue that begins at the brain and extends to the thoracolumbar region along the spinal canal. The distal part of the spinal cord is enlarged and cone shaped (conus medullaris) which subsequently turns into bundle of nerve roots (cauda equina) [74]. The spinal cord is enclosed within three membranes: the arachnoid, the pia mater and the dura mater; the latter is the outermost layer and covers also the cauda equina. The space between the arachnoid and the dura mater is filled with serous fluid, whilst the larger space between the arachnoid and the pia mater contains the cerebrospinal fluid [74]. The spinal nerves originate from the spinal cord, exit the dural sac (i.e. the compartment made by the dura mater), and emerge from the vertebral foramen through the region below the pedicles of each vertebra [74]. Although the function of the neural arch is to protect the nerve roots and the spinal cord, its proximity may also become critical during surgery or in the event of a fracture. In fact, in the lumbar spine the dural sac is located at 1.2 - 1.6 mm from each pedicle whilst the nerves may get as close as 1 mm from the inferior border of the pedicle [75]. The three membranes and the fluid filled spaces protect the nerves from traumas with their viscoelastic behaviour [41] (the fluids also are a mean of transport for nutrients and chemicals [76]). Being the outermost layer, the dura mater represents the first protection against neurogical injury. Therefore, it is made of dense connective tissue with a prevalent alignment of the collagen fibers along the longitudinal direction. Mechanical testing on bovine tissue has shown that the dura mater is significantly anisotropic. The tissue is indeed stiffer in the circumferential direction, although it can reach higher failure strain and stress in the longitudinal direction [77].

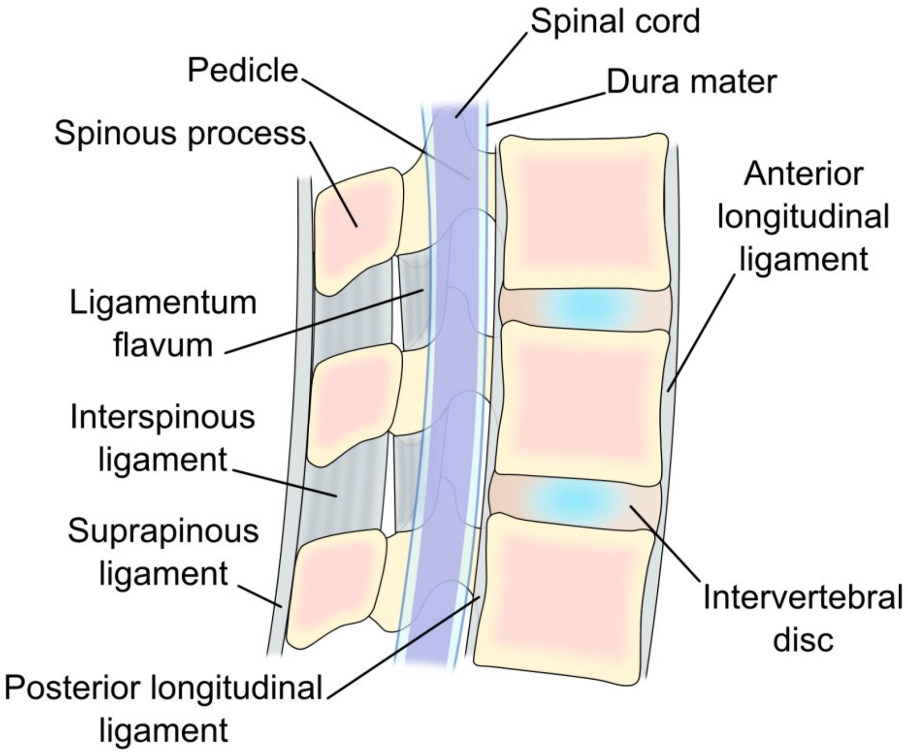

Figure 1-9: Sagittal section of the spine.

1.1.6 Spinal loads

Daily activities induce complex loading scenarios on the spine. Understanding those loads is important not only from a strictly clinical point of view, but also for the design of valid *in vitro* experiments. Several approaches have been developed to estimate spinal loads, exploiting both *in vitro* and *in vivo* measures, as well as numerical simulations. However, given the complexity of spinal biomechanics, it is difficult to provide accurate estimations, whilst each method has different advantages and disadvantages[78]. *In vivo* measures are perhaps the most representative source, although they can be invasive and affected by natural inter-subject variability [78]. Bergmann et al. [79] has provided a series of *in vivo* studies using instrumented vertebral body replacements and spinal fixators. Measurements from vertebral body replacements have shown that the resultant force exerted during level walking can reach about 170 % of that measured when standing (ranging 100 - 300 N between two subjects). Loads increase when performing activities involving upper body flexion (e.g. ascending/descending stairs), during which the resultant can exceed 250 % of the standing force [80]. The direction of the resultant force acting on the vertebral body replacement during common daily activities can be approximated to span a cone with an aperture of 15°. This angle was estimated in a previous work [81], using data available from [79]. Measures over 10 patients with instrumented spinal fixators have shown that walking, as well as ascending/descending stairs, induces a peak bending moment of ~110 % of standing value [82]. Similar trends have been found also in another study where walking has induced a maximum bending moment ranging from 2 – 9 Nm and a maximum resultant force ranging from 50 – 400 N on the fixator rods [83]. However, it must be borne in mind that those *in vivo* measurements are not representative of a physiological condition and that instrumented implants share loads with other spinal structures (e.g. bone grafts, facet joints) [80].

An alternative site of measure is the intervertebral disc. Wilke et al. [84] has provided *in vivo* measurements by inserting a pressure transducer within the nucleus, showing an increase from 0.5 MPa when standing, to 2.3 MPa when lifting a 20 kg weight. McNally et al. [85] developed an *in vitro* stress profilometry technique, which was extensively used by Adams and his group [86-88]. The stress profile is obtained by inserting a transducer (continuously recording pressure) through the disc and then sliding it to the opposite side whilst the spine undergoes a constant load. Results showed that, in a healthy disc, the internal stress increases from the outer annulus towards the nucleus, where a plateau is reached (i.e. hydrostatic pressure condition). Conversely, a degenerated disc showed an altered load transfer, with stress concentration in the middle annulus and reduced stress within the nucleus [66] (Figure 1-7). Such technique may also be used to estimate the force transmitted to the endplate. If the geometry of the disc is known, the integral of the pressure over the CSA will provide the force borne by the disc itself [89], although corrections factors may be required [90]. *In vivo* data were then used to estimate forces of about 400 – 600 N when standing, which may reach 1200 – 1500 N when bending forward [91-93].

Together with the intervertebral disc, the facet joints are responsible for transmitting the whole load between two adjacent vertebrae, with the facets bearing about 2 - 7 % of the force in axial compression [70]. Furthermore, the load sharing between the disc and the facet joints depends on posture: the more the extension the more load sharing shifts posteriorly [70]. In addition, the facet joints have a substantial role in resisting anterior shear, by bearing 55-65 % of such loading component [71].

Numerical modelling has the great advantage of being non invasive whilst allowing replicating several loading conditions, although requiring a thorough validation process to achieve sufficient accuracy [78]. Dreischarf et al. developed an FE model of the disc, which was validated using force estimations from intradiscal pressure measurements [90]. Results predicted forces ranging 430 – 600 N when standing, with an error below 4 %. An alternative numerical approach is multibody dynamics, where bones are typically modelled as rigid segments undergoing forces exerted by multiple muscle groups (i.e. output of the model). External forces and kinematic can be measured *in vivo* non invasively (e.g. gait analysis) and then used as input for the model, as boundary conditions or for its validation. This method has allowed generating complex spinal models with up to 18 degrees of freedom and 154 muscles, estimating up to 238 Nm occurring at L5-S1 in extension [94]. The same approach was exploited to estimate a moment of 8 Nm acting on L1 when standing with both arms elevated, which increased by 5 Nm per additional kg of weight held in the hands [95].

1.1.7 Spinal kinematics

Each pair of adjacent vertebrae (together with the disc and facets) can be seen as an independent six degrees of freedom joint. Therefore, the overall kinematics of the whole spine is the complex resultant of the kinematics of all intervertebral joints. An alternative definition of spinal instability is indeed the incapacity of the spine to counteract motion that deviate from its own physiological kinematics [41, 57].

When each level is considered individually, the flexion/extension ROM in the thoracic spine increase caudally from 3 - 5° at the top levels, up to 6 - 20° at the thoracolumbar junction. The lateral bending shows a similar trend, ranging 5 – 10° on the frontal plane at the thoracolumbar junction. On the other hand the axial rotation decreases in the caudal direction from ±14° to 2 - 3° [41]. In the lumbar spine ROM for flexion/extension keeps increasing downwards up to 10 - 24° where L5 joints with the sacrum. Axial rotation and lateral bending ROM are approximately constant along the lumbar levels, ranging 1 - 3° and 3 – 10°, respectively [41]. However, it is worth noting that the trend of ROM in axial rotation actually follows that of the geometry of the facet joints (see 1.1.3).

Spinal motions which are usually approximated as uniplanar (e.g. flexion/extension, lateral bending) are actually achieved through a combination of several movements on multiple planes occurring at different levels [41]. However, during daily activities the ROM undertaken by the lumbar spine is relatively limited. Direct measurements of lordosis angle show that out of the 4400 spinal movements performed daily, 66 % of them are within 5 - 10°. This does not account for walking, where the change in the lordosis angle is usually less than 5° [96]. In fact, an average person is estimated to make two million strides (i.e. one million gait cycles) and 125000 significant bends per year [97].

1.2 Aetiology of vertebral fractures

Vertebral fractures occur when the loading conditions exceed the strength of the vertebrae [45]. However, the mechanism and outcome of that event is an extremely complex topic which involves several factors. Bone quality is a fundamental discriminant in the mechanics of traumatic and pathological fractures. Pathological conditions hinder bone quality and physiological loads may become too demanding for the vertebral structure. Therefore, daily activities may induce a micro-damage whose continuous accumulation causes back pain and may lead to fracture [98]. Conversely, traumatic fractures arise when the spine undergoes non physiological and extreme/impact loading conditions. Dissipation of such a high amount of energy may result in the fracture of the vertebra and/or damage to spinal soft tissue [41].

1.2.1 Fracture classification

Effective fracture classification is paramount to assess the nature of the injury, allow communication among the clinicians and aid planning of treatment [99]. In order to better understand the failure mode of the spine, Denis has considered each spinal segment as made by three biomechanically relevant columns (Figure 1-10) [15]. Although no exact anatomical demarcation exists, the three regions can be defined as follows:

- Anterior column: represents the anterior part of the vertebral body and disc, including the ALL.
- Middle column: represents the posterior part of the vertebral body and disc; including the posterior wall, the root of the pedicles and the PLL.
- Posterior column: represents the posterior part of the spinal segment; including the neural arch, facet joints and posterior ligamentous complex.

Denis developed a classification of the spinal injuries based on the failure mode of those three columns [15]. Magerl et al. extended the Denis classification with morphological considerations on the appearance of the fracture and developed a more comprehensive spinal injury classification [18] (Table 1-2). Although several classification systems can be found in the literature, the Denis and Magerl classifications are the most popular and widely used in the clinical literature [16, 100, 101].

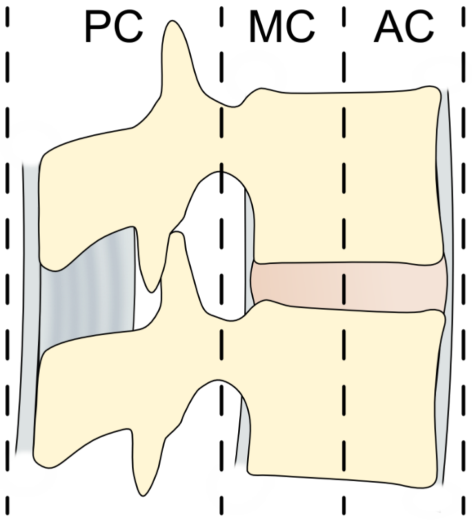

Figure 1-10: The Denis three column concept. AC: anterior column; MC: middle column; PC: posterior column. Adapted from [15].

Table 1-2: Overview of the Magerl injury classification [18].

Subgroup	Type A Vertebral body compression	Type B Anterior and posterior element injury with distraction	Type C Anterior and posterior element injury with rotation
1	Impaction fractures	Posterior disruption predominantly ligamentous	Type A injuries with rotation
2	Split fractures	Posterior disruption predominantly osseous	Type B injuries with rotation
3	Burst fractures	Anterior disruption through the disc	Rotational-shear injuries

Morphological fracture classification has often aimed at providing insight about the extent of the neurological deficit [15, 99]. However, it is extremely difficult to integrate a formal description of the deficit with that of the fracture [100, 101]. Therefore, the Frankel system [102] is commonly used to independently assess neurological impairment (Table 1-3).

Table 1-3: Frankel grading system for neurological impairment [102].

Classification	Injury severity
A: Complete	No motor or sensory function
B: Sensory only	Sensory function but no motor function
C: Motor useless	Some motor function present but not useful
D: Motor useful	Motor function present but weak
E: Intact	Normal sensory function

Radiographic assessments are performed to quantify the alignment of the spine and the deformity caused by the fracture as well as the success of a treatment in restoring/maintaining the spinal geometry [103]. The features typically evaluated are sagittal alignment, vertebral body height and spinal canal area. However, different relevant measures can be taken from plain radiographs as well as CT scans [22, 104, 105]. Variation with respect to intact conditions is usually approximated by estimating the intact value from the average between that measured from the two adjacent vertebrae [31]. A common parameter used to assess sagittal deformity is the Cobb angle which is defined as the angle between a line parallel to the cranial and caudal endplate of the vertebrae above and below the fracture [103]. Alternatively, the two lines can be taken directly from the endplates of the fractured vertebra. Both methods have been shown to be reliable and repeatable, though the first is considered to be the best choice [106]. Although the Cobb Angle was initially developed to measure deformity on the frontal plane (e.g. scoliosis), it is now extensively used in fracture assessment as well as progression of related deformity [103].

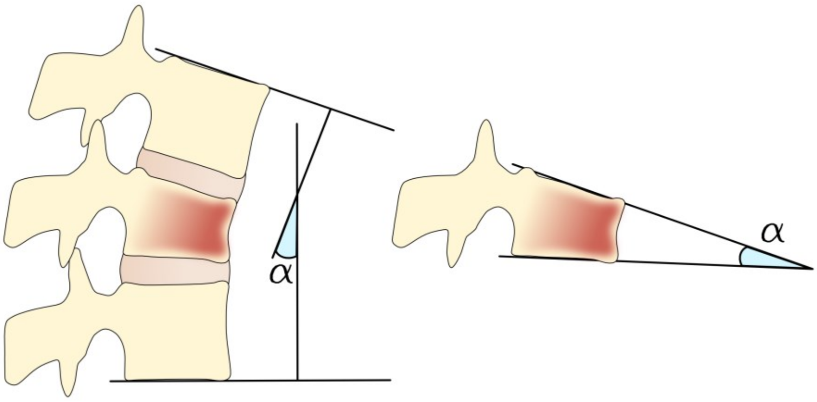

Figure 1-11: Definition of the Cobb angle for sagittal alignment in a fracture case. The two approaches should provide the same angle. Adapted from [106].

1.2.2 Cancer

MM is a malignancy of plasma cells which causes: replacement of bone marrow cells by myeloma cells, diffuse osteopenia, bone destruction, renal injuries and systemic harmful deposit of proteins [107]. Spinal biomechanics is mostly affected by the origination of osteolytic lesions, usually small sized and spread all over the vertebra [108]. The most common symptom is indeed bone pain, present in up to 70 % of patients [8]. However, the aetiology of MM is still unknown [107].

About 30 % of metastases arising from primary tumours are located in the spine [109] and they are mostly associated with breast, lung, renal, prostate, thyroid, melanoma, lymphoma and colorectal cancer [10]. Metastatic infiltration usually results in focal lesions where bone is replaced by cancerous soft tissue enclosed within a layer of fibrous tissue and immature bone. Depending on the degree of spreading the lesion can breach the cortical shell, as well as invade the foramen, compressing the spinal cord [110].

Disruption of the trabecular bone architecture results in structural weakening that may lead to fracture [111]. Typical fractures involve the failure of the anterior column whilst the middle column is intact and acts as a hinge [15]. This type of fracture is commonly called wedge fracture because of the significant loss of anterior height, resulting in an increase of the kyphotic angle of more than 5° [18]. Compression fractures may also occur, which are caused by failure of the anterior column and partial failure of the middle column (without ligamentous injury) [15]. Compression fractures usually present a change in shape of the endplates (increased curvature) as well as anterior and posterior height loss. Both wedge and compression fractures are characterised by compaction of trabecular bone rather than fragmentation [18]. This type of fractures is classified as A1 according to the Magerl system. They are stable fractures with no failure of the posterior wall, thus significant neurological involvement is quite rare [15, 18].

1.2.3 Osteoporosis

Osteoporosis is a metabolic disease which results in loss of bone mass and deterioration of the bone micro-architecture. It mostly affects the bony structures where the trabecular bone is prevalent, such as the femoral neck, wrist and vertebral body. Therefore, the weakened structure becomes susceptible to fracture. The pathology mostly affects women as the post-menopausal oestrogens deficiency enhances the bone resorption activity of osteoclasts [5].

Vertebral fractures associated with osteoporosis are overall similar to those caused by cancer (1.2.2).

1.2.4 Trauma

Traumatic fractures are a significant cause of neurological injuries and spinal instability. Events like distraction of the spine, disruption of the posterior ligamentous complex and fragmentation of the vertebra expose the neurological structures to dangerous mechanical stimuli. Although type A fractures (vertebral body compression) account for 66 % of cases, the majority of neurological injuries happen in type B and C fractures where there is disruption of the spinal structures and/or rotation. In fact, 32 % of type B and 55 % of type C fracture present some neurological impairment [18].

Traumatic fractures mostly occur in young adults (median age 36 years) since they have a more active lifestyle and are more involved in motor accidents [13, 112]. Therefore, bone quality is usually higher in traumatic patients compared to pathological fractures [5, 111]. However, in some pathological cases minor overloads may exceed the vertebral strength and induce a trauma-like fracture. The voids created by metastatic infiltration may indeed weaken the vertebral structure to the extent of causing a burst fracture [9].

1.2.5 Burst fracture

Burst fractures account for about 28 % of all spinal injuries, which makes them the most common type of fracture after A1 (compression) [18]. The most common causes of fracture are falls from height and motor vehicle accidents [112]. In a study from Meves et al., 77 % of burst fractures they investigated were the result of a fall from height whilst 19 % were related to motor vehicle accidents [21]. Due to the traumatic nature of the fracture, they are inherently a severe cause of neurological deficit. The incidence of neurological impairment (i.e. A, B, C and D Frankel grades) has been reported to vary from 32 to 47 % [15, 18].

The majority of burst fractures happen at the thoracolumbar junction (T12-L1-L2), where the incidence of acute neurological injuries has been reported to range from 48 to 77 % [113]. Results from Bensch et al. [104] show a fracture distribution amongst the spinal regions of 11 % cervical, 21 % thoracic, 45 % thoracolumbar junction, 23 % lumbar. The biomechanics of the thoracolumbar junction makes it more prone to injury, compared to the rest of the spine. The region is typically either straight or slightly kyphotic (0° - 10°), which makes axial compression the major force component [42]. The loading conditions also change as shown by the anatomical changes of the facet joints as well as vertebral body (see 1.1.1 and 1.1.3). In addition, stress concentration happens as a result of the transition between the stiff kyphotic thoracic region and the lordotic lumbar region. However, there has been a rise in low lumbar burst fractures in recent years amongst the military population due to the nature of current military deployments. The main causes of the fracture are helicopter crashes [114] and underbody blasts [115] where the spine undergoes extremely high acceleration rates (up to 400 m/s^2 in helicopter crashes and even higher in underbody blasts [114]). It has been supposed that the loading conditions in combination with the stiffness of body armours result in a shift of the transition zone downwards, hence making the lower lumbar spine more prone to burst [116].

A burst fracture has been defined by Denis as failure by axial loading of the anterior and middle column whilst the posterior column remains intact [15, 18]. The failure of the middle column may also cause rupture of PLL and/or annulus of the disc [15]; disruption of PLL has been confirmed in 28 % of thoracolumbar burst fractures [113]. Conversely to the classical Denis definition, several clinical series have reported disruption of the posterior ligamentous complex, which severely aggravated spinal instability [19, 105, 113]. However, soft tissue injuries require magnetic resonance imaging (MRI) to be adequately diagnosed [105].

The main features of a burst fracture detectable from radiographic assessment of are [18]:

- Partial or complete comminution of the vertebral body.
- Failure of the posterior wall with retropulsion of fragments within the spinal canal.
- Spinal canal occlusion (SCO).
- Interpedicular widening (IPW).
- Possible laminar fracture (LF).

In addition, Magerl et al. have identified nine subtypes of burst fractures based on their CT morphology (Table 1-4). Incomplete burst fractures denote only partial burst of the vertebral body thus either the superior, inferior or lateral portion. Therefore, only one of the endplates appears to be comminuted although additional flexion/extension may cause retropulsion of the fragments within the canal. Burst-split fractures show an incomplete burst of the vertebral body together with a split fracture on the sagittal plane through the opposite endplate. Those fractures are associated with more instability than incomplete burst fractures. Complete burst fractures represent the most unstable type of burst fractures and are characterised by complete burst of the vertebral body and acute kyphosis. Both the endplates are comminuted and the spinal canal is usually extremely narrowed because of fragment retropulsion (Figure 1-12).

Table 1-4: Magerl classification for burst fractures [18].

Subgroup	Type A3.1. Incomplete burst fracture	Type A3.2. Burst-split fracture	Type A3.3. Complete burst fracture
1	Superior incomplete burst fracture	Superior burst-split fracture	Pincer burst fracture
2	Lateral incomplete burst fracture	Lateral burst-split fracture	Complete flexion burst fracture
3	Inferior incomplete burst fracture	Inferior burst-split fracture	Complete axial burst fracture

Despite the details offered by the different fracture classifications, there is still lack of agreement about the requirements to consider a burst fracture unstable [117]. Petersilge et al. [113] have associated instability in the thoracolumbar spine with:

- IPW and increase of interlaminar distance.
- Translation of more than 2 mm and dislocation.
- Kyphosis of more than 20°.
- Fracture of posterior articulating process.
- Height loss of more than 50 %.

Preservation of the facet joint capsules and posterior ligamentous complex has been recently considered paramount for stability [34]. In addition, comminution of the endplates causes a disruption of the metabolism of the intervertebral disc as well as a change in load transmission. Loss of disc integrity with intrusion of material within the vertebral body is commonly seen on MRI scans [118]. *In vivo* data have confirmed an increased disc cell apoptosis rate following trauma which may lead to degeneration [119]. Definite disc degeneration, involving both the nucleus and annulus, has also been found in cultured rabbit discs which underwent a burst fracture [120].

1.2.5.1 Spinal canal occlusion

The extent of SCO has been traditionally associated with neurological deficit. However, the relationship between the two phenomena is poorly understood and discordant results are present in the literature [104]. Meves et al. [21] has reported a correlation with SCO (range 33 – 70 %) and neurological injury only for incomplete deficits (Frankel grade E to B). On the other hand, they have reported similar SCO for Frankel grade E (33 %) and A (39 %). In Deng et al. [121], no relationship was found between SCO and Frankel grade in thoracolumbar burst fractures with neurological deficit.

The extent of the neurological deficit strongly depends on the level where the fracture occurs, probably because of the histological organisation of the neurological structures. The cauda equina appears to be less sensitive to impact loading but more to continuous compression [15]. It has been reported that SCO up to 60 - 90 % in the lumbar spine may not cause any deficit [15, 34], whilst Frankel B deficit has been diagnosed at T12 with 25 % SCO [15]. In the study from Hashimoto et al. [122], a threshold value of SCO has been associated with the presence of neurological deficit as follow:

- 35 % SCO at T11 and T12.
- 45 % SCO at the level of the conus medullaris.
- 55 % SCO at the level of the cauda equina.

Yugué et al. [19]performed a logistic regression combining kyphotic angle, SCO, disruption of the posterior ligamentous complex and spinal level as risk factors. No significant association between SCO and neurological deficit has been found when considering L1 alone, only the disruption of the posterior ligamentous complex was a significant risk factor. On the contrary, SCO has appeared to be a significant risk factor when all the samples were considered together or different regions were considered independently (Table 1-5).

Table 1-5: Average SCO grouped for different regions of the spine divided by presence of neurological deficit [19].

	All cases	T11 and T12 cases	L1 cases	L2 to L5 cases
Deficit	60.3 %	54.3 %	48.1 %	76.3 %
No deficit	52.0 %	28.9 %	47.1 %	59.8 %
Significance	$p<0.05$	$p<0.05$	$p>0.05$	$p<0.05$

The significance value refers to the results of the multiple logistic regression by Yugué et al. [19].

Vaccaro et al. [20] have not found any significant association with neurological injury when considering the areal SCO. On the contrary, a significant association has been shown when considering the transverse and sagittal diameter of the canal. Similarly, Hashimoto et al. [122] have identified a lower incidence of neurological injuries in the patients where the shape of canal was more circular or semi-circular. Those findings confirm that neurological injuries are more susceptible to the shape of the canal rather than its absolute size [20]. Given the complexity of the phenomenon, studies have suggested that other parameters must be involved in the origination of the injury [21].

1.2.5.2 Interpedicular widening

IPW is one of the hallmarks of burst fracture, as well as failure of aspects on the neural arch [15, 18]. Hashimoto et al. [122] has reported disruption of lamina and pedicles in 29 % of cases and disruption of the facet joints in 47 %. IPW in burst fractures can vary enormously: clinical measurement may range 3 - 54 % [123] as well as 5 – 114 % [23]. In addition, there is an increasing trend from thoracic to lumbar region (Table 1-6). Daffner et al. have suggested [124] that an IPW of more than 2 mm with respect to the average of the two adjacent levels is to be considered indicative of a non-physiological condition. The relationship between the severity of burst fractures and IPW has been investigated by Caffaro et al. [23]. IPW has appeared to be significantly lower in patients without any neurological deficit (15.3 ± 11.9 %) compared to those with deficit (24.7 ± 12.6 %). In addition, a ~25 % IPW has been shown to be associated with a 50 % probability of neurological impairment and the risk increases to 80 % when IPW is ~55 %.

Table 1-6: Average *in vivo* values of IPW in spinal burst fractures by spinal regions (mean ± standard deviation).

	Cervical	Thoracic	Thoracolumbar	Lumbar
Bensch et al. [104]	4.5 ± 3.4 mm	0.8 ± 1.8 mm	2.6 ± 2.2 mm	3.5 ± 3.3 mm
Caffaro et al. [23]	–	25.4 ± 20.0 %	35.8 ± 19.1 %	46.4 ± 20.3 %

A dural tear is a laceration of the dura mater hence causing nerve entrapment and leakage of cerebrospinal fluid. If not treated, the leakage may lead to meningitis and post-traumatic meningocele [22, 125]. Dural tears have been detected in 25 % of lumbar burst fractures and they have been associated with IPW [126] and neurological compromise [123]. In addition, surgical intervention without identification of the laceration may result in additional damage to the dura mater and iatrogenic neurological injury [22]. Lee et al. has found an increased risk of dural tears when the interpedicular distance exceeds 28 mm [125]. A significant difference in the interpedicular distance has been also identified by Park et al. [22] if a dural tear is present (32.4 ± 3.9 mm) or absent (28.4 ± 3.8 mm).

1.2.5.3 Laminar fractures

LFs are mostly present in complete burst fractures [31] and are associated with significantly higher SCO and IPW (Table 1-7).

Table 1-7: Differences in IPW and SCO in presence of LF (clinical data).

		Presence of LF	Absence of LF
IPW	Caffaro et al. [23]	25 ± 16 %	13 ± 8 %
SCO	Tisot et al. [127]	47 ± 18 %	28 ± 14 %

Although their contribution to instability is negligible [18], the likelihood of neurological deficit increases when in presence of LF [23, 125]. In particular, LFs have been detected in every case where also dural tears were diagnosed [123] and neural elements have been often found entrapped within the edges of the fracture [123, 128]. Moreover, the width of the LF is significantly higher when dural tears are diagnosed, making it a severe risk factor (Table 1-8). However, there appear to be no clear guidance to the diagnosis of dural tears in relation to LF and IPW [22].

Table 1-8: Average width of the laminar fracture in presence of a dural tear (clinical data).

	Presence of dural tear	Absence of dural tear
Ozturk et al. [126]	4.4 mm	1.9 mm
Lee et al. [125]	1.8 mm	0.9 mm
Park et al. [22]	2.4 ± 1.2 mm	1.0 ± 0.6 mm

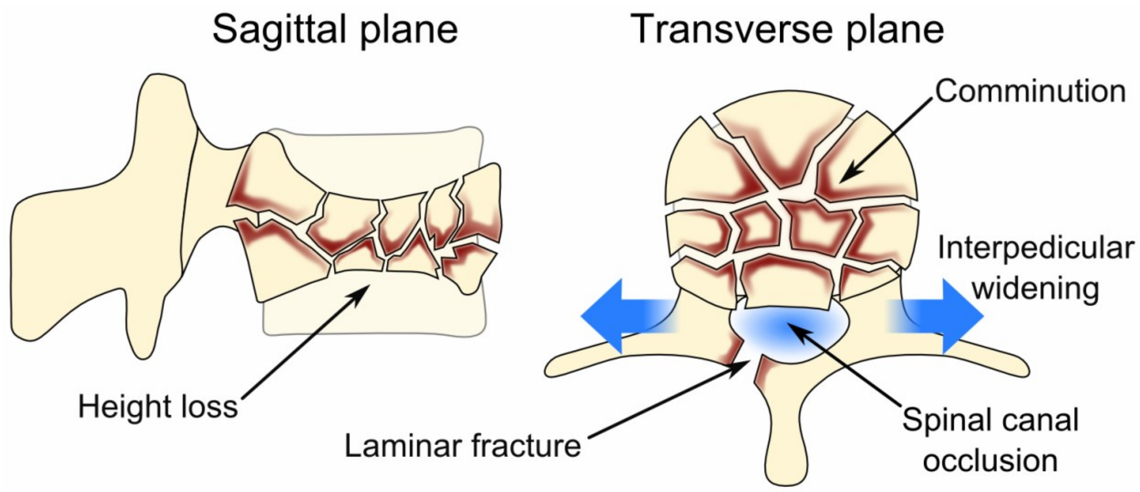

Figure 1-12: Complete burst fracture type A3.3.3 according to Magerl classification. Adapted from [18].

1.3 Clinical management of spinal burst fractures

Definition of the optimal treatment for spinal burst fractures is highly debated and has led to much discussion in the literature [30, 32, 129]. Furthermore, timing of the intervention is extremely important as early management (<72 hours) has been proved to reduce morbidity [130, 131]. The aim of the treatment is the restoration of spinal biomechanics and quality of life, which is paramount as only 54 % of all patients with spinal injuries return to their previous level of employment [132]. The restoration of spinal biomechanics requires providing stability and load bearing capability as well as correction of deformity and avoidance of any further kyphosis or vertebral body collapse [133].

The choice between non-operative and surgical treatment is the first hurdle that clinicians face at presentation of the patient. Supporters of non-operative treatment advocate that conservative intervention reduces costs, risks of complications and iatrogenic injury [30]. Several works have shown that conservative treatment can be as successful as operative treatment in terms of pain relief and spinal alignment at follow-up [29, 30, 117]. Non-operative treatment consists of bed rest, functional rehabilitation and body orthosis, requiring an average hospitalisation of ~30 days [31, 117]. In their case series, Mumford et al. [31] have reported an 8 % vertebral body height loss at two year follow-up. On the other hand, they have detected a reduction of SCO from 37 to 14 % (e.g. resorption of bony fragment) within the first year. However, non-operative treatment is advised only in case of stable fractures without neurological deficit [34, 117].

In presence of neurological deficit or severe instability surgical intervention is usually undertaken. Additional recommendations for surgery are [22, 30, 117]:

- SCO more than 50 %.
- Vertebral body height loss more than 50%.
- Kyphotic angle more than 20-25°.

There are three main surgical approaches [117]:

- Anterior approach: used to perform reconstruction and stabilisation of the vertebral body. It usually requires vertebral body replacement or a plate to bridge the fracture.
- Posterior approach: posterior spinal instrumentation constructs are implanted through dorsal opening. Additional transpedicular techniques (e.g. kyphoplasty) may be performed.
- Combination of anterior and posterior approach: this is the most invasive approach and it is chosen in the most severe cases.

Surgical intervention also allows direct nerve decompression to tackle neurological deficit and inflammation. For instance, laminectomy is a procedure where the lamina is removed to reduce the pressure against the neurological structures. However, the facet joints are kept intact and keep providing load transfer.

1.3.1 Short segment spinal instrumentation

Spinal instrumentation consists of fixator rods connected to the spine by means of hooks or bone screws. Therefore, the fixator rods become an additional load bearing structure, relieving the injured level from part of the load. The aim is to provide stability, protect neurological structures and permit ambulation whilst the injury heals and bone union occurs [133].

Pedicle screws are the most common type of fixation device. They are inserted from the dorsal cortex of the lamina to reach the core of the vertebral body through a transpedicular trajectory [134] (Figure 1-13). Pedicle screw fixation can be used in case of laminectomy or LF as it does not depend on the integrity of the lamina [133]. The head of the screw (or the nut connected to it) provides housing for the fixator rod to be fastened within. In polyaxial screws the nut is free to pivot with respect to the head (Figure 2-2). Hence, rod alignment is not constrained by that of the screw (conversely to monoaxial screw). The mechanism is designed so that the nut locks in place when the grub is tightened to fasten the rod. Together with the design of the screw, accurate positioning and trajectory is paramount for the success of treatment. Tapping the pilot hole is considered to improve trajectory [135], although reducing pull-out strength [136]. Insertion torque is generally considered by surgeons a good feedback for screw purchasing, however it has been shown not to be a good predictor of long-term loosening [137]. Radiographic assessment has shown that loose screws present a radiolucent zone around the thread indicating a lack of purchase [138].

Long-segment posterior instrumentation (LSPI) is the oldest approach and involves bridging the fractured vertebra/vertebrae over several spinal levels, hence using long fixator rods. Conversely, in short-segment pedicle instrumentation (SSPI) pedicle screws are implanted only one level above and below the fracture (involving only three adjacent vertebrae). Although LSPI overall provides more stability and correction, SSPI has been proved to be as effective as LSPI in several cases in terms of correction and disability scores [33, 117, 139]. In addition, SSPI results in significantly shorter operation time and less blood loss, therefore reducing costs and risk of complications [140]. SSPI is currently the most widely practiced intervention for spinal burst fractures [133].

Implanting posterior instrumentation also allows the surgeon to perform reduction manoeuvres to re-align the spine (i.e. ligamentotaxis). This is achieved by exerting forces through the screws as well as appropriate positioning of the fixator (may require rod contouring to follow the spinal curvature). The exerted forces result in tensioning the ligaments hence reducing the fragment of the fractures. Leferink et al. [141] measured SCO at admission and post-operatively showing a decrease from 76.5 to 18.4 % obtained through ligamentotaxis and SSPI. In addition, at two year follow-up, about 97 % of all patients have shown complete clearance of the spinal canal due to successful bone remodelling. A similar trend has been shown also by Mohanty et al. [142] where SCO has decreased from 47.4 to 26.6 % post-operatively and down to 14.9 % at follow-up.

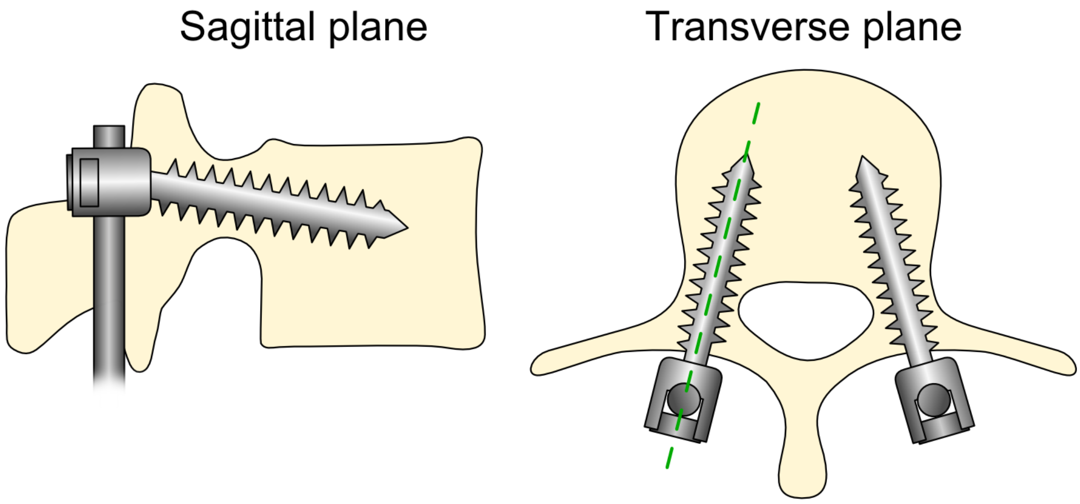

Figure 1-13: Alignment of pedicle screws within the vertebra in SSPI.

Fusion has been used in combination with posterior instrumentation to achieve better stabilisation through the formation of an additional load bearing structure. *In vivo* measurements have shown a decrease of strain on the lamina as fusion progresses [143]. However, grafting does not seem to help maintaining the correction when performed with SSPI in thoracolumbar burst fractures [133]. Moreover, many patients undergoing fusion have long-term harvest site pain without any actual improvement in terms of quality of life [144].

As mentioned above, SSPI is widely used but clinical outcomes appear not to be consistent (Table 1-9), showing good initial re-alignment followed by progressive kyphosis and vertebral body compression. Although the technique has proven significantly better initial pain relief and correction when compared to non-operative treatment, Shen et al. [145] have obtained the same correction results at two years, with the conservative treatment being four times cheaper. The cause of dissatisfactory results may lie in the lack of anterior support in SSPI. Whilst it can provide indirect reduction of the fracture, there is no direct intervention on the vertebral body. If the anterior and middle column cannot bear the load shared with the fixators, then the SSPI construct is deemed to fail [34, 133]. In such conditions the axial load is transferred to the screws in a more demanding cantilever bending mode which loosens the screw hence decreasing their purchase. As kyphosis progresses again, loads shift anteriorly resulting in stress concentration and increased moments acting on the rods. The lack of stability induces further aggravation of kyphosis and loss of vertebral body height hence leading to a vicious cycle whose result is implant failure. Although Wei et al. [146] have found similar failure rates in LSPI and SSPI (5 – 6 %), McLain et al. [139] have reported an implant failure rate as high as 15 % (5 % requiring revision) with 33 % of patients showing a 10 – 20° progressive kyphosis.

As mentioned above, a combined anterior and posterior approach can be undertaken to stabilise the anterior column. Anterior reconstruction requires removal of the fragments and replacement of the vertebral body with a vertebral body replacement and/or bone graft [34]. It is surgically more challenging and thus it comes at higher costs and risk for complications [117]. Orthosis can be used as a conservative aid to provide additional support during fracture union. However, *in vivo* measurement have shown that wearing a brace only provide a negligible reduction of the load borne by the fixators [83].

SSPI may be removed after 8 – 12 months from surgery to allow higher mobility to younger patients. However, it requires further surgery with subsequent iatrogenic effects and increased risk for recurrent deformity [147].

Table 1-9: Clinical outcomes of SSPI.

	VB compression (%)			Kyphosis (°)		
	Pre	Post	FU	Pre	Post	FU
Deng et al. [121]	60 ± 9	–	28 ± 12	17 ± 7	–	8 ± 5
Muralidhar et al. [148]	–	–	–	24	–	13
Parker et al. [33]	–	–	–	11	-1	3
Sanderson et al. [149]	38 ± 14	16 ± 7	21 ± 9	21 ± 9	6 ± 3	14 ± 8
Shen et al. [145]	–	–	–	23 ± 6	6 ± 8	12 ± 8
Tezeren et al. [140]	41 ± 14	5 ± 1	15 ± 1	19 ± 1	4 ± 1	10 ± 1
Wang et al. [150]	44 ± 13	10 ± 16	14 ± 15	25 ± 6	8 ± 6	9 ± 6
Yang et al. [151]	46	3	11	20	3	8

VB compression: percent loss of VB height with respect to intact conditions; Pre: pre-surgery; Post: post-surgery; FU: follow-up.

1.3.2 Kyphoplasty

Kyphoplasty (KP) is a cement augmentation technique which combines vertebroplasty (VP) with direct reduction of the fracture. Cement augmentation is a minimally invasive procedure where bone cement is delivered within the vertebral body. In order to provide better mechanical stability, the cement bolus should ideally be located within the anterior third and centre of the vertebral body [152]. The pain relief effect has been supposed to arise from the stabilisation of the micro motions within the fracture [153]. The peculiarity of KP is the uses of an inflatable balloon tamp (IBT) mounted on the tip of a thin cannula to reduce the fracture prior to cement injection. The aim of the reduction is restoration of the vertebral body height as well as correction of kyphosis. Fluoroscopic imaging is commonly used throughout the procedure to provide real-time assessment and guidance. KP is carried out as follows (Figure 1-14) [152]:

1) With the patient prone, a cannula is inserted through each pedicle by breaching through the posterior cortex of the lamina. The cannulae are advanced towards the anterior portion to suit the target alignment. The outcome of the procedure strongly depends on the correct initial positioning of the cannulae. If both the endplates are compromised than a more horizontal trajectory is preferred. On the other hand if only one endplate is compromised, then the IBT should be closer to the opposite endplate hence allowing room for adequate reduction of the fragments.
2) The stylus is removed from the cannula (the cannula is now a port within the vertebral body) and the hand drill is inserted to create a channel within the trabecular structure for the IBT up to 2 - 3 mm before the cortical wall.
3) An IBT is inserted through each cannula and progressively inflated to obtain a uniform reduction of the fragments. The inflation is stopped when satisfactory realignment of the endplates is achieved, the IBT is in contact with the cortical shell or the maximum pressure/volume of the IBT is reached.
4) Following deflation, the IBT is removed and bone cement is injected through the cannula until considered satisfactory. Care is taken to avoid leakage of cement in the paravertebral space.

Polymethylmethacrylate (PMMA) has been firstly used as cement for VP and it is still the most popular choice for wedge fractures [154]. However, in recent years ceramic cements have become more popular due to their osteoconductivity and potential for resorption. Calcium phosphate (CaP) cements are one the most commercially used formulations and *in vivo* studies have proved their osteoconductivity and better integration in comparison to PMMA. Libicher et al. [155] have shown resorption at the interface of the CaP cement bolus at 12 months post-KP, as well as significant higher presence of osteons and better bone contact. Likewise, Chen et al. [156] have found in SSPI – VP (with calcium sulphate cement) patients a gradual resorption at 12 weeks with substantial resorption at 12 month follow-up. However, a fraction of the cement will always remain, since maximum resorption at 10 year follow-up has not exceeded 56 % (average 23 %) of the initial cement volume [154]. Conversely to PMMA, ceramic cements do not set by means of a polymerization reaction. Due to the nature of the compound, ceramic cements set by forming crystals through a slow reaction at body temperature [157]. CaP cement is therefore considered safer than PMMA, not only because less toxic [157], but also because the high temperatures reached during polymerisation may cause tissue necrosis and/or neurological damage in the event of leakage [39]. Complications due to cement leakage may be catastrophic, leading to paraplegia and even death [158]. Due to the comminuted nature of burst fractures, the risk of cement extravasation is higher than in wedge fractures and therefore PMMA augmentation is often ill-advised [117]. On the other hand, CaP cement is more expensive than PMMA whilst having inferior mechanical properties [157]. However, Grafe et al. [159] have obtained similar *in vivo* outcomes in terms of pain relief and height restoration comparing PMMA and CaP KP for osteoporotic compression fractures.

KP is a relatively new treatment option in burst fractures and several surgeons have advised using CaP cement because of the younger age of the patients [38, 160]. Younger patients can indeed benefit more from the osteoconductivity of the biomaterial through the promotion of bone integration and resorption [154]. On the contrary, PMMA augmentation would result in an inert mass of resin within the vertebral body, which, in combination with the necrotic effect of the polymerisation reaction, may lead to degenerative problems in the long term in young patients [161]. Clinical outcomes of CaP KP for trauma patients have been so far satisfactory. Maestretti et al. [154] have studied 21 patients and at 10-year follow-up they have shown an improvement of the disability scores with no evidence of disc degeneration. In addition, kyphosis progressed by just 1° (from 10 to 11°) whilst there were no signs of vertebral height loss. However, the authors have not observed as much cement resorption as expected.

Consistency of KP strongly depends on accurate planning of the cement volume to be injected [162]. In fact, cement volume is considered the most relevant predictor of pain relief. Röder et al. [163] have recommended injection volumes higher than 4.5 ml to achieve relevant pain alleviation. However, the authors have shown that type A3.1 fractures (i.e. superior burst fractures) only have about a third of the probability of pain relief compared to type A1.1 fracture (i.e. endplate impaction with no comminution). Therefore, the extent of the comminution of the vertebral body is a significant risk factor for the outcome of the intervention.

The risk of fracture of the levels adjacent to the treated vertebra is a diffused concern when cement augmentation techniques are carried out, whilst clinical case series have shown a higher incidence of adjacent fractures in KP compared to VP [164]. The stiffening effect of the cement bolus within the vertebral body increases surface strains on the adjacent vertebrae, as a result of the stress concentration at the treated level [165, 166]. Several authors have shown that reducing the elastic modulus of PMMA cement may help mitigating the risk of subsequent fractures, since it prevents over strengthening of the spinal segment [167, 168]. In addition, the cement bolus affects normal deformation of the endplate [169], hence increasing pressure within the nucleus [166], resulting in compression of both the adjacent intervertebral space and vertebra [170]. Although it is clear that augmentation alters the load transfer through the spine, the phenomena leading to the fracture are still poorly understood, as they are also linked to progression of osteoporosis [153, 171].

KP has shown to be effective in treating burst fractures also in comparison to SSPI. Zhang et al. [172] have not found any significant difference in terms of loss of correction at 2 year follow-up. In addition, KP had a significantly smaller blood loss and operative time, though it must be noted that the initial correction achieved by SSPI was significantly better. KP provided a 5° kyphosis correction whilst in SSPI it was about 13°, similarly, KP provided ~16% height recovery whilst SSPI achieved more than 30%.

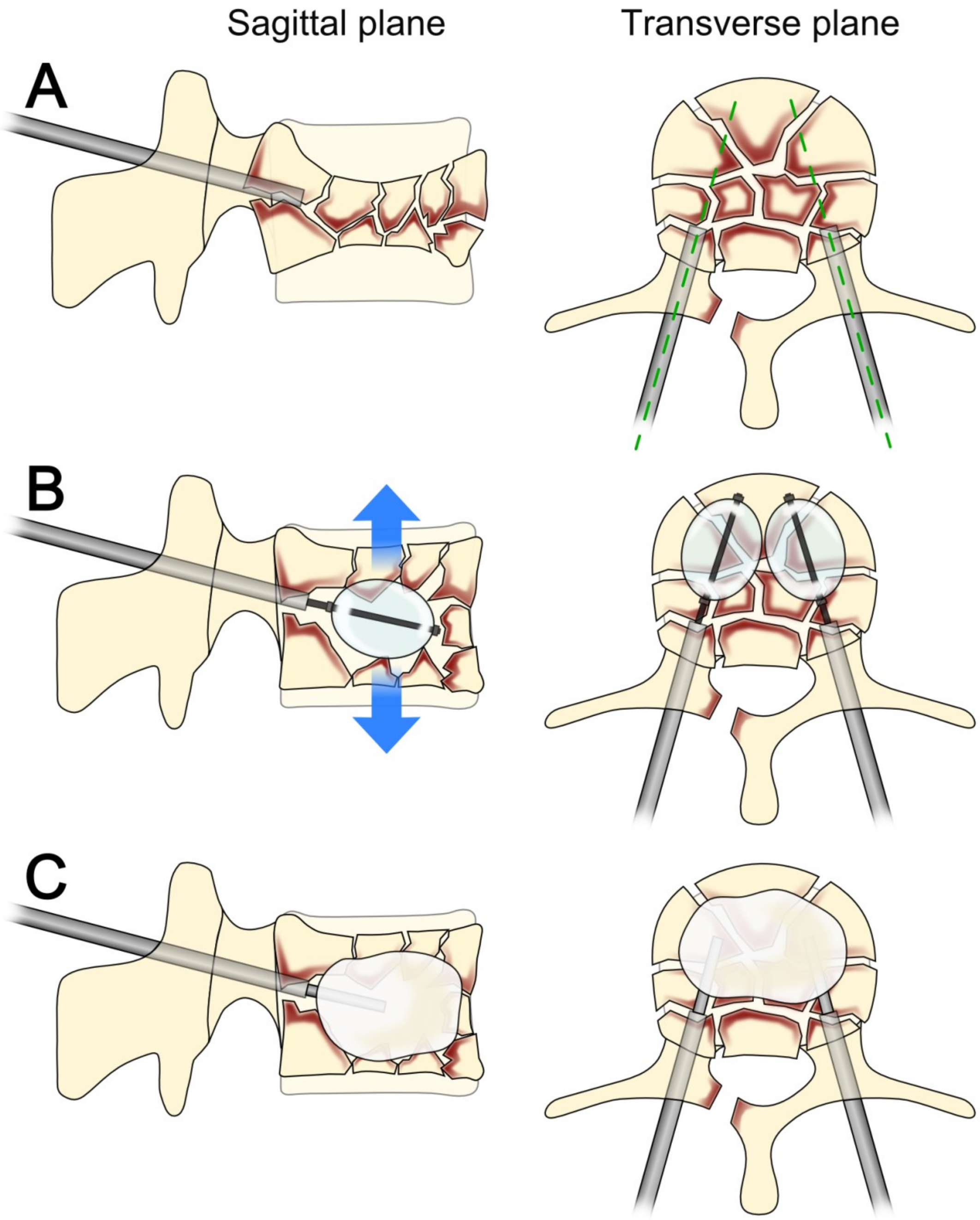

Figure 1-14: Representation of kyphoplasty procedure on a complete burst fracture. A: positioning of the cannulae. B: reduction of the fracture by inflation of the IBT. C: injection of the cement within the vertebral body.

1.3.3 Short segment posterior instrumentation with kyphoplasty

KP has proved its effectiveness in treating burst fractures, yet it is not able to deliver the reduction performance of SSPI. On the other hand, SSPI has shown inconsistent results due to lack of anterior support [156]. The major concern is indeed the loss of correction over time, although bone union appears to occur in all cases [147]. KP is a minimally invasive procedure which can provide stabilization of the anterior column through cement augmentation whilst aiding further fracture reduction [117, 173]. Therefore, several surgeons have decided to combine the advantages of the two techniques and perform both (SSPI – KP) (Figure 1-15). Extensive description of the surgical procedure can be found in Marco et al. [40], where the authors have treated unstable burst fractures with and without neurological deficit. In addition to SSPI and KP, laminectomy was also performed to provide further nerve decompression. On average, the procedure lasted about 120 minutes with a blood loss of 300 ml and required a six day hospitalisation. Although all the patients improved at least one Frankel grade, several authors discouraged the use of laminectomy since canal remodelling starts within 2 - 3 weeks from surgery [174].

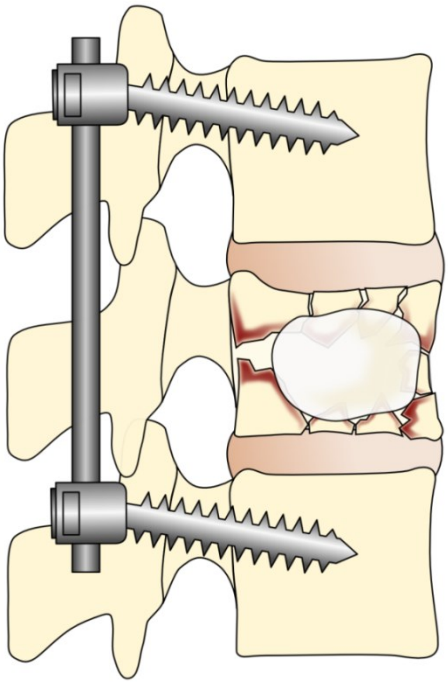

Figure 1-15: Representation of a single level burst fracture treated with SSPI – KP.

SSPI - KP has proved to be clinically effective since patients undergoing it have shown earlier recovery than those treated non-surgically [175] with up to 95 % of them reporting early and long-lasting pain relief [34]. As mentioned above, post-traumatic disc degeneration is a concern in the treatment of burst fractures. In addition, recurrent kyphosis following SSPI seems to happen in patients where the nucleus has crept back into the depressed portion of the endplate [118]. Verlaan et al. [176] have advocated the benefits of IBT reduction in restoring the shape of the endplate and disc space hence preventing nucleus intrusion. In a subsequent study, the same authors have shown clinically that when burst fractures are treated with SSPI - KP, there appears not to be any significant progress in disc degeneration at 12 – 18 month follow-up [177]. On the other hand, the stress shielding provided by the fixators has been shown to induce changes in the mineralisation of the bridged facet joints as well as the adjacent ones [178]. He et al. [173], have compared KP with SSPI – KP using PMMA and better correction and disability score improvement were achieved in the second group. Loss of correction at follow-up has been observed in both groups but it was lower in SSPI – KP (no implant failure or screw loosening detected). Similar trends can be found in other clinical case (Table 1-10).

Although it is not clear whether CaP cement can lead to better long-term results than PMMA [177], the majority of the studies where younger patients were treated used CaP cement, for the reasons already described. In addition, younger patients seem to be less prone to loss of correction than the older ones (where PMMA is typically used) [179]. When compared to SSPI (Table 1-9) a trend of loss of correction can be identified in SSPI – KP too. However, the latter seems to be able to tackle the phenomenon better.

Table 1-10: Clinical outcomes of SSPI in combination with KP.

	VB compression (%)			Kyphosis (°)			CV (ml)
	Pre	Post	FU	Pre	Post	FU	
Acosta et al. [36]	46 ± 4	14 ± 8	20	36 ± 4	5 ± 6	9	–‡
Afzal et al. [180]	33	17	–	9 ± 9	-2 ± 9	–	–‡
Bironneau et al. [179]	31	10	14	15	5	6	7.6*
Blondel et al. [38]	–	–	–	14	3	5	7.8*
Fluentes et al.[181]	35	11	14	14	3	5	6.4*
Korovessis et al. [182]	34	8	–	12	-2	–	3.0-6.0†
Toyone et al. [183]	–	–	–	20	-1	1	–$^{+}$
Verlaan et al. [39]	34	12	–	11	-2	–	–†

VB compression: percent loss of VB height with respect to intact conditions; Pre: pre-surgery; Post: post-surgery; FU: follow-up; CV: cement volume; †: CaP cement; ‡: PMMA cement; *results from PMMA and CaP cement pooled together; $^{+}$: solid hydroxyapatite.

1.4 Biomechanical investigations

Biomechanical investigations are paramount to gain a thorough understanding of spinal biomechanics and related treatments. The following section is meant to provide an overview of the literature relevant to the experiments carried out in this study.

1.4.1 Burst fracture mechanics

As introduced above, the major limitation in effective diagnosis of the injury arising from a spinal burst fracture is that it arises during a highly dynamic event that cannot be investigated at presentation of the patient [28, 184]. Therefore, the dynamics of burst fracture has been an area of debate and study in biomechanics.

Due to the high amount of energy involved in the fracture, the viscoelastic properties of the spine have been considered the major determinants of the fracture. Several authors have supposed that it originates from the forceful displacement of the nucleus hence causing the endplate to shatter. The nucleus may indeed behave like a solid at high strain rate due its high water content [185] and experimental tests have shown that the healthier the disc the more likely is a burst fracture to occur [186]. Ochia et al. [187] delivered axial loads to single vertebral bodies at different strain rates and have found that the endplates are more prone to fail at higher strain rates (2500 mm/s) than the core of the vertebra. In addition, the same authors have shown an increased pressurisation of bone marrow during the impact which may cause damage to the trabecular bone [185]. The viscoelastic properties of the spinal structures are clearly important since increasing the loading rate of the impact results in a 17 % increase of the ultimate force of the lumbar spine [188]. However, several authors have argued that the origination of the fracture/injury may be driven by more complex phenomena, rather than the sole failure of the endplate.

Hongo et al. [189] applied axial compression to three-adjacent-vertebrae segments whilst measuring surface strains at different locations. The highest tensile strain was recorded on the vertebral body at the base of the pedicles. On the other hand, strain at the same location significantly decreased when the pedicles were resected. Those results prove that a significant amount of load is transferred from the facet joints to the vertebral body through the pedicles and the authors have indicated this region as critical for the fracture onset. Areas of strain concentration at the same location have been also detected in a computational simulation of impact loading [190]. Langrana et al. [191] have published a comprehensive assessment of burst fracture mechanics where they have provided evidence that the fracture originates from a combination of axial and shear loading. In addition to the commonly accepted endplate loading, the authors have demonstrated the importance of the load transferred at the facet joints. The axial impact results in a forceful displacement of the posterior articular processes within the adjacent joints. Therefore, the authors have advocated that this wedging effect is transmitted from the facets, through the pedicles, to the vertebral body which fails where strains concentrate the most: at the root of the pedicles. Thus, the fragment retropulsed within the spinal canal originates from the breakage of the cortical shell where the root of the pedicles joins the posterior wall. The authors corroborated their hypothesis through experimental and numerical simulations where they compared different loading scenario on single vertebrae and three-adjacent-vertebrae segments.

The drop-weight protocol is the most widely exploited methodology to induce burst fractures *in vitro* [192]. The technique is based on dropping a mass onto the sample from a known height hence delivering an impulsive amount of energy. This experimental protocol allows generating high strain rate and simulating impact conditions such as in trauma (e.g. fall from height, car accident). The investigator can vary the mass of the dropped weight (m) as well as the height where the weight is dropped from (h) to adjust the velocity (V) and energy (E) at the impact as follows [193]:

$$V = \sqrt{2gh} \tag{1-1}$$

$$E = gmh \tag{1-2}$$

Higher energy and velocity usually result in more severe fractures and canal occlusion (Table 1-11). Panjabi et al. have developed a protocol where incremental impacts are delivered until fracture occurs to achieve more consistent fracture patterns and experimental conditions [194]. Spine segments have been often tested in flexion/extension condition by placing a wedge between the extremes of the sample and the impact surface [194-196]. In addition, some authors have deliberately pre-damaged the vertebra under study to drive the burst and resultant fracture appearance [195]. However, there is no consensus about what experimental protocol can replicate the *in vivo* conditions at best.

Several works have focused on understanding the dynamics of SCO. Kifune et al. tracked the changes in SCO under different static loading condition by applying radio-opaque beads within the canal of burst fractured samples and then taking lateral radiographs [24]. However, this technique does not allow measuring SCO during the fracture onset. Tran et al. [25] have developed a sensor based on a plastic tube fitted within the spinal canal. Therefore, the authors have been able to extrapolate the dynamic SCO during the fracture from the variation of the pressure within the tube. The same technique was exploited again in other works to investigate different loading conditions and spinal regions [27, 197, 198]. A different methodology to quantify the dynamics of SCO during the fracture onset has been developed by Wilcox et al. [26]. The authors shone a light through the spinal canal and filmed its projection throughout the impact to estimate the changes of the canal CSA. Results from those works have demonstrated that SCO reaches a maximum at the fracture onset when the fragment is retropulsed within the canal. Following the transient phase, the fragment is recoiled leading to the lower of SCO which is measured clinically at rest (Table 1-11).

Table 1-11: *in vitro* creation of spinal burst fractures using drop-weight protocol.

	Sample	Energy (J)	Velocity (m/s)	Flexion (°)	SCO (%)	SCO$_{max}$ (%)
Carter et al. [197]	Human	66.2	5.4	0	22 ± 11	72 ± 3
Jones et al. [196]	Human	245.3	4.4	15	30 ± 15	–
Kallemeier et al. [195]	Human	117.7	5.4	15	41 ± 12	–
Kifune et al. [24]	Human	–	5.2	8/15	30 ± 16	31 ± 16
Panjabi et al. [28]	Human	30.7 – 164.0	5.2	8/15	18 ± 6	33 ± 11
Panjabi et al. [194]	Human	100.3	5.2	8	30 ± 21	–
Tran et al. [25]	Bovine	35.1	3.7	0	–	48 ± 14
Wang et al. [193]	Bovine	137.2	4.4	0	33 ± 18	–
Wilcox et al. [26]	Bovine	20.0 – 140.0	6.3	0	–	50 ± 20

SCO: spinal canal occlusion; SCO$_{max}$: maximum spinal canal occlusion.

1.4.2 Kyphoplasty

Verlaan et al. [199] used a drop-weight protocol to create *in vitro* burst fractures and then performed SSPI – KP. Results in terms of cement leakage and reduction have confirmed its safety for treating spinal burst fractures. In a subsequent study, the same authors have investigated the displacement of the anterior and posterior bone fragments at different stages of SSPI – KP through radiographic image processing [200]. Ligamentotaxis significantly reduces the displacement of the fragments from their intact position whilst inflation of IBT displaced them again. However, the fragments returned to the post-reduction position following deflation of the IBT, hence not worsening SCO. In addition, Verlaan et al. [176] have investigated the evolution of vertebral body height and intervertebral space throughout the SSPI – KP procedure. Inflation of IBT significantly increased vertebral height further to what obtained with ligamentotaxis. The additional reduction was lost at deflation of IBT, although injection of CaP cement partially recovered the height loss. Disch et al. have also detected a loss of kyphosis correction following deflation of IBT [201].

Several studies have investigated the mechanical properties of the cement augmented spine. Fatigue testing by application of cycling loading is an effective way to simulate follow-up conditions and assess the long-term outcomes of a procedure. In the study by Kim et al. [202] single vertebrae were compressed to failure, treated with KP and then cyclically loaded to 100000 cycles. Although KP allowed significant initial height restoration; post-test assessment has shown a complete loss of correction. Wilke et al. [203] have also detected an increase of vertebral body compression after cyclic loading of KP treated osteoporotic segments. Fatigue testing is also a worthwhile paradigm for the investigation of the occurrence of adjacent fractures. Several works have applied cyclic loading following VP and assessed whether factors such as PMMA cement stiffness are responsible for inducing the failure of the adjacent vertebra [167, 204]. Nagaraja et al. [170] applied cyclic loading (150000 cycles with amplitude 685 – 1370 N) to osteoporotic samples treated with VP. The authors measured the compression of the adjacent vertebral bodies and intervertebral disc spaces from CT scans by measuring the distance between the outer boundaries of the endplates. Results have shown that VP causes 3 % higher strain in the adjacent vertebral body when compared to the untreated group.

1.4.3 Spinal instrumentation

The majority of the studies aim at providing indication for surgeons in selecting the treatment that provides the best fracture stabilisation. Most of the literature consists of kinematic assessments of the treated spine to quantify changes in the ROM, stiffness and NZ. Therefore, testing apparatuses are designed to apply physiological loading conditions (i.e. moments, forces) whilst displacements and rotations are measured. The instability caused by burst fracture has been shown to result in an increase by 150 % of ROM in flexion/extension [205]. Overall, SSPI constructs have been found to provide sufficient stabilisation by significantly reducing ROMs in flexion/extension, lateral bending and axial rotation [205-208]. However, SSPI has been shown to induce an increase of the intradiscal pressure at the treated level [207] together with an increase of the surface strains on the posterior articular processes of the non-treated adjacent vertebrae [209].

Those studies show that SSPI, although providing stabilisation, alters the load transfer through the construct; which has been supposed to be an additional leading cause for post-implant disc/facet degeneration. Hartensuer et al. [210] have shown that VP with PMMA cement does not significantly improve the stabilisation obtained with SSPI alone. However, the authors have suggested that the increase in rotational stiffness in flexion provided by VP may reduce the risk of implant failure.

Kinematic investigations have been integrated with load sharing assessments where implants (i.e. screws, rods) were instrumented with strain gauges and then calibrated to measure the loads acting on them [211-213]. Results from Kettler et al. [214] have shown that lateral bending is the most demanding task for the fixator rods. A moment of 7.5 Nm resulted in a tensile force of 140 N and a moment of 1.1 Nm whilst the same moment applied in flexion induced 100 N and 0.4 Nm, respectively. Melnyk et al. [215] have studied load sharing in shear conditions and shown that the rods are responsible for bearing 76 % of the total shear force when the facets are removed. Mermelstein et al. [216] compared SSPI and SSPI – KP with CaP cement on T10 – L3 human segments after inducing a burst fracture on L1. The authors have found KP to induce an increase of rotational stiffness in flexion whilst decreasing the moments acting on the screws from ~1 to ~0.4 Nm (5 Nm flexion applied). Those results have shown that, under quasi-static loading conditions, SSPI - KP may be able to provide the additional anterior stabilisation required to reduce the risk of implant failure and loss of correction.

Fatigue properties of SSPI have been mainly investigated according to international standards for spinal implant testing [217, 218]. Therefore, the majority of studies exploited a corpectomy model where SSPI bridges two solid blocks with no anterior support [218, 219]. Alternatively, springs of known stiffness are added in between the blocks to mimic the stiffness of the spinal structures [217]. Lindsey et al. [220] have tested SSPI on a corpectomy model by applying up to two million cycles (i.e. run-out) at four Hz. The loading profile was a sinusoidal waveform where the ratio between the maximum and minimum value was set to 10 (25 – 250 N and 70 – 700 N). The authors have shown that contouring the rods to match the kyphosis of the spine significantly reduces the fatigue life of titanium

(Ti6Al4V alloy) fixators. Similar results have been obtained for other alloys using the same experimental protocol [221].

Fatigue loading of fixators has been seldom performed on cadaveric tissue. Although it allows a more authentic replication of the clinical setting, the irreversible decay of the tissue is a strong limitation [78, 222]. The mechanical viability of the sample is tied to the length of the test and the number of cycles has to be reduced for the sake of reliability of results. Kinematic investigations have been carried out pre- and post-fatigue loading to simulate post-operative conditions. For instance, Morgenstern et al. applied 10000 compression cycles at 2 Hz with amplitude 0 – 200 N to four level constructs [223], whilst Deviren et al. applied 35000 cycles of flexion/extension (8/- 6 Nm) at 2 Hz with a constant 400 N axial compression to LSPI treated segments. Keeping the sample moist when tested aids reducing changes in the mechanical properties of spinal soft tissue [222]. In addition, temperature controlled baths have been used to keep the sample submerged throughout the experiment and extend the length of the test up to 18 hours [224].

1.4.4 *In situ* testing

In situ testing is an experimental paradigm where stepwise loading is integrated with CT scanning, hence allowing the investigator to perform high-resolution scanning of the sample under load. Therefore, the testing cell is designed to deliver a known force to the sample as well as satisfy the requirements for CT scanning. One of the firstly developed protocols allowed axial compression of a 9 x 22 mm specimen within a micro CT with a resolution of 34 μm [225]. However, that testing cell required loading through a universal testing machine, with obvious issues to consistently maintain the applied strain when the rig was fitted into the scanner. Subsequently, the *in situ* protocol has been used with synchrotron radiation source CT to achieve resolution up to a few nm [226, 227].

Despite the high resolution, micro CT typically has a limited field of view and sealed scanning chamber. High-resolution peripheral quantitative CT (HR-pQCT) has provided a viable alternative for whole bone scanning since it allows a cylindrical field of view up to 126 x 150 mm, although at lower resolutions (41 to 246 μm). The first instance of an *in situ* investigation with HR-pQCT is from Hulme et al. [67]. The authors developed a rig to be fitted within the scanner where the axial compression could be applied manually by means of a screw-driven actuator. Load and displacement were recorded throughout the test as the rig was equipped with a load cell and displacement transducer. The authors tested functional spinal units which underwent scanning (82 µm resolution) at consecutive load steps (200, 500, 1500-200 N). Image processing based on rigid registration of the two datasets was used to compute the deflection of the endplates.

1.4.5 Anatomical reference frame

As the candidate has already stated in a previous literature review paper [78], an accurate and consistent definition of a reference frame is paramount to allow consistent result collection/interpretation as well as comparison amongst different works/laboratories. An anatomical reference frame is based on the definition of axes and planes that are meaningful to the biomechanics of the bone/joint under study. Therefore, results can be reported in clinically relevant terms and allow comparison between *in vitro* and *in vivo* studies. The International Society of Biomechanics (ISB) has provided recommendations and urged some form of standardisation for joint coordinate systems [228]. However, there is still poor agreement on the subject and its relevance has not been fully appreciated yet.

In their study series on vertebral quantitative anatomy, Panjabi et al. [58, 59] have implemented a reference frame based on digitisation of the following anatomical landmarks (Figure 1-16):

- Points A, B, D and E define respectively the right, left superior and right, left inferior edges of the posterior wall of the vertebral body. The four points have shown to be consistently identifiable and less subjected to osteophytes.
- A sufficient amount of points to describe the rim of the cranial endplate.

A plane was fitted through the points A, B, D and E using the least-squares method. Therefore, the local axes and planes were defined as follows:

- The origin of the reference frame (C) is the centroid of the points describing the cranial endplate.
- The frontal plane is the plane parallel to that fitted through A, B, D and E and passing through C.
- The z-axis defines the antero-posterior (AP) direction. It is the line originating from C and orthogonal to the frontal plane.
- The x-axis defines the left-right direction. It is the line originating in C and parallel to that passing through A and B (hence lying on the frontal plane).
- The y-axis defines the cranio-caudal direction. It is the result of the cross product between the x- and z-axis.
- The sagittal plane is the z-y plane.
- The transverse plane is the z-x plane

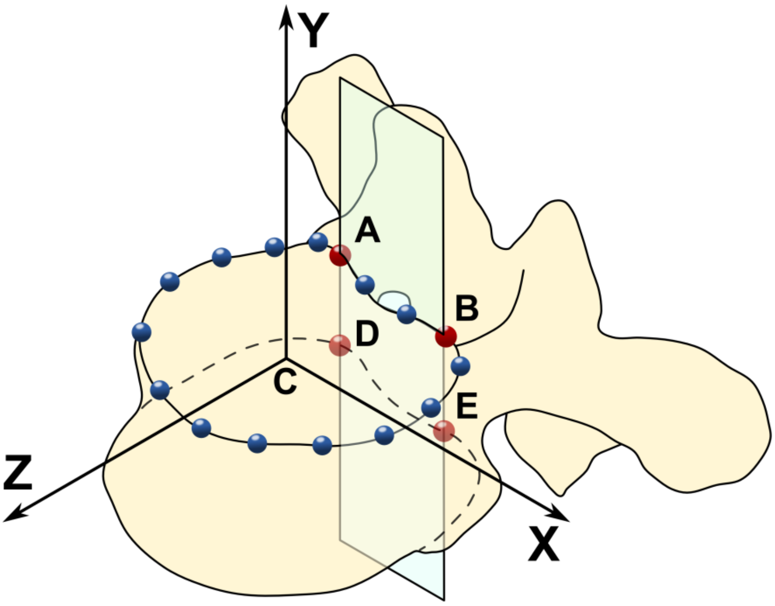

Figure 1-16: Local anatomical reference frame defined by Panjabi et al. Adapted from [59].

Measurements are usually taken using equipment that refers to its own reference frame or to what is considered to be the "laboratory" one. Therefore, it is often necessary to transform coordinates between reference frames to obtain results with respect to the planes of interest. The required transformation can be generalised for a single point as follows (Figure 1-17) [229].

Given a point whose coordinates are described in the global reference frame as $p = (x^g, y^g, z^g)$, it is possible to apply a linear transformation so that the same point can be described in a local reference frame as $P = (x^l, y^l, z^l)$. The local reference frame has origin in O^l defined by its position vector in global coordinates as:

$$\bar{O} = O^l - O^g = (O_x^g, O_y^g, O_z^g) \tag{1-3}$$

The axes of the local reference frame can be described in global coordinates using unit vectors as:

$$\overline{X^l} = (u_x^g, u_y^g, u_z^g) \tag{1-4}$$

$$\overline{Y^l} = (v_x^g, v_y^g, v_z^g) \tag{1-5}$$

$$\overline{Z^l} = (w_x^g, w_y^g, w_z^g) \tag{1-6}$$

A transformation of coordinates from global to local reference frame can be generalised to a combination of a translation and rotation. Therefore:

$$P = R_g^l \cdot (p - \bar{O}) \tag{1-7}$$

Where the translation component is the distance from the origin of the local reference frame whilst the rotation matrix from global to local reference frame is built as:

$$R_g^l = \begin{bmatrix} u_x^g & u_y^g & u_z^g \\ v_x^g & v_y^g & v_z^g \\ w_x^g & w_y^g & w_z^g \end{bmatrix} \tag{1-8}$$

The inverse transformation requires the definition of a rotation matrix from local to global coordinates, which can be calculated as:

$$p = R_l^g \cdot P + \bar{O} = (R_g^l)^{-1} \cdot P + \bar{O} \tag{1-9}$$

Since the rotation matrix is orthogonal with determinant 1, the following relationship applies $(R_g^l)^{-1} = (R_g^l)^T$ and the transformation of coordinates from local to global reference frame can be rewritten as:

$$p = R_l^g \cdot P + \bar{O} = (R_g^l)^T \cdot P + \bar{O} \tag{1-10}$$

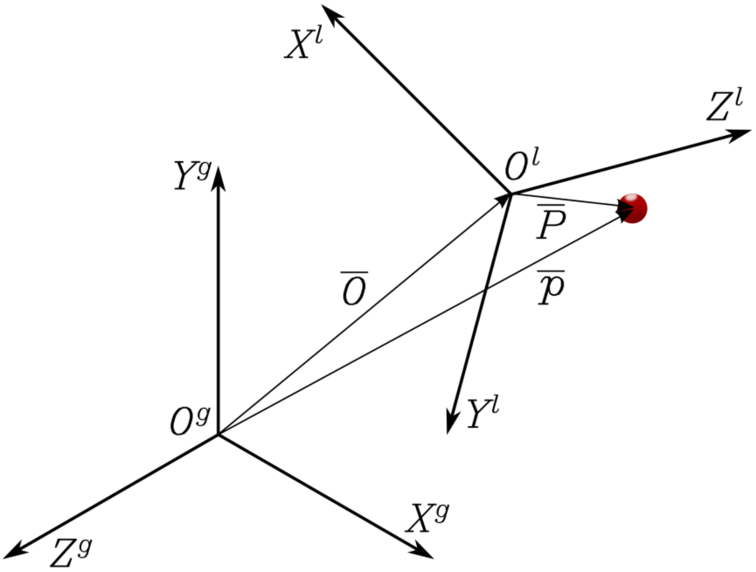

Figure 1-17: Generalised representation of a transformation of coordinates for a point from global to local reference frame.

1.4.6 Strain gauge measurements

Strain gauges have been extensively used in biomechanics for measuring surface strains on the vertebra [189, 230] as well as implants [231-233]. In a previous work from Cristofolini et al., the candidate investigated the surface strain distribution in lumbar vertebrae using tri-axial strain gauges [81].

A strain gauge is a sensor whose electrical resistance varies proportionally to the strain it undergoes [234]. Several configurations of strain gauges are available on the market, depending on the application. Uniaxial strain gauges are the simplest configuration where a single grid is laid on a carrier film to measure strains along the major axis of the gauge. The change in resistance caused by the strain is measured using a Wheatstone bridge circuit where the output voltage is function of the unbalance amongst the resistances connected to its arms. The basic configuration is the quarter-bridge, where only one arm of the bridge is active (i.e. where the strain gauge is connected). However, the measurement may be affected by experimental errors. The strain gauge is usually bonded onto the surface of the body under study and connected to the active arm of the bridge by means of lead wires. Therefore, uneven lead wire resistances and their variation due to temperature changes may induce measurement artifacts. Such errors can be compensated physically using a three-wire connection (Figure 1-18).

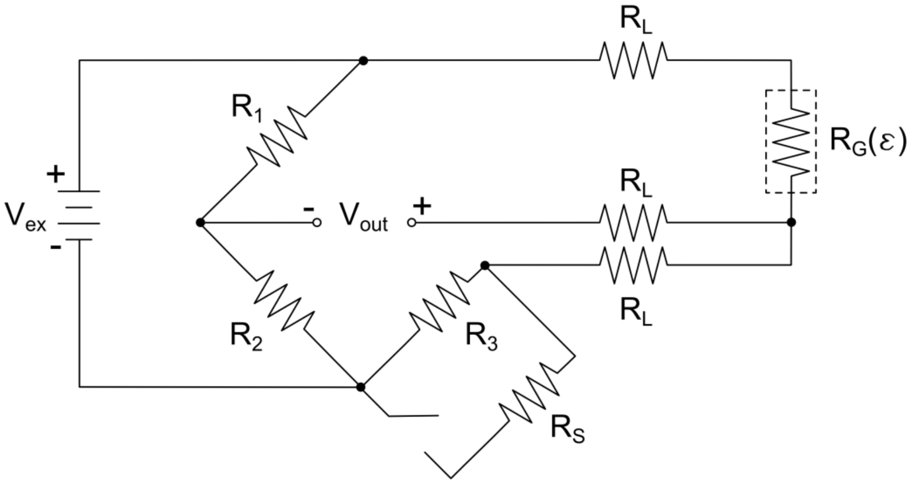

Figure 1-18: Three-wire connection of quarter-bridge circuit with shunt resistor applied across R$_3$.

A fundamental parameter in strain gauge measurement is the gauge factor (G$_f$) which represents the sensitivity of the gauge to strain. Together with the grid resistance is the main nominal parameter of the strain gauge and is defined as:

$$G_f = \frac{\frac{\Delta R_g}{R_g}}{\varepsilon} \tag{1-11}$$

Given a three-wire configuration of quarter-bridge, the strain is calculated as:

$$\varepsilon = \frac{-4\frac{V_{out}}{V_{ex}}}{G_f\left(1+2\frac{V_{out}}{V_{ex}}\right)}\left(1+\frac{R_L}{R_g}\right) \tag{1-12}$$

Shunt calibration is an additional procedure which involves simulating an input strain by shunting an arm of the bridge with a resistor of known amount (R$_s$). The actual output of the bridge is then compared to that expected if all the components had their nominal values. The calibration procedure returns a constant which is multiplied to G$_f$ to compensate for errors over the measurement path.

Reliability of strain measurements was verified by applying four-point bending to a titanium rod (same material used for experiments, see 2.1.3). A uniaxial strain gauge was bonded onto the surface of the rod (2.2.3.1), where the maximum strain was estimated to occur, and good association was found between experimental results and those calculated analytically using beam theory.

Research Objectives

From the overview of the literature provided, it is evident that traumatic vertebral fractures may lead to severe impairment and the performance of the treatment is crucial for its safety and successful outcome.

Spinal burst fractures are a common cause of instability and neurological deficit. It is generally acknowledged that the injury arises during the dynamic phase of the fracture. IPW is a distinctive feature of the fracture and is relevance in the neurological insult has been proven clinically. However, little is known about its biomechanics.

Treatment for spinal burst fractures aims at restoring biomechanics and providing stability. SSPI is currently the most chosen surgical option. However, clinical outcomes have been inconsistent showing loss of correction, re-fracturing and implant failure. SSPI – KP is a relatively recent surgical option which combines cement augmentation and spinal fixation. Clinical results have been so far encouraging; however long-term follow-ups are not yet available. Biomechanical investigation can help understand whether SSPI – KP can actually overcome the limitations of SSPI.

1.4.7 Study aim

The main aim of this work was to develop novel methodology for the investigation of spinal burst fracture: from onset to treatment. Therefore, the ultimate goal of the candidate was to provide a comprehensive biomechanical analysis to gain further insight on the mechanics of the fracture as well as the performance of the treatment.

1.4.8 Collaboration on multiple myeloma FE model

Collaboration with Dr. Nicholas Roberts and the University of Toronto aimed at the development of a FE model of MM infiltrated vertebrae to better understand pathology related fractures. It was responsibility of the candidate to develop a test protocol and provide experimental data for the definition and validation of the FE model.

1.4.1 Objectives

The following objectives were pursued by the candidate to satisfy the aim of the study:

- To develop a protocol for the consistent creation and investigation of spinal burst fractures in human cadaveric three-adjacent-vertebrae segments.
- To provide comprehensive *in vitro* investigation of spinal burst fracture and dynamics of IPW.
- To develop a protocol for the investigation of fatigue in human cadaveric three-adjacent-vertebrae segments treated with SSPI.
- To provide comprehensive *in vitro* dynamic comparison/investigation of SSPI and SSPI – KP as treatment for spinal burst fractures.
- To develop methods for 3D quantitative investigation of vertebral anatomy through medical image processing and integrate them with mechanical testing.
- To develop an *in situ* testing protocol for use with human cadaveric three-adjacent-vertebrae segments.
- To provide experimental data using *in situ* testing for the development/validation of an FE model of MM infiltrated spine.

Chapter 2: Materials and Methods

This chapter provides description and details of the materials and methods used in this work. The candidate's first task was to develop the *in situ* protocol and the related experiments necessary to Dr. N. Roberts for the development of an FE model of the MM infiltrated spine. In parallel to that collaboration, the candidate developed and exploited the methods to pursue the main aim of the work: investigate spinal burst fractures and related treatment. All the methods were developed through a comprehensive approach, were mechanical testing was closely tied to image processing. Such novel methods allowed the investigation of clinically relevant biomechanical issues. The main work can then be divided into two sub-projects, each requiring specific methods to suit the experimental requirements. In the first part, the candidate developed the protocol for the investigation of the onset of the fracture. Subsequently, the second part of the project required the development of methods for investigation of fatigue performance following SSPI and SSPI - KP. Image processing methods were developed to analyse HR-pQCT scans undertaken at all the stages of the two sub-projects hence to follow the fracture pathway.

2.1 Materials

The materials used in this work comprise the human cadaveric tissue required for the experiments and the surgical material used to carry out SSPI and KP.

2.1.1 Specimens

Authorisation for the use of cadaveric tissue was provided by the regional NHS research ethics committee (in situ testing: REC No. 10/H1306/60; burst fracture experiments: REC No. 10/H1306/83). All the procedures were carried out in compliance with University of Leeds research ethics and human tissue act (HTA) requirements. Specimens were tracked throughout the experiments and storage using dedicated software for sample management (Achiever medical; Interactive Software Ltd., Birmingham, UK).

For the burst fracture investigation four spines were acquired through the Leeds Tissue Bank (Leeds Teaching Hospitals Trust, Leeds, UK). Following dissection, 12 three-adjacent-vertebrae segments were obtained and tested (Table 2-1). The same samples were used for both the fracture creation and fracture treatment experiments.

Table 2-1: Details of the donors and specimen division for burst fracture investigation.

Donor	Age	BW (kg)	Height (m)	Gender	Level
A	44	55.0	1.60	F	T9-T10-T11
A	44	55.0	1.60	F	T12-L1-L2
A	44	55.0	1.60	F	L3-L4-L5
B	46	89.5	1.70	M	T9-T10-T11
B	46	89.5	1.70	M	T12-L1-L2
B	46	89.5	1.70	M	L3-L4-L5
C	56	70.0	1.73	M	T9-T10-T11
C	56	70.0	1.73	M	T12-L1-L2
C	56	70.0	1.73	M	L3-L4-L5
D	38	85.6	1.75	M	T9-T10-T11
D	38	85.6	1.75	M	T12-L1-L2
D	38	85.6	1.75	M	L3-L4-L5

BW: body weight.

For the *in situ* investigation a total of seven spines were acquired through an international tissue provider service (Science Care Inc., Phoenix, AZ, USA). All the donors were diagnosed with MM and the pathology was considered the primary or secondary cause of death. Following dissection, eight three-adjacent-vertebrae segments were obtained and tested (Table 2-2). The residual tissue was used by other researchers from the group in other studies.

Table 2-2: Details of the donors and specimen division for *in situ* investigation.

Donor	Age	BW (kg)	Height (m)	Gender	Level
E	57	64.4	1.62	F	T2-T3-T4
F	83	88.4	1.80	M	T2-T3-T4
G	67	49.9	1.55	F	T2-T3-T4
G	67	49.9	1.55	F	T5-T6-T7
H	53	49.9	1.83	M	T2-T3-T4
I	62	72.6	1.85	M	T2-T3-T4
J	90	67.1	1.70	M	T11-T12-L1
K	60	113.4	1.75	M	T11-T12-L1

BW: body weight.

Samples were stored frozen at -18°C in sealed bags and thawed overnight when required for preparation/testing. Freezing – thawing cycles were reduced to the minimum possible and at completion of each procedure/experiment the sample was promptly returned to freeze storage to minimise tissue decay.

2.1.2 Kyphoplasty

KP was performed using commercially available kit and cement. All the components of the kit belonged to the same manufacturer series (KYPHON series; Medtronic, Memphis, TN, USA), which comprised the IBT (KYPHON Xpander IBT; Medtronic), cannulae, trocars and syringes equipped with pressure gauge to inflate the IBT (KYPHON Xpander Inflation Syringe; Medtronic). All the IBTs used where the same size (Table 2-3). Two syringes were required to inflate two IBTs at a time.

CaP cement (Kyphon Injectable Bone Void Filler, Medtronic Sofamor Danek, Memphis, TN, USA) was injected in all the samples which undertook KP. Each cement box contained 10 g of CaP salts and 4.3 ml of aqueous phosphate water that were mixed according to manufacture specifications. Details provided by the manufacturer required mixing the two components for 45 seconds and completing the injection within four minutes. Following injection, the patient (in this case the specimen) is not to be moved for the first 20 minutes, then the cement is designed to reach its full strength in 24 hours (Figure 2-1).

Table 2-3: IBT specifications.

IBT type	Initial Length (mm)	Cannula diameter (kg)	Max pressure (psi)	Max diameter (mm)	Max length (mm)	Max volume (cm^3)
15/3	15	4.2	400	14	20	4

The maximum values refer the maximum inflation conditions of the IBT.

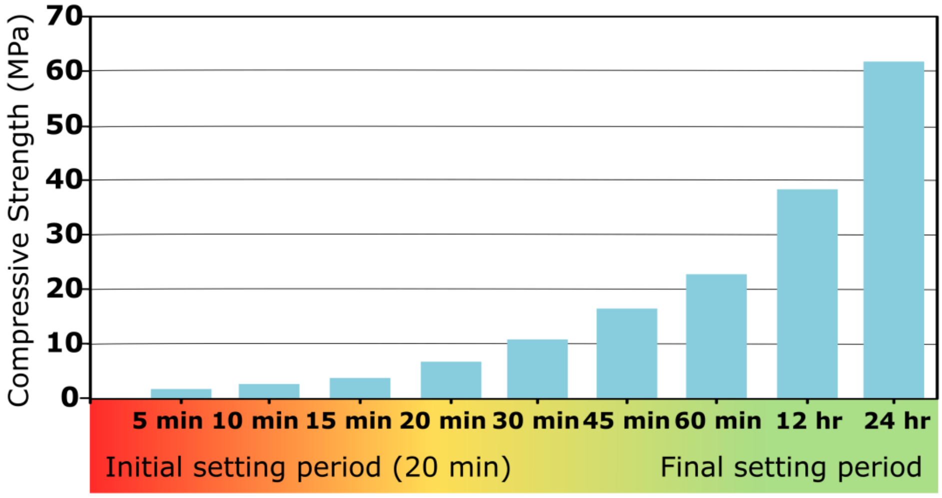

Figure 2-1: Compressive strength at 37°C of the CaP cement used. Data obtained from manufacturer specifications.

2.1.3 Short segment pedicle instrumentation

SSPI kit and implants were purchased from an orthopaedic implant manufacturer (Vishal Surgitech Pvt. Ltd., Rajkot, India). The SSPI implants used in this work consisted of polyaxial pedicle screws and fixator rods made of Ti6Al4V (Titanium alloy commonly used in SSPI). The nut of the screw was allowed to tilt within a 50° cone about the main axis of the screw. The size of each screw (core diameter and length) and length of the fixator rods were chosen for each samples based on evaluation of the vertebral geometry from HR-pQCT scans. All the constructs were equipped with 5 mm diameter fixator rods. The SSPI implants were purchased from the above mentioned manufacturer mainly due to budget limitations. A total of 48 screws were purchased at the individual cost of about £ 30 ($ 45); whilst the cost of a pedicle screw from more affirmed manufacturers can be as high as £ 800. From a qualitative inspection, the purchased screws were all intact and presented the main common features (e.g. variable thread profile) as other commercially available designs (Figure 2-2).

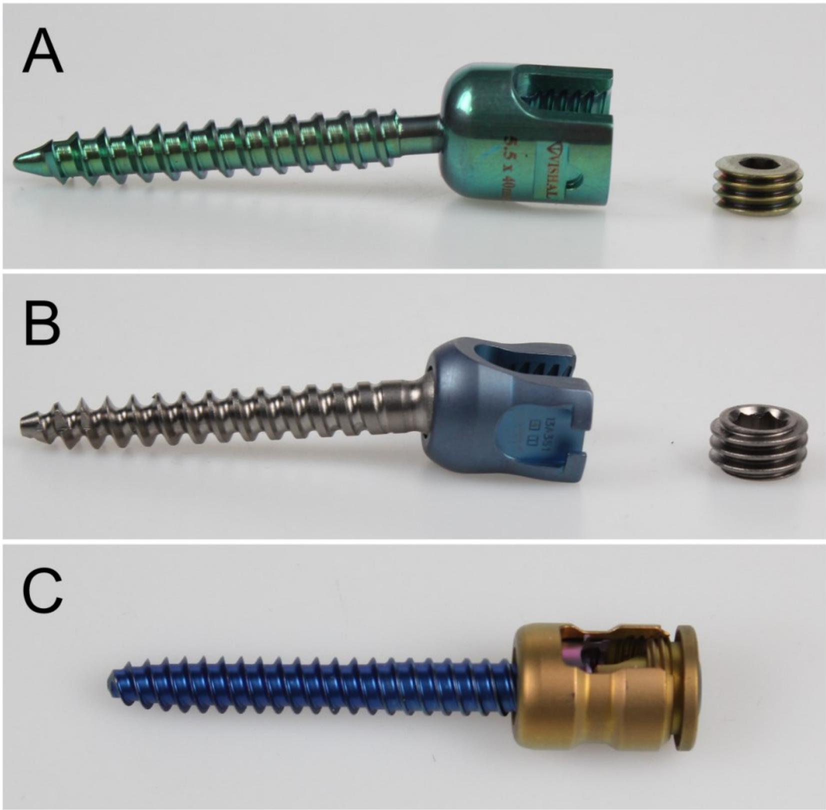

Figure 2-2: Polyaxial pedicle screw designs from different manufacturers. A: Vishal Surgitech (used in this study); B: Stryker; C: DePuy Synthes.

2.2 Methods

The methods described below were all developed by the candidate except for that necessary for the development of the FE model (2.2.1.4). That section was taken from the manuscript prepared by Dr. N. Roberts for submission to a peer-reviewed journal [2], where the candidate was second author. The methods used for the investigation of the mechanics of spinal burst fractures have been published as a research article on a peer-reviewed journal where the candidate is first author [1]. All the bespoke fixtures and components used in the experiments, except when specified, were designed by the candidate in a CAD suite (SolidWorks; Dassault Systèmes, Waltham, MA, USA), who also liaised with the technical team for the manufacturing/assembly. The candidate developed autonomously all the bespoke software used for data logging/processing and interface with sensors. All the applications implemented paradigms (e.g. event structure, state machine, FPGA) to comply with best coding practices, as learnt through dedicated training completed during the first year of doctorate.

2.2.1 In situ testing

As described before (1.4.4), the *in situ* approach was firstly developed by Hulme et al. [67]. Therefore, the design of the testing rig used [67]by the aforementioned authors was of significant influence for that used in this work. Their protocol was developed for testing functional spinal units whilst in this work three-adjacent-vertebrae were tested. When the candidate embarked on the collaboration the testing rig had already been partially developed by other researchers within the group. However, the apparatus was lacking substantial features and components to make it operative. Therefore, the candidate designed additional fixtures (e.g. sample embedding rig) and added displacement measurement capability. In addition, software for data logging was developed.

2.2.1.1 Specimen preparation

Three-adjacent-vertebrae segments were excised from whole spines through careful tissue dissection. Care was taken not to damage the facets and the intervertebral discs adjacent to the central vertebra of the segment. Except for the facet capsules, ligamentous structures were removed to ensure load transmission only through the endplates and facet joints. Any residual soft tissue on the most external endplate surface of the adjacent vertebrae was removed to obtain a clean surface for embedding.

The two extremities of each segment were embedded in laboratory grade PMMA (WHW Plastics, Hull, UK) to consistently align the specimen within the testing rig as well as provide two flat parallel loading surfaces. A steel rod was fit within the spinal canal and secured against its anterior surface, as previously done by Oakland et al. [168], to firmly hold the specimen. The rod was fastened on a bracket that kept it perpendicular to the ground. Then, the alignment of the segment was manually corrected by adjusting how the rod fit within the spinal canal. The overall alignment was adjusted with the aid of a set of engineer's squares to keep the endplates of the central vertebra as parallel as possible to the ground (both on sagittal and frontal plane). Rotation around the cranio-caudal axis was neglected as not relevant for the testing conditions. Accurate alignment of the sample at the embedding stage is paramount to maintain the loading direction repeatable and physiologically relevant. Subsequently, the sample was lowered into a lubricated plastic cylindrical pot down to approximatively mid-height of the vertebra; taking care not to lose the alignment. The spinal canal was kept as reference and centred within the pot. PMMA was then mixed and poured up to the brim of the pot (Figure 2-3). When the PMMA was completely set (20 – 30 minutes) the sample was tilted upside down and held parallel to the ground by a bracket. The non-embedded extremity of the segment was then lowered in an equal pot, to a similar depth as above, and PMMA was poured again (Figure 2-4). Care was taken to keep the cement away from the facet joints. At complete setting, the two pots were removed (they are re-usable) to allow fitting the sample within the testing cell. The specimen was then ready for testing, with the central vertebra and facet joints free whilst each adjacent vertebra was embedded in a cylindrical layer of PMMA.

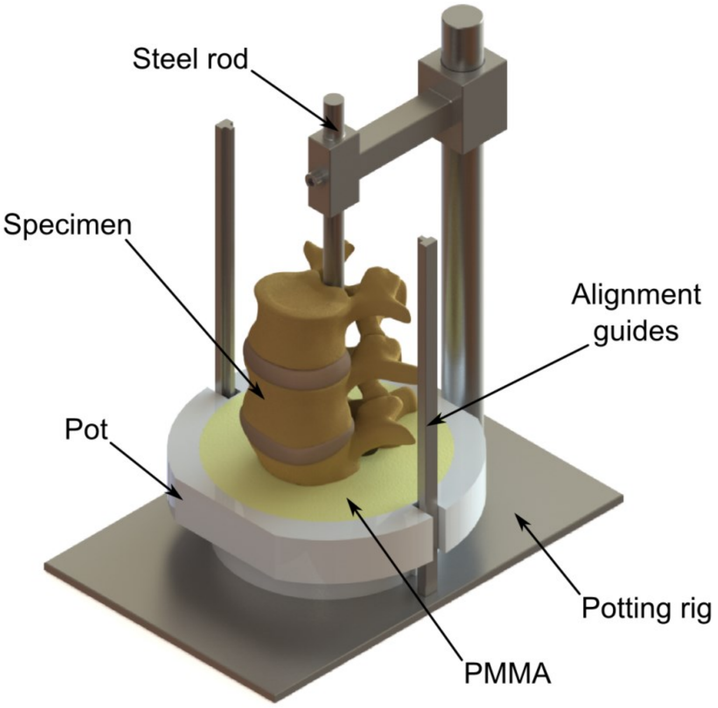

Figure 2-3: Embedding of the most caudal extremity of a spinal segment.

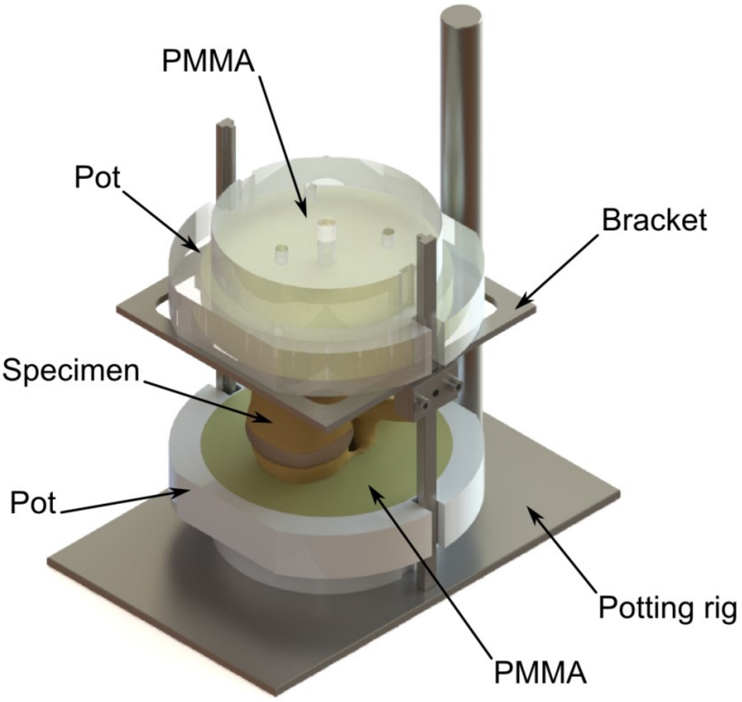

Figure 2-4: Embedding of the most cranial extremity of a spinal segment following embedding of the opposite side.

2.2.1.2 Development of the testing rig

A testing rig was developed to fulfil the requirements for in situ testing (Figure 2-5). Therefore, the apparatus was designed as a sealed cell to be fit within the scanning chamber of the HR-pQCT scanner (Xtreme CT; Scanco Medical AG, Brüttisellen, Switzerland) whilst consistently loading the sample. The testing cell comprised of a radio-transparent Perspex tube, whose extremities were flanged against two plates. One plate was designed to fit the locking joint within the scanning chamber to hold the sample container. The plate on the other side had fittings for the external part of the scanning chamber and housed the actuator. Axial compression was delivered by means of a manual screw-driven actuator. Therefore, the investigator imposed the displacement of the loading plate by tightening a threaded rod (M16x1). The loading plate and the threaded shaft were connected through a thrust bearing which allowed decoupling torque (induced by the rotation of the threaded bar) and transmit axial force. In addition, the clearance between the components which housed the thrust bearing allowed compensating small misalignments between the specimen and the loading plate (i.e. to minimise unwanted moments). A 4.4 kN uniaxial load cell (Model 31; Honeywell-sensotec, Ohio, USA) was mounted between the loading plate and thrust bearing to measure compression. Axial displacement was measured through a linear variable displacement transducer (LVDT, model ACT 1000A; RDP Electronics, Wolverhampton, UK) with 50 mm stroke, fastened on the outer flange of the testing cell. A two mm deep recess was machined both on the loading plate and opposite base (where the other PMMA layer sat) to keep the sample in place when the rig is tilted horizontally within the scanner.

The analogue signals from the load cell and LVDT were preconditioned through dedicated amplifiers (RDP Electronics, Wolverhampton, UK) and then connected to a USB data acquisition (DAQ) device (NI USB-6009 DAQ; National Instruments Corporation, Austin, TX, USA). Custom software was developed (LabVIEW; National Instruments Corporation) to provide the user with real-time zeroing and reading of signals (on the front panel of the code) as well as continuous data logging into a spreadsheet file. The architecture of the software was based on a Producer/Consumer design pattern which allowed data sharing among multiple loops running at different rates. Whilst the producer loop acquired the signals at the user-defined sampling frequency, the consumer loop buffered, processed and logged the data on a file. The consumer loop integrated a state machine to better organise the work flow.

Compliance of the whole rig was assessed to identify measurements error in the displacement, mainly caused by the deformation of the Perspex tube under load. A solid steel cylinder was loaded up to 4 kN within the rig. Since steel can be considered linear elastic, any load decay over time was attributed to the viscoelasticity of the other plastic components of the rig. Elongation of the steel rod and Perspex tube were estimated analytically and compared to what measured by the LVDT. At 4 kN compression, the elongation of the rig and steel rod were estimated to be 77 and 2 µm, respectively. The LVDT measured 177 ± 10 µm whilst the load decayed by 3.2 % over 5 minutes. The experiment showed that the testing rig is clearly affected by the compliance of its component. However, given the significantly lower stiffness of a spinal segment with respect to that of steel, the effect of compliance was considered negligible.

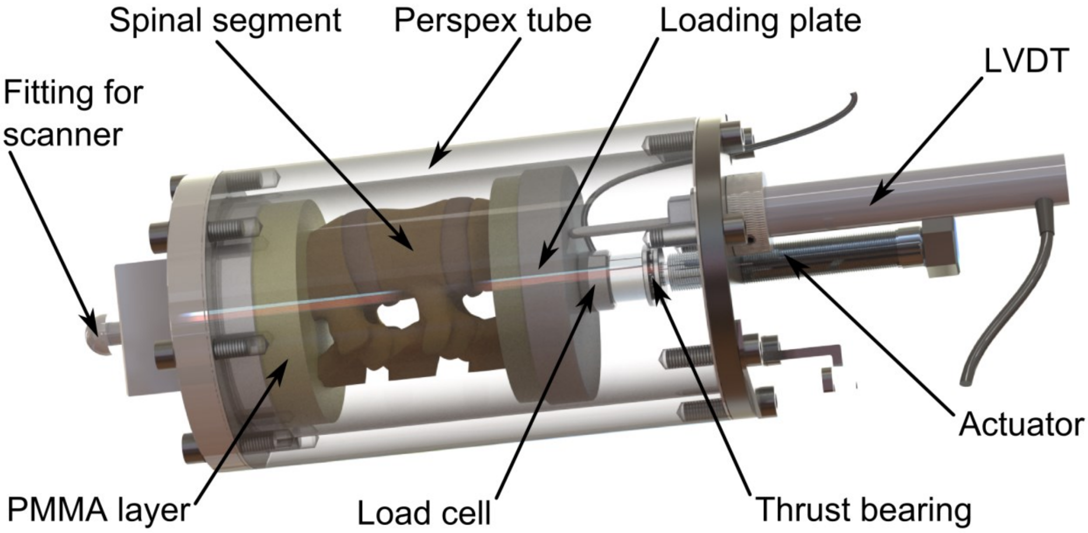

Figure 2-5: Representation of the *in situ* testing rig.

2.2.1.3 Experimental protocol

Specimens were wrapped in wet tissues (to keep them moist throughout the test) and then positioned within the rig with the cranial extremity in contact with the loading plate. The embedding procedure allowed the cranio-caudal axis to be consistently aligned with the loading axis. The testing rig was then positioned within the testing rig as per any other standard sample holder. The data-logging code was run throughout the test so that load and displacement could be logged continuously at 2 Hz. Transducer signals were zeroed before starting the loading procedure. Following an axial preload of 50 N, the specimen underwent three consecutive load steps at one kN increases (Figure 2-6). Therefore, load was increased from 50 N to 1, 2 and 3 kN, or until failure occurred. Failure was defined as a sudden drop in load (detected from the load cell measurement) together with a significant loss in stiffness (user feedback in advancing the screw-driven actuator). When the target load was reached, it was kept constant for two minutes by adjusting the position of the actuator. Then, the specimen was left relax (actuator still) until the next load step. Two scans were performed at each load step. First, a low resolution scan (246 µm, 250 projections) was taken to image the whole segment. Subsequently, a high resolution scan (41 µm, 1000 projections) was taken; limiting the area of scanning to the central vertebra. All scans were done at 60 kVp and 900 µA. The whole testing protocol took approximatively five hours, mostly because of the time required for the high resolution scans.

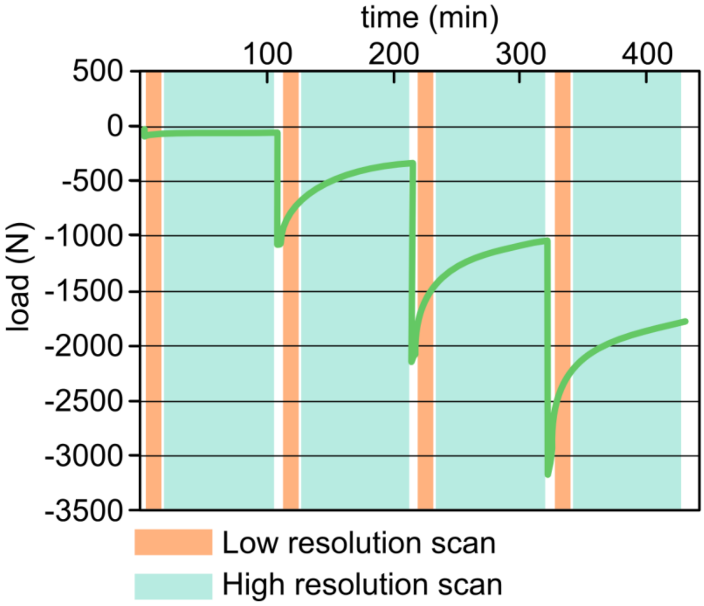

Figure 2-6: ***In situ*** **loading protocol: example of a loading curve throughout the experiment. Two scans were taken after reaching the target load.**

2.2.1.4 Numerical model development

Low resolution scans were used to assess signs of gross bone failure within the segment as well as make sure that the experimental conditions matched what expected. The high resolution scans were used to develop the FE model and identify boundary conditions. Each central vertebra was segmented in an image processing suite (Amira; Visualization Sciences Group, Burlington, MA, USA) and triangulated surfaces were created from the segmented volumes. A continuum tetrahedral mesh was then created from the 50 N load step data. The original mesh was then down sampled and used for sensitivity studies. An arbitrary greyscale to elastic modulus conversion [235] (based on a power law equation) was exploited to check the meshes' sensitivity to element density. The mesh was considered to be insensitive to further discretisation when the reaction forces on the loading surfaces stabilised. Subsequently, definitive material properties were assigned by optimising the multiplier of the greyscale to modulus conversion for each model. Optimisation was based on the comparison between the reaction forces calculated by the model and that measured experimentally at the end of the scan (since load relaxation occurred).

Boundary conditions were imposed as a displacement field to the endplates and facets, based on the work by Hojjat et al. [236], and Herblum et al. [237];

where a similar approach was used for FE modelling of rat vertebrae. Each load step surface was aligned to the reference one (50 N load) by applying an affine rigid registration. Then, six loading surfaces (two endplates, two cranial and two caudal facets) were identified on the triangulated mesh of the vertebra at each load step. A built-in function was used to calculate the distance between the nodes of each loading surface at the reference state and subsequent load step (Figure 2-7). Therefore, the distance between the two selected regions could be assumed as the displacement that the surface underwent because of the applied load. Results were exported and the displacement of each node on the loading surface was imposed as boundary conditions for the nodes of the tetrahedral mesh (Figure 2-8). All models were solved using a software suite for FE analysis (Abaqus 11.1; Dassault Systèmes, Paris, France).

Segmentation from high resolution scans allowed achieving higher accuracy and consistency in the identification of the boundary conditions as well as meshing. This was assessed qualitatively through an initial study where the low resolution scans where also segmented and processed.

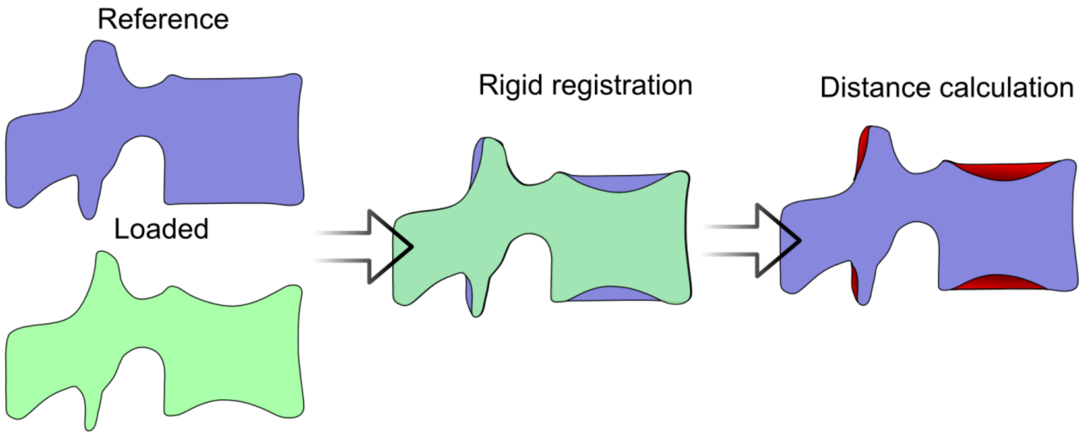

Figure 2-7: Schematic of the image processing procedure used to calculate the displacement of the loading surfaces.

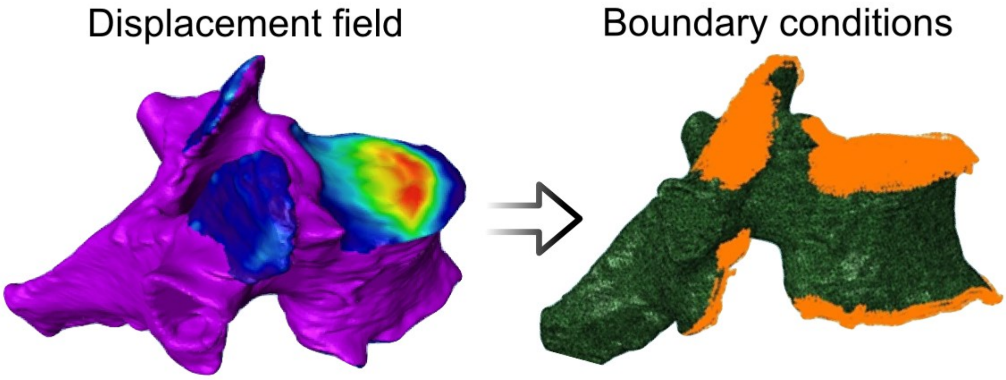

Figure 2-8: Surface displacement caused by loading was used to define the boundary conditions of the FE model. Adapted from [238].

2.2.2 *In vitro* creation of spinal burst fractures

The candidate autonomously developed an experimental protocol for the creation and investigation of spinal burst fractures. The protocol focused on providing dynamic measurement of IPW during the impact. This was done to study the phenomenon in detail since there were no equivalent measures in the literature. As stated above, part of this section has been published in a journal article where the candidate was first author [1].

2.2.2.1 Specimen preparation

Three-adjacent-vertebrae segments were excised from whole spines through careful tissue dissection (Table 2-1). Care was taken not to damage the intervertebral discs and facet joints adjacent to the central vertebra of each segment. In addition, care was taken to preserve the integrity of the main ligamentous structures, in particular PLL and ALL. Any residual soft tissue on the most external endplate surface of the adjacent vertebrae was removed to obtain a clean surface for embedding. The same procedure described above (2.2.1.1) was used to embed the extremities of the specimen in PMMA. In addition, the most anterior region and spinous process of the central vertebra were used as reference to define the orientation of the sagittal plane and align it with the centre line of the pots. In order to provide additional support, the adjacent vertebrae were embedded slightly above mid vertebral height. In addition, modelling clay was fit within the vertebral foramen prior to pouring PMMA and removed after it cured hence creating an opening through the spinal canal of the segment (Figure 2-11).

No alterations were made to any of the vertebra to force occurrence and appearance of a burst fracture. Samples were kept wrapped in moist tissues throughout the test to keep them hydrated.

2.2.2.2 Testing rig

Fractures were created *in vitro* using a drop weight protocol to simulate an axial impact load. The drop weight apparatus was already in existence at the University of Leeds and it has been used in previous works on animal tissue [190, 239]. The rig consisted of a frame which housed a guide rod used to drive the fall of a mass cartridge (Figure 2-9). Weight of the mass cartridge could be changed by means of removable elements of known weight. The weight was dropped by releasing a latch mechanism through an external handle.

The candidate designed an additional testing rig to house human cadaveric segments and be used within the drop weight apparatus (Figure 2-10). The caudal extremity of the sample was secured within a steel pot and its frontal plane was aligned with the centre line of the base of the rig. The guide rod drove the mass cartridge to deliver an impact against the upper surface of the impactor which rested onto the cranial extremity of the sample. The mass of the impactor resulted in a preload of approximately 50 N being applied to the specimen. The displacement of the impactor was constrained to be only axial by a ball bushing, which also minimised friction. Housing for a 45° mirror was machined both in the pot and impactor to create a light path through the spinal canal (Figure 2-12), as in the work of Wilcox et al. [26]. The position of the sample with respect to the impactor axis could be adjusted through slits machined on the different components.

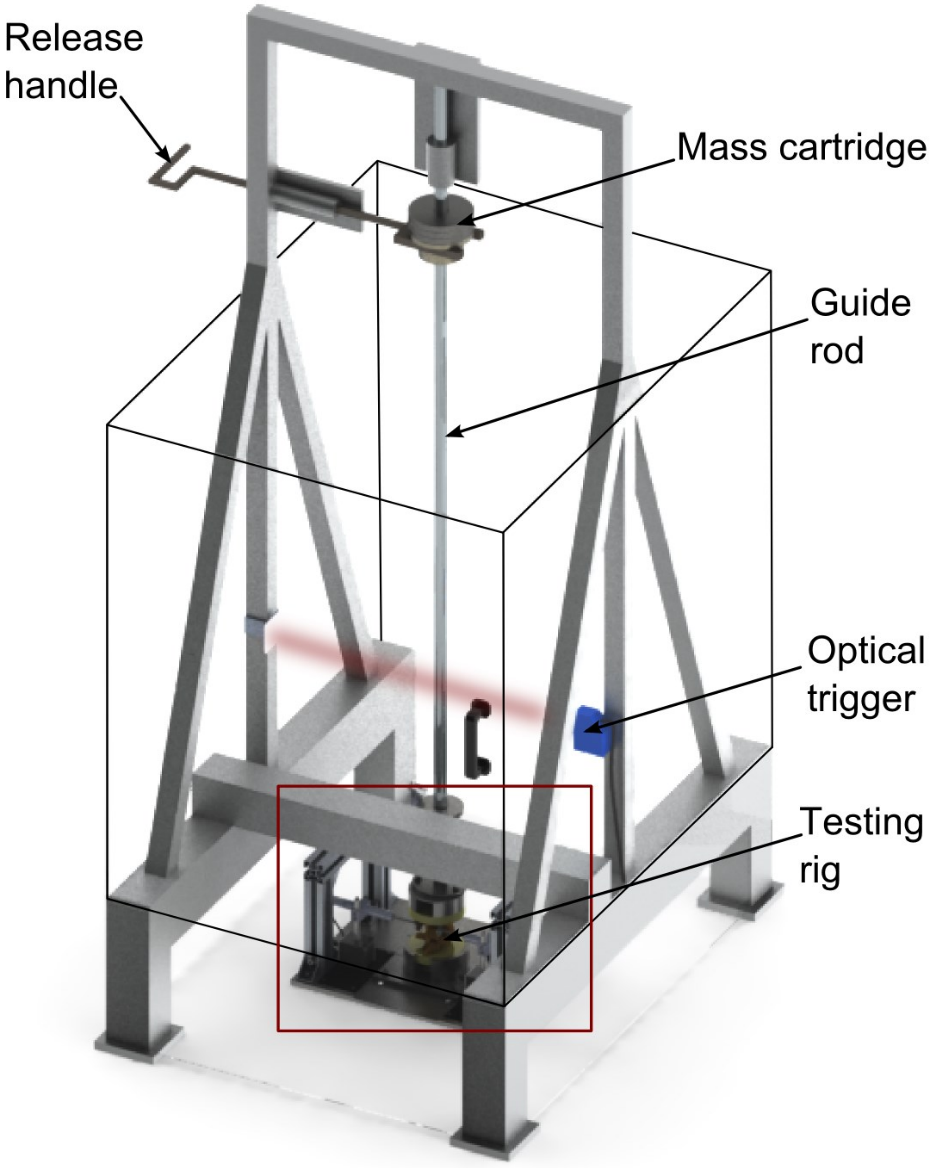

Figure 2-9: Drop weight testing apparatus used to create *in vitro* burst fractures on human cadaveric spinal segments.

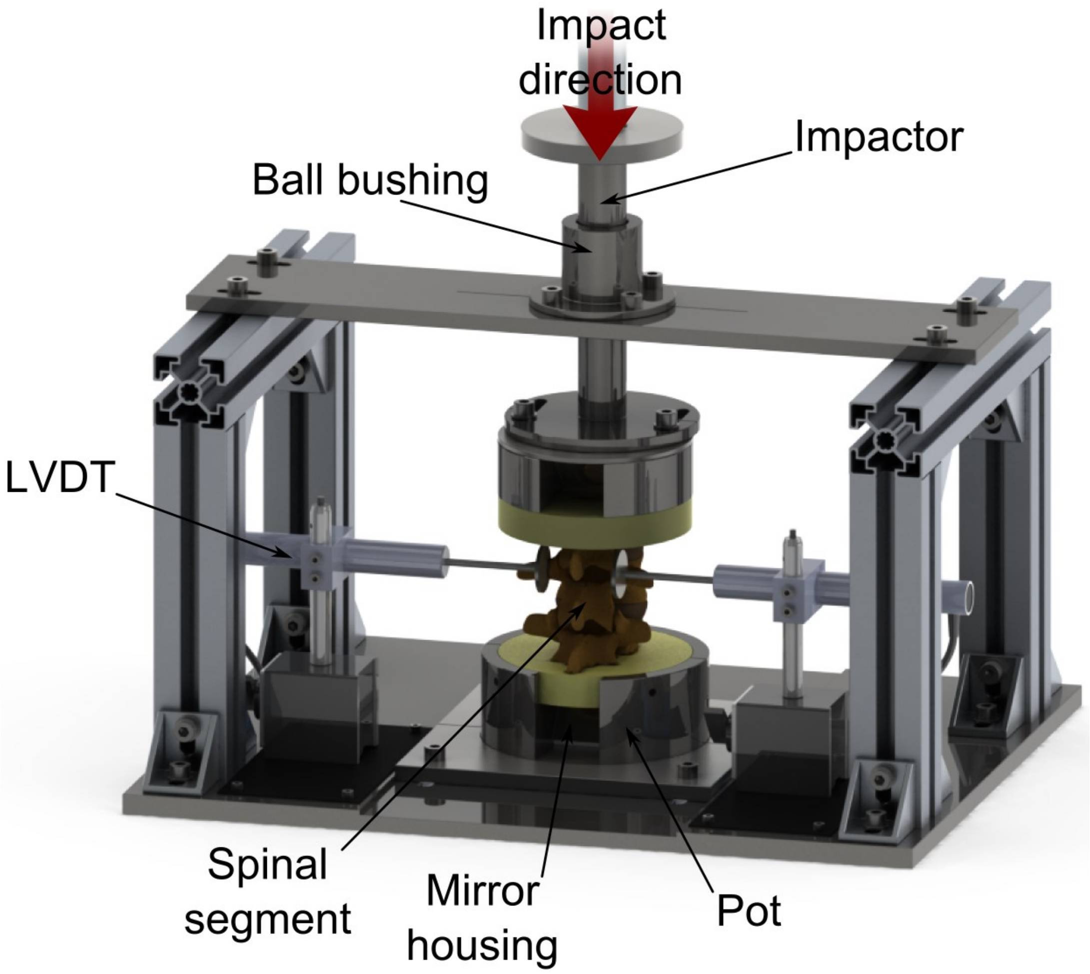

Figure 2-10: Testing rig used to investigate spinal burst fractures *in vitro*. The rig is to be positioned within the drop weight testing apparatus (Figure 2-9). Adapted from [1].

2.2.2.3 Dynamic measurements

Dynamic IPW was calculated from the output signals of two LVDTs (Type AC1000A; RDP Electronics) connected to dedicated amplifiers (RDP Electronics). Accuracy of the LVDTs was assessed periodically by mounting the transducer within a bespoke rig equipped with a micrometer head (Mitutoyo, Kawasaki, Japan). Calibration was performed by comparing readings from the software to the displacement physically imposed. Position of the LVDT within the testing rig could be adjusted through magnetic stands whilst the height could be set through custom fixtures that also maintained the LVDT parallel to the ground. The measuring direction of the LVDT coincided with the main axis of its stem which was aligned perpendicularly to the sagittal plane of the specimen (centre lines on the pot used as reference). The measurement location was chosen on each specimen to ensure adequate contact of the LVDT tip against a reproducible measurement point. Custom LVDT tips where designed to suit the measurement technique. A flat dish-shaped tip was fastened onto the stem of the LVDT to measure IPW on lumbar vertebrae (L1, L4). The tip was then put in contact with the most external aspect of the cranial facet joints (Figure 2-11). A spherical tip was fastened onto the LVDT stem when measuring IPW on thoracic vertebrae (T10). The shape and limited size of the thoracic facet joints did not allow a consistent access to the articular process as in the lumbar vertebrae. In addition, the thoracic facets do not protrude laterally as the lumbar ones and the other bony aspects would have physically interfered with the measurement. Therefore, the LVDT tip was put in contact with the region posterior to the root of the pedicles and above the costovertebral joint. The exact position of the LVDT tip was adjusted on each sample to minimise the influence of irregularities of the bony surface. In the lumbar vertebrae, the initial interpedicular distance (l_0) was measured experimentally as the distance between the flat tips of the LVDTs. In the thoracic vertebrae, the initial distance was measured on the HR-pQCT scans (l_{0CT}) by matching anatomical features recognisable on the specimens.

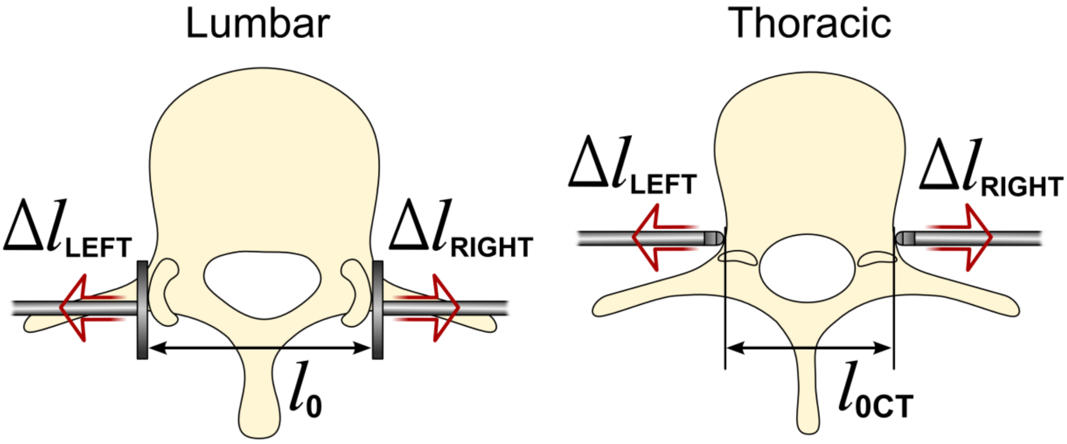

Figure 2-11: Positioning of the LVDTs for dynamic IPW measurement. Different positioning was required in lumbar and thoracic vertebrae.

The displacement measured by the left and right LVDT was named Δl_{left} and Δl_{right}, respectively, whilst the percent instantaneous IPW was calculated as follows (using l_{0CT} in the thoracic specimens):

$$IPW = \frac{\Delta l_{left} + \Delta l_{right}}{l_0} 100 \tag{2-1}$$

From each instantaneous measurement the following relevant parameters were identified:

- IPWmax: the maximum percent IPW corresponded with the maximum value assumed by IPW during the impact.
- IPWres: the residual percent IPW corresponded with the final value assumed by IPW at the end of the transient phase (i.e. at rest conditions).

Recordings from the LVDTs were set off by an optical trigger (W250 series; Sick, Waldkirch, Germany) whose output dropped when the mass cartridge crossed its light path during the fall (Figure 2-9). Signals were sampled at 5000 Hz over a period of 1 second from the triggering event.

In order to acquire the signals of interest, both the LVDTs and optical trigger were connected to a DAQ board (NI cRIO-9074; National Instruments Corporation) equipped with a 4 channel analogue input module (NI 9215; National Instruments Corporation). The acquisition board was connected to a laptop computer (via Ethernet) running custom software (LabVIEW; National Instruments Corporation). The candidate autonomously developed the code which allowed processing the signals and logging the data into a spreadsheet file. The first requirement of the software was to work at a high sampling frequency (i.e. to be able to track the displacement of the pedicles in impact conditions). Hence, an application was developed to run on the reconfigurable field-programmable gate array (FPGA), which the DAQ board was equipped with. FPGA programming allowed deterministic interaction with the I/O modules at high frequency. The FPGA application sent the raw LVDT signals to the local host application (running on the laptop) via FIFO architecture. A FIFO is based on the first-in first-out queue concept, hence provides buffering capability when transferring data between hardware/applications. Therefore, the two applications could run asynchronously without any risk of data loss. The sampling frequency specified by the user was also the clock frequency on the FPGA, whilst the main local application ran at 10 Hz. The purpose of the main application was to process (e.g. calibration), visualise and log the signals into a spreadsheet format (i.e. .csv file) for further analysis. The FPGA application was launched by the main application at run-time, whilst the whole system operated in two subsequent modalities: test preparation and data-logging. During the first phase, signal from the LVDTs were displayed in real-time so the user could zero the transducers as well as adjust the stroke of the LVDT (using the output voltage as reference). At this stage, the output of the optical trigger did not have any effect. When the experiment was set up, the user armed the data-logging session and the main application waited for the optical trigger to change its state (i.e. the mass was dropped) and activate the logging of data into file (over a specified period of time). When the logging was completed, the file was closed and the software stopped.

Wilcox et al. [26], developed a methodology to investigate dynamic SCO in burst fractures and applied it on bovine tail three-adjacent-vertebra segments. The candidate replicated the same technique in his experiments as it had never been used on human tissue. As described in Wilcox et al. [26], two 45° mirrors housed in the pots were used to create a light path through the spinal canal that was representative of its minimum CSA. A high intensity halogen light was shone against the upper mirror (within the impactor) whilst a high-speed camera (Phantom v7.3; Vision Research Inc., Wayne, NJ, USA) filmed the projection onto the lower mirror (Figure 2-12). The camera was connected to a laptop computer running its proprietary software for video-acquisition and set to film at 5000 frame per second with a resolution of 608 x 600 pixels. Recording was set off by the same optical trigger used for the LVDTs, hence allowing synchronisation between the two measurements. The videos were then exported as a series of frames in uncompressed format (i.e. .tiff) and processed using a bespoke code (Matlab; The MathWorks Inc., Natick, MA, USA). Once imported within the software, the images were converted from grayscale to binary through application of a threshold to retain only the values with sufficient luminosity. The binary images underwent morphological filtering/labelling to remove noise and undesired components. Finally, the dynamic SCO was calculated as the area of the binary foreground. SCO_{max} represented the maximum occlusion (i.e. the minimum instantaneous canal CSA) whilst SCO_{res} was identified as the residual SCO.

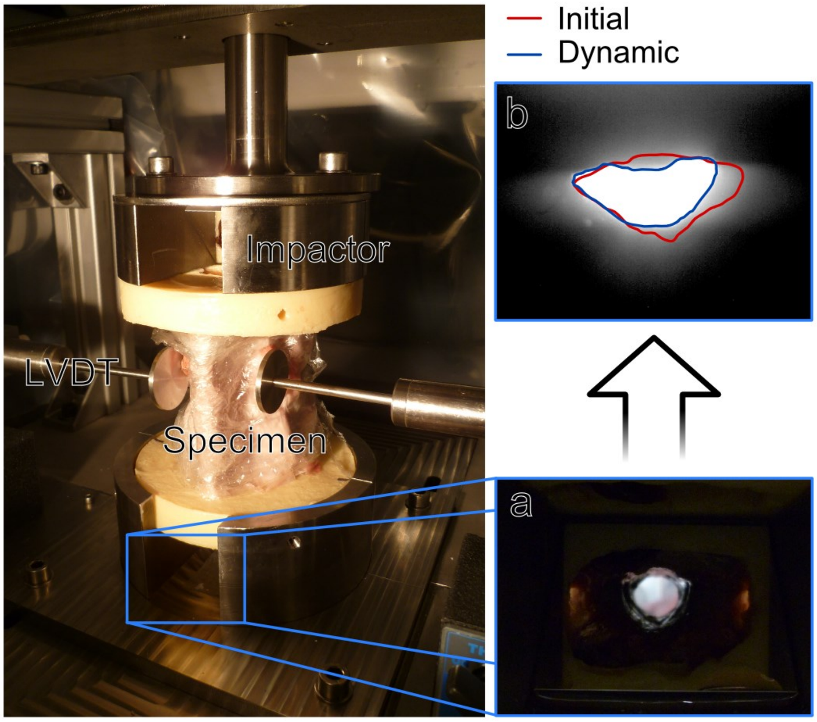

Figure 2-12: Experimental set-up ready for testing. a: view from the bottom 45° mirror; b: Dynamic SCO obtained from high-speed filming.

2.2.2.4 HR-pQCT assessment

Each specimen (whole three-adjacent-vertebrae segment) was scanned on HR-pQCT before and after testing using an isotropic voxel size of 82 µm (750 projections). The scans were used to calculate the following parameters on the central vertebra using an image processing software suite [240, 241]:

- BMD: calculated over a cylindrical volume centred at 40 % of AP distance, with diameter 60 % of AP distance and height 80 % of total vertebral height (identified as the distance between the deepest regions of the endplates) (Figure 2-13). Such volume was considered representative of the core of the vertebral body, the same procedure has been used in previous works [242].
- Pedicle angle: defined as the angle between the direction of the root of the pedicle and the AP direction (Figure 2-14), as in Zindrick et al. [62].
- SCO_{CT}: the minimum area within the spinal canal pre- (SCA_0) and post-fracture (SCA_1) was manually outlined on the slices of interest (Figure 2-15). Percent SCO was calculated as follows [122, 194]:

$$SCO_{CT} = \frac{(SCA_0 - SCA_1)}{SCA_0} 100 \qquad (2\text{-}2)$$

- SCO$_{clin}$: this is the SCO typically measured in clinics, where the pre-fracture spinal canal area is estimated as the average between the spinal canal area of the two adjacent intact vertebrae (SCA'$_{adj}$ and SCA''$_{adj}$) [31]:

$$SCO_{clin} = \frac{\left(\frac{SCA'_{adj} + SCA''_{adj}}{2}\right) - CA_1}{\left(\frac{SCA'_{adj} + SCA''_{adj}}{2}\right)} 100 \qquad (2\text{-}3)$$

- IPW$_{CT}$: this is the static IPW calculated from the HR-pQCT scans. The post-fracture interpedicular distance (l_{1CT}) was estimated by identifying the measurement location of the LVDTs on the CT slices and compared to l_0 (or l_{0CT} in thoracic vertebrae):

$$IPW_{CT} = \frac{(l_{1CT} - l_0)}{l_0} 100 \qquad (2\text{-}4)$$

- CSA$_{min}$: the minimum CSA of the vertebral body was calculated as the minimum area from the binary stack representing the whole volume of the vertebra (2.2.4.1).

Images from the scans were also used to identify the presence of LF and fragment retropulsion. In addition, the fractures induced were graded in accordance with the classification of Magerl et al. [18]. In addition, more comprehensive image processing applications were developed, as described below (2.2.4).

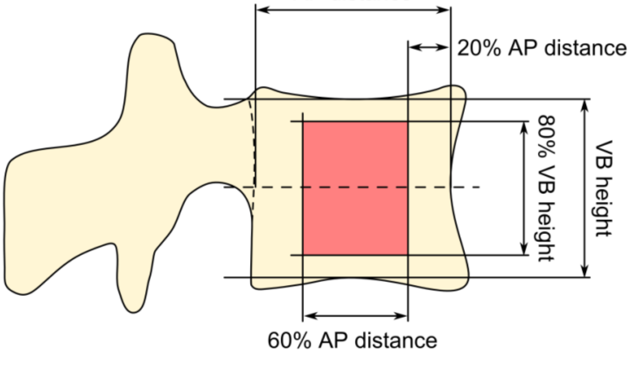

Figure 2-13: Region of interest for BMD calculation.

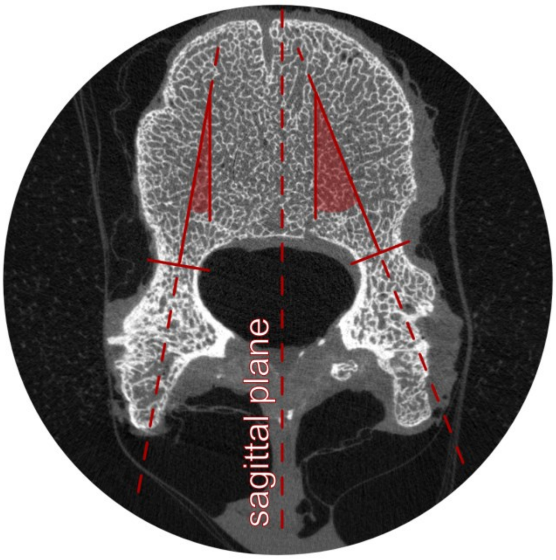

Figure 2-14: Measurement of the pedicle angles on the intact scan.

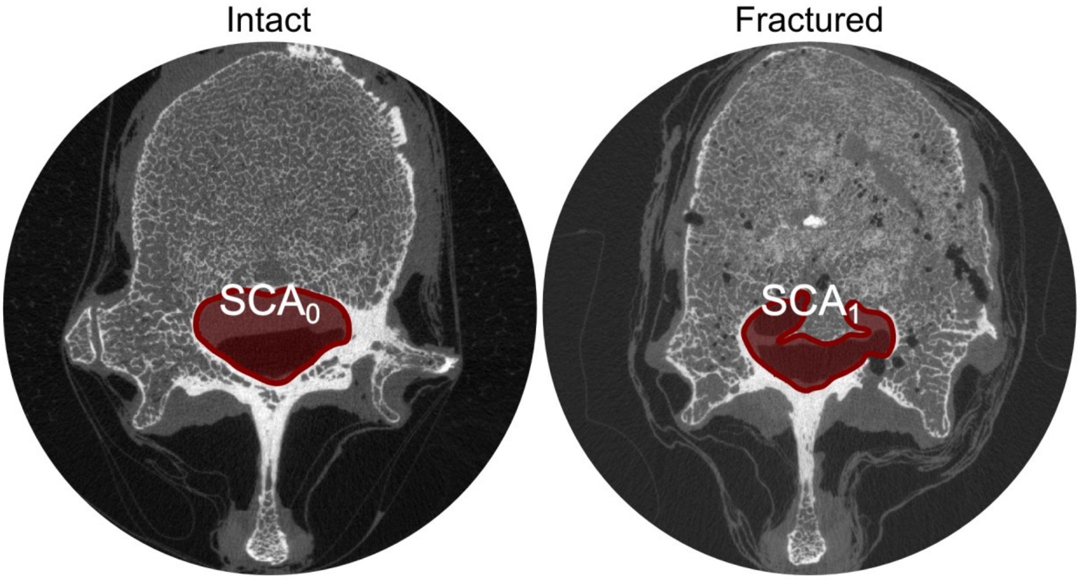

Figure 2-15: Measurement of the spinal canal area on HR-pQCT scans. Note the fragment retropulsion.

2.2.2.5 Experimental protocol

Feasibility of the experiments, reliability of the measuring technique and its data-logging software were assessed through a concept-validation trial were a synthetic three-adjacent-vertebra segment was tested (Sawbones, Pacific Research Laboratories, Vashon Island, WA, USA). Noise on the LVDT signals was estimated to affect the displacement measurement by approximatively ± 8 µm (amplitude of the signal measured with the LVDT in static conditions).

Human cadaveric specimens were divided in two groups, in order to have two T10, two L1 and two L4 per group. Samples were considered evenly distributed since no difference was found between the two groups in terms of BMD (Mann-Whitney U, p=0.59) and anatomy (Table 2-4). The latter was assessed by comparing the measurements described above (2.2.2.4). No difference was found regarding the initial interpedicular distance (Mann-Whitney U, p=0.63), the initial spinal canal area (Mann-Whitney U, p=0.94), and the pedicle angles (Mann-Whitney U, p=0.67). In agreement with the literature (1.1.1), the pedicle angles increased in the caudal direction (Kruskal-Wallis, p=0.0098).

Table 2-4: Details of the specimen and group division.

Donor	Level	Group	BMD mg HA/cm^3	CSA$_{min}$ (mm^2)	PA (°) Left	PA (°) Right	CA$_0$ (mm^2)	l$_0$ (mm^2)
A	T9-T10-T11	LE	148.3	953	4.8	-0.5	174	31.5
A	T12-L1-L2	HE	138.6	1000	22.8	5.2	350	44.3
A	L3-L4-L5	LE	100.5	1217	6.1	17.1	461	51.1
B	T9-T10-T11	HE	150.6	866	5.6	8.9	201	29.6
B	T12-L1-L2	HE	156.2	953	16.1	8.8	360	44.6
B	L3-L4-L5	HE	143.5	1153	14.2	21.1	305	49.8
C	T9-T10-T11	LE	128.0	1223	12.3	10.7	203	35.6
C	T12-L1-L2	LE	98.5	1439	21.2	16.2	273	46.7
C	L3-L4-L5	HE	111.0	1487	19.5	19.9	246	53.0
D	T9-T10-T11	HE	191.9	891	14.0	9.0	214	32.6
D	T12-L1-L2	LE	184.5	1006	14.5	20.2	314	44.6
D	L3-L4-L5	LE	161.7	1139	37.4	35.8	258	55.7
	Median		145.9	1072	14.3	13.4	266	44.6

BMD: bone mineral density; CSA$_{min}$: minimum cross sectional area; PA: pedicle angle; CA$_0$: intact canal area; l$_0$: intact interpedicular distance.

Each group was representative of a high-energy (HE) and low-energy (LE) impact, therefore, two different levels of energy were delivered. The exact amount of energy delivered to each segment was tuned based on the group (HE or LE), BMD and CSA$_{min}$ of the central vertebra. Such criterion was chosen to minimise the effects of inter-specimen variability. After an initial set of experiments, a value of energy for LE group was estimated as the minimum value of energy required to consistently induce a spinal burst fracture (E$_{min}$, also based on the values used in the literature). The specific value of energy for each sample of the LE group (E$_{LE}$)

was proportional to the generalised value E_{min} and the product between BMD and CSA_{min} of that vertebra.

$$E_{LE} = E_{min} \times BMD \times CSA_{min} \qquad 2\text{-}5)$$

Likewise, the amount of energy delivered to the samples belonging to the HE group (E_{HE}) was calculated as a 20 % increase with respect to the value calculated with the same method used for LE group. (

$$E_{HE} = 1.2 \times E_{min} \times BMD \times CSA_{min} \qquad (2\text{-}6)$$

2.2.3 Fatigue testing of SSPI – KP

This section describes the methods developed by the candidate to carry out the second phase of his project. In order to follow the patient pathway from fracture occurrence to surgical treatment, SSPI or SSPI – KP was performed on three-adjacent-vertebrae segments with a spinal burst fracture. Therefore, the same specimens which underwent fracture creation (2.2.2) were used again for the second phase of the project. The PMMA layers were removed to ease implant procedure and allow new alignment for the experiments. Following implantation, the fatigue behaviour of the constructs was investigated. Therefore, a bespoke testing rig and protocol were developed. The testing protocol also required the development of custom software for data logging and analysis. Mechanical testing was integrated with image processing (2.2.4) to provide tools for a comprehensive investigation of the performance of the treatment. All the surgical procedures were carried out by the candidate in accordance to training/documentation provided by the manufacturer.

2.2.3.1 Specimen preparation

Twelve three-adjacent-vertebrae segments (Table 2-1) with a spinal burst fracture at the central vertebra were divided into two groups to undertake the following procedure:

- SSPI group: six samples implanted with SSPI.
- SSPI – KP group: six samples implanted with SSPI followed by KP with CaP cement.

Specimens were considered evenly distributed between the two groups in terms of SCO_{CT} (Mann-Whitney U, p=0.82), which was considered more indicative of comminution and risk of cement leakage than IPW.

The size of the screw (i.e. diameter and length) to be implanted in each pedicle was assessed on HR-pQCT scans. The samples were let thaw overnight and then SSPI was performed as follows:

- The entry point for each screw was created by breaching the posterior surface of the lamina with a bone awl.

- A pilot hole for the screw was created by inserting a tap tool (one size inferior to that of the screw). The trajectory was defined according to the anatomy of the vertebra (the endplates were exposed) and basics of SSPI (1.3.1). Care was taken not to breach the pedicle cortex and invade the spinal canal.
- Screws were inserted in each tapped hole and tightened until purchase was considered satisfactory and/or the nut was aligned to suit the fixator rod.
- Each fixator rod was placed within its two nuts and then fastened with a grub screw to lock it in place. Grub screws were tightened up to 9 Nm using a torque limited screwdriver provided by the manufacturer. No reduction manoeuvre was attempted other than that induced by the alignment of the fixator rods.

Following SSPI, the neural arch of the central vertebra of each segment was excised through resection of the pedicles (Figure 2-16). The procedure was similar to a laminectomy with bilateral facetectomy and allowed full access to the posterior wall of the canal whilst forcing the whole load sharing exclusively through the fixator and the vertebral body. None of the fixator rods was contoured (i.e. they were all kept straight) to avoid any risk of stress concentration (Ti6Al4V is particularly sensitive to notching), as shown in Lindsey et al. [220]. In addition, keeping the rod straight resulted in a simplified and more repeatable condition for the measurement of surface strains.

The SSPI – KP group underwent KP in addition to SSPI. The samples were let thaw overnight and the whole procedure was performed under fluoroscopic guidance in accordance to clinical practice (1.3.2). Target parameters for KP were defined for each sample based on measurements from HR-pQCT scans:

- BIV: balloon inflation volume was 20 % of the total vertebral body volume (estimated as described in 2.2.4.1) (Figure 2-17). BIV represents the total inflation volume of the two IBTs together (i.e. the inflation volume of each IBT was half BIV). The manufacturer advised a target BIV of 25 %, however, such value would have exceeded the maximum volume allowed (limited by the size of the IBTs available) on same samples. Therefore, the BIV was reduced to 20 % to keep consistency among all the specimens. As recommended by the manufacturer, the IBTs were inflated progressively in 0.25 ml increments.

- CV: total volume of cement injected was 25 % of the vertebral body volume. Therefore, the amount of cement to be injected per side was equal to half CV. CaP cement was mixed and then injected 1 ml at a time using the instruments provided by the manufacturer. Injections were stopped when the target volume was reached or a leakage was detected (Figure 2-17).

Following KP, the samples were kept for 24 hours submerged in phosphate buffered saline (PBS) at 37°C within a temperature regulated chamber. The procedure allowed the cement to cure and reach its maximum strength (Figure 2-1).

Details of the surgical procedures performed as well as related complications encountered were logged for all the samples (Appendix A).

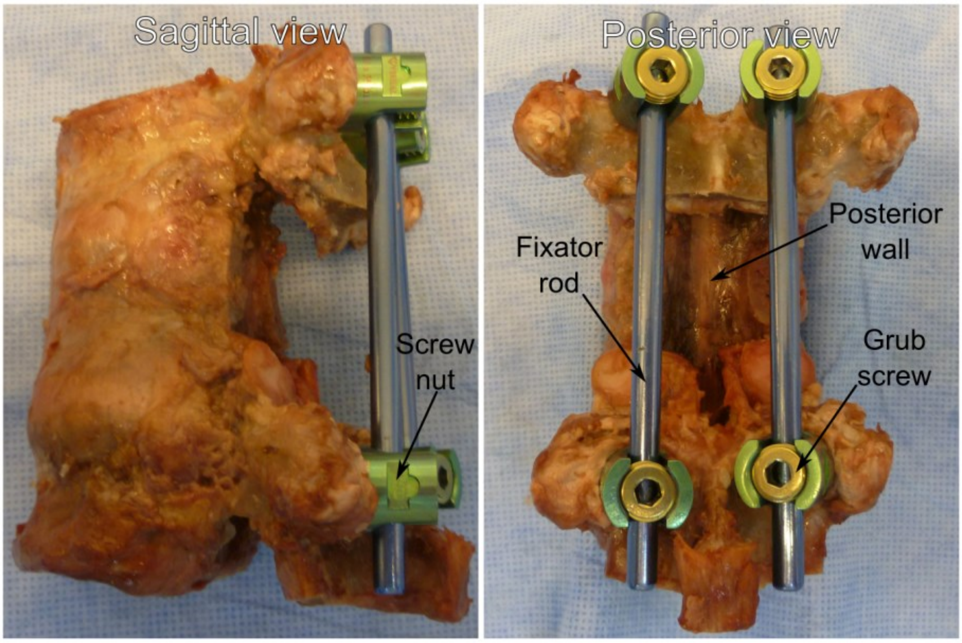

Figure 2-16: SSPI with neural arch excised. Photographs are representative of the actual sample group.

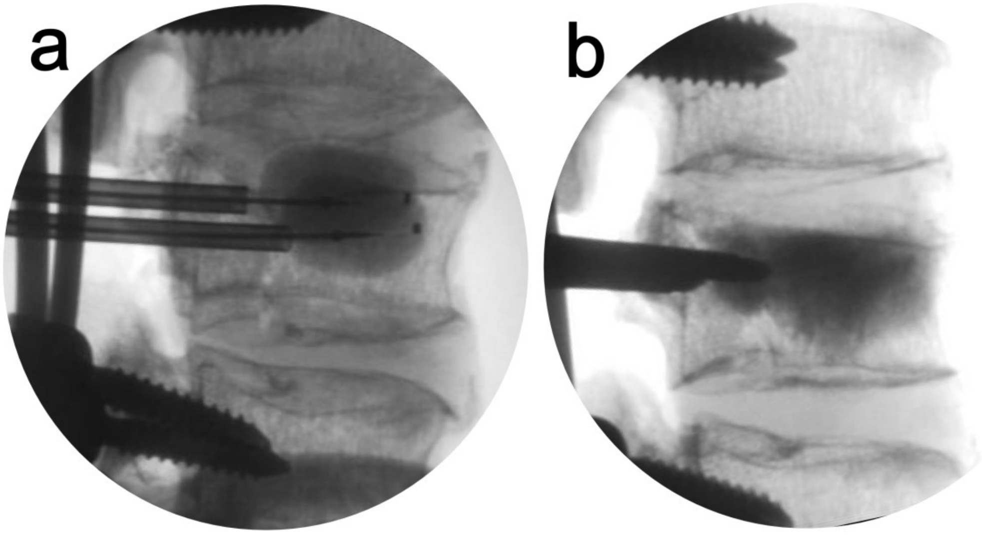

Figure 2-17: KP performed under fluoroscopic guidance. Images are representative of the actual sample group. a: inflation of IBT; b: injection of CaP cement.

Specimens’ extremities were embedded in a layer of PMMA using the same procedure described above (2.2.1.1). The segments were positioned within the pots to have the sagittal and frontal plane aligned accordingly within the testing rig (as in 2.2.2.1). In this case modelling clay was placed around the nuts of the screws to avoid embedding them. Therefore, the rods were able to transfer the load they were undergoing to the screws without any external support/constraint.

One uniaxial strain gauge (UFLA-5-11; TML, Tokyo Sokki Kenkyujo Co. Ltd., Tokyo, Japan) was bonded on each fixator rod. The gauges had a nominal resistance of 120 Ω; a grid length and width of 5 and 1.5 mm, respectively. The main axis of the measuring grid was aligned with the main axis of the rod whilst the shorter axis was centred at about mid height of the rod (Figure 2-23). The surface was prepared for installation by polishing with sandpaper (grit P120) and then degreasing with laboratory grade acetone. The gauge was bonded onto the rod using cyanoacrylate glue (CN; TML, Tokyo Sokki Kenkujo Co. Ltd.) and coated with resin (N – 1; TML, Tokyo Sokki Kenkujo Co. Ltd.) to make it waterproof.

2.2.3.2 Testing rig

A bespoke testing rig was designed and manufactured to be fastened within a universal testing machine (E10000; Instron, Norwood, MA, USA) and house the prepared sample (Figure 2-18). That specific model of testing machine was used because suitable for fatigue loading. The rig was designed to deliver a cyclic axial compression (i.e. sine wave, described in 2.2.3.4) to the treated spinal segment. The sample was fastened within the pots used for PMMA embedding with circumferential grub screws. Then the pots were fit within steel housings flanged against the table of the testing machine and the actuator. Consistent alignment was achieved through matching dowels on the steel housings and pots.

In order to avoid testing in overconstrained conditions two linear bearings were mounted orthogonally to each other (as an x-y table) between the upper steel housing and the actuator (i.e. the flange of the load cell). Therefore, the axial translation perpendicular to the ground was controlled by the machine, whilst translations parallel to the ground were left unconstrained.

Two LVDTs were used to measure the displacement of the anterior surface of the vertebral body and that of the posterior wall. The displacement measurement served to track how the central vertebra moved because of cyclic loading. The LVDTs were positioned to have their measuring axis perpendicular to the frontal plane and parallel to the ground. The two LVDTs, magnetic stands and brackets were the same used for measuring IPW during fracture onset (2.2.2.3). Custom tips were designed and manufactured to be mounted onto the stem of the LVDTs. The tips were made out of plastic and had an increased contact surface with different curvatures to follow better the geometry of the anterior region of the vertebral body and spinal canal (Figure 2-23).

Surface strain on the fixator rods was measured through the uniaxial strain gauges bonded on the posterior region of the rod. Such location was supposed to be repeatable and most representative of the overall strain distribution of the fixator (away from the stress concentration region close to where the rod is fastened [220]). In addition, one uniaxial strain gauge was bonded on one separate fixator rod that was not implanted on any sample. This instrumented rod acted as a dummy gauge to quantify any artifact (e.g. temperature drift).

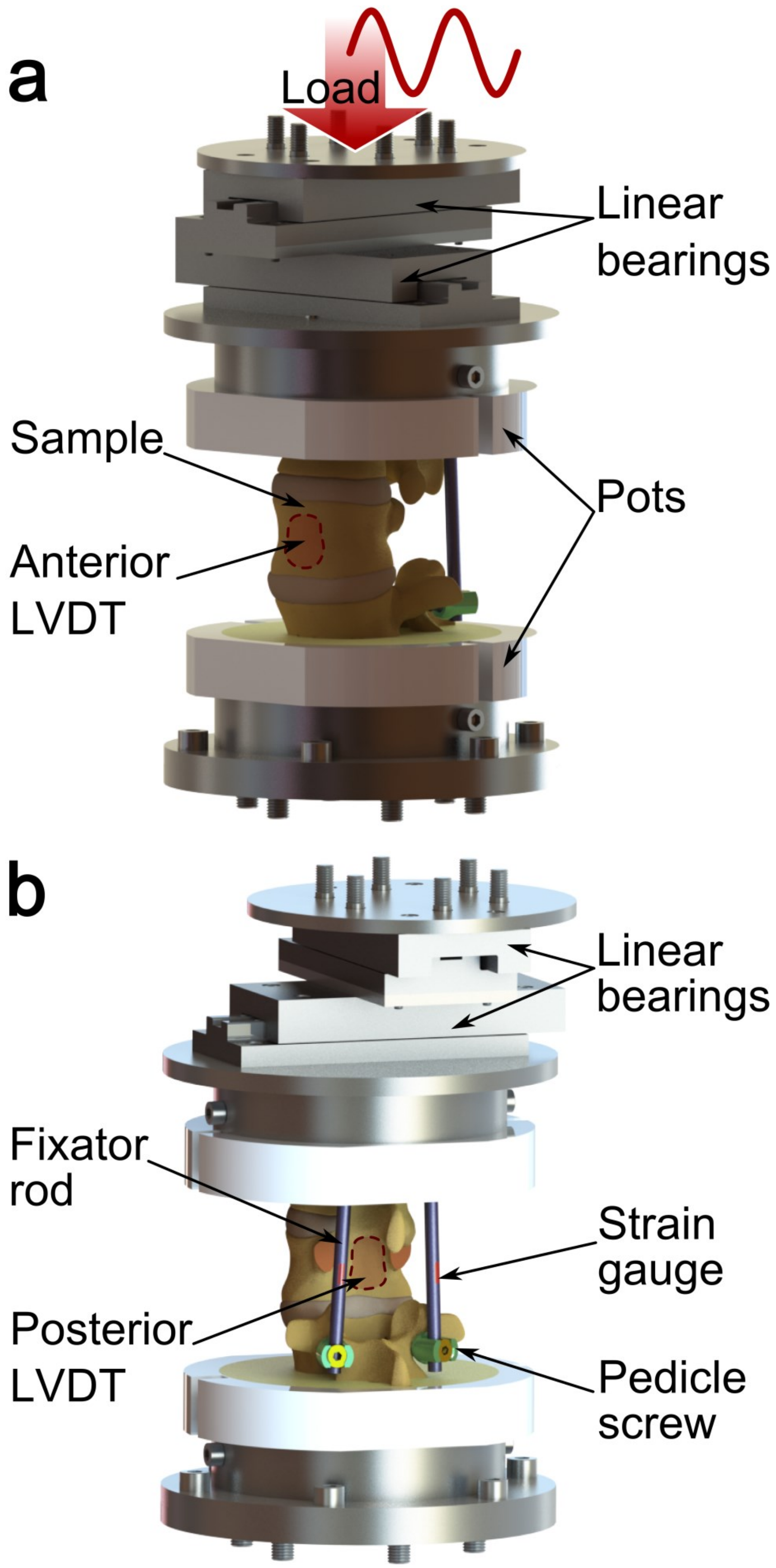

Figure 2-18: Testing rig for fatigue testing. The highlighted regions show the measurement locations of the LVDTs. a: Lateral view; b: posterior view.

2.2.3.3 Data logging and analysis

Experimental signals were acquired through a DAQ board (NI cRIO-9074; National Instruments Corporation) equipped with dedicated modules and connected to a laptop computer running bespoke software (LabVIEW; National Instruments Corporation). The following differential signals were connected to a 4 channel analogue input module (NI 9215; National Instruments Corporation):

- Displacement from the testing machine;
- Load from the testing machine;
- Displacement from the anterior LVDT;
- Displacement from the posterior LVDT.

In addition, the two strain gauges (on the implanted fixator rods) and the dummy gauge (on the unloaded fixator rod) were connected to an 8 channel quarter-bridge strain gauge module (NI 9235; National Instruments Corporation) using a three-wire connection.

In addition, the software had to satisfy the below specifications:

- Sampling of the signals at 100 Hz or higher;
- Calibration and initial processing of the signals;
- Show acquired data through user interface;
- Continuous logging of data over long periods of time (more than 12 hours).

Fulfilling the above specifications required implementing several coding paradigms and architectures to achieve robustness and reliability. Therefore, three main applications were developed: local host, real-time (RT) and FPGA. The local host application ran on the laptop computer whilst both the RT and FPGA application ran on the DAQ board (Figure 2-19). The most critical part was the implementation of data transfer between applications. Firstly, the raw signals were acquired directly by the FPGA from the modules. A FIFO was exploited to transfer the raw signals from FPGA to RT. Then, the raw signals underwent initial pre-processing (calibration, zeroing) within the RT application. After being organised into a spreadsheet-like matrix they were sent to the local host via a network stream. A network stream is a lossless communication paradigm for distributed applications. The data are streamed from a writer endpoint (i.e. RT) to a reader endpoint (i.e. local host) based on their reference address (URL). The local host application controlled the other applications through the user interface (Figure 2-20). Therefore, the user launched the FPGA application; then set the parameters for the calibrations (e.g. gauge factor, slope) and sampling frequency. If enabled on the user interface, the first task of the FPGA application was performing the shunt calibration. Hence, the RT application calculated the correction factors of each strain gauge and applied it when calculating the strain from the bridge output. For convention, tensile strains were set as positive whilst compression strains were negative. Once received by the local host, the data were plotted on video and the user could enable the logging function (i.e. save the data to .csv file) by pressing a dedicated button. After creating the spreadsheet header, the data were subsequently appended to the file every time a new block of data was received from the network stream. When the file reached a pre-set size, it was closed and a new one was created to increase the robustness of the software for long recordings.

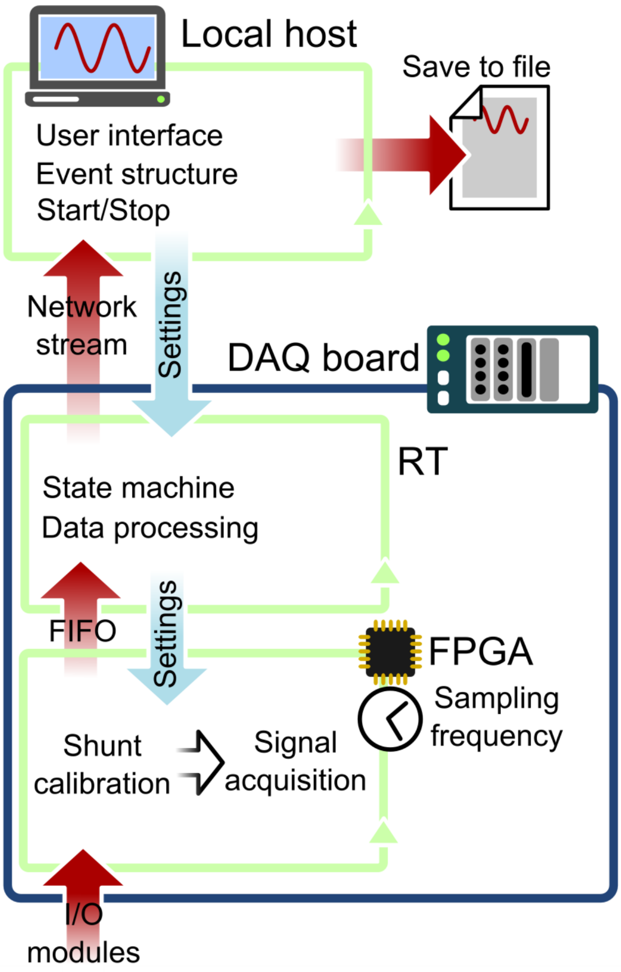

Figure 2-19: Architecture of the data logger.

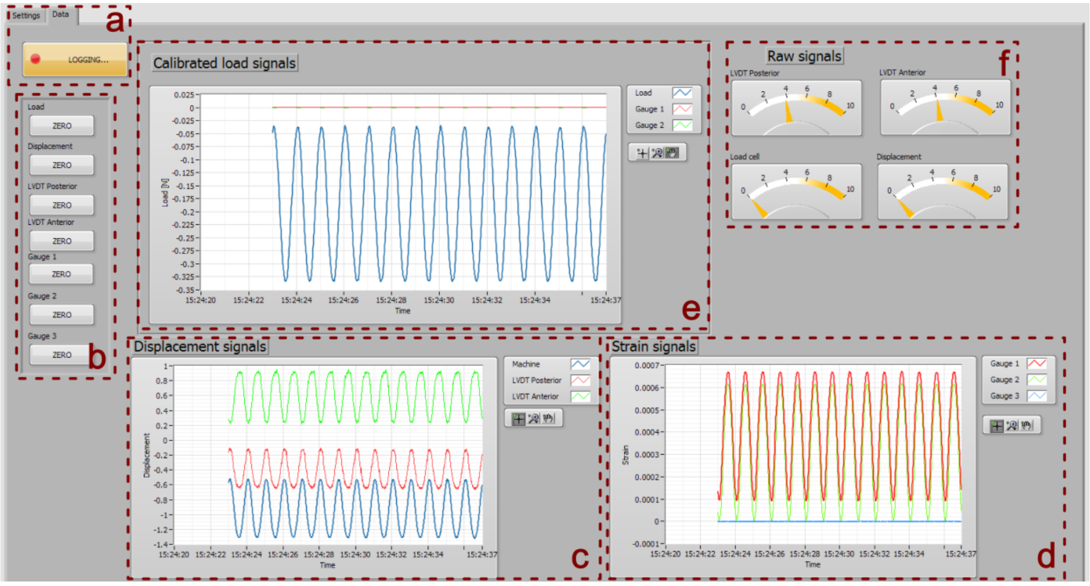

Figure 2-20: User interface of the data logger. a: controls and settings; b: signal zeroing; c: displacement graph; d: strain graph; e: load graph; f: raw signals.

Following the experiments, the spreadsheet files were imported into a bespoke application developed within a technical computing suite (Matlab; The MathWorks Inc.) for further processing. Since the loading curve was a sine wave, it was assumed that all the other signals (except the dummy gauge) were periodical too, because inherently induced by it. Firstly, each signal was processed to remove measurement artifacts (e.g. off-scale values) and then smoothed (using a Savitzky-Golay filter). Subsequently, peaks throughout the curve were detected to divide the signal in consecutive periods. Mean and peak to peak value were calculated over each period, therefore two additional signals (with number of samples equal to number of cycles) originated from each calibrated signal (Figure 2-21). The calibrated signal from the dummy gauge served as reference to check if there was any signal drift.

In addition, each period from the load waveform was processed against its correspondent displacement cycle to estimate the instantaneous stiffness of the construct. The stiffness was calculated as the slope over the 90th percentile of each peak to peak tract (to retain the most linear part of the curve). Thus, two values of stiffness were calculated per each period(Figure 2-21):

- $\text{Stiff}^{\text{Fall}}$: stiffness calculated over the falling edge of the curve (i.e. during the loading tract of the profile, when compressive load increases);
- $\text{Stiff}^{\text{Rise}}$: stiffness calculated over the rising edge of the curve (i.e. during the unloading tract of the loading profile, when compressive load decreases).

To allow comparison and quantify the effect of fatigue testing, the signals were averaged at the beginning and end of the test. The initial values were averaged over 1800 cycles following the first 1200 cycles. The initial wait was necessary to allow appropriate settling of the sample. The final values were calculated over the last 1800 cycles. The following quantities were obtained:

- $\text{MaxStrain\_mean}_{\text{in}}$ and $\text{MaxStrain\_mean}_{\text{fin}}$: maximum between the average mean strains from the left and right rod at the beginning and end of the test.

- MaxStrain_p2p$_{in}$ and MaxStrain_p2p$_{fin}$: maximum between the average peak to peak strains from the left and right rod at the beginning and end of the test.
- Disp_mean$_{in}$ and Disp_mean$_{fin}$: average mean axial displacement (i.e. with respect to the crosshead of the testing machine) at the beginning and end of the test.
- Disp_p2p$_{in}$ and Disp_p2p$_{fin}$: average peak to peak axial displacement (i.e. with respect to the crosshead of the testing machine) at the beginning and end of the test.
- Post_mean$_{in}$ and Post_mean$_{fin}$: average mean posterior displacement (posterior LVDT) at the beginning and end of the test.
- Post_p2p$_{in}$ and Post_p2p$_{fin}$: average peak to peak posterior displacement (posterior LVDT) at the beginning and end of the test.
- Ant_mean$_{in}$ and Ant_mean$_{fin}$: average mean anterior displacement (anterior LVDT) at the beginning and end of the test.
- Ant_p2p$_{in}$ and Ant_p2p$_{fin}$: average peak to peak anterior displacement (anterior LVDT) at the beginning and end of the test.
- Stiff$_{in}^{Rise}$ and Stiff$_{fin}^{Rise}$: average stiffness calculated over the rising edge at the beginning and end of the test.
- Stiff$_{in}^{Fall}$ and Stiff$_{fin}^{Fall}$: average stiffness calculated over the falling edge at the beginning and end of the test.

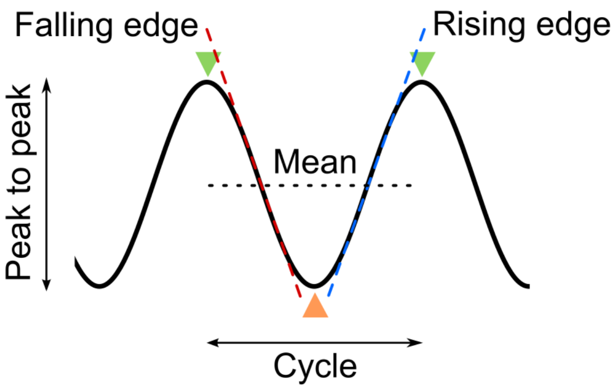

Figure 2-21: Schematic of the signal processing on the load waveform.

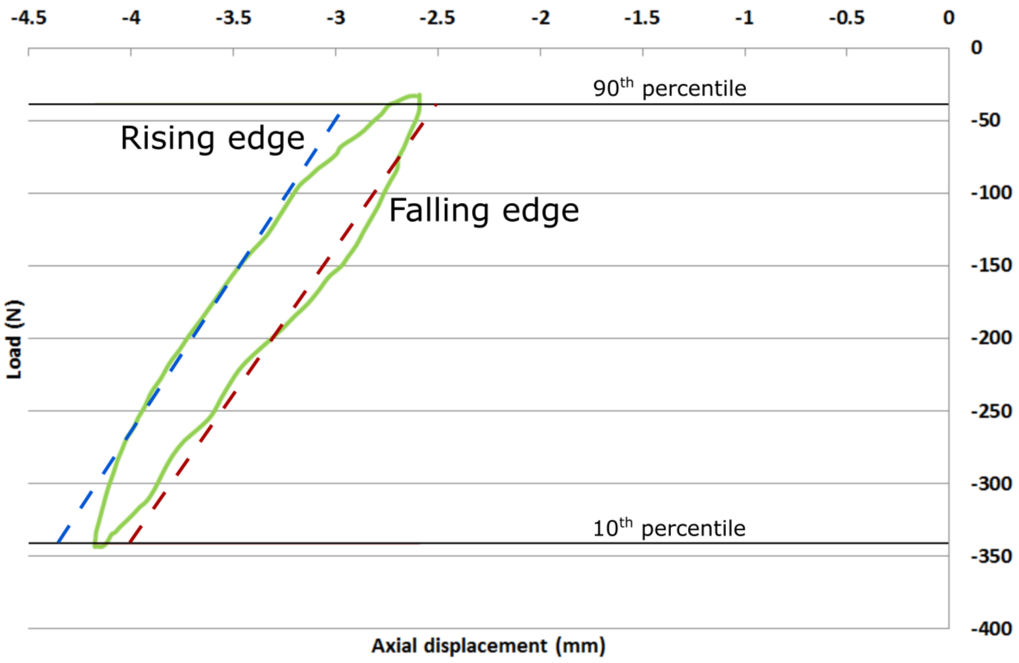

Figure 2-22: Actual experimental data showing one load-displacement cycle; stiffness was calculated over both the rising and falling edge.

2.2.3.4 Experimental protocol

Once the segment was mounted within the rig, all the transducers were zeroed and the test was started (Figure 2-23). All the signals were sampled continuously throughout the experiment at 100 Hz using the software described above (2.2.3.3). The machine was programmed to first reach an axial preload of -50 N and then impose a cyclic axial loading regime. A load controlled sine wave was set to be applied for 70000 cycles at 1 Hz (19 hours and 27 minutes). The test stopped at run-out or if the axial displacement exceeded 20 % of the initial distance between the pots.

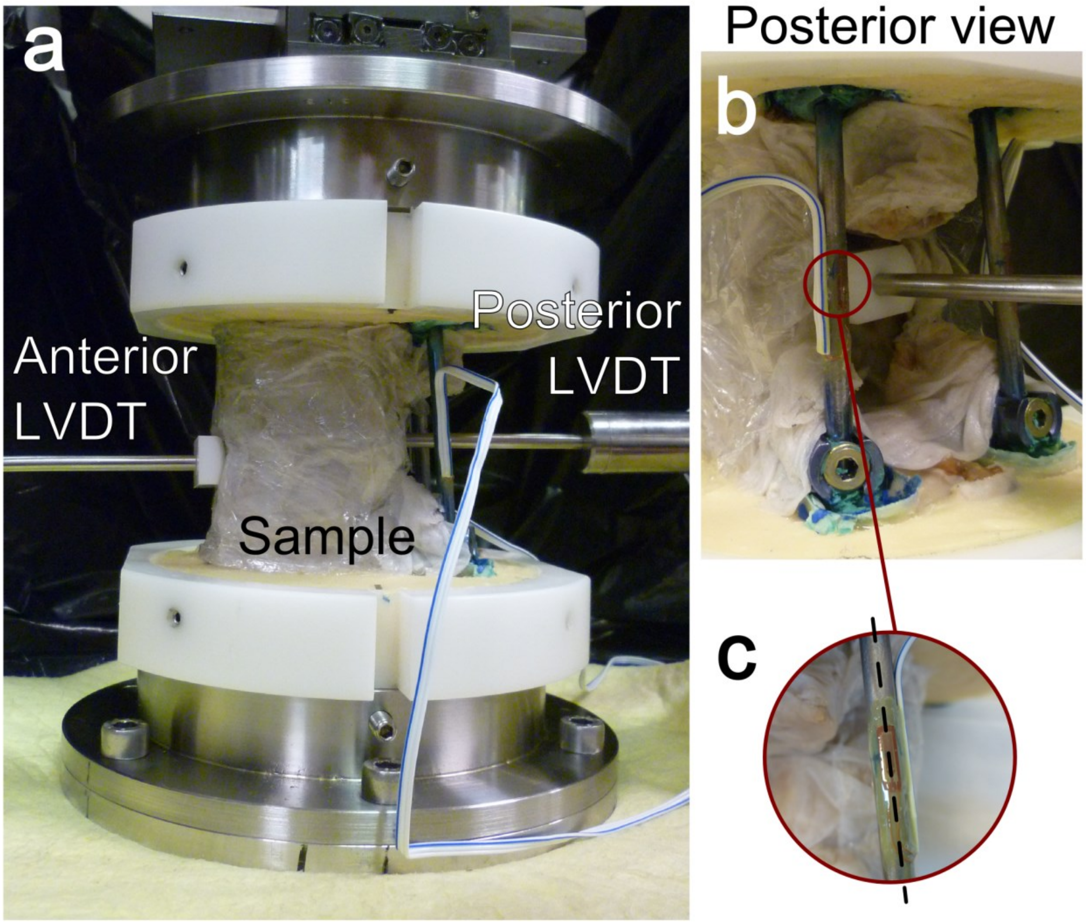

Figure 2-23: Specimen mounted within the testing rig. a: overview of the setup; b: Measurement location of the posterior LVDT; c: alignment of the strain gauge.

The maximum (F_{max}) and minimum (F_{min}) value of compressive force (i.e. in absolute terms) reached by the sinusoidal profile were tuned for each sample as a fraction of body weight (BW) (Figure 2-24). Such reference values represented the dead weight born by that spinal level when standing, as estimated by Duval-Beaupere et al. [243]. According to the central vertebra of the segment under test, F_{max} was set as:

- 32.1 % of BW for T10;
- 39.4 % of BW for L1;
- 46.6 % of BW for L4.

F_{min} was set to maintain a ratio F_{max}/F_{min} equal to 10; as in Lindsey et al. [220]. Such cyclic loading profile was chosen to simulate light physical activity, as it occurs in the postoperative time.

Following tests, SSPI was removed from all the samples. Screw loosening was detected using a torque limited screwdriver. If the extraction torque was lower than 0.4 Nm, the screw was considered loose. This criterion is based on clinical evidence [138] and it has been used in other experimental works [244].

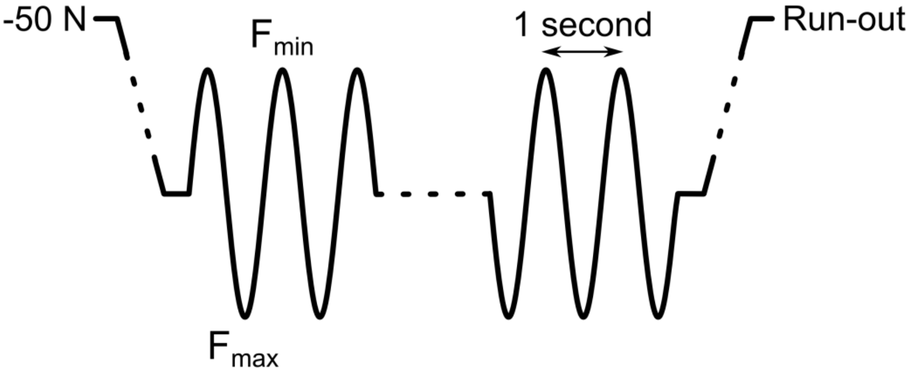

Figure 2-24: Definition of the loading profile for fatigue testing.

2.2.4 3D analysis

Image processing was extensively integrated with the methods developed to investigate the fracture (2.2.2) and their treatment (2.2.3). The integration between the two techniques provided tools for a comprehensive investigation of the fracture phenomena. The methods described below were developed and exploited in different applications to fulfil specific requirements.

The 12 three-adjacent-vertebra segment were scanned on HR-pQCT (voxel size 82 µm, 750 projections) at each experimental stage and the resultant image dataset processed (Figure 2-25). The 3D surfaces of the vertebrae extracted from the image datasets were analysed to get clinically relevant measurements of deformity (2.2.4.3) as well as the deflection of the endplates (2.2.4.4).

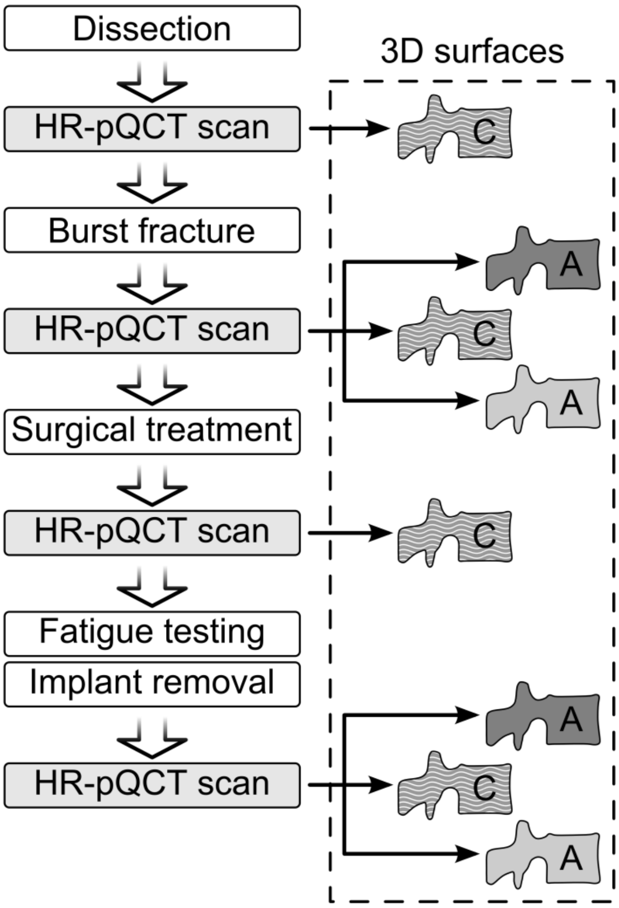

Figure 2-25: Flow diagram of the scans undertaken at different stages and 3D surfaces extracted from each image dataset. Central vertebra and its adjacent ones marked as C and A, respectively.

2.2.4.1 Creation of 3D surface model of the vertebra

In order to perform any kind of 3D anatomical analysis, the vertebra had to be converted into a 3D model. The 3D surface of the vertebra under study was segmented out of each image dataset using a semi-automated segmentation procedure (Figure 2-26). Firstly, an arbitrary threshold was used to separate the foreground (bone) from the background. Then a series of morphological operations were performed to extract a solid vertebra (i.e. outer surface with no trabecular structure). A number of dilation cycles were run to join porous structures which were then filled, subsequently the same number of erosion cycles was run to shrink the selected area. Finally, the surface was smoothed using Gaussian blurring.

The same procedure was applied in different contexts in an image processing [240, 241] or technical computing suite (Matlab; the MathWorks Inc.) depending on the application developed. The segmented vertebra conserved the slice-stack format (a CT dataset can be considered as a 3D array) so datasets could be easily overlaid. Thus, reliability of the procedure could be qualitatively assessed by comparing the boundary of the solid vertebra over the greyscale images (Figure 2-27). CSA of the vertebra was estimated as the area within the boundary of the solid vertebra to get the value CSA_{min} used above (2.2.2.4). In addition, such boundaries could be used to identify a complex region of interest to perform other morphological operations (e.g. stereology assessment).

Alternatively, the segmentation procedure was performed in an image processing suite which also provided meshing tools (Amira; Visualization Sciences Group) to create 3D models of the vertebra. Once the solid vertebra was segmented out of the greyscale dataset (as described above), the volume was meshed to create a triangulated surface. This procedure was applied to all the vertebrae that were used in any of the below described 3D applications.

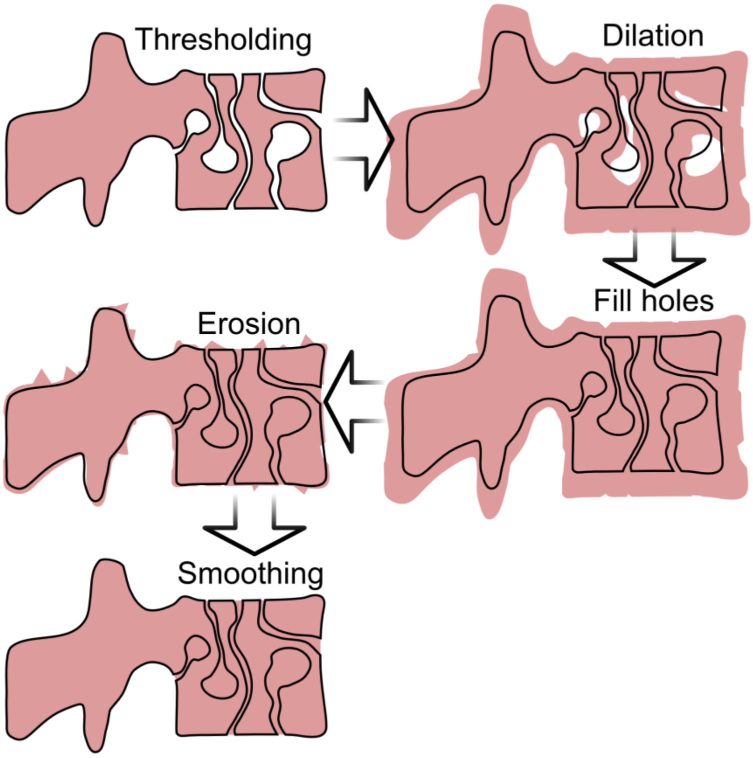

Figure 2-26: Schematic of the semi-automated segmentation procedure to identify the outer surface of the vertebra.

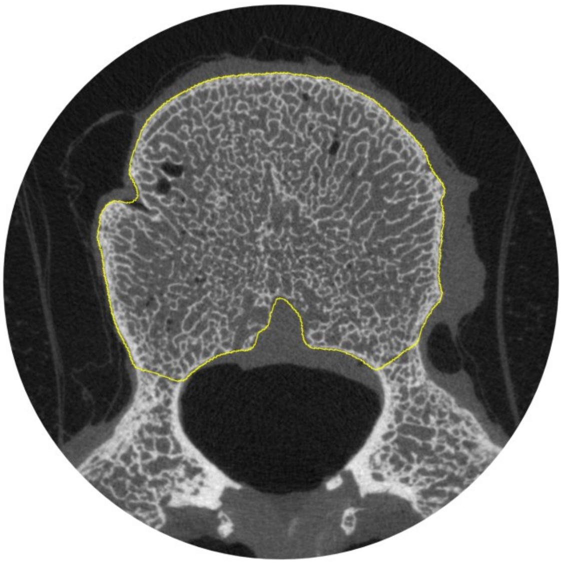

Figure 2-27: Boundary of the vertebral body overlaid on the original greyscale HR-pQCT slice. Image representative of the result of the semi-automated segmentation procedure.

2.2.4.2 Local anatomical reference frame

A local reference frame was defined to quantitatively perform 3D analysis with respect to anatomically relevant axes. The formal definition provided by Panjabi et al. [59] and described before (1.4.5) was implemented. Therefore, the landmarks had to be virtually palpated on the 3D surface (Figure 2-28). This process was carried out in the same software used for the segmentation and meshing (Amira; Visualization Sciences Group). The original coordinates of the landmarks were inherently defined with respect to the coordinate system of the CT scanner and they represented the indices of each element (i.e. voxel) of the 3D array that makes up the CT dataset. Thus, any measurement taken in this coordinate system would depend on the alignment of the sample within the scanner. The coordinate list was exported and processed with bespoke code (Matlab; the MathWorks Inc.). Firstly, the code implemented the operations described in 1.4.5 to define the axes and origin of the local reference frame. Therefore, the rotation matrix and position vector could be calculated to transform any set of coordinates from the CT reference frame to the local anatomical reference frame. Such transformation of coordinates allowed a more clinically relevant investigation as well as removing any limitation due to alignment of the sample within the scanner.

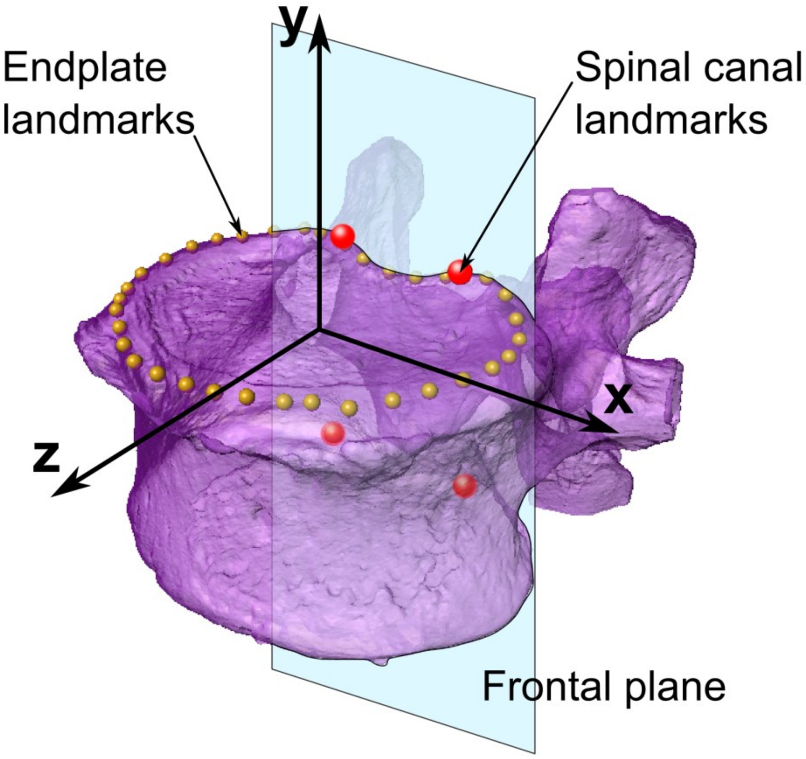

Figure 2-28: Definition of the local anatomical reference frame on a 3D surface representative of the specimens.

2.2.4.3 Measurement of vertebral deformity

An image processing protocol was developed to perform clinically relevant geometrical measures on the 3D surfaces of the vertebra. The procedure was performed on the central vertebra at all experimental stages. Hence, four 3D models of the central vertebra were processed per segment (Figure 2-25).

The intact state, prior to burst fracture and subsequent to dissection, was taken as reference for all the subsequent stages. Segmentation (2.2.4.1), meshing and any landmark identification were performed in the same software suite (Amira; Visualization Sciences Group). Firstly, the local anatomical reference frame was built on the intact vertebra based on a set of relevant landmarks (2.2.4.2). The 3D surfaces obtained at the subsequent stages (i.e. post-fracture, post-implant, and post-fatigue) were aligned to the intact 3D surface by means of rigid affine registration. An arbitrary cloud of landmarks was identified on each endplate to describe its surface (Figure 2-29). The most posterior aspect of the cranial endplate was not taken into account to minimise the error in the calculation of the kyphotic angle [103]. In addition, the landmark cloud could provide a representation of the overall shape of the endplate even when the vertebral body was severely comminuted.

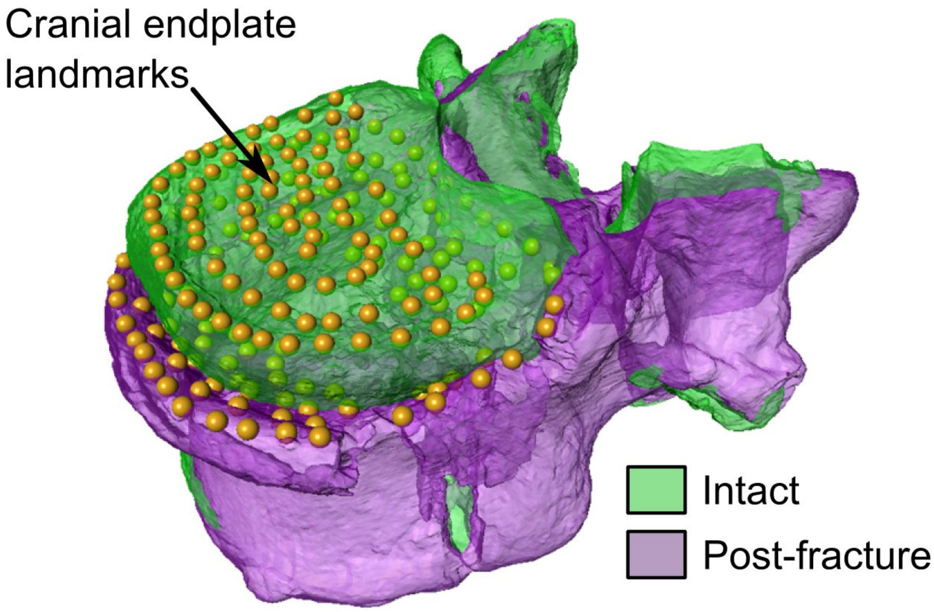

Figure 2-29: Identification of the landmarks representative of the vertebral endplate. The post-fracture surface is registered over the intact surface.

The landmark lists were imported into a custom software application (Matlab; the MathWorks Inc.). All the coordinates taken at every stage were transformed to the local anatomical reference frame built from the intact state. Hence, all the measurements referred to the anatomical axes of that state. It was chosen to exploit one reference condition because the posterior wall at all the subsequent experimental stages was often disrupted, hence causing a misalignment of the frontal plane.

A plane was fitted through the cranial and caudal landmarks using principal component analysis. The angle between the endplates was calculated as the angle between the normal to the planes. The kyphotic angle was calculated through the projection of such planes on the sagittal one. For convention, a positive value indicated kyphosis, whilst negative indicated lordosis. The same was done to calculate the angle on the coronal plane.

The height of the vertebra was calculated as the median distance between the endplates. In particular, each landmark on the cranial endplate was selected and the distance between it and each landmark on the caudal side measured. The minimum of such set of distances was then used for the final median calculation to obtain the overall distance estimation (Figure 2-30). Median was chosen over average because it is less sensitive to outliers. The rim of the endplate did not collapse as much as the central area (where most of the landmarks were taken). Hence, the median was able to show such phenomenon better.

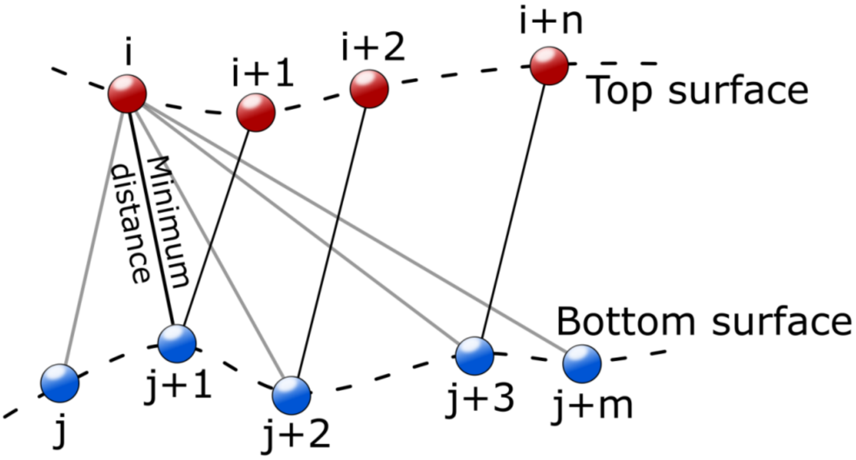

Figure 2-30: Schematic of the metric implemented to measure the distance between two surfaces, each defined by a set of markers.

The curvature of the endplate was calculated both locally and in terms of overall radius. The local mean curvature (H) was calculated over a grid of nodes fitted through the landmarks. H is the arithmetic mean of the principal curvatures and in a smooth surface represents roughly the radius of the sphere fitted under the node [229]. The overall curvature calculation firstly required fitting a polynomial surface through the markers, to generalise the shape of the endplate. A second order polynomial surface was considered the best approximation since higher order functions were more susceptible to local irregularities. A sphere was fitted within that surface using the mean least squares method. Therefore, the radius of the sphere was taken as the overall curvature radius of the endplate. Goodness of fit was estimated by calculating the mean squared error (MSE) between the fitted surface and the markers.

The results from all the calculations described above were presented in a graphic window to make the application more user-friendly (Figure 2-31). Reliability of the calculation was assessed by measuring mock 3D surfaces of known curvature and height.

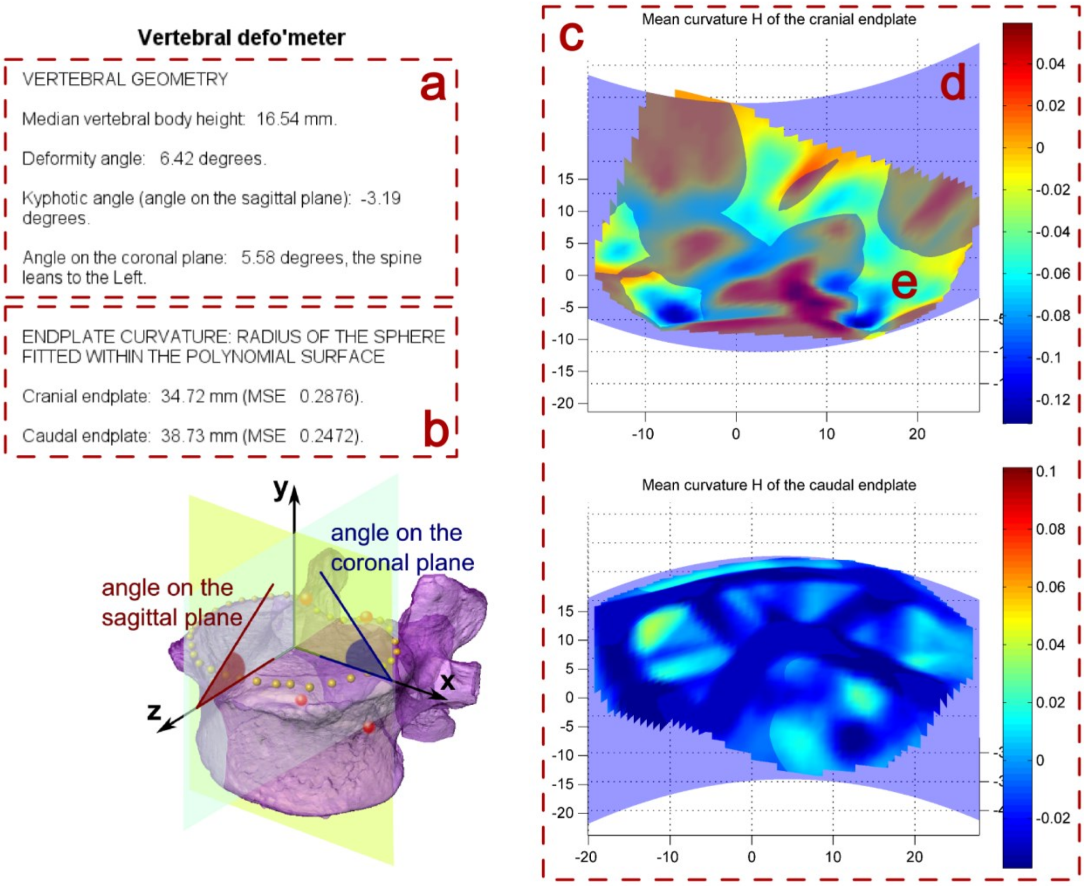

Vertebral defo'meter

VERTEBRAL GEOMETRY

Median vertebral body height: 16.54 mm.

Deformity angle: 6.42 degrees.

Kyphotic angle (angle on the sagittal plane): -3.19 degrees.

Angle on the coronal plane: 5.58 degrees, the spine leans to the Left.

ENDPLATE CURVATURE: RADIUS OF THE SPHERE FITTED WITHIN THE POLYNOMIAL SURFACE

Cranial endplate: 34.72 mm (MSE 0.2876).

Caudal endplate: 38.73 mm (MSE 0.2472).

Figure 2-31: Screenshot of the custom application for the measurement of vertebral deformity. a: angles and median height; b: curvature radius of the endplates; c: graphic representation of the endplate curvature; d: second order polynomial surface; e: mean local curvature.

2.2.4.4 Endplate deflection

The procedure developed by Dr. N. Roberts, on the definition of image based boundary conditions for FE modelling (2.2.1.4), was adapted to investigate the damage induced by fatigue loading to the endplates.

The 3D surfaces of the two vertebrae adjacent to the central one were extracted from the post-fracture and post-fatigue scans. Therefore, four surfaces were processed each segment (Figure 2-25). Segmentation, meshing and identification of landmarks for the local reference frame were carried out in an image processing suite (Amira; Visualization Sciences Group). The adjacent vertebrae could not be segmented from the post-implant scan because of the artifacts induced by the pedicle screws. However, it was supposed that implanting the screws (and resultant ligamentotaxis) affected only the geometry of the central vertebra. Therefore, as far as the adjacent endplate surfaces are concerned, pre-fatigue testing and post-surgery (SSPI or SSPI – KP) conditions were considered equivalent. Similarly to what described above (2.2.4.3), the post-fracture surface was taken as a reference state and the landmarks for the local anatomical coordinate system were identified on each vertebra. The post-fatigue testing surfaces were aligned over the post-fracture ones by means of affine rigid registration. The surface of the endplate adjacent to the central vertebra was trimmed from the rest of the model and the displacement between post-fracture and post-fatigue state calculated (Figure 2-32). The obtained displacement field was representative of the deflection of the endplates induced by fatigue loading.

The triangulated endplate surfaces, displacement fields (three axial components per node of the surface) and landmark list were imported into a custom software application (Matlab, the MathWorks Inc.). The anatomical reference frame was built and the coordinates of the nodes of each surface and their displacement were transformed from global to local reference frame. Therefore, the three components of displacement were now actually aligned according to relevant anatomical directions (i.e. left-right, AP, cranio-caudal). For simplicity, only the displacement along the cranio-caudal direction (i.e. y axis, see Figure 2-28) was used in the analysis, because it was considered most relevant for this biomechanical application. The 5th and 95th percentile was calculated for each set of displacement data as an effective indication of the extremes of the distribution. Percentiles were chosen over mean and maximum to neglect peak values that would be representative of the behaviour of only few nodes.

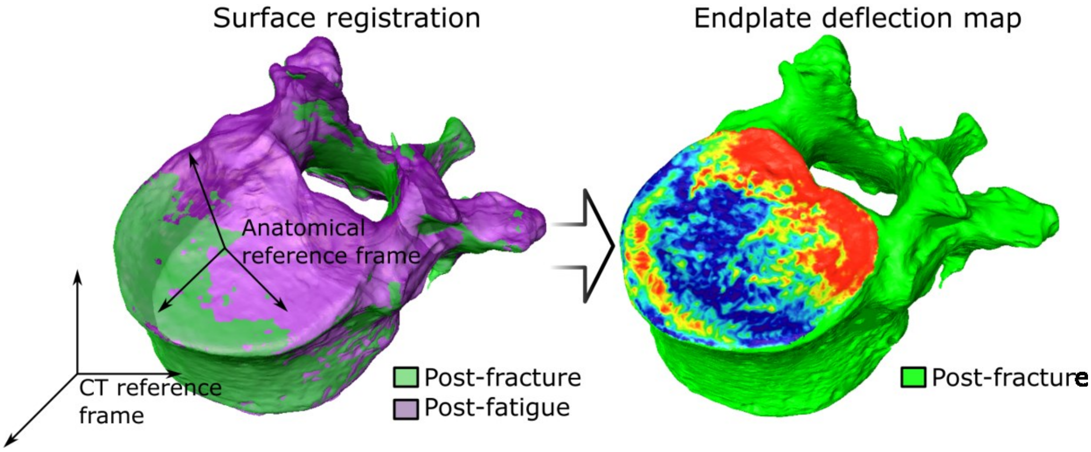

Figure 2-32: 3D assessment of endplate deflection induced by fatigue loading.

2.2.5 Statistics

Given the limited sample size, it was obviously not possible to make any assumptions about the probability distribution of the results. Therefore, non-parametric statistical analyses were performed. Differences between two groups were assessed using Mann-Whitney U test (equivalent to Wilcoxon rank-sum test), whilst Kruskal-Wallis one-way analysis of variance by ranks was used to assess difference where more than two groups were taken into account (e.g. difference across spinal levels). Paired data conditions where applied whenever results under analysis were obtained from the same sample at different stages, hence Wilcoxon signed-rank test was performed. Ansari-Bradley test was carried out to compare variability between datasets (i.e. test of dispersion). Association between variables was assessed by means of Spearman rank correlation coefficient (r_s). In all cases, a nominal significance level (p-value) of 0.05 was used. Agreement between different measurement techniques was analysed using the method defined by Bland and Altman [245].

All the analyses were carried out using dedicated software for statistics (R; R foundation for Statistical Computing, Vienna, Austria).

Chapter 3: Results

This chapter presents the results from the experiments carried out exploiting the materials and methods previously described. The first section provides the results from the collaboration for the development of FE models of multiple myeloma spine. The subsequent three sections detail the results from the main project about spinal burst fractures. The first of these sections presents results from the creation of the fractures whilst the subsequent one provides results from fatigue testing of the treated fractures. Results from the fracture creation focused on the dynamics of IPW whilst those from fatigue testing aimed at assessing the performance of SSPI and SSPI – KP. Finally, the 3D analysis tied together the experiments from the two previous sections to detail the anatomical changes of the fractured vertebra throughout the experimental stages.

3.1 *In situ* testing

The experimental protocol was successfully used on all the specimens and time-lapse HR-pQCT scans were collected for all of them. However, only three out of eight segments were suitable for the development of the FE model. The main reason for discarding the remaining five datasets was that the experimental data were not suitable for the definition of the boundary conditions of the numerical simulation (2.2.1.4). Although image processing was successfully performed, the resultant displacement fields were either too low in magnitude or no substantial increase in endplate deflection was found between consecutive load steps. In some cases, gross failure of the endplate occurred at the first load step, compromising the load transfer to the vertebral body and resulting in erroneous displacement calculation. The FE models were run, and von Mises Stresses and axial strains were calculated at load steps of interest (Table 3-1), for the following samples:

- Donor E: T2-T3-T4;
- Donor F: T2-T3-T4;
- Donor G: T2-T3-T4.

From a qualitative assessment of the HR-pQCT scans of the sample from Donor E, it was possible to detect areas of densification beneath the superior endplate at all the load steps. Densification was identified as regions where there was a clear compaction of trabeculae, indicative of local damage accumulation and also found in the numerical simulations. In fact, stress concentration was found directly under the endplates where the stress reached the 90th percentile values (Figure 3-1). Simulations from the same samples showed another particular behaviour. Throughout the load steps, the axial strain map (E_{33}) gradually changed from a predominantly compressive state to a predominantly tensile state. On the other hand, the strain component orthogonal to E_{33} changed from being predominantly tensile to compressive (Figure 3-2). This strain pattern is indicative of bulging of the structure, which may lead to burst fracture in the cancer infiltrated spine [246]. Likewise, areas of densification were detected on the sample from Donor F. In addition, failure occurred in the region where the highest stresses were calculated by the model. Only the 1st load step was modelled for the sample from Donor G since failure occurred afterwards. However, loading through the sparse trabecular structure could be qualitatively replicated. In addition, the location of the failure of the cortical shell corresponded to a region of high compressive strains in the model (Figure 3-3).

Table 3-1: Mean Von Mises stress and axial strain (E_{33}) ± one standard deviation together with 10th and 90th percentiles at each load step.

Donor	Step	Von Mises Stress (kPa)			E_{33} (strain)		
		Mean	10th %	90th %	Mean	10th %	90th %
E	1st	5.3 ± 14.5	1.7	9.7	-0.004 ± 0.007	-0.001	0.000
	2nd	35.8 ± 405.4	6.9	57.6	-0.000 ± 0.010	-0.010	0.008
	3rd	82.0 ± 865.4	15.0	136.7	0.004 ± 0.012	-0.007	0.015
F	1st	8.9 ± 19.0	1.3	18.0	-0.011 ± 0.015	-0.025	-0.001
	2nd	191.7 ± 207.9	34.0	429.8	-0.073 ± 0.045	-0.130	-0.023
	3rd	273.9 ± 379.0	44.8	586.9	-0.130 ± 0.069	-0.220	-0.050
G	1st	74.6 ± 70.1	28.3	138.5	-0.156 ± 0.073	-0.252	-0.063

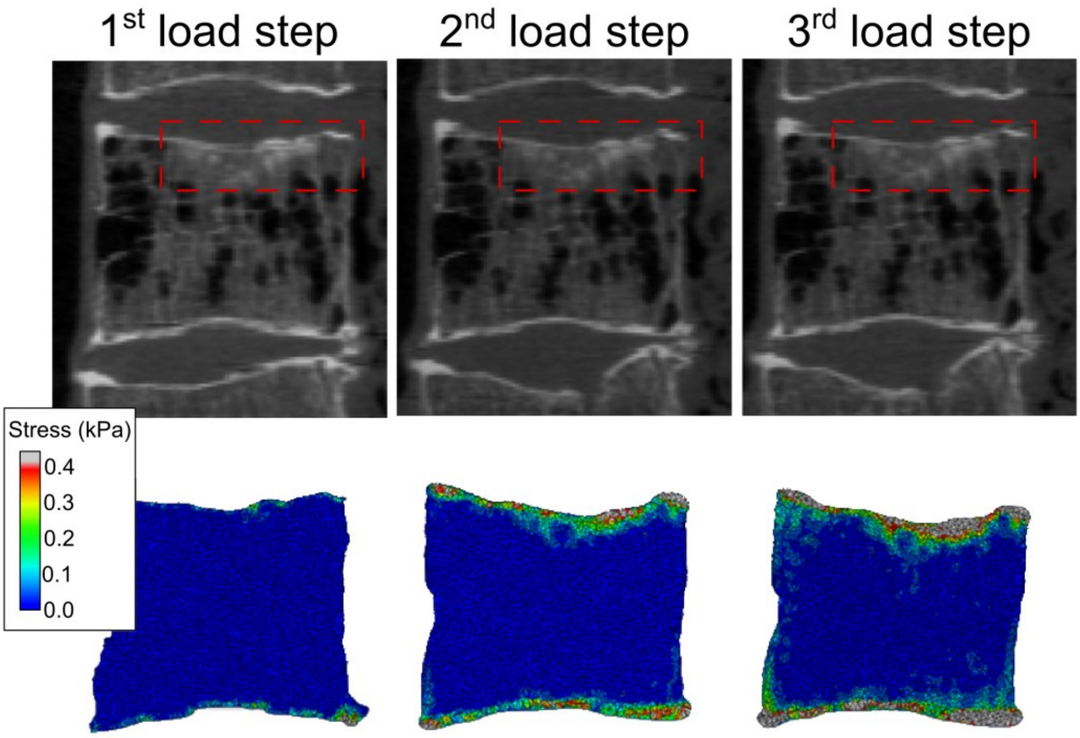

Figure 3-1: Areas of densification detected on HR-pQCT scans and the correspondent von Mises stress concentration on the FE model. Adapted from [2].

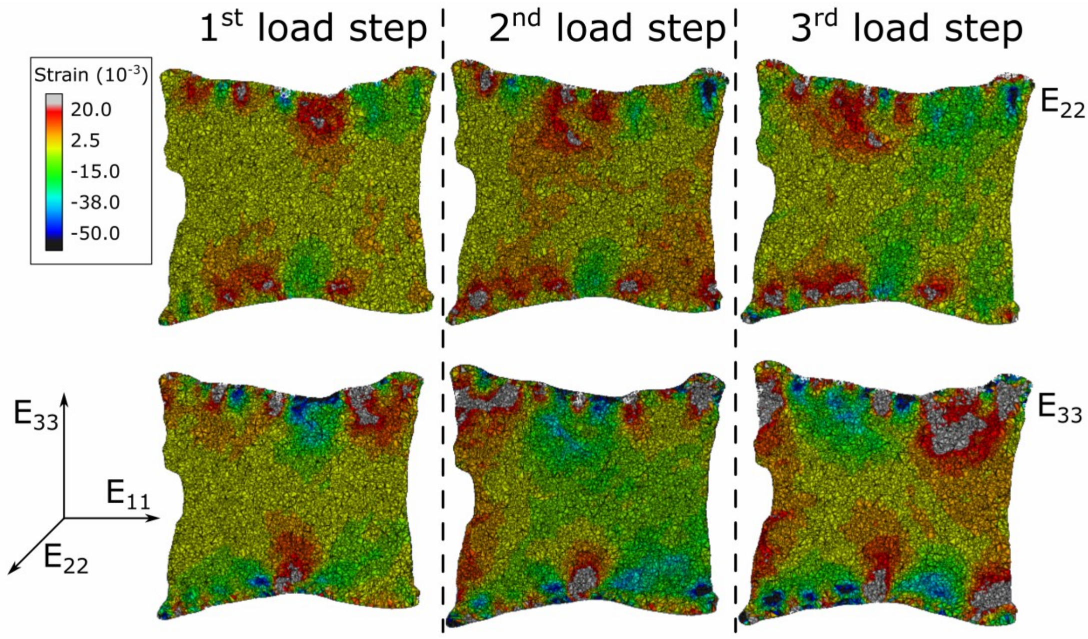

Figure 3-2: Change in strain distribution throughout consecutive load steps. Adapted from [2].

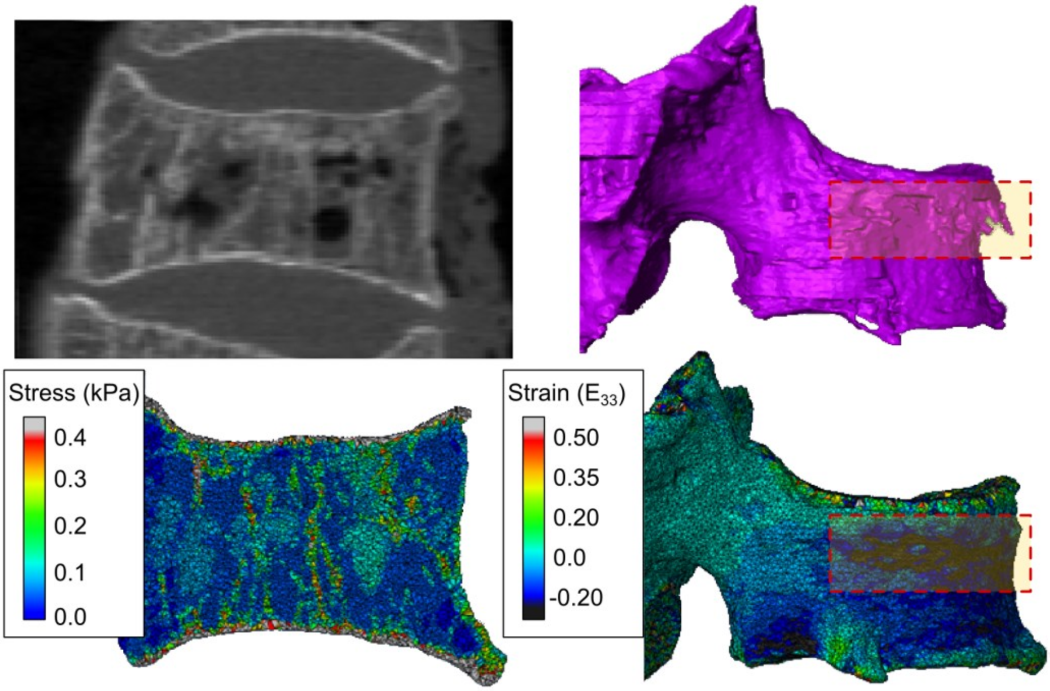

Figure 3-3: Von Mises stress and strain predicted by the FE model. Adapted from Roberts at al., [2].

3.2 Burst fracture creation

Fractures were induced in all the three-adjacent-vertebrae segments, as confirmed by HR-pQCT assessment, which allowed grading of the central vertebrae according to Magerl et al. [18] (Table 3-2). Burst fractures (Type A3) were detected in the central vertebra of 11 out 12 of the segments (Figure 3-4), and the only case where burst fracture was not induced was in L3-L4-L5 from Donor A. In this sample, the fracture on L4 was classified as B2.3.1 (i.e. fracture of the pedicles associated with a compression fracture). However, comminution of the cranial endplate (typical of A3 fractures) was detected on the adjacent L5. The CT scans also confirmed fracture of the pedicles of various severities on all the central vertebrae.

The median energy delivered at the impact was 200.3 J (range 166.2 – 223.8 J) and 157.6 J (range 146.0 – 184.2 J) for the HE and LE group, respectively. The actual drop height was subjected to small variations due to the different height of the segments. However, the effect of such variability was neglected as the velocity at the impact (median among samples 5.35 m/s, range 5.32 – 5.39 m/s) could be considered constant (Mann-Whitney U test, p=0.37). Both energy and velocity were calculated analytically and therefore are to be considered estimations of the actual values.

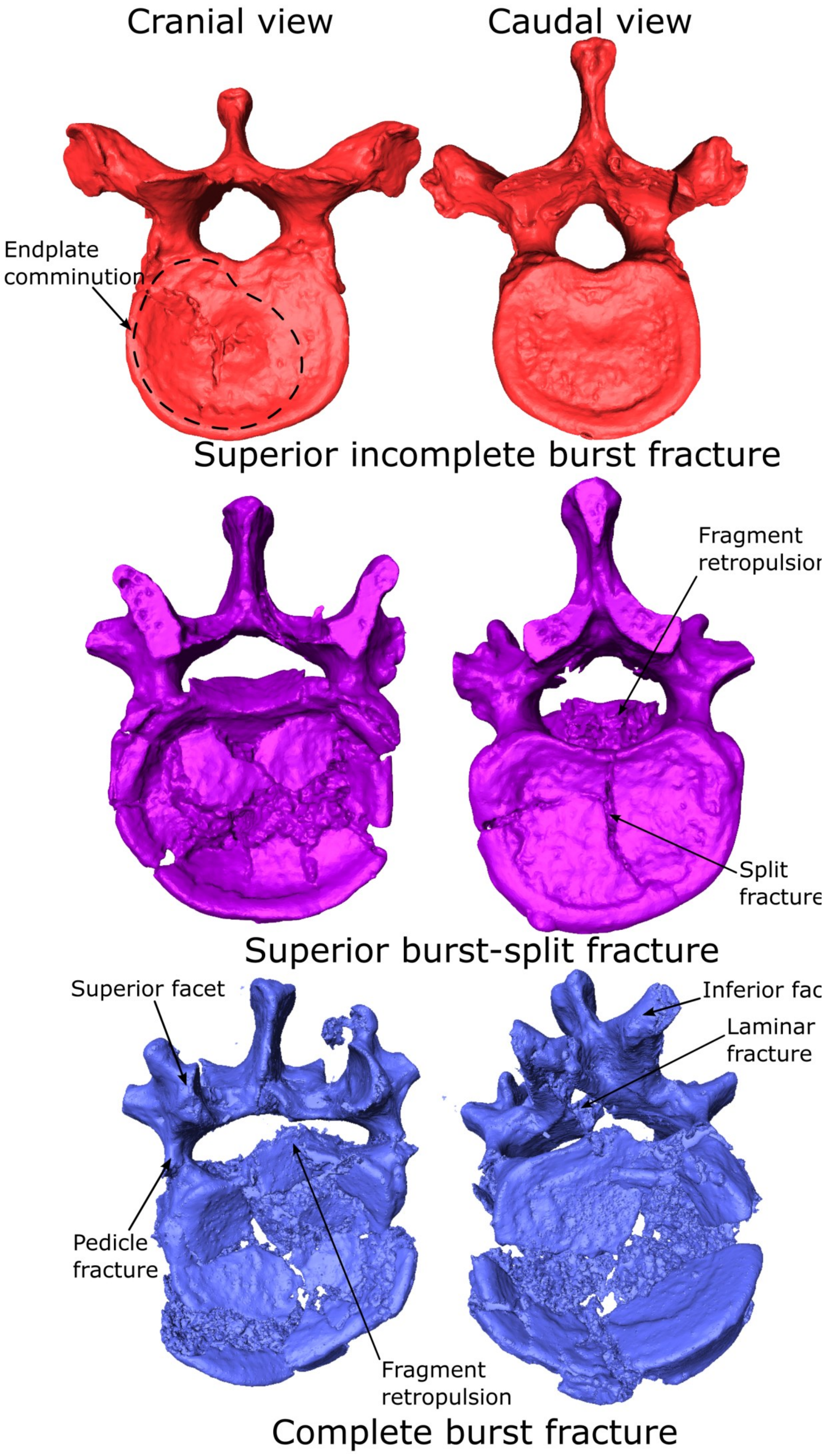
Cranial view
Caudal view
Endplate comminution
Superior incomplete burst fracture
Fragment retropulsio
Split fracture
Superior burst-split fracture
Superior facet
Inferior fac
Laminar fracture
Pedicle fracture
Fragment retropulsion
Complete burst fracture

Figure 3-4: 3D models representative of the fractures induced experimentally. Fractures are presented in order of increasing complexity; note the change in canal shape.

Table 3-2: Details of the fractures induced *in vitro*.

Donor	Level	Group	Energy (J)	Grade	FR	LF
A	T9-T10-T11	LE	148.0	A3.1.1	✗	✗
A	T12-L1-L2	HE	182.0	A3.2.1	✓	✓
A	L3-L4-L5	LE	146.0	B2.3.1	✗	✗
B	T9-T10-T11	HE	166.2	A3.3.3	✓	✓
B	T12-L1-L2	HE	200.6	A3.3.3	✓	✓
B	L3-L4-L5	HE	218.5	A3.3.3	✓	✓
C	T9-T10-T11	LE	167.3	A3.2.1	✗	✗
C	T12-L1-L2	LE	146.6	A3.2.2	✓	✓
C	L3-L4-L5	HE	200.0	A3.3.3	✓	✗
D	T9-T10-T11	HE	223.8	A3.3.3	✓	✓
D	T12-L1-L2	LE	184.2	A3.3.3	✓	✓
D	L3-L4-L5	LE	183.5	A3.2.2	✗	✗

FR: fragment retropulsion present; LF: laminar fracture present.

3.2.1 Interpedicular widening

Agreement between dynamic measures (LVDT based) and static measures (HR-pQCT) was calculated based on IPW_{res} and IPW_{CT} (Figure 3-5), and was found to be about ± 4% (95% agreement interval). It must be noted that IPW_{res} could not be calculated in two samples because the LVDT tips lost contact with the bony surface subsequently to the transient phase (i.e. IPW_{max} could still be calculated).

Figure 3-6 presents a representative curve of instantaneous percent IPW over one second for one the tested samples; a close-up of the same data over the first 20 ms is shown in Figure 3-7 to highlight the initial dynamics. At the impact IPW increased to IPW_{max}, then following the transient phase, the pedicles were recoiled to their resting position IPW_{res}.

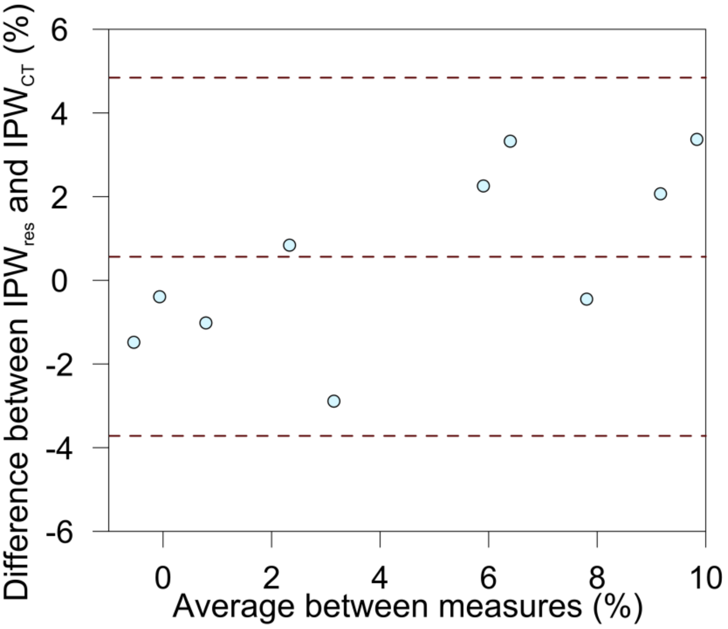

Figure 3-5: Bland & Altman plot showing the agreement between IPW_{res} and IPW_{CT}.

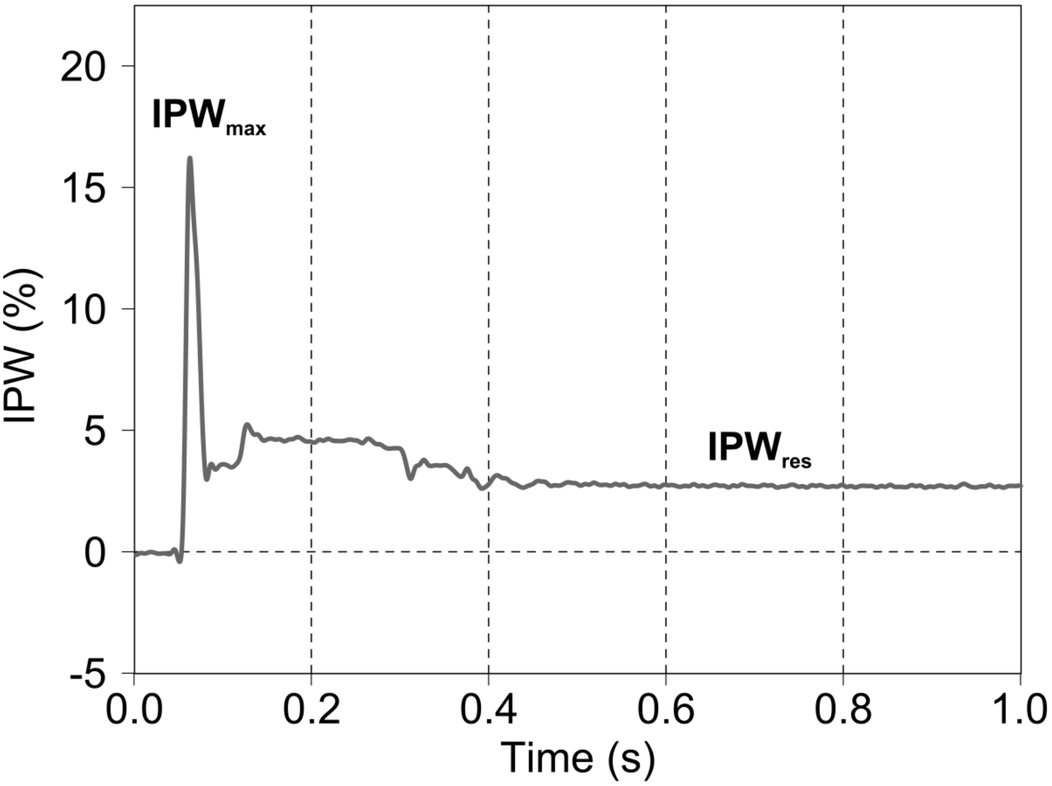

Figure 3-6: Instantaneous IPW trend throughout the fracture onset. Representative curve from donor A, segment T9-T10-T11.

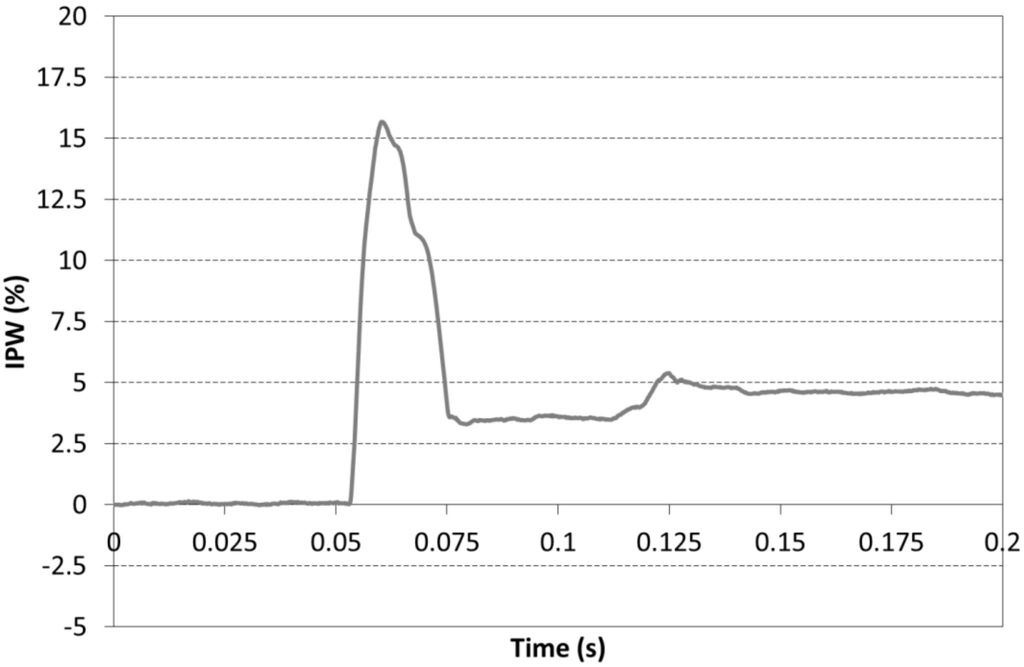

Figure 3-7: Close-up of the first 20 ms of the data presented in Figure 3-6.

The median IPW_{max} was 11.0 % (range 4.3 – 40.7 %) in the HE group and 17.3 % (range 6.9 – 21.8 %) in the LE group; details reported below (Table 3-3). Although results from HE group appeared more scattered (Figure 3-8), such variability was not significant (Ansari-Bradley, p=0.43). The median IPW_{res} was 1.7 % (range 0.3 – 10.2 %) for the HE group and 7.0 % (range 1.3 – 11.5 %) for the LE group. No difference was found between the two groups for both IPW_{max} (Mann-Whitney U, p=0.70) and IPW_{res} (Mann-Whitney U, p=0.84). Therefore data were pooled together; the average IPW curve was calculated as the instantaneous average amongst the 12 samples and plotted within the instantaneous minimum-maximum interval (**Error! Reference source not found.**). The trend clearly shows that, at the impact, IPW increased up to IPW_{max} in about 20 – 25 ms; the transient phase lasted approximatively 400 ms and IPW_{max} was always significantly higher than IPW_{res} (Mann-Whitney U, p=0.011).

A moderate correlation was found between IPW_{max} and IPW_{res} (r_s=0.58, p=0.088) whilst no association was found between IPW and the delivered energy for both IPW_{max} (r_s=-0.29, p=0.37) and IPW_{res} (r_s=-0.14, p=0.71).

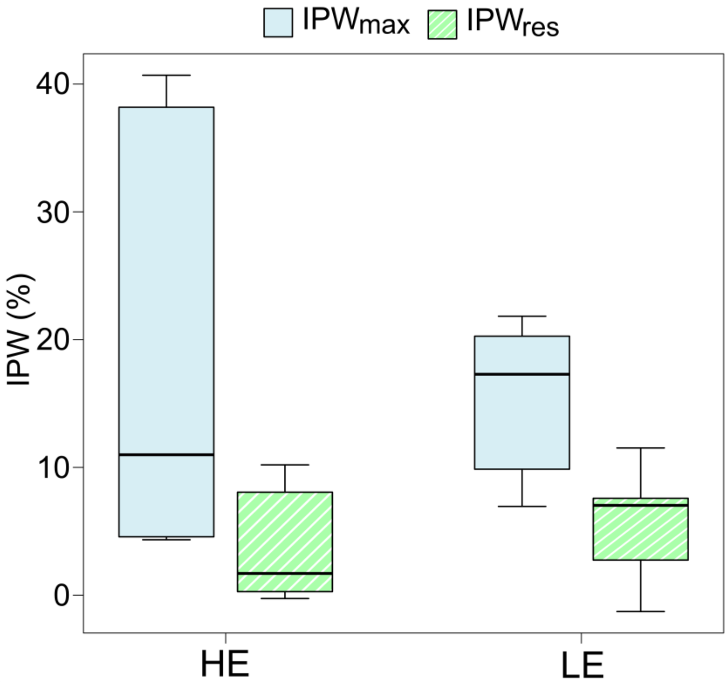

Figure 3-8: Maximum and residual IPW divided by group. Adapted from Brandolini et al., [1].

IPW_{max} (Kruskal-Wallis, p=0.077) and IPW_{res} (Kruskal-Wallis, p=0.055) were only marginally influenced by the spinal level where they were measured, although results suggest a decreasing trend in the caudal direction for IPW_{max} (Figure 3-9), whose median values by level were:

- T10: 25.8 % (range 15.7 – 40.7 %).
- L1: 18.1 % (range 4.3 – 21.8 %).
- L4: 6.9 % (range 4.6 – 9.9 %).

However, when considering the maximum of the measurements of each LVDT in absolute values (Δl_{left} and Δl_{right}), a significant difference was found among spinal levels (Kruskal-Wallis, p=0.022). In particular, the displacements measured on T10 and L1 were higher than that on L4 (Mann-Whitney U, p=0.038 and p=0.0070, respectively). The absolute displacement values did not show any difference between groups (Mann-Whitney U, p=0.84) and the variability of the HE group was not significantly higher than that of LE (Ansari-Bradley, p=0.28). The maximum absolute displacements were not associated with the orientation of the pedicle on the coronal plane measured in intact conditions (r_s = -0.14, p=0.51).

Laminar fractures were detected in seven out of 12 specimens (Table 3-2), but did not appear to be associated with any specific spinal level. Median IPW_{max} was

20.3 % (range 4.3 – 40.7 %) when the fracture was present and 9.9 % (range 4.6 – 18.9 %) when it was not; whilst median IPW_{res} was 7.3 % (range 0.3 – 10.2 %) and 1.2 % (range -1.3 – 11.5 %), respectively (Figure 3-10). However, no significant difference was found in both IPW_{max} (Mann-Whitney U, p=0.27) and IPW_{res} (Mann-Whitney U, p=0.48) when considering the presence of a laminar fracture. IPW_{max} was not significantly affected by higher variability when a laminar fracture was present (Ansari-Bradley, p=0.40).

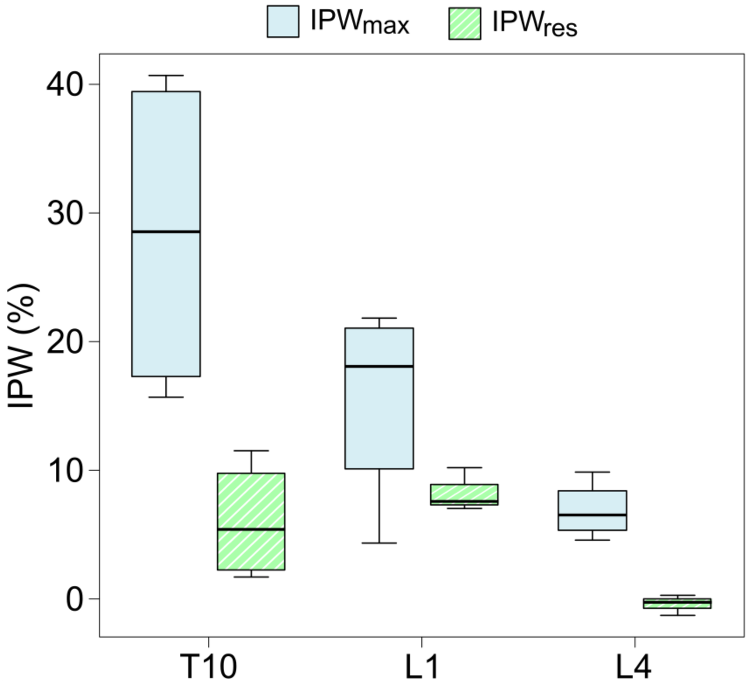

Figure 3-9: Maximum and residual IPW divided by spinal level. Adapted from Brandolini et al., [1].

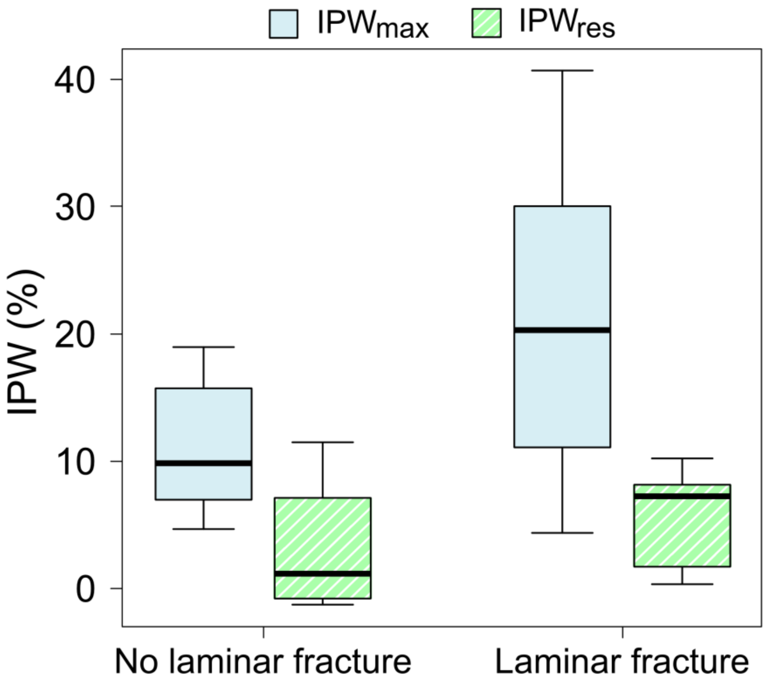

Figure 3-10: Maximum and residual IPW associated with presence of laminar fracture.

3.2.2 Spinal canal occlusion

SCO_{CT} (i.e. the percent canal occlusion measured on the HR-pQCT scans) was considered the most precise measure of SCO and thus taken as reference for the analysis. Median SCO_{CT} was 32.4 % (range 9.7 – 41.2 %) in the HE group and 11.8 % (range -9.0 – 51.5 %) in the LE group; details reported below (Table 3-3). No statistical difference was found between groups (Mann-Whitney U, $p=0.13$) as well as among spinal levels (Kruskal-Wallis, $p=0.23$) (Figure 3-12). However, when the outlier from the LE group (Figure 3-11) was removed, a significant difference could be seen (Mann-Whitney U, $p=0.017$). In addition, a moderate correlation was found between SCO_{CT} and the delivered energy ($r_s=0.56$, $p=0.063$) (Figure 3-13).

Laminar fractures were associated with significantly higher SCO (Mann-Whitney U, $p=0.048$). Median SCO_{CT} was 5.4 % (range -9.0 – 30.7 %) and 34.1 % (range 9.7 – 51.5 %), when the fracture was and was not present, respectively.

No association was found between IPW and SCO_{CT}; both for IPW_{max} ($r_s=0.042$; $p=0.90$) and IPW_{res} ($r_s=-0.24$, $p=0.50$).

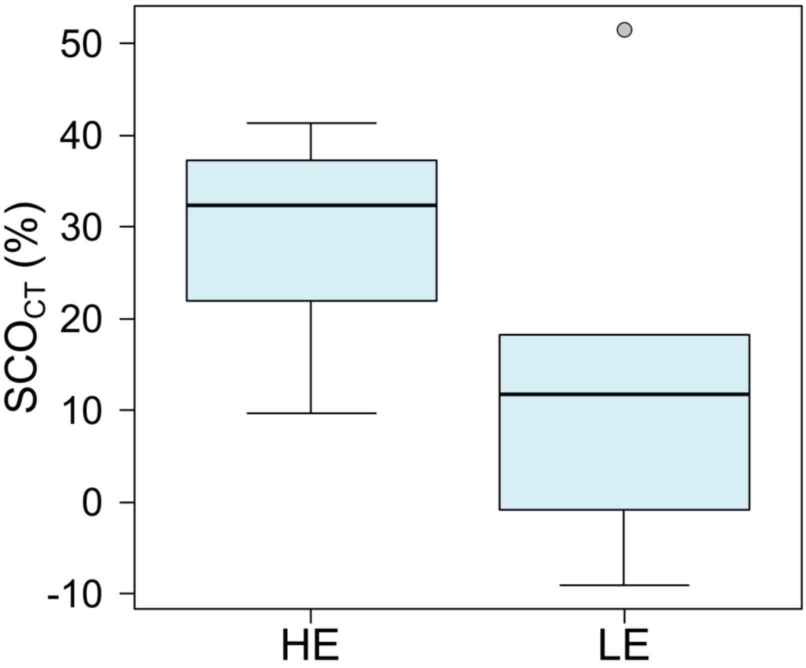

Figure 3-11: SCO$_{CT}$ calculated on the central vertebra of each segment, by group.

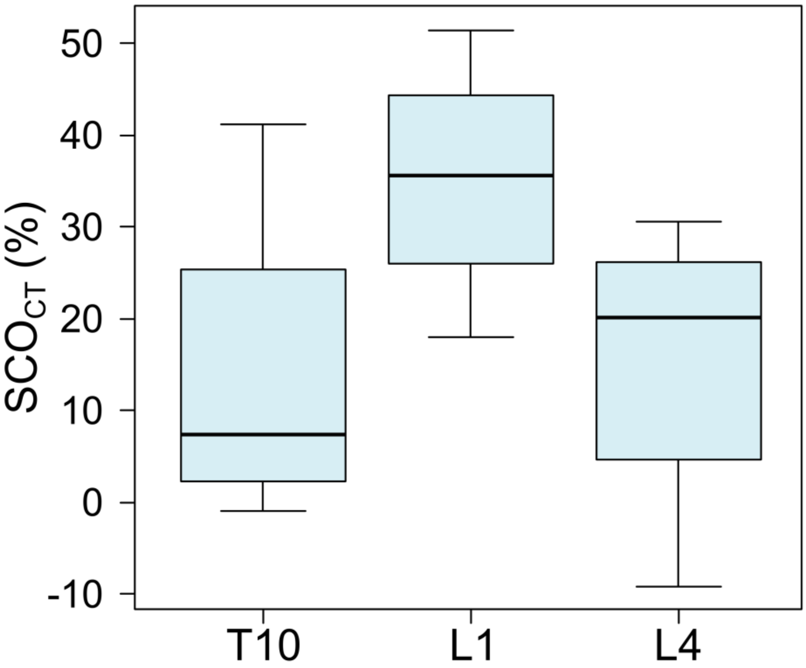

Figure 3-12: SCO$_{CT}$ calculated on the central vertebra of each segment, by spinal level.

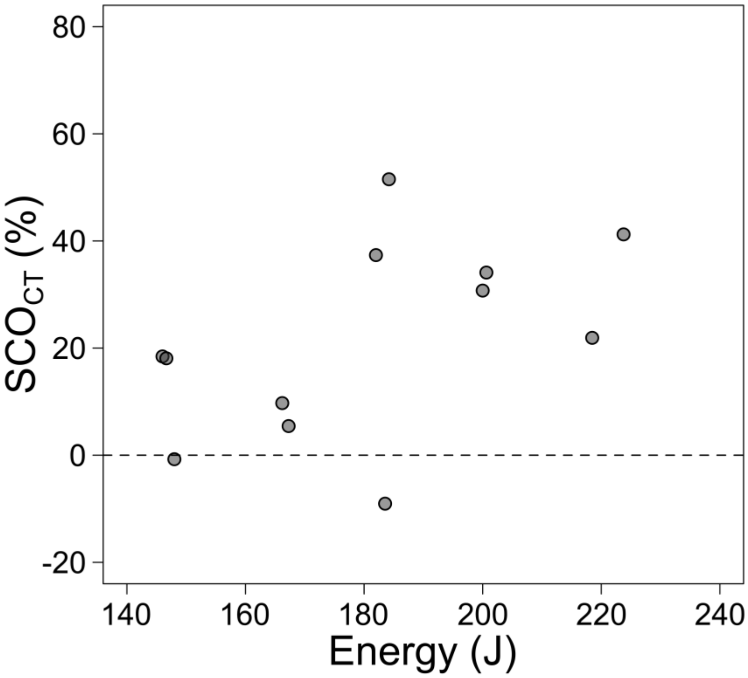

Figure 3-13: Association between impact energy and SCO.

The estimation of the actual SCO based on the CO of the adjacent vertebrae (SCO$_{clin}$) showed an agreement with SCO$_{CT}$ of about ± 20% (95% agreement interval) (Figure 3-14). Median SCO$_{clin}$ was 29.5 % (range 14.4 – 47.8 %) for the HE group and 5.9 % (range -13.3 – 51.2 %) for the LE group. Although no difference was found among levels (Kruskal-Wallis, p=0.73), the method returned a marginal difference between the two groups (Mann-Whitney U, p=0.065).

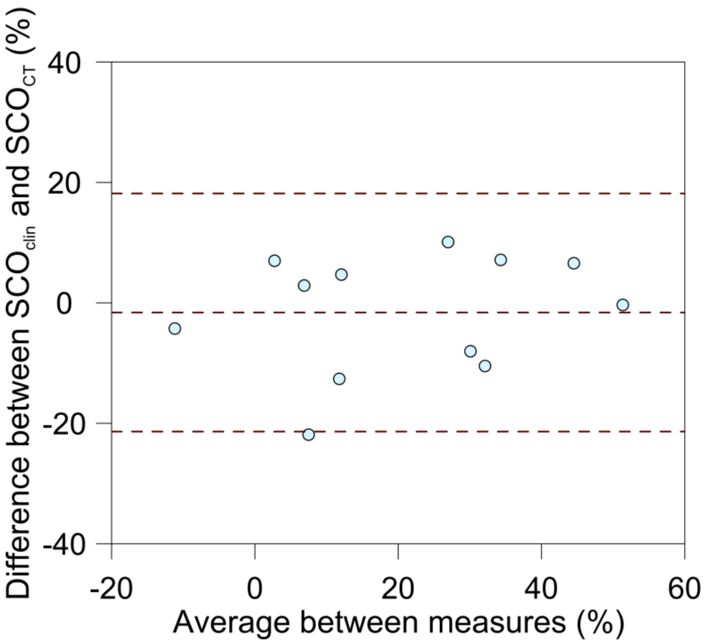

Figure 3-14: Bland & Altman plot showing the agreement between SCO_{clin} and SCO_{CT}.

As previously described (2.2.2.3), the dynamic of SCO was assessed through high-speed filming. Two out of 12 videos could not be used. In one case, a fragment broke off the PMMA layer and covered the bottom mirror; whilst in the other case the camera software did not work correctly (the file was not saved). It must be noted that image processing of the frame sequences was always problematic. Splatters of fluid from the posterior wall often crossed the light path and in some cases ended on the bottom mirror. Those events induced artifacts that affected the identification of the canal CSA. Therefore, poor agreement was found between SCO_{res} and SCO_{CT}, which was about ± 70 % (95% agreement interval) (Figure 3-15).

Median SCO_{max} was 99.0 % (range 92.4 – 100.0 %) in the HE group and 62.6 % (range 23.3 – 100.0 %) in the LE group, whilst SCO_{res} was 87.5 % (range 68.3 – 100.0 %) and 46.8 % (range -16.8 – 91.3 %), respectively (Table 3-3). No difference was found between the groups for both SCO_{max} (Mann-Whitney U, p=0.59) and SCO_{res} (Mann-Whitney U, p=0.24). A positive correlation was found between SCO_{max} and SCO_{res} (r_s=0.88, p<0.001).

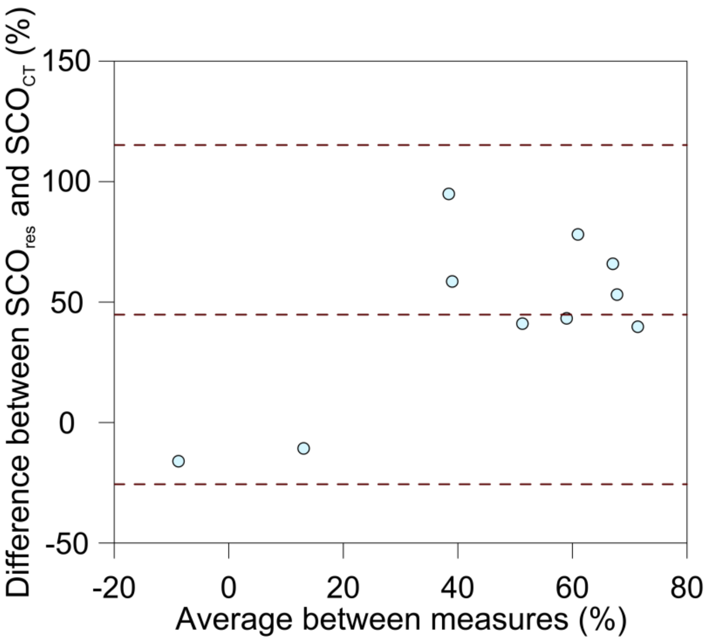

Figure 3-15: Bland & Altman plot showing agreement between SCO_{res} and SCO_{CT}.

Table 3-3: Experimental results for SCO and IPW. Description of the abbreviations can be found in sections 2.2.2.3 and 2.2.2.4.

Donor	Level	Group	SCO_{max} (%)	SCO_{res} (%)	SCO_{CT} (%)	SCO_{clin} (%)	IPW_{max} (%)	IPW_{res} (%)	IPW_{CT} (%)
A	T9-T10-T11	LE	23.3	-16.8	-0.7	6.2	15.7	2.8	1.9
A	T12-L1-L2	HE	92.4	80.6	37.4	26.9	15.9	10.2	8.1
A	L3-L4-L5	LE	27.3	7.7	18.4	-3.4	9.9	-1.3	0.2
B	T9-T10-T11	HE	93.2	68.3	9.7	14.4	40.7	8.1	4.7
B	T12-L1-L2	HE	100	100	34.1	26.1	4.3	–	-1.1
B	L3-L4-L5	HE	100	100	21.9	32.0	6.1	0.3	1.3
C	T9-T10-T11	LE	–	–	5.4	8.3	18.9	11.5	8.1
C	T12-L1-L2	LE	–	–	18.1	5.5	21.8	7.6	8.0
C	L3-L4-L5	HE	98.3	71.8	30.7	37.9	4.6	-0.3	0.1
D	T9-T10-T11	HE	99.7	94.3	41.2	47.8	38.2	1.7	4.6
D	T12-L1-L2	LE	99.9	91.3	51.5	51.2	20.3	7.0	4.8
D	L3-L4-L5	LE	100	85.9	-9.0	-13.3	6.9	–	5.5
	Median		99.0	83.2	20.2	20.3	15.8	4.9	4.7

SCO: spinal canal occlusion; IPW: interpedicular widening.

3.3 Spinal fixation in burst fractures

This section provides the results from the *in vitro* investigation of surgical treatment of spinal burst fracture with particular focus on the comparison between SSPI and SSPI – KP. The first section provides details of the surgical procedure carried out to prepare the samples, whilst the second section details the results from fatigue testing of the treated segments. Statistical analysis was carried out to assess whether the structural properties of the construct decreased over time and SSPI – KP could improve such properties better than SSPI alone.

3.3.1 Surgical treatment

Pedicle screws were successfully implanted in all the samples. Insertion of the screw caused a breach of the medial pedicle cortex in four out of 48 implants with a resultant minor invasion of the vertebral foramen. It must be noted that in all the screws the nut did not lock in place (against the screw head), at the time of rod fastening, as it was supposed to. Therefore, the rods where still allowed some minor movement because of the looseness of the polyaxial nut.

Qualitative assessment at the moment of neural arch excision showed overall integrity of PLL in all the samples.

KP was performed on six selected samples under fluoroscopic guidance; following SSPI. Median maximum inflation pressure of the inflatable bone tamps (IBT) was 132 psi (range 51 – 350 psi) whilst the median inflation volume was 7.1 ml (range 4.9 – 8.7 ml). One of the syringes broke at the junction between the nozzle and IBT and could not be used any longer. Therefore, in the last two samples, KP was performed by swapping the same syringe between two IBTs (Appendix A). Since the IBT had a valve at the inlet, the inflation previously achieved could be retained when alternating the syringe.

All six cement injections were stopped when the target amount of cement was delivered. Extravasation was detected in four out of six samples, with no evidence of leakage within the vertebral foramen. In all the cases, the cement leaked from the anterior portion of the vertebral body, through the fissures between the bone fragments. The median volume of cement injected was 8.6 ml (range 6.0 – 10.5 ml).

3.3.2 Fatigue testing

All the tested segments reached run-out (70000 cycles) and all the signals could be collected and processed accordingly. At implant removal eight out of 48 screws (16.7 %) were considered loose (Appendix A). Loose screws were present on three segments from the SSPI group and two from the SSPI – KP group.

Data acquired throughout each test from the sensors were processed as periodic signals (since they were the resultant of a sinusoidal load waveform). Therefore, mean and peak to peak values were calculated over each period; description of the nomenclature can be found in the methods chapter (2.2.3.3), and summarised results are provided in Appendix B. The reported mean values are to be intended as the mean value of a periodic waveform and represent its deviation from the initial point (post-treatment condition); Figure 3-16 presents a representative trend of the measured displacement, showing that over time the segment underwent increasing compression, whilst both the anterior and posterior region migrated posteriorly. Mean values of the signals are presented in Table 3-4 together with statistical significance for the comparison between the two groups. The reported median values were calculated amongst different samples and are indicative of the trend within each group of samples. In addition, results were pooled together (to increase statistical power) and the initial values compared to those at the end of test to assess changes over time. Likewise, results for the peak to peak values of the signals are reported in Table 3-5.

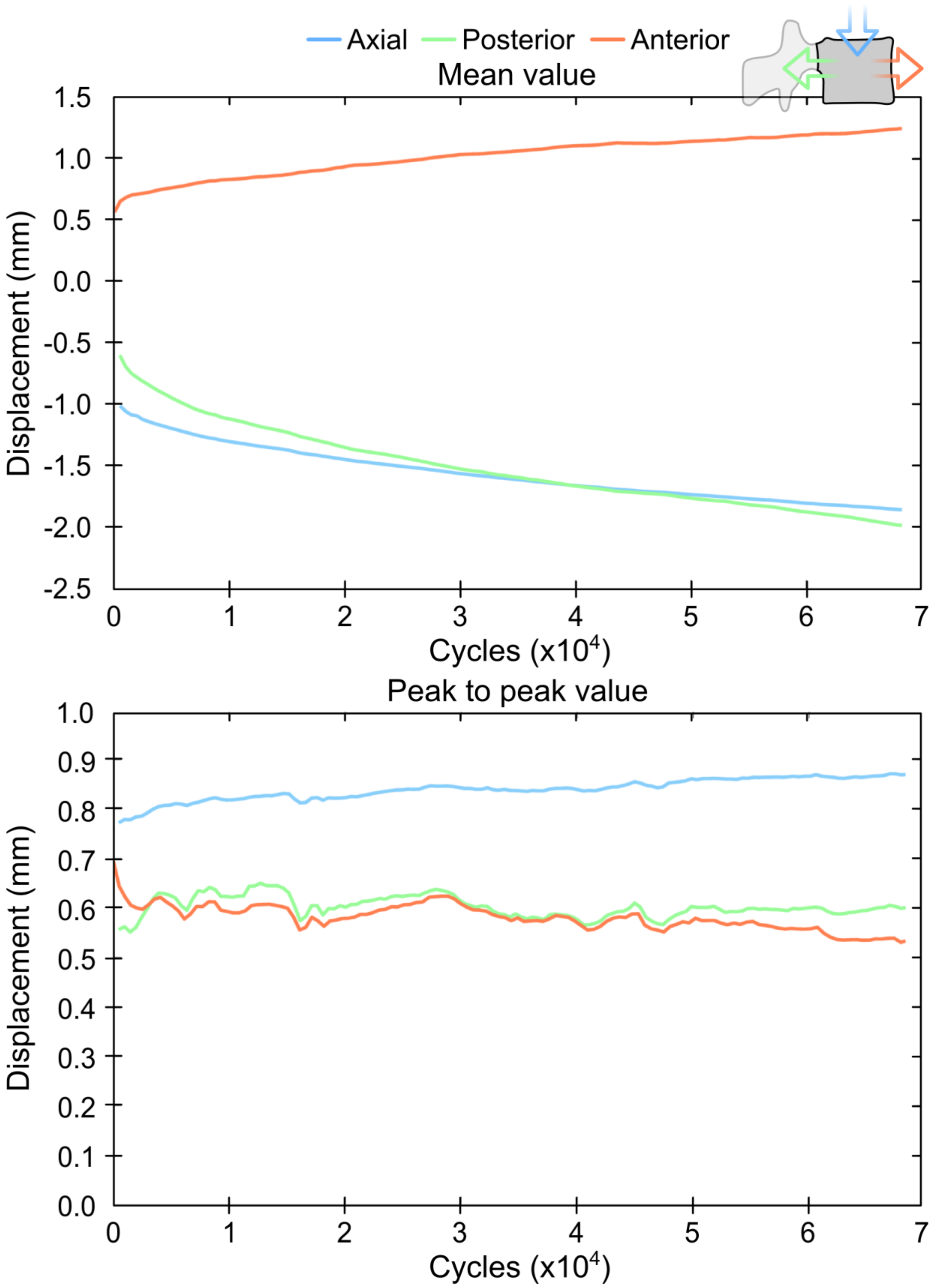

Figure 3-16: Example of mean and peak to peak values of the signals acquired throughout the test for the axial, posterior and anterior displacement. The schematic of the vertebra indicates the directions of negative displacement.

Table 3-4: Mean values calculated from the signals throughout the test and divided by group. All quantities are in mm, except for strain (με).

Parameter	SSPI		SSPI – KP		p†	p‡
	median	range	median	range		
Disp_mean$_{in}$	-1.1	-6.2 – -0.3	-0.5	-1.3 – -0.3	0.48	<0.001*
Disp_mean$_{fin}$	-2.1	-11.0 – -0.5	-0.9	-6.7 – -0.4	0.48	
Post_mean$_{in}$	-0.2	-2.4 – 5.4	-0.1	-0.9 – 0.4	0.93	0.017*
Post_mean$_{fin}$	-1.4	-6.1 – -0.3	-0.3	-1.9 – 2.3	0.093†	
Ant_mean$_{in}$	0.1	-0.9 – 2.6	0.1	-0.8 – 0.5	1.0	0.38
Ant_mean$_{fin}$	0.0	-5.6 – 4.8	0.0	-2.0 – 1.4	1.0	
MaxStrain_mean$_{in}$	371	291 – 756	284	223 – 552	0.31	0.48
MaxStrain_mean$_{fin}$	374	316 – 439	306	230 – 612	0.24	

† p-value relative to the comparison between SSPI and SSPI – KP group.

‡ p-value relative to the comparison between initial and final value (results pooled together).

* p-value < 0.05.

† marginally significant.

Table 3-5: Peak to peak values calculated from the signals throughout the test and divided by group. All quantities are in mm, except for strain (με).

Parameter	SSPI		SSPI – KP		p†	p‡
	median	range	median	Range		
Disp_p2p$_{in}$	0.7	0.2 – 2.4	0.4	0.3 – 0.8	0.48	0.054†
Disp_p2p$_{fin}$	0.7	0.3 – 2.3	0.5	0.3 – 0.9	0.70	
Post_p2p$_{in}$	0.6	0.1 – 2.5	0.2	0.0 – 0.2	0.026*	0.63
Post_p2p$_{fin}$	0.2	0.0 – 0.6	0.2	0.1 – 0.3	0.59	
Ant_p2p$_{in}$	0.2	0.1 – 1.0	0.2	0.1 – 0.3	0.59	0.039*
Ant_p2p$_{fin}$	0.2	0.0 – 0.9	0.2	0.1 – 0.4	1.0	
MaxStrain_p2p$_{in}$	575	391 – 880	511	360 – 889	0.81	0.23
MaxStrain_p2p$_{fin}$	555	400 – 671	471	355 – 744	0.31	

† p-value relative to the comparison between SSPI and SSPI – KP group.

‡ p-value relative to the comparison between initial and final value (results pooled together).

* p-value < 0.05.

† marginally significant.

The only significant difference between SSPI and SSPI – KP was the amplitude of the posterior displacement at the beginning of the test; such difference was not present anymore at the end of the test.

The mean value of the axial displacement significantly decreased (i.e. increased compression of the segment) over time (Wilcoxon signed-rank, p<0.001), whilst its peak to peak value decreased only marginally (Wilcoxon signed-rank, p=0.054).

The mean displacement measured by the posterior LVDT significantly decreased over time (Wilcoxon signed-rank, p=0.017; i.e. the posterior wall/bony fragment moved posteriorly) whilst the anterior region remained overall stationary (Wilcoxon signed-rank, p=0.38). On the contrary, the amplitude of the posterior displacement remained constant over time (Wilcoxon signed-rank, p=0.63), whilst that of the anterior displacement decreased (Wilcoxon signed-rank, p=0.039). However, KP significantly prevented the migration of the posterior fragment. In fact, if the comparison between initial and final values is carried out within the two groups, it is possible to notice that the mean value of the posterior displacement decreased only in the SSPI group (Wilcoxon signed-rank, p=0.016) whilst it remained overall constant in the SSPI – KP one (Wilcoxon signed-rank, p=0.34).

Maximum posterior displacement was estimated as the mean value plus the amplitude of the oscillation (half the peak to peak value). The median at the initial stage of the test and at run-out was -0.1 mm (range -2.2 – 6.7 mm) and -1.2 (range -6.1 – -0.2 mm), respectively, for SSPI; and -0.1 (-0.7 – 0.5 mm) and -0.2 (range -1.9 – 2.4 mm) for SSPI – KP. From a qualitative point of view, SSPI – KP resulted in less posterior displacement than that observed in SSPI (Figure 3-17). However, no difference was found between the groups both at the beginning (Wilcoxon signed-rank, p=0.82) and end of test (Wilcoxon signed-rank, p=0.13). When results were pooled together the median at the beginning was -0.14 mm (-2.2 – 6.7 mm) and -0.50 mm (-6.1 – 2.4 mm) at the end. A significant decrease was found over time (Wilcoxon signed-rank, p=0.017); in line with what seen for the mean and peak to peak values. However, such decreasing trend was only found in the SSPI group

(Wilcoxon signed-rank, p=0.016), confirming the ability of SSPI – KP to reduce excessive of the posterior wall.

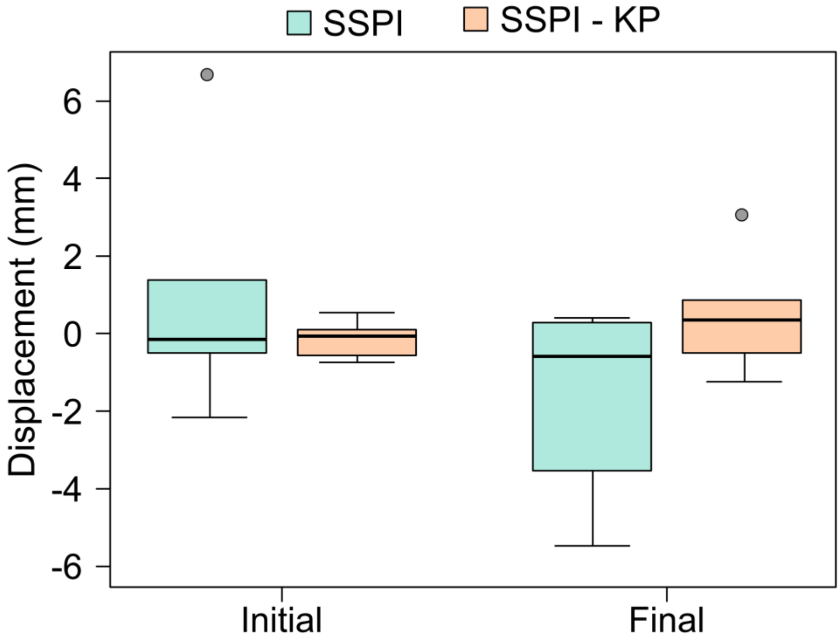

Figure 3-17: Maximum posterior displacement measured at the beginning and end of test.

Representative curves of the strain recorded on the left and right rod are presented in Figure 3-18; as above, the mean and peak to peak value of each signal were calculated over each cycle throughout the test. The actual maximum strain was calculated from the recordings of the left and right gauge of each sample in the same way described above for the maximum posterior displacement. The median at the initial stage of the test and at run-out was 647 με (range 538 – 1196 με) and 637 με (range 589 – 704 με), respectively, for SSPI, and 531 με (range 403 – 996 με) and 553 με (range 407 – 984 με), for SSPI – KP. Despite strains being qualitatively lower in SSPI – KP (Figure 3-19); only a marginal difference was found when comparing values at the end of test (Mann-Whitney U, p=0.093). When results were pooled together, the maximum strain at the beginning and at run-out was 607 με (range 403 – 1196 με), and 605 με (range 407 – 984 με), respectively. However, no difference could be seen over time (Wilcoxon signed-rank, p=0.97).

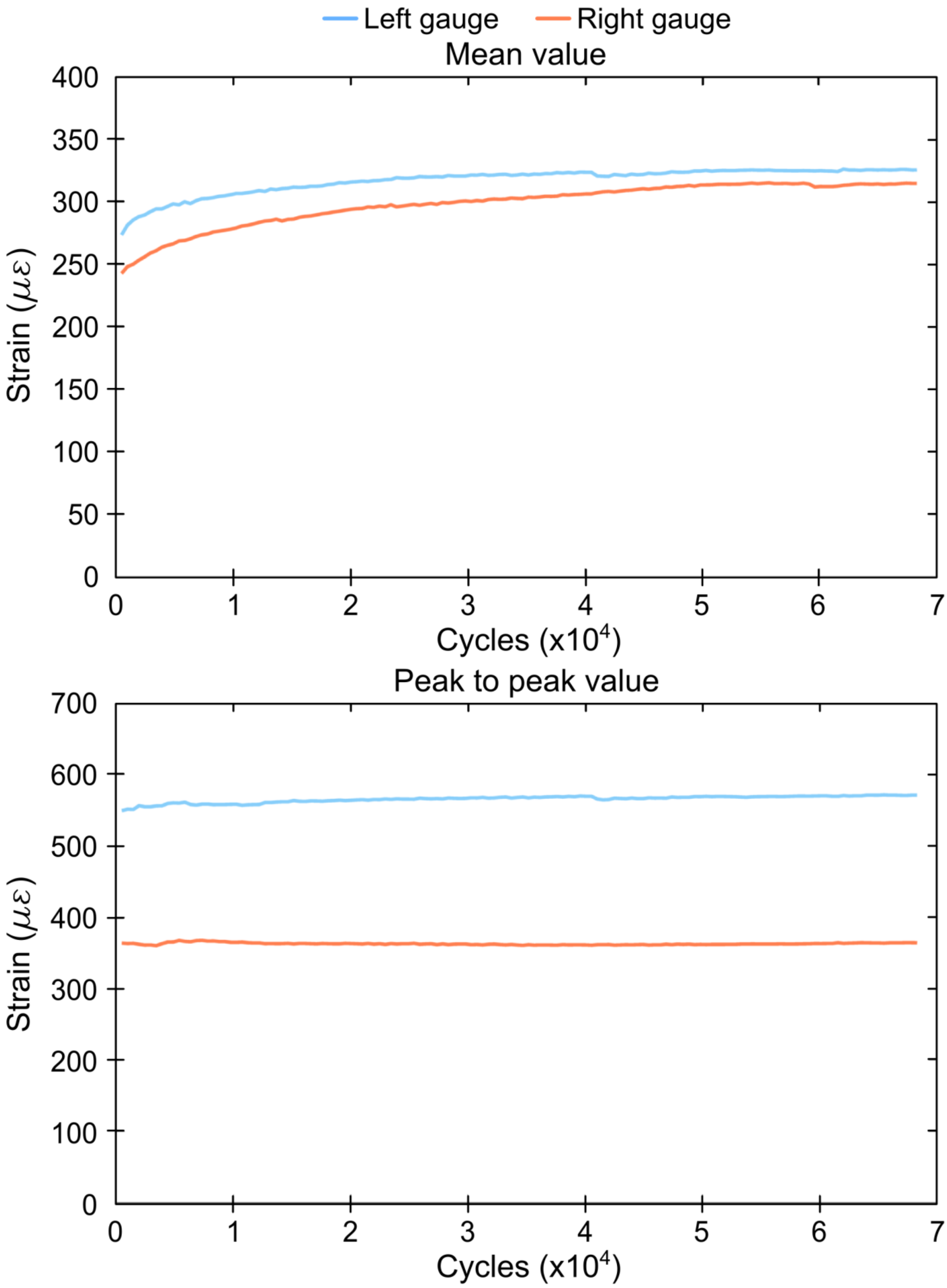

Figure 3-18: Mean and peak to peak values of the signals acquired throughout the test from the strain gauges bonded on the left and right fixator rod.

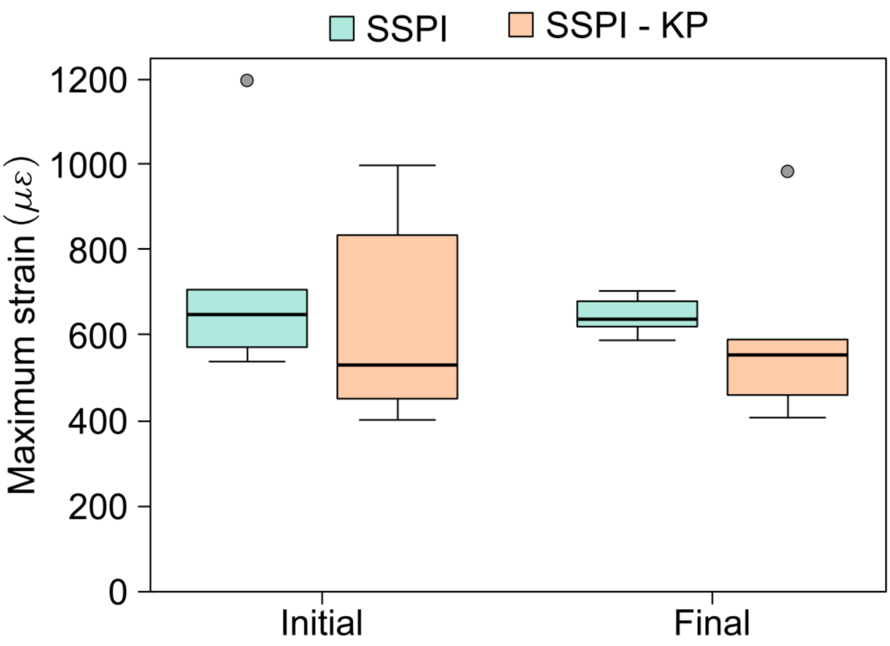

Figure 3-19: Actual maximum strain recorded on the fixator rods at the beginning and end of test.

The stiffness was calculated throughout the test at each cycle both on the rising ($Stiff^{Rise}$) and falling ($Stiff^{Fall}$) edge (Figure 3-20); detailed description of the calculation method can be found in 2.2.3.3. In all cases no significant difference was found between groups, although an approximate 5 % decrease was found over time comparing the values at the beginning and end of test (Table 3-6). Initial stiffness values were predictive of the final stiffness and a strong correlation was found: $Stiff^{Rise}$ ($r_s=0.99$, $p<0.001$), and $Stiff^{Fall}$ ($r_s=0.99$, $p<0.001$).

The stiffness calculated on the rising edge was significantly higher than that calculated on the falling edge both at the initial stage ($p<0.001$) and at run-out ($p<0.001$). $Stiff_{in}^{Rise}$ was 6 % higher than $Stiff_{in}^{Fall}$, however such difference was considered constant throughout the test as it increased by just 1 % when calculated for the final values ($Stiff_{fin}^{Rise}$ and $Stiff_{fin}^{Fall}$). In addition, $Stiff^{Rise}$ and $Stiff^{Fall}$ were strongly correlated between each other both when considering the beginning ($r_s=0.99$, $p<0.001$) and of test ($r_s=0.99$, $p<0.001$). Therefore, for simplicity of reading, all the following results and discussion will refer to only $Stiff^{Fall}$ (Figure 3-21), and could be assumed to be equally valid for $Stiff^{Rise}$. The constant difference between the two quantities was imputed to viscoelasticity of the samples, where energy is lost due to creep.

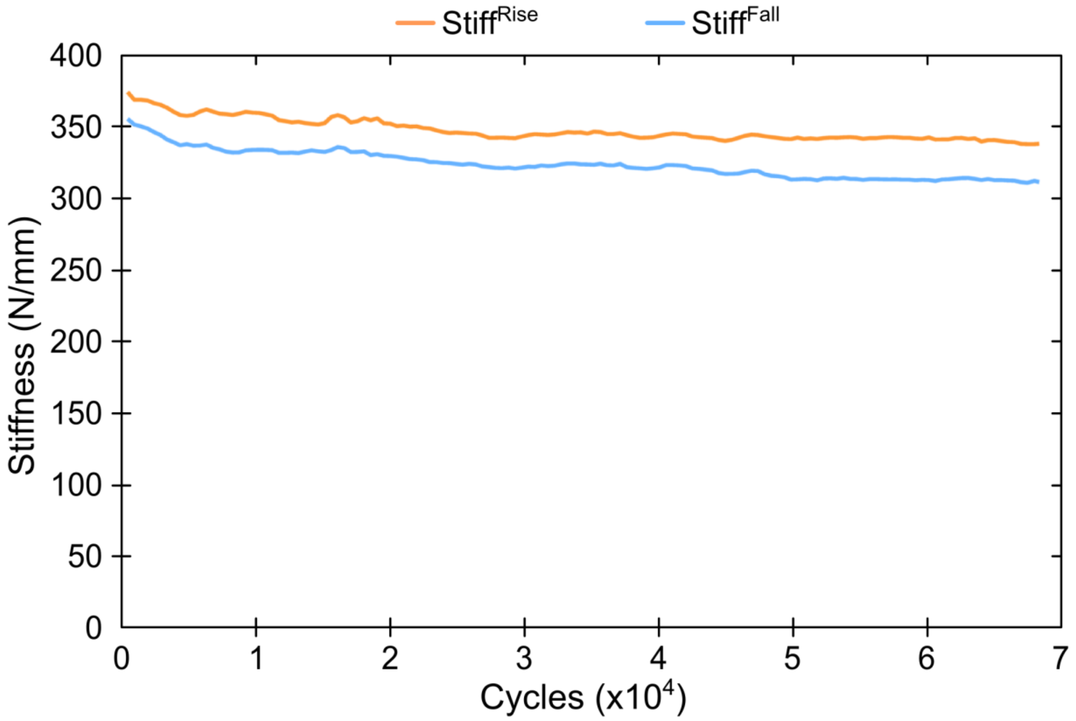

Figure 3-20: Sample curves showing evolution of stiffness over time calculated on both falling and rising edge of the load-displacement curve.

Table 3-6: Stiffness (N/mm) of the construct calculated throughout the test and divided by group.

Parameter	SSPI		SSPI – KP		p†	p‡
	median	range	median	range		
Stiff$_{in}^{Rise}$	399	130 – 633	516	479 – 732	0.13	0.026*
Stiff$_{fin}^{Rise}$	370	139 – 632	480	402 – 688	0.13	
Stiff$_{in}^{Fall}$	379	113 – 603	497	453 – 710	0.13	0.010*
Stiff$_{fin}^{Fall}$	338	125 – 594	463	373 – 661	0.13	

† p-value relative to the comparison between SSPI and SSPI – KP group.

‡ p-value relative to the comparison between initial and final value.

* p-value < 0.05.

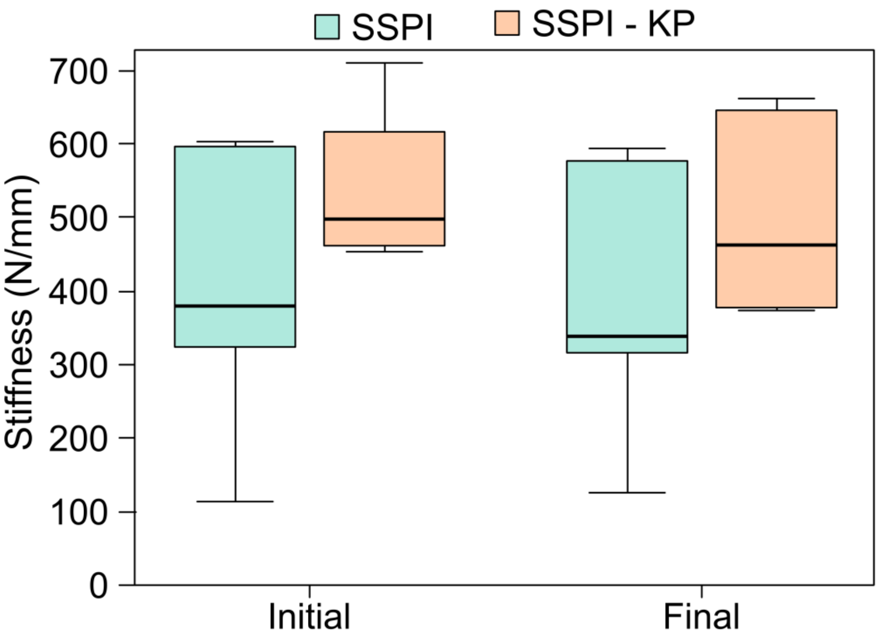

Figure 3-21: Stiffness of the construct at the beginning and end of test. Difference between SSPI and SSPI – KP can be qualitatively appreciated.

Initial stiffness was positively correlated with the initial mean value of the axial displacement (r_s=0.79, p=0.0036) and negatively correlated with its peak to peak value (r_s=-0.85; p<0.001), meaning that lower stiffness resulted in greater axial compression

The final mean value of the posterior displacement was correlated with both the initial (r_s=0.61, p=0.040) and final stiffness (r_s=0.60, p=0.043), whilst no correlation was found with the initial value (p>0.80 in both cases). On the contrary, only the initial peak to peak value of the posterior displacement showed a significant negative correlation with the initial (r_s=-0.69; p=0.016) and final stiffness (r_s=-0.70; p=0.015).

Initial stiffness was negatively correlated with the actual maximum strain at the beginning (r_s=-0.80; p=0.0031) and end of test (r_s=-0.61; p=0.040). Likewise the final stiffness negatively correlated with the initial (r_s=-0.80; p=0.0027) and final actual maximum strain (r_s=-0.62; p=0.034). The actual maximum strain at the beginning of the test was negatively correlated with both the initial (r_s=-0.81; p=0.0024) and final (r_s=-0.82; p=0.0017) mean axial displacement. Conversely, no significant correlation was found between the final actual maximum strain and the initial and final mean displacement. The initial actual maximum strain was predictive of the amplitude of the axial displacement, both at the beginning

(r_s=0.92, p<0.001) and end of test (r_s=0.92, p<0.001). No correlation was found between strain and posterior displacement for any of the calculated parameter.

None of the above mentioned parameters appeared to be influence by the grade of the fracture at the central vertebra of the segment (p>0.05 in all cases).

Presence of a loose screw did not induce any significant variation in all the measured parameter except for the mean value of the axial displacement. The sample that developed screw looseness where subjected to initial higher compression (Mann-Whitney U, p=0.030) which remained higher also at the end of test (Mann-Whitney U, p=0.018).

3.3.3 Endplate deflection

3D maps of endplate deflection were calculated for the endplate cranially and caudally adjacent to the treated level (i.e. central vertebra of the segment). Displacement fields were transformed and decomposed according to anatomical axes, as described previously (2.2.4.4). The vertical component (i.e. cranio-caudal direction: y-axis) was considered the most biomechanically relevant for the study, thus it was the only included in the analysis presented below.

Table 3-7 details the 5th and 95th percentile of the endplate deflection fields in the cranio-caudal direction divided by group, and the statistical difference between them. Each deflection map (Figure 3-22) was treated as a distribution of values; whose extremes were represented by the 5th and 95th percentile (2.2.4.4). Complete presentation of all the vertical displacement maps calculated per each sample can be found in Appendix C. To allow comparison, and pooling of results from cranially and caudally adjacent endplates, data were sorted to have negative values always indicating displacement towards the core of the vertebra. In fact, in accordance with the definition of the reference frame (2.2.4.2), cranially adjacent endplates showed positive values for displacement towards the core of the vertebra, since it is the positive direction of the vertical axis.

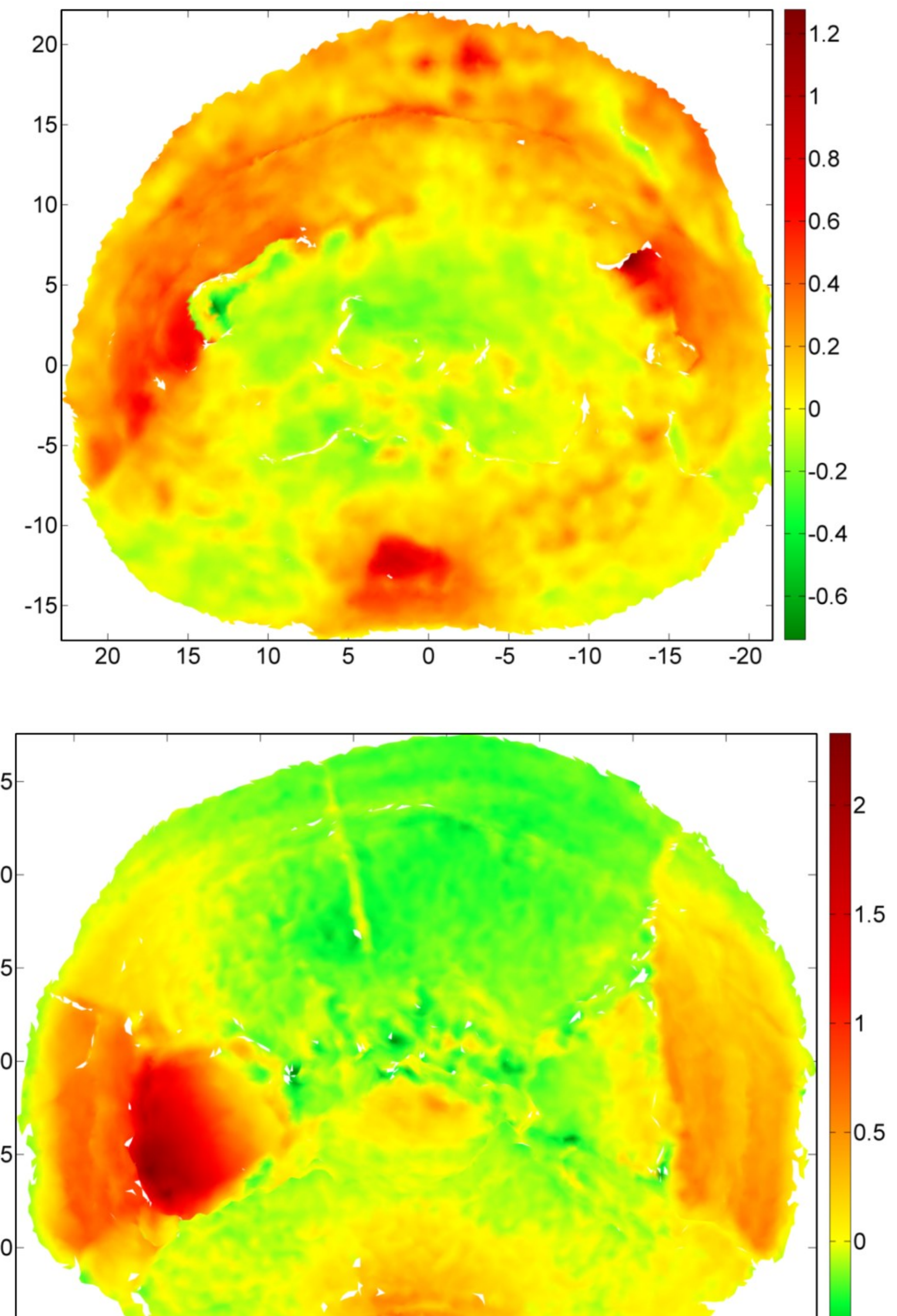

Figure 3-22: Example of displacement maps (mm) for cranial endplates of vertebrae caudally adjacent to a treated one (see Appendix C)

Table 3-7: 5th and 95th percentile of cranio-caudal endplate deflection field calculated at post-fatigue.

Deflection	SSPI		SSPI – KP		p†	p‡
	median	range	median	range		
Cranial 5th	-0.3	-1.0 – -0.1	-0.1	-1.0 – 0.0	0.48	0.42
Caudal 5th	-0.1	-0.4 – 0.0	-0.3	-0.4 – -0.1	0.18	
5th percentile	-0.2	-1.0 – 0.0	-0.2	-0.9 – 0.0	0.68	–
Cranial 95th	0.3	0.1 – 1.0	0.1	0.0 – 0.9	0.48	0.79
Caudal 95th	0.2	0.0 – 0.7	0.3	-0.1 – 1.1	0.93	
95th percentile	0.2	0.1 – 1.0	0.1	-0.1 – 1.1	0.59	–

† p-value relative to the comparison between SSPI and SSPI – KP group.

‡ p-value relative to the comparison between pooled results from cranially and caudally adjacent vertebra.

* p-value < 0.05.

No significant difference between groups was found for both the median 5th (Mann-Whitney U, p=0.68) and 95th percentile (Mann-Whitney U, p=0.59) of endplate deflection (Figure 3-23). When data were pooled together, the median of the 5th and 95th percentile was -0.2 (-1.0 – 0.0) and 0.2 (-0.1 – 1.1), respectively. The 95th percentile was significantly higher than the 5th (p<0.001). The spinal level did not influence both the 5th (Kruskal-Wallis, p=0.59) and 95th percentile (Kruskal-Wallis, p=0.50), and no difference was found between cranially and caudally adjacent endplates (Wilcoxon signed-rank, p=0.42 for 5th, and p=0.79 for 95th) (Figure 3-24).

A significant correlation was found between 5th and 95th percentiles of endplate deflection (r_s=-0.71, p<0.001), whilst no correlation was found between deflection and all the results describing stiffness (p>0.05), axial displacement (p>0.05) and posterior displacement (p>0.05). However, the 95th percentile appeared to be associated with the mean value of the strain on the fixator rods (beginning of test r_s= 0.43, p=0.036; end of test r_s= 0.57, p=0.0036).

The fracture grade did not influence both the 5th (Kruskal-Wallis, p=0.51) and 95th (Kruskal-Wallis, p=0.36) percentiles, and neither did the presence of fragment retropulsion (Mann-Whitney U, p=0.98; p=0.19, respectively).

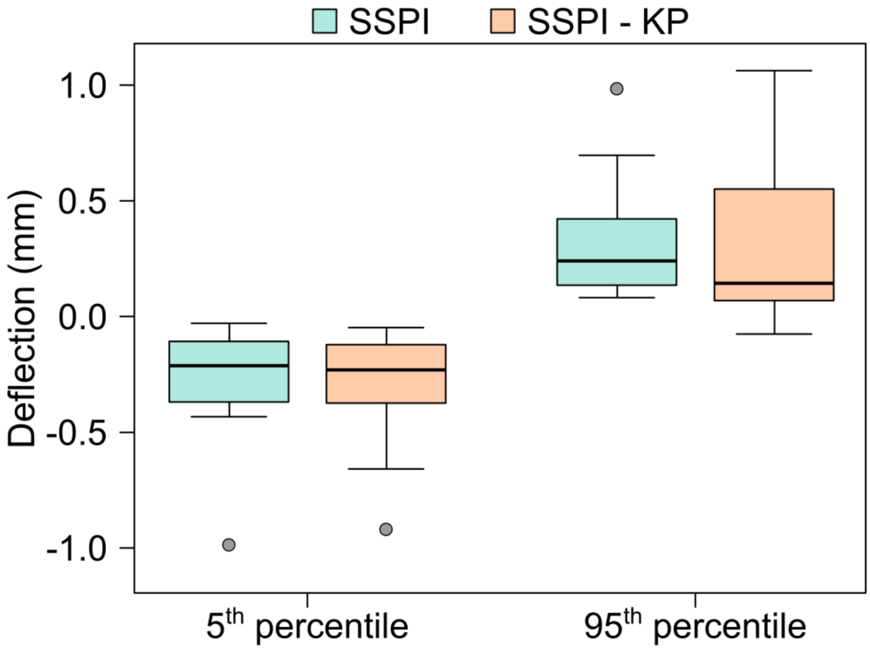

Figure 3-23: 5th and 95th percentile of the deflection field on the adjacent endplates along the cranio-caudal direction, for SSPI and SSPI – KP.

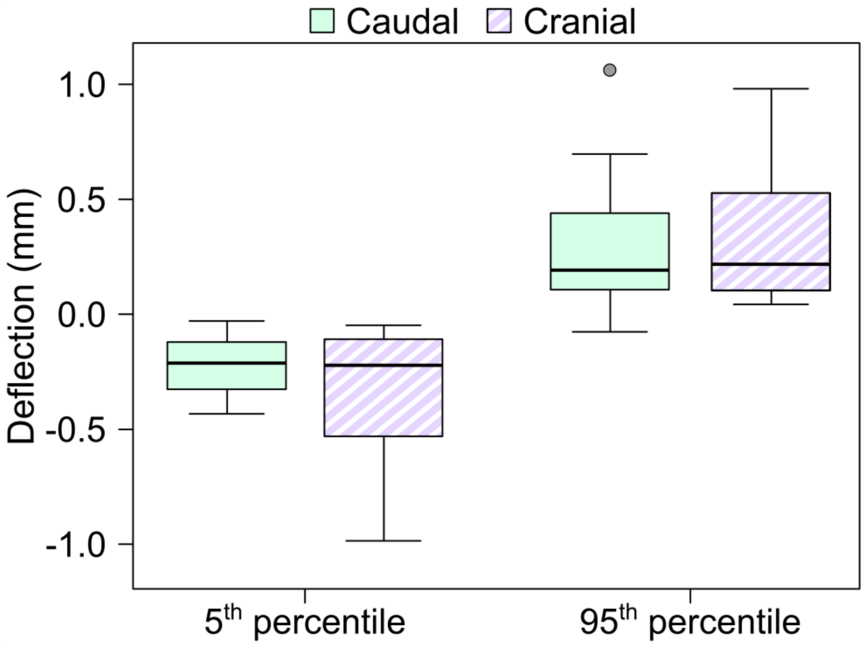

Figure 3-24: 5th and 95th percentile of deflection field on the adjacent endplates along the cranio-caudal direction, divided by side of adjacency to the treated vertebra.

3.4 3D analysis

This section details the results from quantitative 3D investigation of the central level of each segment. Therefore, the methods developed (2.2.4.3) allowed following the anatomical changes of the vertebral body throughout the different experimental stages (intact to post-fatigue) and link them to the results from mechanical testing. The angle on the frontal plane was not included in the analysis presented below, for simplicity and because it was of limited interest for the study.

The median height, kyphotic angle and endplate curvature of the samples in intact conditions was 25.7 mm (range 19.6 – 28.2 mm), 0.4° (range -9.8 – 6.8°) and 250.1 mm (range 55.9 – 1088.0 mm), respectively. The level of the vertebra significantly influenced both the vertebral height (Kruskal-Wallis, $p=0.024$) and kyphotic angle (Kruskal-Wallis, $p=0.0097$). The endplate curvature was overall independent from the spinal level (Kruskal-Wallis, $p=0.39$), but the curvature of the cranial endplates was significantly higher (i.e. they were flatter) than that of the caudal ones (Wilcoxon signed-rank, $p=0.016$).

A significant difference in the percent height loss (Mann-Whitney U, $p=0.015$) was found between HE (34.2 %) and LE group (13.0 %) (Figure 3-27), but not across spinal levels (Kruskal-Wallis, $p=0.78$). In addition, the absolute height loss (i.e. not relative to the intact condition) was marginally influenced by the fracture type (Kruskal-Wallis, $p=0.057$), and positively correlated with the delivered energy ($r_s=0.75$, $p=0.0074$), and SCO_{CT} ($r_s=0.60$, $p=0.040$). No correlation was found between IPW_{max} ($r_s=-0.021$, $p=0.95$), IPW_{res} ($r_s=-0.055$, $p=0.89$) and absolute height loss. In addition, no difference was found between groups for the change in kyphotic angle (Mann-Whitney U, $p=0.24$), whose absolute median increase was 2.5° (range -8.5 – 8.8°); no association was seen with the above mentioned variables.

The fracture caused an increase in the convexity of the endplates, which meant a significant decrease in the curvature radius (Figure 3-25) (Wilcoxon signed-rank, $p<0.001$) from 172.0 mm (range 55.9 – 1088.0 mm) to 77.5 mm (range 34.7 – 591.3 mm). Sample results obtained from CT scans are presented in (Figure 3-26). The cranial endplates were subjected to a higher percent increase in convexity than the caudal ones (Wilcoxon signed-rank, $p=0.027$) (Figure 3-28). No difference was found in such decrease between HE and LE (Mann-Whitney U, $p=0.57$), as well as among spinal levels (Kruskal-Wallis, $p=0.54$), and fracture type (Kruskal-Wallis, $p=0.28$). However, the percent variation in curvature radius was correlated with the delivered energy ($r_s=0.49$, $p=0.018$) and the percent vertebral compression ($r_s=0.56$, $p=0.0054$). Conversely, no association was found with IPW_{max} ($r_s=-0.18$, $p=0.40$), IPW_{res} ($r_s=-0.18$, $p=0.45$) and SCO_{CT} ($r_s=0.34$, $p=0.12$).

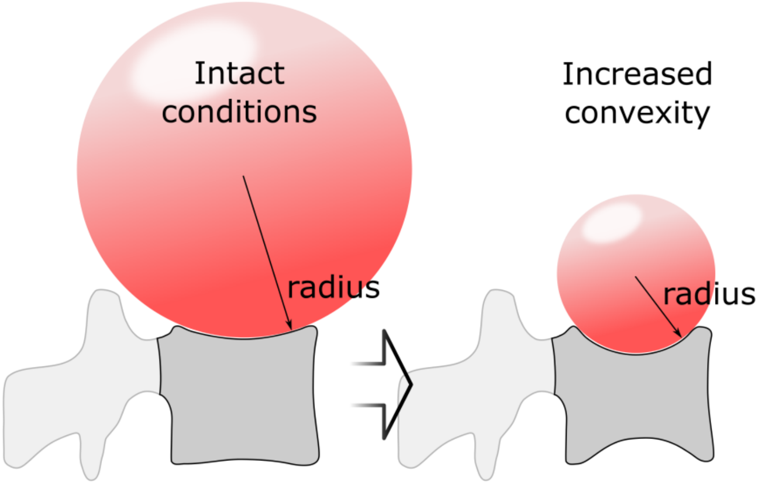

Figure 3-25: A decrease in the radius of the sphere fitted onto the endplate indicated an increase in its convexity.

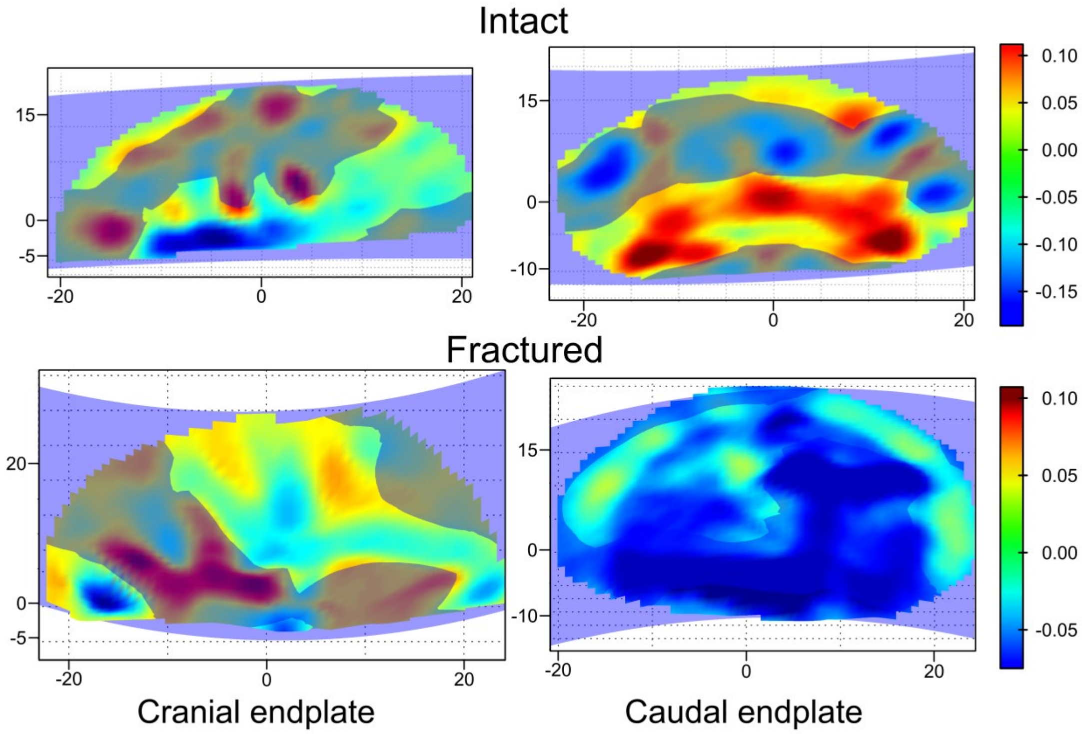

Figure 3-26: Example of endplate curvature calculated before and after fracture. Global curvature is represented by a fitted surface whilst local curvature (mean curvature H) is plotted directly on the endplate surface.

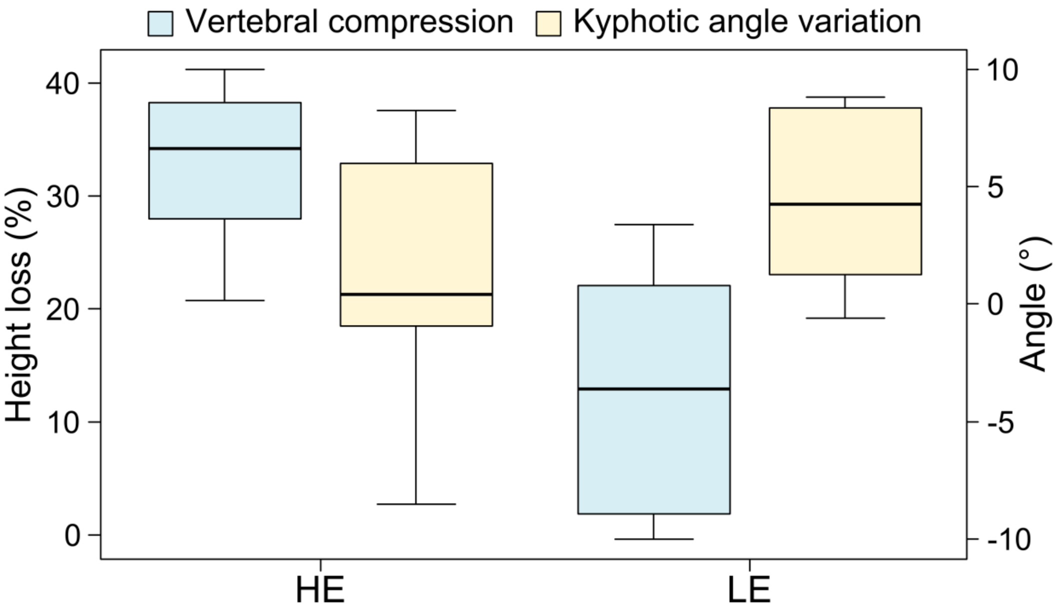

Figure 3-27: Percent height loss and variation in kyphotic angle caused by creation of a burst fracture. Difference between HE and LE group.

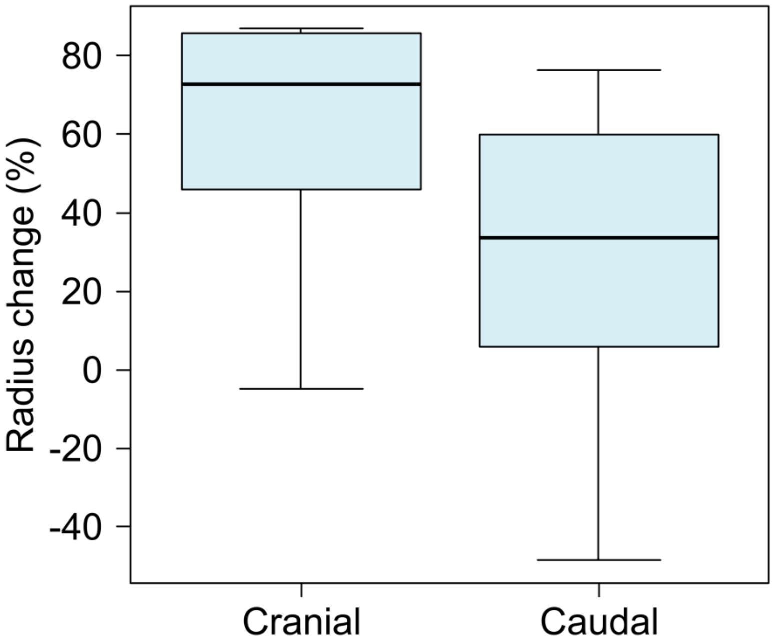

Figure 3-28: Percent variation of endplate curvature radius at post-fracture with respect to intact conditions. Comparison between cranial and caudal endplates.

Post-treatment and post-fatigue testing stages were added to the analysis, to compare SSPI – KP and SSPI, and investigate the performance of the treatment. Details of the vertebral body height throughout the experimental stages by group are presented in Table 3-8, whilst Table 3-9 details the changes in the kyphotic angle.

No significant difference was found at all experimental stages between SSPI and SSPI – KP, for both vertebral body height and kyphotic angle. Results were then pooled together to assess differences across consecutive stages (Figure 3-29). Burst fracture caused a significant 24.8 % compression of the vertebral body (p<0.001). Following surgical treatment, the vertebral body height was increased by 12.3 % with respect to post-fracture condition. In absolute terms, the height significantly increased from 18.5 mm to 21.4 mm (p<0.001).

Fatigue testing induced a non-significant increase (Mann-Whitney U, p=0.69) in vertebral body compression (with respect to post-treatment condition) by 0.30 % and 0.48 %, in SSPI and SSPI – KP, respectively. Overall, from intact to post-fatigue stage, height decreased by 19.8 % (range -0.69 – 25.5 %) in SSPI and 11.9 % (range -1.2 – 21.4 %) in SSPI – KP (Figure 3-30), but no significant difference between groups was found (Mann-Whitney U, p=0.48). When considering the kyphotic angle, fracture overall induced lordosis of the vertebral body. However, the only significant change was found between pre- and post-fatigue testing.

Table 3-8: Vertebral body height (mm) at consecutive experimental stages, comparison between SSPI and SSPI – KP.

Experimental	SSPI		SSPI – KP		p†	p‡
stage	median	range	median	range		
Intact	25.7	22.5 – 28.2	25.6	19.6 – 27.8	0.70	–
Post-fracture	18.6	15.6 – 27.7	17.9	14.1 – 26.6	0.70	<0.001*
Post-treatment	20.8	18.7 – 27.9	22.6	16.5 – 27.5	0.87	<0.001*
Post-fatigue	20.9	18.7 – 27.8	21.8	17.1 – 27.4	0.94	0.69

† p-value relative to the comparison between SSPI and SSPI – KP group.

‡ p-value relative to the difference with the previous stage.

* p-value < 0.05.

Table 3-9: Vertebral kyphotic angle (°) at consecutive experimental stages, comparison between SSPI and SSPI – KP.

Experimental	SSPI		SSPI – KP		p†	p‡
stage	median	range	median	range		
Intact	-1.6	-9.8 – 3.1	2.7	-8.3 – 6.8	0.48	–
Post-fracture	-4.5	-10.5 – -1.8	-2.0	-11.7 – 4.7	0.24	0.092
Post-treatment	-4.7	-6.4 – -1.2	-0.6	-8.5 – 2.7	0.48	0.42
Post-fatigue	-4.9	-7.9 – -2.9	-4.9	-7.7 – 3.4	0.94	0.02*

† p-value relative to the comparison between SSPI and SSPI – KP group.

‡ p-value relative to the difference with the previous stage.

* p-value < 0.05.

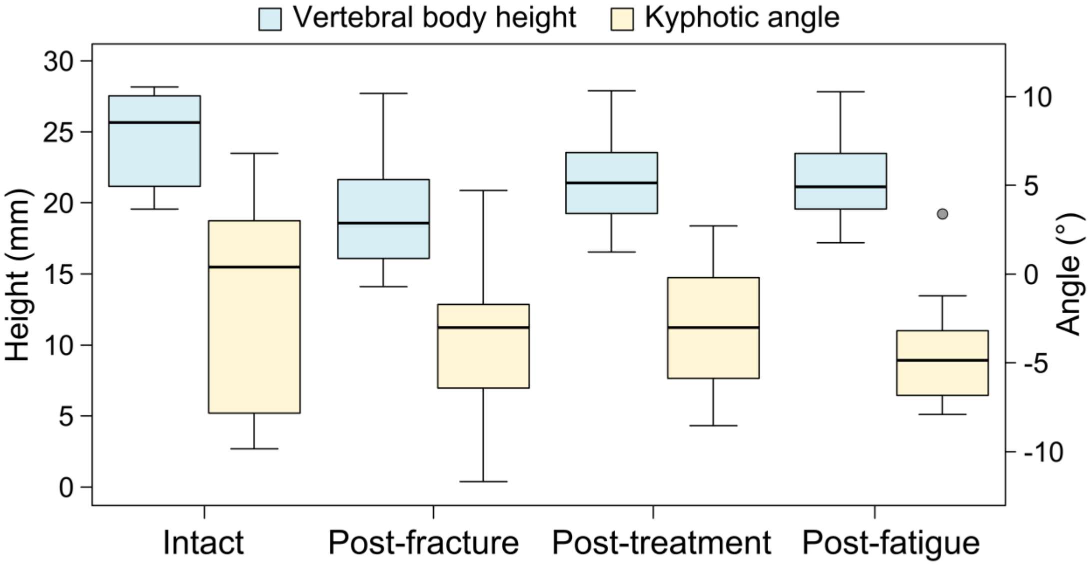

Figure 3-29: Vertebral body height and kyphotic angle across experimental stages with all results pooled together.

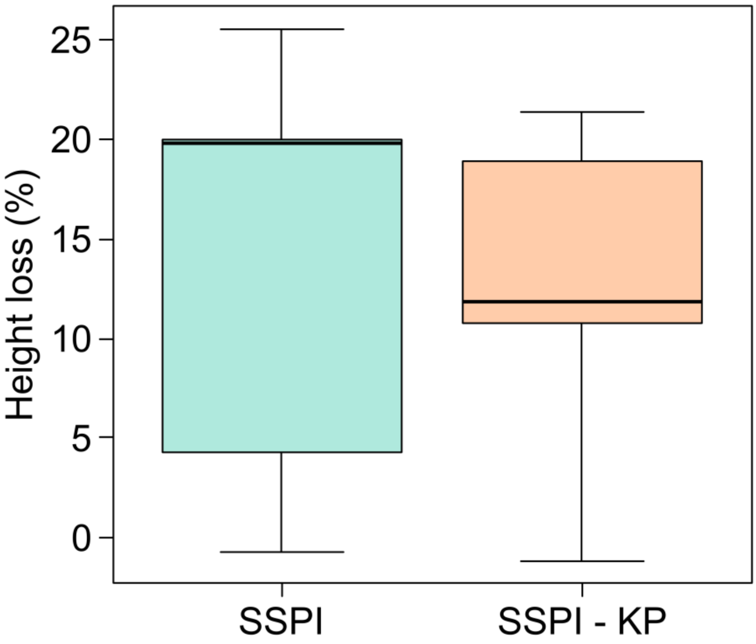

Figure 3-30: Percent vertebral body compression at post-fatigue, with respect to intact conditions, by treatment group.

No significant difference was found between the two groups after the treatment in terms of endplate curvature radius (Mann-Whitney U, p=0.11) (Table 3-10). Such results might suggest that both techniques provided the same endplate restoration. However, if the analysis is undertaken within each group, and comparing post-fracture with post-treatment absolute values, a remarkable difference arises. SSPI worsened the convexity of the endplates (Wilcoxon signed-rank, p=0.0061), in fact, a 7.9 % (range -53.5 – 4.2 %) increase in the curvature radius was detected. Conversely SSPI – KP showed a significant 21.7 % (range -4.0 – 119.2 %) reduction of convexity (Wilcoxon signed-rank, p=0.0081). This result meant that KP achieved an additional degree of restoration of the endplate curvature, otherwise not possible through SSPI alone, which instead aggravated the curvature. Such difference between SSPI and SSPI – KP was even more marked when comparing the aforementioned percent variations with respect to post-fracture conditions (Mann-Whitney U, p<0.001), although no clear correlation was seen with the height increase (r_S=0.31, p=0.14).

Following fatigue testing, the percent curvature improvement (which aims at recovering the intact value), with respect to post-fracture conditions, was still higher in SSPI – KP than in SSPI (Mann-Whitney U, p=0.0045) (Figure 3-31). In addition, no significant change was seen between consecutive post-treatment and post-fatigue stages in both SSPI (Wilcoxon signed-rank, p=0.24) and SSPI – KP (Wilcoxon signed-rank, p=0.45), showing that both treatments overall retained what initially achieved. However, a peculiar trend could be identified. Although the variation was shown not to be statistically significant, in SSPI the endplate radius decreased by 4.3 %, whilst in SSPI – KP it increased by 6.0 %. Such qualitative observation suggested that fatigue testing flattened the endplates in SSPI, whilst increasing the convexity in SSPI – KP.

When comparing the whole experimental process, the curvature radius at post-fatigue underwent a 54.7 % increase with respect to intact conditions in SSPI-KP, whilst in SSPI it was 66.4 % (note that higher percent variations indicate higher increase in convexity with respect to intact conditions). Although the endplates in SSPI overall showed a higher percent increase, no significant difference could be seen between groups (Mann-Whitney U, p=0.56), because the variation caused by the fracture overshadowed that of the treatment. None of the two techniques was able to fully restore the curvature of the endplate.

Table 3-10: Endplate radius of curvature (mm) at consecutive experimental stages, comparison between SSPI and SSPI – KP.

Experimental stage	SSPI median	SSPI range	SSPI – KP median	SSPI – KP range	p†	p‡
Intact	133.5	80.3 – 1088.0	179.0	55.9 – 715.9	0.41	–
Post-fracture	75.9	34.7 – 591.3	80.0	38.4 – 329.7	0.71	<0.001*
Post-treatment	56.2	35.1 – 275.2	94.2	45.9 – 576.2	0.11	0.68
Post-fatigue	56.2	46.5 – 273.4	87.5	46.5 – 324.6	0.13	0.50

† p-value relative to the comparison between SSPI and SSPI – KP group.
‡ p-value relative to the difference with the previous stage.
* p-value < 0.05.

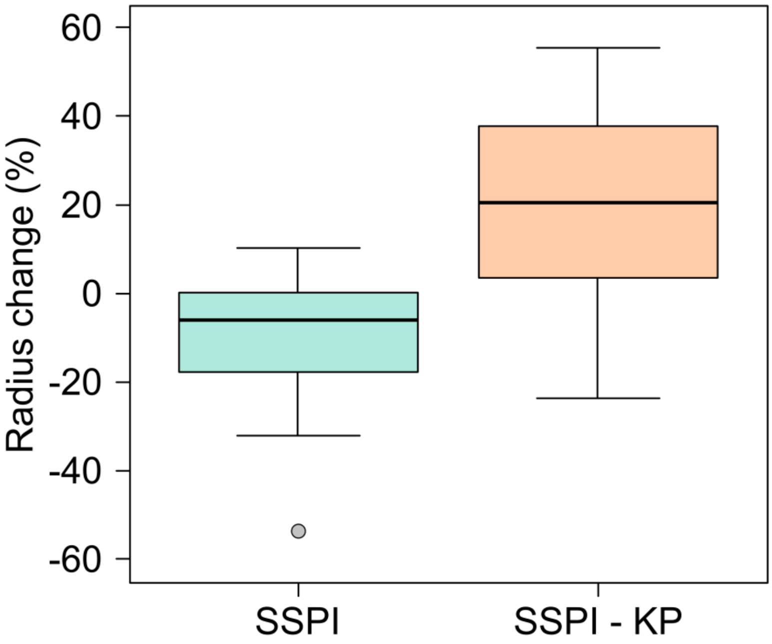

Figure 3-31: Percent variation of endplate curvature radius at post-fatigue with respect to the post-fracture (before undergoing treatment) stage, results grouped by treatment.

Table 3-11 presents the correlation coefficients between results from fatigue testing and the vertebral height compression, and curvature change, induced by the treatment (percent variation at post-treatment with respect to fractured conditions). The results from fatigue testing used for the analysis were those calculated at the end of the test, hence to assess if anatomical restoration could be predictive of the mechanical outcome. In particular, parameters under investigation were stiffness, mean value of the axial displacement, maximum actual displacement measured by LVDT and maximum strain measured on the fixator rods. Although no correlation was found with the stiffness, the vertebral compression was positively correlated with the axial displacement (r_S=0.71, p=0.013), which means that the more the height restored, the higher the compression of the construct due to cyclic loading. However, when data where grouped by treatment, it appeared that this phenomenon happened almost exclusively in SSPI. In fact, despite the marginal significance, a correlation in SSPI was still present (r_S=0.83, p=0.058), whilst no association was found in SSPI – KP (r_S=0.37, p=0.49) (Figure 3-32). On the other hand, no association was found between the outcomes of mechanical testing and the percent variation of the endplate curvature induced by the treatment.

Correlation was also calculated between the post-fatigue endplate deflection and percent vertebral height compression, as well as percent curvature change (same parameters used above). No association was found between the endplate deflection and vertebral height compression when considering both the 5th (r_S=0.040, p=0.85) and 95th percentile of endplate deflection (r_S=-0.052, p=0.81). Likewise, the percent variation of endplate curvature did not influence the 5th (r_S=0.16, p=0.44) and 95th percentile (r_S=-0.14, p=0.52). Therefore, the amount of percent height restoration, and endplate curvature restoration, were not related with the extent of adjacent endplate deflection.

Table 3-11: Correlation between percent height and curvature changes following treatment (with respect to post-fracture), and results from fatigue testing (calculated at the end of the experiment).

Parameter	Stiffness		Axial displacement		Posterior displacement		Fixator strain	
	r_S	p	r_S	p	r_S	p	r_S	p
Height (%)	0.34	0.28	0.71	0.013*	0.27	0.40	0.12	0.72
Radius (%)	0.30	0.16	0.21	0.33	0.47	0.021*	-0.040	0.85

Results pooled together with no distinction of treatment group.
* p-value < 0.05.

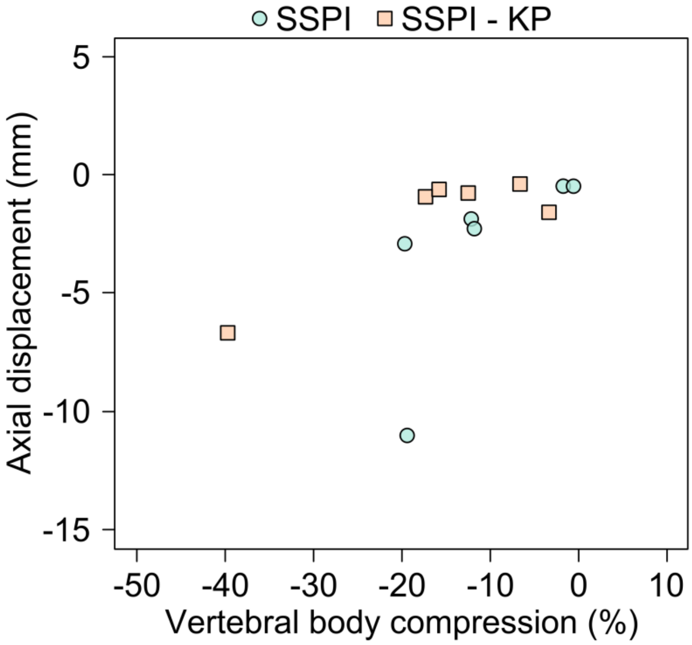

Figure 3-32: Association between vertebral body compression and mean value of axial displacement calculated at the end of fatigue testing. Percent compression is negative because treatment resulted in an increase in height with respect to intact conditions.

Chapter 4: Discussion

This chapter reviews the findings of this study whilst discussing their clinical and engineering relevance. The main aim of the project was to investigate the biomechanics of vertebral fractures, with special focus on the burst fracture pathway (onset to treatment), which was fulfilled by using a methodical approach as defined by the study objectives (Table 4-1).

Table 4-1: Summary of the study objectives and key findings.

Objective	Status	Key findings
Provide experimental data for FE model development through in situ testing (2.2.1).	Completed	Loading surfaces deflection estimated from CT scans. Methodology successfully translated for assessment of endplate fatigue (2.2.4.4). Image based boundary conditions are more efficient and robust.
Develop and integrate methods for 3D analysis of vertebral anatomy (2.2.4).	Completed	Tracked significant anatomical changes throughout experimental stages (3.4). Identified curvature changes induced by fracture and treatment. Potentially suitable for *in vivo* applications.
Investigate in vitro the burst fracture mechanics and dynamics of IPW (2.2.2).	Completed	Provided first ever evidence on dynamics of IPW: IPWmax=15.8% and IPWres=4.9% (3.2.1). Vertebral height is influenced by impact energy (3.4). Fracture causes increase in endplate convexity (3.4). Current dynamic SCO filming technique is not suitable for human cadaveric tissue (3.2.2).
Provide in vitro fatigue comparison/investigation on SSPI and SSPI – KP as treatment for spinal burst fractures (2.2.3).	Completed	SSPI – KP marginally improves mechanical properties better than SSPI and reduces migration of posterior wall (3.3.2). Fatigue loading induces an overall decrease of stiffness of the construct (3.3.2). KP allows better restoration of endplate morphology (potentially preventing post-traumatic disc degeneration) (3.4). Adjacent endplates do not significantly degenerate because of fatigue loading (3.3.3).

The nature of the project made it progress as new methodologies were developed and improved throughout consecutive stages. The software applications that were implemented increased in complexity and capability, especially with regard to data-logging/hardware interface (LabVIEW; National Instruments Corporation) and image-processing (Matlab; the MathWorks Inc. and Amira; Visualization Sciences Group). The 3D analysis allowed tying fracture onset with treatment outcomes, providing further insight on the evolution of vertebral anatomy throughout the fracture pathway. In addition, the collaboration for the development of FE enabled transferring knowledge to the main project, as the methodology for the definition of the boundary conditions was adapted to assess permanent endplate deflection caused by fatigue loading (2.2.4.4).

4.1 *In situ* testing and FE modelling

The *in situ* experimental protocol allowed successful stepwise loading and simultaneous scanning of three-adjacent-vertebrae segments. However, the outcomes of the experimental protocol were not free from limitations and issues. Firstly, although all the segments were tested and image processing could be performed, only three out eight segments were actually suitable for the development of the FE model. In fact, adequate boundary conditions could be extracted only when the displacement fields were sufficiently uniform in distribution and magnitude. Therefore, the experimental data gathering resulted in being time-consuming, since part of the processed datasets had to be discarded (although they can be used for other future applications).

Results from Hulme et al. [67] have shown endplate deformation in osteoporotic vertebrae are between 0.02 and 0.08 mm in magnitude, at loads ranging from 200 to 2000 N. Although correlated with the imposed stress, their displacement measurements showed significant scatter, in agreement with the issues encountered in this study. In fact, endplate properties have been shown to be subjected to high variability [247], which may be emphasised even further by multiple myeloma. Besides, osteolytic lesions may induce erratic endplate biomechanics by disrupting load transfer paths through the trabecular structure.

Another limitation is that the rig was not watertight, as that used by Hulme et al. [67]. Having been able to completely submerge the sample in saline solution would have ensured hydration as well as X-ray attenuation more similar to that occurring *in vivo* [248]. Hence, future amendments to the design should account for those considerations.

This study showed that the *in situ* protocol can be used to develop FE models from consecutive load steps, representative of the resultant increase in structural damage. In addition, HR-pQCT datasets were used to extrapolate boundary conditions, which consisted of the displacement field which the loading surfaces underwent (facets and endplates) from one load step to the subsequent one. Results proved that this approach allowed detecting patterns of stress and strain concentration indicative of pre-failure conditions in MM involved bone, where the trabecular structure was sparse and/or compromised. Hence, the method could be also used to identify areas at higher risk of damage.

Several works have shown the importance of geometrical fidelity to achieve better experimental validation of numerical simulations [50, 249, 250]. However, FE models are commonly constructed directly from micro-CT scans or datasets, downsampled to simulate clinical CT resolution and/or reduce computational complexity [251-254]. Although more clinically relevant, models at relatively low resolution are less accurate at predicting structural damage, whilst lacking geometrical definition [250, 253]. In all three simulations developed for this project, good qualitative comparison between actual areas of damage (detected on the HR-pQCT scans) and stress/strain concentration on the model could be achieved when the average element size was on the order of the mean trabecular thickness; as confirmed by mesh sensitivity studies. Higher resolution also allowed creating meshes which better described the cortical shell of the vertebral body, which was modelled by at least two elements. Hence, artifacts due to partial volume effect could be neglected [50], without the need for assigning idealised mechanical properties to the shell, conversely to previous works in the literature[252, 255, 256]. Exploiting a high resolution mesh also allowed appreciating the behaviour of the thickest trabecular structures (Figure 3-3), without the complexity and computational cost required by micro FE simulations.

Although more accurate, micro FE requires each trabecula to be described by at least 3-4 elements to reach mesh convergence [50, 236, 237].

Numerical simulations are highly sensitive to their boundary conditions, and this issue has been highlighted in several FE studies on vertebrae [249, 254]. The approach used in this study was based on the work by Hojjat et al. [236], and Herblum et al. [237], where displacement of the facets and endplates was imposed, to simulate boundary conditions as close as possible to that *in vivo*. However, the aforementioned works where carried out on rat vertebrae, whereas this study represents the first application of the method on human pathological spinal segments. Accurate image segmentation and registration allowed calculating displacement fields that were representative of the actual loading conditions at the time of scanning. Therefore, displacement based boundary conditions implicitly account for the load transmitted through the facet joints and intervertebral discs, without any need for modelling those soft tissue structures (and the effects of their degeneration). On the other hand, since the displacement fields were assigned node by node, large mesh deformation could occur at the boundary. Hence, results directly at the loading surfaces had to be excluded from the analysis.

Since a simplified linear elastic constitutive law was assigned to the elements, models could be solved in 10-15 minutes, despite the high density of the mesh. However, the material properties were assigned at each load step through the optimisation process based on balancing the reaction forces and that resulted in having different parameters for each model. Hence, further research is needed to develop an effective constitutive law specific/greyscale conversion for the multiple myeloma infiltrated vertebra (also integrating the cancerous tissue).

Although the considerations made above were based on qualitative comparisons, the models showed ability to anticipate gross bone failure, which occurred in areas of stress/strain concentration. In addition, the same approach used for the definition of boundary conditions may be applied to other bones.

4.2 Biomechanics of burst fracture onset

Comminution of the endplates, IPW, SCO and LF are considered the hallmarks of spinal burst fractures [18], which have been found to be associated with the occurrence of neurological impairment [15, 18]. However, the greatest hurdle in the diagnostics of the injury is that it occurs during the abrupt and transient phase of the fracture onset [28]. Therefore, biomechanical studies are paramount to better understand the dynamics of the phenomena involved, hence yielding to better clinical interventions.

Several studies have induced burst fractures with the specimen in flexion/extension (Table 1-11), to better replicate the spinal alignment in motor accidents/fall from heights [257]. On the other hand, zero flexion can be considered the condition where the vertebral body is more resilient, since it is optimised for axial loading [63]. Jones et al. [196] imposed an initial 15° flexion whilst allowing unconstrained further rotation at the impact. Conversely, in this study, pure axial compression impacts were delivered without imposing any flexion of the spinal segment, whilst the design of the impactor avoided any relative rotation between the loading surfaces. Therefore, the loading conditions could be assumed as an overconstrained axial compression, which allowed keeping the simulation as controlled as possible. As a matter of fact, developing an experimental protocol for impact biomechanics requires dealing with complex transient events, as opposed to quasi-static loading. Repeatability of burst fracture experiments has been often disputed, in particular since the fracture patterns seldom match what is seen clinically [191, 192]. Similarly to previous works, all the main ligamentous structures were kept intact, to ensure a realistic simulation. In fact, the PLL plays an important role in recoiling the bony fragment and protecting the spinal cord [258]. Overall, fracture appearance and results for SCO_{CT} were in agreement with the literature (Table 1-11) [18]. However, it must be noted that Panjabi et al. [194] obtained a poorer correlation between SCO and impact energy (R^2=0.27; p=0.15) than that obtained in this study (r_s=0.56; p=0.063), hence confirming the robustness of the experimental protocol here developed. Thus, the loading conditions implemented in this study could be considered relevant to simulate high-energy *in vivo* spinal trauma.

Surgical cuts (on the cortical shell of the vertebra and lamina) have been performed in other works to drive the occurrence of the fracture [195, 210]. This approach was not undertaken in this study to keep the fracture onset more physiological, hence focusing on the actual bone structure and geometry. Although Panjabi et al. [194] have argued that delivering incremental impacts leads to more clinical-like fractures, such protocol was not implemented in this study, to limit the variability of the loading conditions. In fact, the appearance of the fracture was always in agreement with what has been presented in the clinical literature (Figure 3-4) [15, 18, 99]. In addition, PLL remained intact in all the samples, as in the *in vitro* experiments of Verlaan et al. [199], whilst none of the samples had to be discarded because judged inadequate for the analysis. The above considerations further demonstrate the validity of the experimental protocol developed. In particular, special care was taken when designing the testing fixtures, to ensure repeatable and robust testing conditions. Granting consistent alignment within the testing frame was indeed a fundamental requirement to fulfil, as trabecular bone (which the vertebral body is mainly made of) is particularly prone to experimental errors due to off-axis loading [259].

Meves et al. [21] reported a mean patient age of 39 ± 1 (range 13 – 84) for thoracolumbar burst fractures, whilst in this study the median age of the donors was slightly higher 45 (range 38 – 56). Younger/healthier donors may have increased the impact of the study; however it must be born in mind that the characteristics of the sample cohort depended on the restricted availability of cadaveric tissue. The limited sample size was the main limitation of this study, which resulted in a reduction of the statistical power of the analysis. Although some results showed some relevant trend, it was sometime not possible to support those assumptions statistically. This was mainly seen when assessing the dispersion between datasets through the Ansari-Bradley test, which necessitates a number of samples higher than that available in this study to detect a significant difference.

Consistently with clinical practice, fractures were graded using the classification of Magerl et al. [18]. Although it is one of the most widely used and trusted grading systems [101], some authors have argued that this classification may not be the most viable, because it requires morphological inspection based on a CT scan. In this study all the samples required multiple HR-pQCT scanning (to carry out the 3D analysis), thus undertaking the classification did not entail exploiting any extra resource. Despite the consistency of the injury patterns when compared to the clinical literature, it must be noted that the fractures induced on T10 vertebrae may have been altered by the lack of the stiffening effect of the rib cage.

4.2.1 Considerations on interpedicular widening and spinal canal occlusion

The dynamics of SCO have been previously investigated in several *in vitro* studies, which have shown that SCO measured at presentation is always a significant underestimation of what happens at fracture onset (1.4.1). In particular, Wilcox et al. [26] developed a methodology to quantify the SCO dynamically using high-speed filming on bovine spine segments. In this study, the same method was implemented to validate its viability on human spine segments, but results showed that it was not possible to achieve the same performance as in Wilcox et al. [26]. From a qualitative point of view, the filming agreed with the aforementioned study, as during the transient phase SCO reached a maximum (SCO_{max}), which subsequently decreased to its resting value (SCO_{res}). However, extremely poor agreement was found between SCO_{res} and SCO_{CT} (±70 %), which was mainly driven by the behaviour of human soft tissue under impact conditions. Figure 4-1 presents in a qualitative fashion the most common phenomena that impaired image processing when measuring SCO from the video recordings. Bone marrow splatters on the mirrors caused light artifacts that blurred or joined the boundaries of the canal CSA. In some cases, fragments of tissue (e.g. periosteum, connective tissue) detached from the bony surface and crossed the light path. Alternatively, SCO_{max} and SCO_{res} were found not to be actually representative of the vertebral foramen, but of the intervertebral disc bulging. This was confirmed by HR-pQCT scanning where high values of SCO_{res} did not have any connection with the appearance of the fracture on the image dataset. Hence, in many cases what measured may have actually been the bulging of the disc and/or translation of the vertebral body, rather than the deformation of the posterior wall. Wilcox et al. [26] have probably not encountered any of this issues because they used bovine tissue. The quadrupeds' spine undergoes a different biomechanics than the human [78], whilst samples are tipically harvested from young animals. Additionally, bovine intervertebral discs are stiffer, higher and with a higher collagen content [260], which may result in less bulging. The trabecular structure in quadrupeds is significantly denser [261], and that may have helped contain the bone marrow, hence avoiding splatters and resulting artifacts.

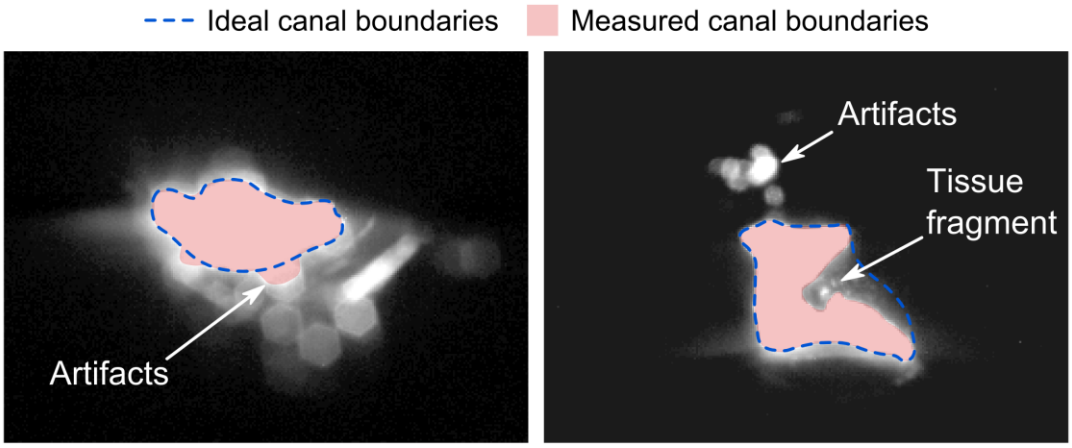

Figure 4-1: Frames from high-speed filming of the spinal canal representative of the sources of error. The difference between the ideal canal area and what actually measured is highlighted.

Although IPW has been speculated to have a dynamic behaviour similar to that of SCO [123], no work has ever corroborated this hypothesis or provided any actual evidence of it. In this study, experimental measurements on cadaveric tissue proved that IPW dynamically evolves throughout the fracture. Figure 4-2 depicts the most significant phases of the evolution of IPW over time in accordance to the curves presented in **Error! Reference source not found.**. When the impact was delivered, IPW reached a maximum value (median IPW_{max}=15.8 %), which resulted in a 223 % increase with respect to what measured at resting conditions (IPW_{res}=4.9 %).

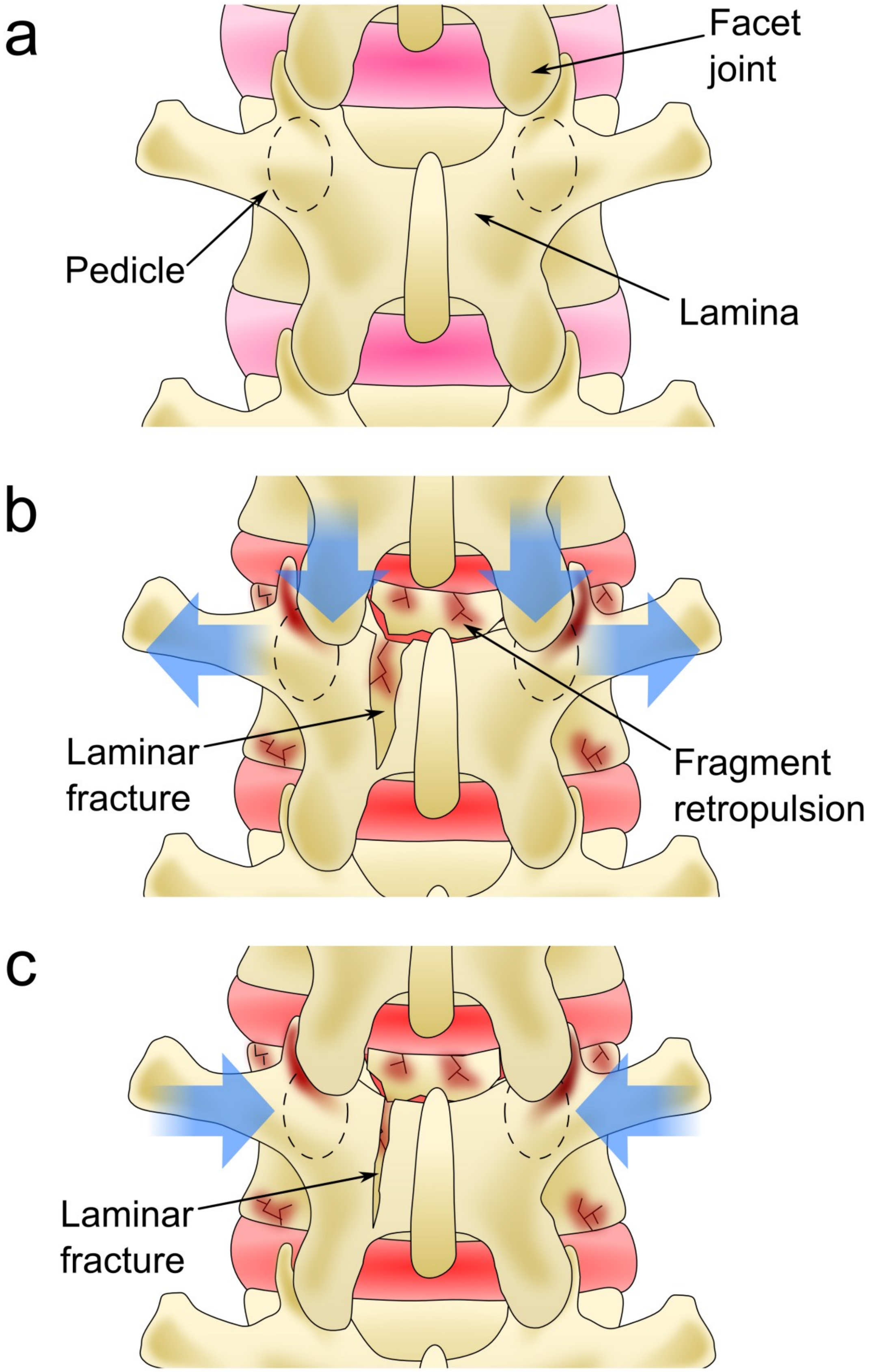

Figure 4-2: Evolution of IPW throughout the fracture onset. a: Posterior view of the intact sample. b: At the impact, the pedicles splay up to the critical value IPW_{max}. c: During the decay of the transient phase the pedicles are recoiled to their resting value IPW_{res}/IPW_{CT}.

Langrana et al. [191] reviewed the loading mechanism leading to the fracture and provided evidence that the fracture originates from the combination of axial loading at the endplates and splaying forces at the root of the pedicles, caused by the forceful downward displacement of the cranially adjacent articular processes. The evolution of IPW over time measured in this study agrees with that theory. It is plausible to assume that the wedging effect of the cranially adjacent articular process drove the abrupt widening of the pedicles up to IPW_{max}, which also represented the critical displacement value that triggered the failure of the root of the pedicles. In this study some degree of pedicle failure was found in all the samples. Although not as clinically common [18], a high incidence of pedicle fractures have been reported in other *in vitro* studies [114, 257].

Tensile strain at the base of the pedicles has been reported to be the highest over the whole vertebra in physiological conditions (490 N compression), ranging 400 – 500 $\mu\varepsilon$ [189], whilst a 3400 $\mu\varepsilon$ strain has been measured on the same region at 75 % of the failure load (2800 N compression) [191]. Drop weight testing by Yoganandan et al. [257], has shown that axial load can reach peaks up to 6700 N at the impact (approximatively 450 J). A simplistic linear interpolation of the aforementioned results suggests that at such load the pedicles would undergo overall strains higher than 8100 $\mu\varepsilon$. Therefore, it is plausible to assume that in impact conditions, at IPW_{max}, the weakest regions of the cortical shell at the root of the pedicles may exceed 10000 $\mu\varepsilon$ (i.e. failure strain of cortical bone [262]). In fact, given the amount of energy involved, even a limited failure may lead to fracture initiation, which would then propagate to the posterior wall and rest of the vertebral body.

Stemper et al. have shown that the maximum compression of the vertebral body is achieved in 30 to 50 ms [188]. Likewise, loading a three-adjacent-vertebrae segment (thoraco-lumbar) at a strain rate of 100 mm/s produces fractures within 50 – 60 ms [191], whilst cervical spine segments have been reported to fail within 20 ms [197]. Ivancic et al. [263] simulated *in vitro* the occurrence of burst fractures due to a fall from height by fitting a cadaveric spine segment within an instrumented crash-test dummy. At the impact, the transducers recorded major transient events up to approximatively 70 ms. Results from this study were in agreement with the aforementioned works, since the time required to reach IPW_{max} was 20 to 25 ms, whilst the whole transient phase lasted less than 400 ms (**Error! Reference source not found.**).

After reaching IPW_{max}, the pedicles were recoiled to the residual value IPW_{res}, which remained constant once the transient event was concluded. Thus, IPW_{res} was considered indicative of what seen at presentation of the patient. Good agreement (approximatively ±4 %) was found between IPW_{res} and IPW_{CT}, confirming the reliability of the developed methodology and relevance of the measurements delivered. However, it must be noted that T10 required the LVDT to be positioned differently because of anatomical differences with the lumbar vertebrae, which may have somehow influenced the results.

The dynamic response of an LVDT depends on the frequency of its excitation voltage, which should be at least ten times greater than the maximum frequency in the measured input [264]. The transducers used in this work where excited at 5000 Hz, whilst the maximum frequency component in the displacement was estimated to be always below 400 Hz. Thus, the measurement system could be considered fit for the dynamic measures carried out. The estimation of the frequency components was based on Fast Fourier transform (Matlab; The Mathworks Inc.) performed on the logged voltage signals.

Clinical studies have suggested that the most relevant determinant of the neurological injury may be the actual shape of the spinal canal, rather than the extent of its occlusion [20, 122]. Vaccaro et al. [20] has reported a higher incidence of neurological injuries in patients with a higher ratio between the transverse and sagittal diameter of the vertebral foramen (i.e. the CSA becomes more elliptical). At the same time, the shape of the vertebral foramen is directly dependant on IPW, since its transverse diameter is the same as the interpedicular distance except for the width of the pedicles. Therefore, IPW_{max} represented the instant where the transverse diameter of the vertebral foramen reached its maximum, hence the most critical condition for the injury of the spinal cord.

Caffaro et al. [23] have provided *in vivo* measurements from plain radiographs and have found IPW to be 24.7 % in presence of neurological injury and 15.3 % in its absence. The experiments carried out in this study yielded to a median IPW_{CT} of 4.7 %. Such a lower value may be indicative of less severe fractures; maybe because the experimental protocol lacked of any muscle simulation. Although radiographic *in vivo* measurements of IPW seem not to be affected if taken with the patient prone or supine [265], the forces exerted by the para-spinal muscles and the intra-abdominal pressure may induce further splaying of the pedicles which could not be replicated *in vitro*, both at the time of the CT assessment as well as during the fracture origination. Saari et al. [266] exploited the follower load paradigm to stabilise the spine segment in *in vitro* impact conditions. Undertaking a similar approach in this study would have increased the complexity of the loading conditions and experimental protocol. In addition, the implementation of a follower load protocol requires anchoring points on the vertebral body (to exert force on it), which would have resulted in stress concentrators, erroneously conditioning the fracture initiation.

IPW_{res}/IPW_{CT} showed only a marginal variation across levels, conversely to the increasing trend in the caudal direction found in the clinical literature (Table 4-2). On the other hand, a significant decreasing trend in the caudal direction was found for IPW_{max} in this study (Figure 3-9). If results from Caffaro et al. [23] and those from this study are taken together, it appears that IPW_{max} and the residual IPW have opposite trends across spinal levels. Some biomechanical insight can be drawn from those results. Although the pedicle angle (Table 2-4) did not influence the results, facet geometry and bone structural properties may be the driving factors for IPW (Figure 4-3). Firstly, CSA of the pedicles increases in the caudal direction (Figure 1-4); if the structural properties are assumed constant across levels, then the strength and stiffness of the pedicle increases caudally too. In addition, the geometry of the facet joints significantly changes across levels and that may be crucial; given that it is also the main determinant of spinal kinematics (see 1.1.3). The flatness of the thoracic facets may be the reason of the highest IPW_{max} and lowest residual IPW. In fact, thoracic facets do not restrain lateral translations; whilst their pedicles should have a lower stiffness (lower CSA). Hence, the combination of the two factors may have induced higher dynamic splaying. On the other hand, as pedicles become stiffer caudally, the interlocking lumbar facets may be more efficient in counteracting IPW. Lumbar facets are almost vertical, but their orientation on the transverse plane increases caudally (the angle between them becomes less acute). Whilst that may help reducing IPW_{max}, it may be detrimental for the recoil of the pedicle instead. Given the lower constraints, thoracic pedicles may be more prone to recoil. Conversely, in the lumbar spine, the downward displacement of the articular processes forced them to actually wedge into each other, preventing the recoil, Whilst the extent of the wedging increases caudally because of the facet angle, additional tensile forces would be required to facilitate the pedicle recoil, hence the caudally increasing IPW trend shown by Caffaro et al., [23].

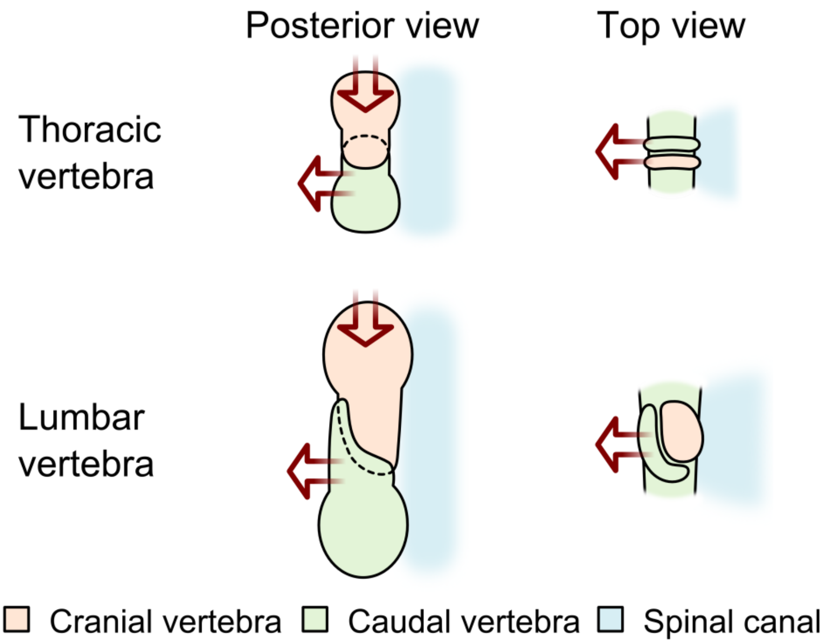

Figure 4-3: Schematic of the facet joint biomechanics at impact in the thoracic and lumbar spine.

Measures of SCO partially agree with the clinical literature (Table 4-2). In this study, the highest SCO was measured at the thoracolumbar junction; whereas *in vivo* there is an overall increasing trend in the caudal direction. However, in agreement with clinical results, SCO measured in the lumbar region was higher than that in the thoracic one. The differences with the clinical literature are likely to be due to the fact that any *in vitro* simulation is always to be taken as a gross approximation of the *in vivo* setting, which is almost impossible to accurately replicate. However, it is worth noting that SCO at the thoracolumbar junction was extremely similar to what measured clinically, hence showing that a good approximation was achieved for this case. In addition, the thoracolumbar junction represents the most relevant case study as it is the most prevalent site of burst fractures (1.2.5).

Table 4-2: Comparison between this study and clinical literature for SCO and IPW.

Spinal region	SCO (%)		IPW (%)	
	This study†	Mumford et al. [31]	This study‡	Caffaro et al. [23]
Thoracic	7.6	29.7 ± 7.8	4.7	25.4 ± 20.0
	(-0.7 – 41.2)	–	(1.9 – 8.1)	–
Thoracolumbar	35.3	38.1 ± 12.4	6.4	35.8 ± 19.1
	(18.0 – 51.5)	–	(-1.1 – 8.1)	–
Lumbar	15.5	40.8 ± 14.9	0.7	46.4 ± 20.3
	(-9.0 – 30.7)	–	(0.1 – 5.5)	–

† median and range of SCO_{CT}; ‡ median and range of $IPW_{CT.}$

SCO_{CT} was associated with impact energy (Figure 3-13) and its median value was 175 % higher in the HE group than in the LE one (Figure 3-11). The susceptibility of SCO to impact energy (hence strain rate) suggests that there was a viscoelastic component involved in the failure of the posterior wall. This agrees with previous results from the literature. Both Stemper et al. [188] and Ochia et al. [187] have measured significantly higher ultimate force and stiffness at higher strain rates, hence proving the viscoelastic behaviour of the whole vertebral body. In addition, the damage induced at high strain rate to the trabecular structure may be aggravated by the significant increase in intra-vertebral pressure caused by the restricted flow of the marrow [185].

IPW was not influenced by impact energy, and no difference was found between groups. Although not significant, IPW_{max} from HE group appeared more scattered than that from LE group (Figure 3-8). Such variability may be because higher impact energy emphasised the dynamics of the loading conditions. Given the overall independence from strain rate and the higher fraction of cortical bone, the behaviour of the pedicles may be grossly approximated as linear elastic, as opposed to the vertebral body. In line with the considerations made above, IPW appeared to be mainly driven by the geometrical interaction between the articular surfaces of the facets alongside mechanical properties of the bone.

Results from this study added further insight to the literature about the mechanics of the fracture. IPW may be the initiator of the fracture, driven by the wedging effect of the cranially adjacent facets [267]. In addition, comminution of the vertebral body originates by the axial compression at the endplate, which results in the burst and comminution of the vertebral body [187]. Both, Mumford et al. [31], and Caffaro et al. [23] have found a moderate correlation *in vivo* between SCO and IPW. However, in this study no correlation was seen between both IPW_{max} and IPW_{res}, and SCO_{CT}. Although it was not possible to provide a detailed association between SCO and IPW; the biomechanics of the two phenomena are definitively linked. In addition to that suggested by engineering studies, anatomical factors also indicate that the root of the pedicles may be a critical area for the retropulsion of the fragment within the canal. There is indeed an abrupt thinning of the cortical shell at the internal root of the pedicle, which is not adequately reinforced by trabecular bone, and this exactly the area where the fragment typically breaks off [268]. In addition, the cortical shell of the vertebral body has been considered to have inferior properties compared to the thicker cortical bone which the pedicles are made of [246]. Therefore, the root of the pedicles may not be able to effectively withstand impact loads, since it is a critical area of transition in structural properties. This supposition agrees with what suggested by *in vitro* [189, 191], and numerical studies [269], where loading at the facet joints has appeared to result in high stress/strain concentration at the root of the pedicles. High-speed filming of the sample has been used in other studies on long bones, to assess the evolution of the fracture over time [270]. Performing additional filming may have provided valuable insight to this study too However, such method could not be implemented because the actual spinal surface could not be imaged, as samples were kept wrapped in moist tissues (to ensure hydration of the soft tissue and contain any ejection of biological material).

Compared to CT scanning, plain radiography is substantially more cost-effective, whilst requiring lower radiation dosage to the patient. On the other hand, it cannot provide the same 3D accuracy, and clinical studies have shown that SCO cannot be accurately measured from plain radiographs as much as IPW [104, 271]. This study also showed that SCO_{clin} had a ±20 % agreement with that measured by SCO_{CT}. Hence, even clinical CT-based measures need improvement, because they are based on a simplistic estimation of the pre-fracture conditions. IPW can be reliably measured on plain radiographies because of the distinctive shape of the pedicles (from a posterior view) [104, 271], without measures being significantly affected if performed with the patient prone or supine [265]. Martijn et al. [272] has shown that significant IPW detected on plain radiographs is always associated with LF, pedicle fracture or injury to the vertebral body. Thus, IPW is an indicator of fracture severity as well as risk of neurological injury (1.2.5.2), and it could be used as an initial and cost-effective decisional tool for trauma. In fact, plain radiography can be more conveniently performed at presentation of the patient; before deciding to undertake a CT scan. In addition, IPW may directly relate to facet joint instability induced by the trauma. Loss of the mechanical function of the ligamentous capsule can happen without signs of gross rupture, since the actual tissue injury has been identified to happen at approximatively 50 % of the displacement required to induce its mechanical failure [273]. Therefore, the dynamics of IPW may also provide indications to retrospectively investigate facet failure. IPW_{max} was overall beyond that functional failure limit, since there were signs of gross rupture of the facet capsule in several samples. Further research may help identifying a tolerance limit for the functional integrity of the facet capsule. Results from this study may help extrapolate some data about the fracture onset since a moderate correlation was found between IPW_{max} and IPW_{res} (r_s=0.58, p=0.088), and that could be used to develop applications for the aforementioned issues.

Finally, understanding the biomechanics of IPW is paramount also for the outcome of the treatment. In fact, in the case series by Mumford et al. [31], the authors have supposed that the severity of IPW negatively affected the outcome of spinal canal remodelling.

4.2.2 Considerations on dural tears and laminar fractures

The occurrence of LFs in this study was in agreement with what seen clinically. Mumford et al. [31] have reported an incidence of 59 % in patients with limited or no neurological deficit, whilst in this study LFs were detected on 58 % of the specimen.

Hashimoto et al. [122] have suggested that injuries of the posterior elements may be indicative of more complex and severe loading conditions at the time of the fracture, which may cause more acute neurological injuries. Results from this study agree with this assumption, since five out of seven LFs were detected on specimens which underwent higher impact energy (HE group).

Results were overall in agreement with what found clinically, where LFs are associated with higher SCO and IPW (Table 4-3). However, as discussed above, *in vitro* results were found to be lower than what shown *in vivo*. SCO_{CT} was significantly higher in presence of LF, whilst no statistical difference was found for IPW_{CT}, despite a qualitative trend could be identified (Figure 3-10).

Table 4-3: Comparison between results from this study and clinical literature for SCO and IPW in presence of LF.

Laminar fracture	SCO (%)		IPW (%)	
	This study†	Tisot et al. [127]	This study‡	Caffaro et al. [23]
Present	34.1 (9.7 – 51.5)	47 ± 18 –	4.7 (-1.1 – 8.1)	25 ± 16 –
Absent	5.4 (-9.0 – 30.7)	28 ± 14 –	1.9 (0.1 – 8.1)	13 ± 8 –

† median and range of SCO_{CT}; ‡ median and range of $IPW_{CT.}$

Dural tears and neurological element entrapment have been found to be associated with higher IPW (1.2.5.2) and wider LFs (1.2.5.3). Following their clinical retrospective study, Cammisa et al. [123] have theorised that the laceration of the dura mater is linked to the dynamics of IPW, posterior wall deformation and LF; this study provided further insight to support their conjectures. Figure 4-2 and Figure 4-4 depict the evolution of the fracture onset over time, highlighting the most significant phases which may lead to the injury. This study confirmed that, at the impact, the pedicles splay to a maximum critical value (IPW_{max}). Therefore, excessive IPW may be the driving cause of LF; since the lamina (mainly made of cortical bone) may not be compliant enough to keep up with the splaying forces at the pedicles. In fact, IPW_{max} was 106 % higher in presence of an LF than in its absence. Although not statistically significant, such trend can be clearly seen in Figure 3-10. Further increase of IPW would then increase the width of the LF too. The concurrent posterior wall deformation would then force the spinal cord posteriorly and part of it may protrude through the edges of the LF. As mentioned above, in accordance with Vaccaro et al. [20], this may also be the phase of the fracture where the canal assumes the most critical shape for the origination of neurological injury. The risk of laceration is not limited to the fact that the dura mater is confined within the sharp edges of the fracture. In fact, when the pedicles are recoiled, the edges of the fracture may narrow and bring the LF width to its resting value (measured at presentation). Therefore, the dynamic widening and narrowing of the LF would sever the dura mater, with consequent leakage of cerebrospinal fluid.

It may be interesting to note that only in one sample (L3-L4-L5 segment) fragment retropulsion was not present in conjunction with LF (Table 3-2). Although IPW may be the driving factor for both events, failure of the posterior wall appeared to be linked also to the viscoelastic properties of the vertebral body (4.2.1). In addition, the lamina of L4 is generally thicker than at more cranial levels. Therefore, whilst the viscoelastic events were sufficient to fracture the posterior wall, the IPW alone did not exceed the critical value which resulted in the breakage of the cortex of the lamina.

Dural tears can be reliably diagnosed with MRI or myelography, which have the disadvantage of being time-consuming and expensive. However, as suggested by Park et al. [22], prediction through IPW from plain radiographs could provide an effective alternative, and results from this study may help developing such decisional tools.

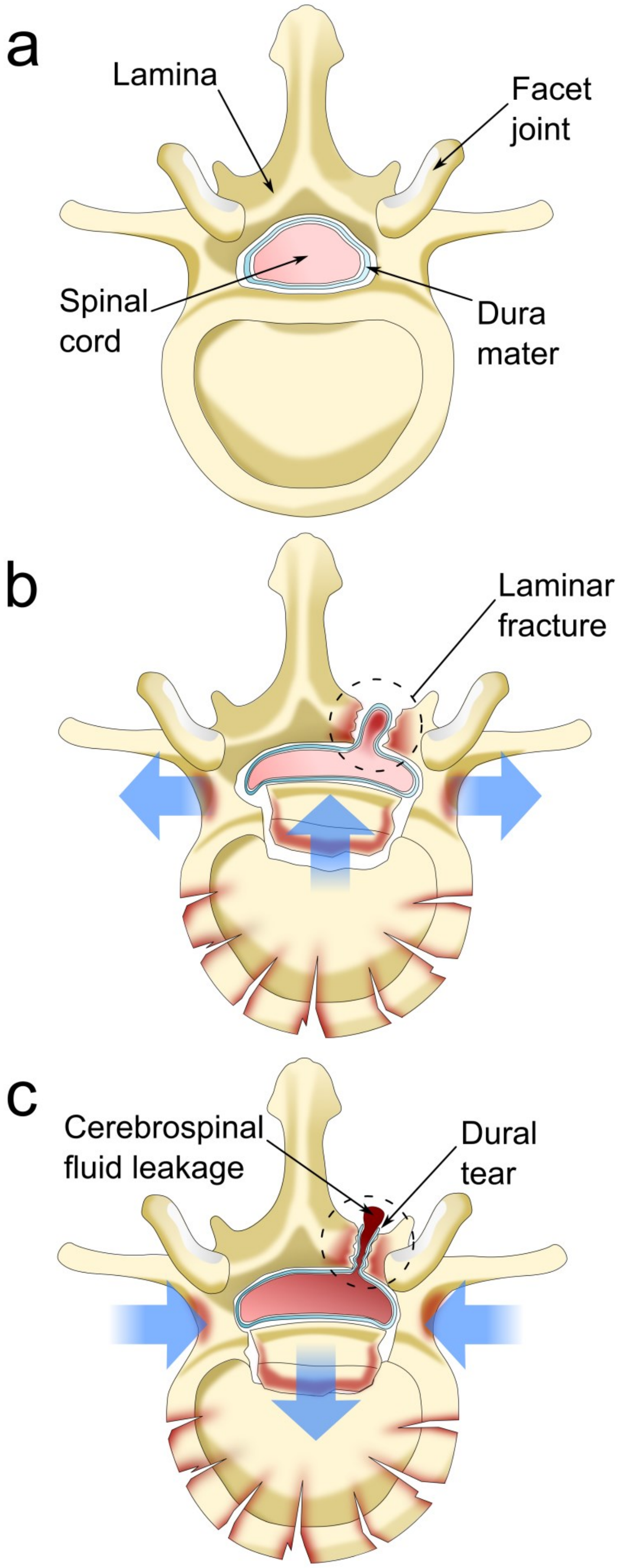

Figure 4-4: Evolution of laminar fracture throughout the fracture onset. a: Top view of the intact vertebra. b: At the impact, the shape of the vertebral foramen changes and the spinal cord is pushed through the edges of the laminar fracture. c: When the pedicles and fragment are recoiled, the dura mater lacerates within the laminar fracture with consequent leakage of cerebrospinal fluid.

4.2.3 Functional anatomy of the vertebral body and fracture

The methods developed in this study enabled a 3D assessment of endplate curvature as well as vertebral body deformity and height. The Cobb angle was measured from the endplates of the fractured vertebra, which has been shown to be less accurate than that measured on the adjacent vertebrae [103, 106]. However, the latter measurement was not taken since the adjacent vertebrae were free to move and their position would not have been representative of the actual spinal alignment. A similar error may have affected the post-fracture measurements, since the vertebral body was comminuted and motion of the adjacent vertebrae may have erroneously distracted the fracture. Qualitative assessment of the data suggested that the measures of curvature and height were more robust and less affected by the distraction of the fracture than the kyphotic angle. Jones et al. [196] have quantified *in vitro* the kyphosis of T10 – L4 segments pre- and post-fracture, which was -6.9° and 7.5°; whilst in this study was 0.4° and 3.4°, respectively. However, they took the measurements based on the inclination of the adjacent vertebrae, whilst the sample underwent a 600 N compressive preload, and induced the fracture with 15° flexion. The differences in the experimental conditions are likely to be the cause of disagreement in the results. Measures of height and kyphotic angle at the intact state were in line with the trends shown in the literature (Table 4-4), although results from this study were always greater than those provided by Panjabi et al. [58, 59]. In this case, disagreement is to be imputed to the different approaches used for the measurement. In this study, the height was taken as the median distance between the markers describing the endplate surface, whilst Panjabi et al. substantially measured the distance between the endplate posterior rims (i.e. the highest region of the vertebral body). On the other hand, the endplate inclination was calculated using the same principle (i.e. fitting a plane through a cloud of markers); although Panjabi et al. included the posterior aspects of the endplate, whilst in this study they were excluded. As advised by Kenyan et al. [103], including the posterior region results in an overestimation of spinal kyphosis, as confirmed by the presented data. This is particularly evident in L4, where the method developed was able to show the lordosis of the area (negative angle), whilst the method developed by Panjabi et al. could not. The curvature radius of the cranial endplates was higher than the caudal ones at all the levels, in agreement with Lakshmanan et al. [274], which have reported that cranial endplates are overall flatter than caudal.

Table 4-4: Anatomical properties by level measured in this study and the literature.

Level	Vertebral body height (mm)		Kyphotic angle (°)	
	This study†	Panjabi et al. [58, 59]	This study†	Panjabi et al. [58, 59]
T10	22.1 (19.6 – 23.3)	20.2 –	0.5 (-1.6 – 3.0)	3.8 –
L1	26.8 (24.1 – 28.2)	23.8 ± 1.0 –	3.4 (2.8 – 6.8)	6.7 –
L4	27.3 (25.4 – 27.6)	24.1 ± 1.1 –	-8.1 (-9.8 – -7.8)	7.4 –

† median and range.

The occurrence of a burst fracture induced significant anatomical changes: the vertebral body height decreased by 25 %, whilst the endplate convexity increased by 55 %. In addition, both parameters were significantly correlated with impact energy (Figure 3-27); in agreement with Wang et al. [275], who have shown an increase of the load-sharing score with impact energy. In addition, vertebral body compression was correlated with SCO, and it is plausible to assume that higher compression resulted in higher displacement of the bony fragments, hence higher SCO. Higher energy seemed to induce less variation in the kyphotic angle, probably because more compression of the vertebral body resulted in more parallel endplates.

The measurement of endplate curvature was considered the most clinically relevant, since it has been shown that failure of the endplate is one of the determinant of post-traumatic disc degeneration, caused by a disruption in the nutrient pathway to the disc [65, 120, 177]. Therefore, a significant increase in convexity meant higher endplate depression and thus damage. However, the variation in endplate curvature was not related to the correspondent fracture type, which meant that conventional fracture grading (i.e. Magerl et al. [18]) was not able to detect such a relevant aspect of the injury. The correlation between impact energy and increase in endplate convexity may be related to the viscoelasticity of the nucleus pulposus. Due to the high water content, the nucleus is generally approximated as a homogenous incompressible fluid [276]. Under this assumption, the higher the strain rate, the more the nucleus behaves like a solid. In addition, the region of the endplate underlying the nucleus is mechanically weaker [247], and has shown higher deflection than the annulus region at failure under quasi-static loading [277]. Hence, higher impact energy would put the nucleus in the condition to cause more damage, as seen in this study. However, it is yet not clear whether the burst of the vertebral body is driven by the failure of the endplate, due to intrusion of the nucleus pulposus. In fact, at high strain rate the endplate appears to be as strong as the vertebral body [187]. The susceptibility of endplate damage to impact energy may be also related to a viscoelastic embrittlement of the endplate as well as a concurrent collapse of the underlying trabecular structure caused by bone marrow flow. Such considerations are also in agreement and extend what was discussed above about the dynamics of the vertebral body failure.

The cranial endplates were subjected to greater damage than the caudal ones since their convexity increased more than at the opposite side (Figure 3-28). This study added further insight to what reported in the literature. Macro-indentation carried out by Grant et al. [247] has shown that caudal endplates are about 40 % stronger than the cranial ones, whilst other works have found that cranial endplates are more likely to fail because they are thinner, with lower BMD and supported by poorer trabecular structure [278, 279]. Hence, the cranial region of the vertebral body is less resilient and more vulnerable to impact loading. In combination with IPW, this may be an additional determinant for fragment retropulsion. In fact, the superior portion of the fragment always included part of the posterior region of the cranial endplate. However, it is most likely that several complex phenomena are involved, which can be further influenced by a multitude of parameters (e.g. disc/bone quality, loading distribution, anatomy).

4.3 Biomechanics of spinal fixation

This section reviews the experiments carried out to investigate the biomechanics of surgical intervention to treat burst fractures. Therefore, fatigue testing represented the natural conclusion of the fracture pathway, as it simulates the early post-operative period. As previously discussed, lack of anterior support is deemed to be responsible for the inconsistent outcomes of SSPI (1.3.1) [33, 150]. Therefore, the ultimate aim of this phase of the study was to provide further insight into the performance of SSPI – KP and better understand how it can actually aid in improving SSPI.

4.3.1 Surgical treatment

The 12 samples that previously underwent fracture creation were divided into two groups, and treated with SSPI and SSPI – KP, respectively. Exploiting the same specimens allowed a more relevant simulation since the same vertebra underwent fracture and then treatment, hence enabling the use of paired statistics. In addition, no additional samples had to be harvested, which was also ethically correct given the restricted availability of human cadaveric tissue.

Firstly, all the samples underwent SSPI. The size of each pedicle screw was decided based on assessment from CT scans. The candidate believes that all the screws were overall 5 mm shorter than their ideal size. However, it was considered an acceptable error, since about 60 % of the pull-out strength and 80 % of the longitudinal stiffness depends on the screw purchase within the pedicle and an 80 % penetration within the vertebra has been supposed to be sufficient [134]. In addition, all pilot holes were tapped using the tool one size below the actual screw size, as undertapping by 1 mm has been advised [134]. The trajectory of the screws was mainly dictated by the pedicle anatomy to avoid breaching within the vertebral foramen, which was overall in line with guideline recommendations of a 30° trajectory convergence [134].

The main limitation of the experimental simulation was that the nut of the pedicle screws did not lock in place (as expected) when the rods were fastened. Since relative motion between screws was not restrained, the samples were allowed a greater extent of AP displacement (i.e. shear) and axial rotation. The former was more prominent, because of the combination of axial compression and unconstrained translation allowed by the linear bearings. On the other hand, the lack of construct rigidity may also be considered representative of a worst case scenario. In fact, the loading conditions were more similar to that of an unstable construct, hence emphasising the load bearing requirements of the fractured vertebra. In fact, the aim of the experiment was not to investigate the mechanical properties of the fixation device, but the biomechanics of the treated construct. Therefore, the issue encountered with polyaxial screws was not considered impairing for the relevance of the study.

Following SSPI, the neural arch of the central vertebra was excised in all the specimens by cutting through the pedicles. Such procedure has been shown not to change the surface strain distribution on the vertebral body (except for the root of the pedicles) [189]. However, Deviren et al. [280] performed LSPI with resection of the neural arch (used as treatment for flat-back deformity) and found a decrease in spinal stability and fatigue life of the fixators. Lubelski et al. [281] have shown that laminectomy followed by unilateral facetectomy does not significantly affect thoracic spine stability, when combined with SSPI. However, the authors kept the rib cage intact. In this study, there was no ribcage and the excision of the neural arch could be considered equivalent as a bilateral facetectomy. Therefore, it is plausible to assume that the procedure induced an additional degree of instability, hence making the loading conditions more demanding. In fact, removal of posterior elements has been shown to significantly increase the moments acting on the fixators by 30 % [213]. The neural arch was excised for two main reasons. Firstly, it allowed the creation of an adequate access window for the LVDT tip, to measure the dynamic displacement of the posterior wall. This measure was considered of particular interest since it has been carried out only in quasi-static loading conditions [200, 282], but never throughout the whole fatigue test. Secondly, to remove any load transfer at the facet joints and force load sharing only between the fixators and the vertebral body. In addition, some degree of pedicle fracture and disruption of the facet capsules was detected in all the samples. Therefore, excision of the neural arch increased repeatability and control of the loading conditions, since each pedicle had different residual load bearing capability (i.e. erratic load transfer paths).

In the SSPI – KP group, fixation was performed before KP to make sure the segment was stable between the deflation of IBT and injection of the cement, thus reducing the risk of loss of achieved reduction or migration of bony fragments. However, there seems to be no difference in the clinical outcome whether SSPI or KP is performed first [38]. Nonetheless, Verlaan et al. [39] have advised to perform ligamentotaxis first to obtain an initial realignment of the cortical fragments, hence facilitating IBT inflation and segregation of the cement bolus during the injection. In fact, cement leakage seems to be less likely when KP is performed subsequently to the implant of SSPI [173]. The maximum inflation pressure of the IBT ranged 51 – 160 psi (excluding the case when the IBT failed at 350 psi), which is in line with both *in vivo* (range 150 – 200 psi [182]) and *in vitro* (range 50 – 200 psi [199]) measurements. The final inflation volume of the IBT in this study ranged 8.0 – 11.5 ml, similarly to the *in vitro* work of Verlaan et al. [200], who have reached 7.2 ± 1.3 ml and 13.6 ± 2.6 ml at the thoracic and lumbar level, respectively. In this study the inflation volume was set at 20 % of VB volume to ensure consistency of procedure, despite the degree of reduction achieved. Higher inflation volumes could not be reached, because limited by the size of the IBT available.

In this study, the median cement volume was 8.6 ml,in agreement with pain relief guidelines (1.3.2) and previous clinical studies (Table 4-5). However, cement leakage was detected in 67 % of cases, whilst clinical data report leakage in 7 – 9 % of cases of KP (KP has a significantly lower incidence of leakage than VP) [38, 283, 284]. The higher occurrence of leakage found in this study was probably caused by the lack of para-spinal tissue, whose pressure would have probably helped containing any extravasation from the vertebral body. However, it is worth noting that cement never leaked within the spinal canal, therefore the primary safety requirement for augmentation was satisfied [285].

It is interesting to note that many clinical studies do not routinely follow general guidelines. Surgical intervention has been advised for vertebral compression and kyphosis higher than 50 % and 20°, respectively (1.3). However, SSPI and SSPI – KP have been usually undertaken at lower level of deformity (Table 4-5). Such lack of consensus within the clinical community strengthens the need for biomechanical investigations, to aid clinicians to better understand how the treatments perform and how to get the best out of them.

4.3.1.1 Restoration of vertebral anatomy

Surgical treatments aim to provide mechanical stability and correction of the deformity induced by the fracture. Insufficient anatomical restoration influences the load transmission and biomechanics of the spine [286], hence triggering a chain of events that can lead to implant failure (1.3.1). In addition, restoration of the endplate biomechanics is paramount for both the biological and mechanical outcome. The endplate is responsible for load transfer through the vertebral body [267], and recovering its integrity, in combination with that of the cartilaginous layer, has been suggested to prevent post-traumatic disc degeneration [65, 177].

Vertebral body height was increased by 12 % with respect to post-fracture conditions after SSPI, whilst SSPI – KP provided a 14 % increase. However, the slightly higher restoration achieved through additional KP was found not to be significant. Therefore, alignment and fastening of the rods in place provided the majority of fracture reduction. However, height could not be fully recovered and samples (results pooled together) exhibited a residual 15 % compression. It must be noted that such residual compression is in agreement with what seen clinically (Table 4-5). The marginally better results achieved *in vivo* are likely to be due to ligamentotaxis performed by the surgeon, which was not carried out in this study, because it would have induced an additional degree of user-dependent variability. In addition, clinical ligamentotaxis is surely more effective than what can be done *in vitro*, since it can benefit from the contribution of the whole spine and muscles, with the reduction forces acting on the whole torso. All these components are absent *in vitro*, especially when three-adjacent-vertebrae segments are treated.

Table 4-5: Comparison between this study and clinical case series. Compression is reported with respect to the intact state.

	VB compression (%)			Kyphosis (°)			CV (ml)
	Pre	Post	FU	Pre	Post	FU	
This study	25	15	15	0.4	-3	-5	8.6†
Bironneau et al. [179]	31	10	14	15	5	6	7.6‡
Fluentes et al. [181]	35	11	14	14	3	5	6.4‡
Korovessis et al. [182]	34	8	–	12	-2	–	3.0-6.0†
Verlaan et al. [39]	34	12	–	11	-2	–	–†

VB compression: percent loss of VB height with respect to intact conditions; Pre: pre-surgery; Post: post-surgery; FU: follow-up (compared to post-fatigue testing in this study); CV: cement volume; †: CaP cement; ‡: results from PMMA and CaP cement pooled together.

Verlaan et al. [176] measured *in vitro* the height of the vertebral body at consecutive stages of SSPI – KP obtaining similar trends to this study in absolute terms (Table 4-6). However, it must be noted that the authors carried out measurements on the same specimens, whilst in this study two separate groups were compared, and this is probably why it was not possible to find a significant difference in the post-treatment height. In terms of percent variations, Verlaan et al. have found that fracture reduction achieved a residual 11 % compression, which was brought down to 9 % after KP, whilst in this study it was 19 % and 13 %, respectively for the two groups. Therefore, in both cases, additional KP provided a marginal improvement, although it may seem that Verlaan et al. have achieved greater height recovery. The disagreement in the results is probably an artifact of the measurement method, since the authors of [176] measured vertebral height as the distance between the two most depressed points on the endplates from a sagittal view. Conversely, the method developed in this study was based on the median of the minimum distance between two sets of markers describing the whole endplate surface. Such approach was considered more efficient because it accounted for a complex set of multiple distances taken from two opposite surfaces, instead of just two extreme points.

Table 4-6: Comparison between *in vitro* measures of vertebral body height (mm) at consecutive stages of SSPI – KP.

		Experimental stages			
		Intact	Fracture	SSPI	SSPI – KP
This study	Median	25.7	18.5	20.8	22.6
	p-value	–	<0.001†	0.031	0.87‡
Verlaan et al. [176]	Mean	19.5	14.6	17.3	17.8
	p-value	–	<0.001	<0.05	<0.05

† Data pooled together; ‡ Comparison between groups.

3D analysis with respect to post-fracture conditions showed that SSPI – KP was able to significantly restore the endplate curvature better than SSPI alone. In fact, SSPI resulted in an increase in convexity by 8 %, hence worsening the endplate shape, whilst a 22 % improvement was seen in SSPI – KP (Table 3-10). In terms of percent variation between post-treatment and intact stage, the contribution of KP over SSPI could not be detected statistically, because the morphological changes caused by the fracture overshadowed those of the treatment.

Results from this study are partially in disagreement with the work of Verlaan et al. [176]. Although the authors have shown that KP improves endplate reduction, they have found that the majority of endplate depression was recovered during ligamentotaxis, whilst in this study SSPI actually worsened the curvature of the endplates. In Verlaan et al. [176], inflation of IBT recovered endplate depression further; however, restoration was almost completely lost at deflation and only partially recovered at the cement injection. However, it must be noted that Verlaan et al. interpreted endplate reduction from 2D measures of height and area of the vertebral and intervertebral space. Conversely, in this study the endplate shape was quantified using a 3D approach, which returned the radius of curvature of each endplate. Such methodology was considered superior to that of Verlaan et al., because it allowed a more pragmatic and user-independent investigation.

Oner et al. [287], as well as Tzermiadianos et al. [166], have postulated that ligamentotaxis only provides reduction of the periphery of the endplate, by tensioning the annulus fibrosus, without acting on the depression of the region underlying the nucleus. This concept agrees with the results from this study, as lifting only the outer boundary of the endplate would induce an increase in its convexity. The same authors then advocated that additional KP would be able to lift the central region of the endplate providing the additional reduction required, hence flattening the fractured endplate, as seen in this study (3.4).

Although the endplate morphology was not restored to its original conditions, the significant improvement provided by KP may be sufficient to prevent/recover herniation of the nucleus within the vertebral body, which has been addressed as a precursor of recurrent kyphosis [118]. Conversely, SSPI alone may increase the risk of nucleus herniation because of the resulting increase in endplate convexity, hence pushing the nucleus further towards the core of the vertebral body.

Achieving consistent reduction is challenging and outcomes difficult to predict, since it appeared that height restoration was not associated with that of endplate morphology. Hence, although ligamentotaxis may provide substantial height restoration, KP proved to be necessary to safely reduce the endplates. As advocated in the literature, positioning of the IBT under the most depressed region of the endplate is paramount for successful reduction [199]. Therefore, more consistent procedures and instruments, implementing also rigorous imaging guidance, may be able to aid KP achieve more substantial reduction, aiming at complete height and endplate shape restoration.

4.3.2 Fatigue performance of surgical treatment

Following surgical intervention, the samples underwent fatigue loading to simulate post-operative conditions. As mentioned above, the ultimate aim of the experimental protocol was not to test the fixators to failure. On the contrary, the experiment was designed to simulate *in vivo* conditions, where the spine and implants undergo physiological loading. Hence, the objective was to investigate the biomechanics of the treated spine as a whole construct and better understand the effects of the surgical intervention.

The long-term outcome of the treatment is strictly linked to the healing and bone remodelling process, which starts within weeks of the operation. SCO has been shown to start decreasing significantly after 3 – 4 weeks, whilst fracture usually achieves bone union in 6 – 8 months [182]. Due to the reduced invasiveness of the procedure, the time from surgery to walking is approximatively 13 hours, hence encouraging mobilisation and early recovery of the patient [173]. However, most of the adjacent fractures occur within 2 months following KP [288], and case series of SSPI – KP (with PMMA cement) have shown a ~3° loss of correction occurring within the first three months, without any sign of subsequent recovery [289]. Therefore, the early weeks after surgery are critical for the long-term outcome of the treatment, which is indeed the condition replicated in this study. The lack of any simulation of bone union/remodelling was not considered a substantial limitation, since its contribution to load bearing *in vivo* was supposed to become effective only at a later stage. Bone remodelling around the CaP cement bolus has been shown to start within the first post-operative year, and radiolucent areas (presence of fibrous tissue is associated with remodelling activity) have been found at 17 months [160]. Therefore, it was plausible to assume that within the first 2 – 3 post-operative months, CaP cement does not effectively influence bone remodelling and its contribution is solely that of its mechanical properties.

All the samples reached run-out at 70000 cycles; based on previous works such number of cycles was considered approximatively representative of the first two post-operative months. In fact, Wilke et al. [203] applied 100000 cycles of axial compression (amplitude 100 – 600 N) to simulate about six weeks of walking in a young patient (equivalent to about three months in an elderly one) and concluded that CaP KP can suffice vertebral strength over that time. Alternatively, Deviren et al. [280] imposed 35000 bending cycles to replicate three post-operative months. However, in their study each cycle comprised -6 – 8 Nm flexion/extension combined with a 400 N compression, which resulted in an substantial bending of the fixator rods.

In this study, the loading profile was defined as a cyclic axial compression where the mean value and amplitude of the sine waveform were tuned for each sample as a function of the body weight of the donor and spinal level. The rationale was chosen to normalise for inter-specimen variation and, overall, the maximum applied load ranged 177 – 410 N, in line with what measured *in vivo* through telemeterized implants [79]. The design of the loading profile was obviously a simplistic representation of the actual loads which the spine undergoes daily. However, imposing only cyclic axial compression allowed more repeatable and controlled experimental conditions, enabling the investigation of a complex biomechanical system through a cause-effect approach and decoupling each contribution.

Samples were kept wrapped in wet tissue throughout the experiment, since moisture has been shown to minimise the changes in ROM due to exposure of the tissue [222]. However, the candidate is aware that results may have been biased by lack of further hydration (particularly to the disc). Although Oakland et al. [204] imposed axial cyclic loading for about 32 hours in similar conditions, in this study the total test time was limited to about 19 hours to minimise the effects of tissue degradation. Alternatively, the testing assembly could have been integrated with a temperature regulated bath, hence keeping the sample submerged throughout the experiment, as in Huber et al. [224]. Such design was not implemented because it would have precluded measuring the displacement of the anterior and posterior wall.

Extraction torque *In vivo* has been reported to be 0.029 ± 0.036 Nm [137], but can vary significantly (range 0.005 – 6 Nm [138]). Therefore, a threshold limit of 0.4 Nm was applied for consistency, based on previous published works [138, 244], and 17 % of the implanted screws resulted loose. This is higher than what has been reported in the clinical literature, where screw loosening happens in about 2.3 % of cases whilst breakage has been reported in 6.7 % [290]. However, none of the screws broke in this study.

4.3.2.1 Structural properties of the treated spine

The developed software application enabled calculating relevant mechanical parameters for each cycle throughout the whole test, hence aiding understanding of how the structural properties of the construct evolved over time.

Results from the literature report that the axial stiffness of a spinal segment ranges about 378 – 649 N/mm in intact conditions [165, 191], and 502 – 557 N/mm following PMMA VP [165, 167], whilst in this study the median initial stiffness was 379 N/mm in the SSPI group and 497 N/mm in SSPI – KP (Figure 3-21). Stiffness calculated at the beginning of the test was representative of post-treatment conditions and showed that both groups exhibited values close to those reported for both intact and VP treated conditions. Although not significantly different, the stiffness in SSPI – KP was 31 % higher than SSPI, which is in agreement with the kinematic study of Mermelstein et al. [216], who showed that KP significantly increased the bending stiffness of the SSPI construct by 37 %. Likewise, Hartensuer et al. [210] have investigated *in vitro* SSPI in combination with PMMA VP and showed that augmentation significantly improved anterior support by restoring bending stiffness to its intact value, although it did not further reduce the ROM when compared to SSPI alone. In this study, axial stiffness was an indicator of stability of the segment, since it was correlated with axial displacement. Stiffer samples exhibited less compression and narrower peak to peak oscillations (tests were performed in load control, hence axial displacement was a dependent output). Axial compression was also correlated to height restoration, meaning that the specimens whose height was increased more with the treatment (with respect to fractured conditions) lost more correction over time. Greater height restoration may have been possible in fractures where the fragments were looser, hence easier to displace. Cyclic loading would then compact the fragment resulting in an increased axial compression (i.e. decrease in stability) over time. However, such association was seen only in the SSPI group, hence suggesting that additional KP helped preventing loss of correction. Cement may have stabilised the fracture by buttressing the fragments and holding them together, hence preventing their progressive compaction and better supporting the anterior column. These conjectures agree with the findings of Mermelstein et al. [216], who have shown that the anterior stabilisation provided by KP reduces the bending moments on the pedicle screws by 59 % with respect to SSPI alone.

Hansson et al. [291] have shown that, in fatigue loading conditions, stiffness of the spine increases over the first cycles until an equilibrium is reached. A sudden drop in stiffness was considered indicative of failure and was imputed to damage of the trabecular structure. Similarly, stiffness of PMMA VP treated segments increased concurrently to loss of segmental height as cyclic loading progressed [204]. However, this behaviour was probably related to the nature of the treatment itself. As damage accumulation in the vertebra increased; the PMMA bolus took on an increasing quota of load, dictating the load bearing and increasing the apparent stiffness of the spinal segment. No drop was detected in the curves from this study (Figure 3-20), however the stiffness decreased steadily over time by 15 % and, although it remained 37 % higher in SSPI – KP than SSPI (calculated at end of test), no statistical difference was found between groups. The observed loss in stiffness may have been caused by several phenomena. In this experiment the trabecular structure was already severely compromised and cumulative load may have aggravated it, preventing from reaching the plateau seen in the literature [291]. In addition, CaP cement has lower mechanical properties than PMMA [157], therefore it may not be able to dominate the behaviour of the whole sample, as it probably happened in the study of Oakland et al., [204].

Compaction of the fracture would typically suggest a progressive increase in stiffness (fragments get closer to each other and tighter), however results suggested otherwise. Cyclic loading have resulted in an increase of the fragment looseness, as shown by the measurements of displacement on the vertebral surface (4.3.2.3); hence decreasing the load bearing capability and stiffness. In addition, axial compression increased over time, probably due to fragment displacement and creep of the segment. Huber et al. [224] have measured over two mm height loss over 20 hours of cyclic loading. However, creep effect in this study was inferior because lower loads were applied, and SSPI provided an elastic structure in parallel to the discs.

Fatigue loading did not induce any significant loss of correction in terms of vertebral body compression, conversely to what has been reported in the clinical literature (Table 4-5). However, as mentioned above, clinical assessments referred to more severe initial conditions, which may have resulted in a higher risk for loss of correction over time. In addition, the follow-up in this study was simulated through 19 hours of axial fatigue loading, whilst *in vivo* loading may be more complex.

Although no difference was found statistically between the two groups, it appeared that SSPI – KP may be able to retain height better than SSPI alone. In fact, a peculiar association was found in SSPI between axial compression and height recovery (Figure 3-32). The more the height increased as a result of the treatment, the more the loss following fatigue loading. Results may thus be indicative of a lack of anterior support in SSPI, since such trend was not seen in SSPI – KP, probably because of the strengthening effect provided by the cement.

Gross assessment of post-fatigue HR-pQCT datasets showed presence of cracks through the CaP cement bolus, especially at the boundary of the fragments; which is an area of high stress concentration as there is no interdigitation between cement and trabecular bone [292]. Likewise, Wilke et al. detected cracks in CaP cement, but not in PMMA, following fatigue loading of KP [203] (Figure 4-5). However, crack propagation can be found in PMMA cement as well, and it is a relevant cause of failure in cemented joint replacements [293]. In addition, Wang et al. [282] identified fissures at the bone-cement interface in PMMA VP, which they addressed as secondary fracture initiators. Therefore, the phenomenon should be investigated more in detail as it may influence stability, adjacent fractures as well as prevention of subsequent fragment migration, as reviewed below (4.3.2.3).

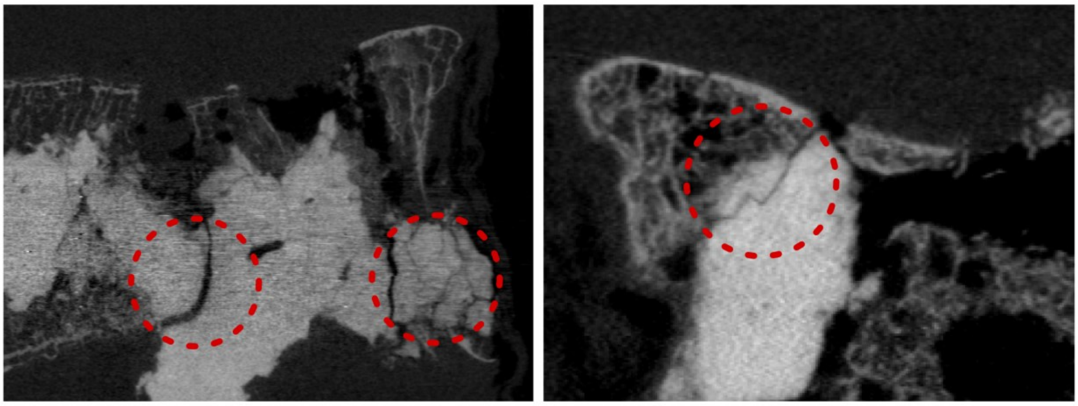

Figure 4-5: Cracks in the cement bolus detected on post-fatigue HR-pQCT scans.

4.3.2.2 Strain on the fixator rods

The strains on the rods were always positive throughout the test, meaning that the implants were always subjected to tensile stresses. Although the controlled loading component was axial compression, the linear bearing did not restrain motions in the other directions, resulting in a cyclic AP translation (usually shearing in anterior direction). Hence, relative translation of the cranial region with respect to the caudal one put the fixators in a constant tensile loading state. Similarly, in the work of Kettler et al. [214], SSPI on cadaveric segments exhibited tensile stresses when undergoing flexion. However, *in vivo* measurements in SSPI patients show otherwise, with compressive loads being measured in all motor tasks [79]. The AP translation seen in this study may be due to the lack of stabilisation provided by spinal muscles, whilst the looseness of the nuts emphasised it. Although this was a strong limitation, because it did not simulate accurately the *in vivo* conditions, it can be seen again as a worst case scenario, putting the spinal segment under more demanding conditions.

Surface strains on the fixators are associated not only with the stresses on the implants [214], but they provided insight on the biomechanics of the whole construct. In particular, the initial peak strains were predictive of the final stiffness and spinal stability, as higher strains were associated with higher axial displacement. Peak strains in SSPI – KP were about 16 % lower than in SSPI and, although not statistically significant, this result further suggests that KP may aid load bearing on the anterior column. No difference was found when comparing the beginning and end of the test, hence showing that the quota of load taken by the implant remained overall constant. Therefore, the decrease in stiffness is to be imputed almost completely to damage accumulation on the tissue, rather than hardware, without a significant posterior shift in load sharing.

No statistical association was found between strain and the measured anatomical parameters (fracture grade, height reduction and endplate curvature). Hence, it is difficult to provide guidelines about the outcome of the treatment based solely on the restoration achieved or clinical fracture grading. On the other hand, it is likely that the extent of the vertebral damage may play a role in load sharing. Comminution of the vertebral body results in a loss of continuity of the trabecular structure; hence reducing its load bearing capability and increasing strain on the implants. Therefore, severely comminuted fractures would be more similar to the ASTM corpectomy model [218], or the ISO model for fatigue testing of spinal implants [217]. However, results from this study showed that, whilst standard tests provide a consistent framework for assessing endurance and mechanical properties of the implant, they fail to replicate and capture the actual biomechanics of the spine. Villa et al. [231] have measured axial strains (at a similar location to this study) in both ASTM and ISO standard models. Upon a 300 N compressive load, the first showed an axial stiffness of 91 N/mm and 1300 με, whilst in the latter stiffness and strain were 465 N/mm and 300 με, respectively. The properties of the spine affected by a traumatic fracture and treated with SSPI are definitely better replicated by the ISO model, which accounts also for the anterior column. In fact, in this study, a median peak compressive load of 280 N resulted in a stiffness and maximum strain of 460 N/mm and 607 με, respectively. Despite the similar stiffness, the cadaveric spinal segments exhibited higher strains, evidence of the higher loads born by the fixators.

Screw loosening did not result in an increase in strain, suggesting that the implants were still functionally safe. However, loosening was detected in the samples which exhibited higher initial axial compression and lower stiffness, both associated with surface strain. Therefore, estimating the strain which the fixators undergo may provide an indirect indication of the risk of failure of the implant. Although not statistically significant, it may be worth noting that it happened in three samples from SSPI and two from SSPI – KP.

Throughout the test, the median maximum strain was about 10 % of the yield strain, for the alloy used ($\varepsilon_{Yield}^{Ti6Al4V}$=6850 με [220]), whilst the maximum strain amongst all the samples was about 1200 με. Such conditions can be considered safe for the survival of the implants and none of the rods showed any visible signs of yield. In fact, implants tested according to ASTM standard (corpectomy model) have survived until run-out (two million cycles) with a maximum compressive load of 250 N. In this conditions, the strain at the most critical point (below the fastening with the screw) has been estimated to be 2600 με [220]. Therefore it is likely that, in this study, even areas of stress concentration never experienced enough fatigue to cause failure.

However, it must be borne in mind that the strain measure in this work mostly provided an indication of the overall load distribution and fatigue, rather than a rigorous quantification of surface stress/strain. In fact, measurements from only one gauge per rod did not allow discriminating between pure tensile strain and bending. This represents a limitation of this measure and each rod should be instrumented with at least a pair of gauges (one on each opposite side of the rod) if the same experimental protocol was to be repeated.

4.3.2.3 Migration of bony fragments

The measurements from the two LVDTs allowed tracking how the fractured vertebral body moved throughout the test. Quasi-static loading has shown to increase the displacement of the posterior fragment. Kifune et al. [24] have shown that a 50 N compression decreases the width of the vertebral foramen by 0.1 mm. In addition, Verlaan et al. [200] have measured displacement on the sagittal plane of the anterior and posterior region at the consecutive stages of SSPI – KP. Ligamentotaxis significantly reduced the displacement of the fragments induced by the fracture, conversely to inflation of the IBT which pushed the posterior fragment externally by about 0.3 and 1.6 mm in the lumbar and thoracic spine, respectively. However, deflation of the IBT and further cement injection brought the posterior fragment back to their post-reduction position (also reducing the inter-specimen variability) of 2.0 ± 0.9 mm and 1.8 ± 0.9 mm in the lumbar and thoracic spine, respectively. Figure 4-6 aims at extrapolating the trend of the anterior and posterior region from fracture to follow-up by combining data from Verlaan et al. [200] and this study. In particular, results were pooled together and the peak displacement (i.e. sum of the mean value and amplitude of the displacement signal) was added to the offset value measured in the literature at completion of cement injection. Therefore, further insight could be provided by extending the work of Verlaan et al. [200] by simulating the initial post-surgery time (beginning of the test) up to the early follow-up (run-out: 70000 cycles). The posterior region significantly increased its displacement within the vertebral foramen over time.

Conversely, the peak displacement of the anterior fragments decreased throughout time; meaning that compaction of the fracture may have stabilised the anterior region. In addition, results agreed with the work of Wang et al. [282], where cyclic loading in osteoporotic samples induced a progressing decrease of the area of the vertebral foramen (measured on the sagittal plane) both at the treated (PMMA VP) and adjacent level.

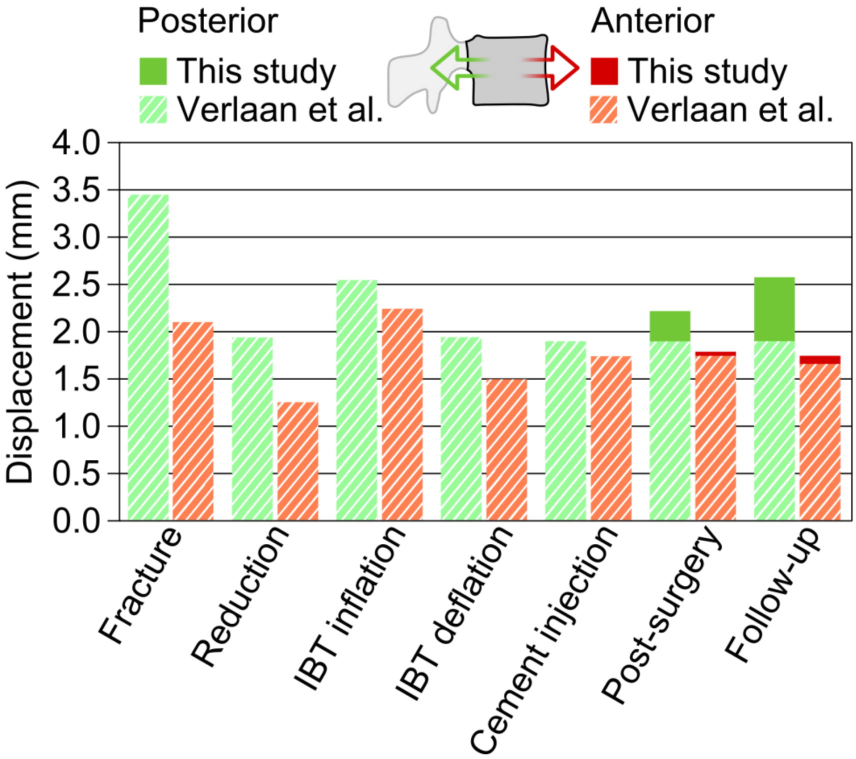

Figure 4-6: Displacement of the anterior and posterior region of the vertebral body throughout the fracture pathway. Results from this study were superimposed to those ofVerlaan et al. [200] obtained at the post-surgery stage.

The displacement of the posterior wall was considered of great interest because relevant for the safety of the spinal cord [24]. Excessive migration of the posterior wall may cause a secondary neurological injury and prevent healing through progressive increase of SCO or strains on the dura mater. In fact, the cauda equina has appeared to be more sensitive to continuous compression rather than impact loading [15]. In Figure 4-6, results were pooled together for simplicity, thus it was not possible to appreciate differences between groups. Statistical analysis of the transducer signals showed a progressive increasing migration of the posterior region in the SSPI group that was not detected in the SSPI – KP. In addition, the final position of the posterior wall in the SSPI was 64 % higher than in SSPI – KP, whilst SSPI exhibited 37 % higher peak to peak values (Table 3-4, Table 3-5), meaning that in this scenario the neurological structures would undergo a combination of increasing constant compression and higher intermittent loads. Therefore, KP showed to be able to effectively reduce both dynamic motion and migration of the bony fragments, probably because of the cohesive effect of the cement. In addition, results suggested an association between endplate curvature restoration and reduced posterior migration (Table 3-11), hence supporting the benefits of KP further. However, it must be noted that better restored endplates were obviously present in less comminuted samples, thus also less prone to significant motion of bony fragments.

In 6 out of 12 twelve samples both the anterior and posterior region migrated posteriorly, which may be indicative of a rigid translation of the vertebral body. However, it is difficult to analyse such event; since the vertebral body lacked continuity and it is not clear how the fragments could influence each other’s motion. However, rigid AP translation of the vertebral body can be as much detrimental as posterior fragment migration alone, because it changes the alignment of the spinal canal, hence increasing stresses on the spinal cord.

The limitations of this *in vitro* simulation made it representative of a worst case scenario for the performance of SSPI/SSPI - KP, and *in vivo* conditions may never get as severe. Firstly, as mentioned above, instability was emphasised by the excision of the neural arch and the looseness of the polyaxial nuts. In addition, clinical remodelling of the canal starts within the first post-operative month [31, 182], which may be able to counteract the migration of the fragment before harming the spinal cord. However, the stress shielding provided by SSPI results in a reduction of the mechanical properties of the spinal ligaments at the treated level, especially PLL [294], which plays a fundamental role in retaining bony fragments [200, 258]. There is probably a fine balance between bone remodelling and spinal stability, which may become a risk factor and should be monitored post-operatively. On the other hand, cement augmentation showed to reduce such risk and the osteoconductivity provided by CaP over PMMA, may help reducing it even further.

4.3.2.4 Fatigue of the endplates

Cement augmentation has raised much debate regarding the risk of adjacent fractures. In fact, some authors have even advocated that adjacent fractures may outweigh the benefits of cement augmentation itself [170]. Although the treatment has shown to partially restore the stress profiles within the intervertebral disc [295], it is still not clear how the presence of the cement bolus may affect the load transfer over time. The main concern is that cement has a higher stiffness than trabecular structure, hence becoming a stress concentrator, which may have a detrimental effect on the load transfer to the adjacent vertebra. Kayanja et al. [165] have concluded that overstrengthening the vertebra causes an increased deformation at the adjacent endplates and increases surface strain on that vertebral body. However, in this study, the instability of burst fractures, together with the use CaP cement (lower stiffness than PMMA), may have made the construct less sensitive to the overstrengthening effect of cement augmentation. In fact, stiffness calculated from cyclic loading was similar to intact values from the literature, whilst KP only provided a marginal increase (4.3.2.1).

Damage to the endplates has been shown to alter disc loading by reducing pressure within the nucleus, and shifting stresses towards the annulus [296]. In addition, Tzermiadianos et al. [166] have found that cement augmentation caused a 94 % increase in the surface strain on the vertebra adjacent to the fractured endplate, whilst no significant increase was found at the side where the endplate was intact. Therefore, endplate failure has been considered an additional risk factor for adjacent fractures. In this study, different extent of endplate damage was detected, with 8 of 12 samples showing at least comminution of one endplate at the treated level. Although SSPI samples did not undergo augmentation, impaired load transfer due to endplate damage was still considered a risk factor for adjacent fracture.

As discussed above (4.3.1.1), SSPI – KP enabled achieving a superior restoration of the endplate curvature at the treated level than SSPI, which was maintained throughout fatigue testing, since the variation in the curvature radii was not significant (Figure 3-31). It is, however, interesting to note that cyclic loading seemed to have opposite effects on the two groups (Table 3-10). In fact, fatigue appeared to flatten the endplates in SSPI, whilst SSPI – KP exhibited an increase in convexity. Such results did not mean that fatigue loading improved the outcome of SSPI. On the contrary, they may confirm a higher instability of the bony fragments due to the lack of support and cohesion provided by cement. The flattering of the endplates was probably a by-product of the compaction of the fracture and peripheral loading, in agreement with what discussed above (4.3.2.1, 4.3.2.3) as well as measures of intradiscal stress [296]. Conversely, SSPI – KP confirmed the behaviour initially hypothesised. Since endplate biomechanics was better restored than in SSPI, the centre of the endplate transferred the majority of the compressive load (as it happens in intact conditions [67, 297]), and damage accumulation resulted in a slight increase in convexity. In *in vivo* conditions, CaP cement may be able to preserve the endplate curvature better than as observed in this study, since it may promote bone remodelling to withstand the nucleus stress.

Previous studies in the literature have investigated fatigue in cement augmentation to better understand adjacent fractures. In particular, it has been confirmed that augmentation increases the stiffness of the spine, leading to early failure of the spinal segment [167, 168]. However, damage to the adjacent vertebrae has been usually assessed visually from CT scans, or as a drop in load/stiffness, hence based on indicators of gross failure. Conversely, this study aimed at replicating more physiological conditions and non-destructive fatigue loading was applied, whilst the developed image processing method enabled quantifying endplate deflection (2.2.4.4). It must be noted that the deflection maps obtained (Appendix C) were a measure of permanent deformation of the endplate surface, since CT scanning was performed with the sample unloaded, pre- and post-fatigue testing. Such approach was considered more clinically relevant than destructive testing, as it provided insight on the functional outcome of the treatment in the early follow-up. A similar protocol was carried out by Nagaraja et al. [170], where image processing of CT scans was performed to estimate the 3D compression of the vertebra and intervertebral space. However, to the candidate's knowledge, this study provided for the first time experimental fatigue investigation of the adjacent endplates in traumatic fractures treated with SSPI/SSPI - KP.

Hulme et al. [169] exploited an *in situ* protocol to show that cement augmentation prevents deflection of the portion of the endplate overlying it. On the other hand, no clear difference was found in the deflection at the adjacent endplate to prove an alteration of load transfer due to PMMA VP. Moreover, numerical simulations by Xu et al. [298] of SSPI – VP in burst fractures, have suggested a 40 – 50 % reduction in stress at the endplates adjacent to the treated vertebra. Results from this study agree with the aforementioned works, and no difference was found between SSPI and SSPI – KP (Figure 3-23). Therefore, it appeared that CaP KP and the resultant marginal increase in construct stiffness did not have any detrimental effect. Hence, with the respect to the experimental conditions undertaken in this study, KP was not considered to constitute a risk factor for adjacent fractures.

Qualitative assessment of CT scans did not highlight any fracture of the adjacent endplate or vertebral body, caused by fatigue loading. In fact, the highest deflection (5th percentile) was -1.0 mm, whilst the median value was -0.2 mm. Results were in line with those of Hulme et al. [169], where the endplate has shown an average deflection of 0.082 ± 0.25 mm, although peaks exceeding 1 mm were identified. However, in this study, the endplates may have actually reached a higher deflection in dynamic conditions, since measures from Hulme et al. were taken under compressive loading. However, the reported permanent deflection can be considered relatively low and not indicative of any substantial failure. In fact, adjacent fractures have been shown to be anticipated by a marked progressive depression of the anterior portion of the endplate, which can be easily detected visually [166]. Nonetheless, this study could not guarantee whether further fatigue accumulation would have triggered a catastrophic failure of the endplate. Results must thus be taken as indicative only of the short term and cannot be generalised to state that the adjacent endplate were safe from subsequent collapse.

As far as the fracture onset was concerned, results confirmed the cranial endplate to be weaker than the caudal ones (4.2.3). On the other hand, both sides exhibited same values of deflection following fatigue loading (Figure 3-24) and were independent from the spinal level; showing that in such conditions the plastic damage was equally distributed. However, results were not in agreement with Nagaraja et al. [170], which found higher compression of the vertebral body and intervertebral space at the cranially rather than caudally adjacent side. Likewise, fatigue loading has been found to induce higher collapse of the trabecular structure underlying the cranially adjacent endplate [282]. Such disagreement may be because the loading conditions in this study were not sufficient to exceed the load capacity of the endplate. As mentioned above, further fatigue accumulation may have resulted in a more marked damage of the cranially adjacent endplate.

Permanent endplate deformation is a complex phenomenon, because depression of an area often resulted in bulging at another location (Appendix C). In fact, 95th percentile values were always positive (indicating outward bulging), as opposed to 5th percentile values (Table 3-7). This was also confirmed by the strong correlation between 5th and 95th percentile of the displacement maps. This was in disagreement with Nagaraja et al. [170], who has only identified permanent inward deflection. However, most of the disagreements between this and the aforementioned study may lie in the extreme complexity of the loading conditions arising from a burst fracture, as opposed to a wedge fracture (usually simulated in the literature). Burst fractures result in more spinal instability than wedge fractures [99] (emphasised in this study by the excision of the neural arch), whilst comminution of the endplates affects stress transfer within the disc. In addition, some of the adjacent endplates showed damage/fissures, resulting from the creation of the fracture, where regions of positive deflection (95th percentile) were typically identified. Such behaviour was probably related to some form of adjustment of the geometrical orientation of the damaged portion, induced by repeated loading. In addition, load was shared with the fixators, hence reducing the extent of the endplate deflection, whilst implant strain was partially associated with deflection. All those factors may have differently influenced the load transfer through the adjacent endplates, with respect to other experimental models presented in the literature.

Chapter 5: Conclusions and Future Work

This study delivered a comprehensive investigation on vertebral fractures, through the experimental protocols developed, which enabled following the whole fracture pathway. Through that, it was possible to review both the biomechanics underlying the origination of the injury and the performance of its surgical treatment. The development of an image processing protocol for 3D analysis enabled tying together the evolution of vertebral anatomy throughout the process, hence providing further insight besides mechanical testing. Fatigue testing was carried out on the treated spine to better understand the long-term performance of SSPI and its combination with KP. It must be noted that the aim was not to test the fatigue life of the implants. In fact, a standardised test (e.g. [217, 218]) would have been more appropriate for it. The experiments were developed to understand the biomechanics of the construct made by the fractured spine and SSPI, whilst understanding how KP can improve it.

In addition, this doctorate project involved a collaboration for the development of an FE model, to investigate *in silico* the biomechanics of fractures of multiple myeloma infiltrated spine.

A set of main objectives were defined and completed to provide the presented investigation:

- Develop an *in situ* testing protocol and provide experimental data for FE model development (collaboration with Dr. Nicholas Roberts).
- Develop image processing applications for 3D analysis of vertebral anatomy and integrate them with mechanical testing.
- Develop an experimental protocol to create *in vitro* burst fractures and investigate the biomechanics of the fracture, providing evidence of the dynamics of IPW and assessing relevant anatomical changes.
- Develop an experimental protocol for *in vitro* investigation of fatigue in spinal segments, following surgical intervention. Provide a comparison/investigation on SSPI and SSPI – KP as treatment for spinal burst fractures, hence aiding treatment planning.

5.1 General conclusions

Burst fracture biomechanics is extremely complex because of its highly dynamic onset, which is also the main hurdle for clinical diagnostics and treatment planning. IPW has been associated with neurological injury [23] and imputed to be a driving factor in the origination of the fracture [191]. In addition, authors have speculated IPW to be a dynamic phenomenon, strictly linked to LF and SCO [123]. This work provided for the first time evidence of such dynamic behaviour.

Previous studies have not found any significant correlation between SCO_{max} and SCO_{res} [194, 269]. Although a strong correlation was found in this study, it must be noted that those measurements were clustered towards the extremes of the measurement range and the poor agreement showed by the technique proved it not suitable for human tissue, unless further improvements are made. The overall lack of correlation present in the literature for the dynamics of SCO strengthened the importance of IPW in understanding the mechanics of the fracture, whilst showing that SCO alone cannot explain the full nature of the injury.

Burst fracture creation and its investigation showed that:

- IPW is a dynamic phenomenon. At the impact the pedicles splay up to a maximum value (IPW_{max}=15.8 %) and are subsequently recoiled to their resting position (IPW_{res}=4.9 %, i.e. what measured clinically).
- IPW_{max} is reached in 20 – 25 ms, whilst the whole transient phase lasts about 400 ms (although the main event is the IPW_{max} peak).
- IPW_{max} is moderately correlated with IPW_{res}, whilst no association is present between both IPW_{max} and IPW_{res}, and SCO.
- IPW_{max} may represent the instant where the shape of the spinal canal is most critical for the neurological injury as its lateral diameter reaches its maximum (whilst the AP diameter decreases due to deformation of the posterior wall).
- Anatomical variation of the facet joints and pedicles across levels influences IPW.

- Vertebral compression and SCO are associated with impact energy, as opposed to IPW. Therefore, damage to the vertebral body has a viscoelastic component, conversely to IPW.
- Laminar fractures may be a dynamic phenomenon directly driven by IPW. Hence, the dynamics of IPW is crucial for the origination of dural tears.
- Burst fractures induce a substantial increase in convexity of the endplate, which is associated with impact energy. Cranial endplates are more sensitive to the convexity increase, thus they might be more prone to post-traumatic disc degeneration.

As highlighted by Fakurnejad et al. [192], in the majority of works where surgical treatments have been investigated, little care has been taken about using clinically relevant fractures. Conversely, in this study, the treatment was performed on specimens that previously underwent consistent creation of clinical-like burst fractures. In addition cyclic loading provided a simulation of the early follow-up, whilst the experimental protocol enabled quantifying the evolution over time of structural properties and vertebral anatomy. To the candidate’s knowledge, this work was novel as it investigated SSPI/SSPI – KP on cadaveric tissue using a combination of image processing and fatigue loading, and no equivalent could be found in the literature.

Based on the review of the results from this study, and the literature, KP is recommended to be performed in combination with SSPI because of the following considerations. Firstly, KP is minimally invasive and requires approximatively 25 minutes of extra operative time compared to SSPI alone [180]. The presented experimental investigation showed that SSPI – KP may provide several benefits to the patient:

- Significant restoration of endplate geometry (21.7 % curvature recovery) and decrease of depression of the region underlying the nucleus pulposus, conversely to SSPI alone. The achieved reduction was retained following fatigue loading, thus SSPI – KP showed potential to prevent post-traumatic disc degeneration and nucleus herniation within the vertebral body.

- Improved spinal stability: marginal increase in compressive stiffness (31 %) and better retention of the achieved correction.
- Marginal reduction of peak surface strains on fixator rods following fatigue (13 %). Increased strains were associated with higher spinal instability, as well as screw loosening.
- Significantly improved safety of the neurological structures by limiting migration of bony fragments (median migration of posterior wall in SSPI and SSPI – KP were 1.6 and 0.2 mm, respectively). SSPI – KP also decreased initial oscillation of the posterior wall by 72 %.
- No increased risk of adjacent fracture (same damage as SSPI within early-stage follow-up under reduced loading conditions).
- Potential for improvement of the abovementioned benefits through osteoconductivity of CaP cement (i.e. promotion of bone remodelling and cement resorption).

However, one might question whether VP could be a more cost-effective alternative; since it does not require any IBT inflation kit, and most of the height was recovered through SSPI. However, both this work and the literature suggest that the use of the IBT is key to the success of the treatment [181, 287], especially concerning endplate reduction [166, 176], whilst also reducing the risk of leakage [182].

It may be interesting to note that, from a qualitative point of view, results from SSPI – KP appeared, overall, less scattered than SSPI (also in terms of curve trends, see Appendix B). This may be an additional indication of the mechanical stability provided by SSPI – KP. However, in all the cases dispersion tests failed to return any statistical significance (Ansari-Bradley test, p>0.5 in all cases), because of the limited sample size.

5.2 Future work

This work provided a set of tools for the comprehensive investigation of the fracture pathway. Nonetheless, some aspects could be developed further to better address clinical needs and/or transferred to other projects.

5.2.1 Biomechanics of burst fracture onset

The experiments conducted in this work proved the dynamics of IPW and highlighted its importance. However, future work is necessary to glean more evidence and understanding, also given the difficulty to provide tolerance limits for burst fracture as easily as for quasi-static loading [188]. The integration of the results presented herein with more extensive investigations on the dynamics of laminar fractures and SCO may enable implementing novel clinical decisional tools. Thus, the final aim would be the retrospective estimation of the evolution of the spinal canal shape during the fracture onset; to ease the assessment of the neurological deficit, predict the risk of dural tears and design the optimal intervention (or at least choose between surgical and conservative treatment).

Several works have shown that plain radiography can reliably identify IPW without the need for CT scanning [104, 271, 272]. Advanced biomechanical models could be developed based on work stemming from this project, which may eventually find a clinical application using x-ray data as input. It would be then possible to increase the sensitivity of plain radiography, providing prompt estimations of the neurological injury, whilst reducing radiation dosage and costs for the healthcare providers. Therefore, an initial screening of the patient at presentation may be able suffice enough information to decide on the severity of the case and necessity of further CT/MRI assessment, as already suggested for the detection of dural tears [125].

The LVDT measures developed in this study could be advanced by exploiting image processing of high-speed filming of the vertebral surface. Firstly, tracking the displacement of markers painted on the vertebral body could provide an extensive 3D IPW assessment. In addition, it would be possible to detect the vertical motion of the pedicles, which may cause an additional injury to the root of the nerve. A technique similar to that of Hedrick et al. [299] could be implemented since it has been validated to track extremely rapid displacement changes.

As mentioned above, the next step towards a complete characterisation of the vertebral foramen failure necessitate of a thorough understanding of the dynamics of laminar fractures. .. To this end, image processing could be advanced to digital image correlation (DIC) techniques, which would exploited a speckled pattern painted onto the laminar posterior surface to determine the full field surface strains as well as regions of failure. Such approach has been successfully used on other bones, such as the femur [300], and could provide extremely valuable insight on the dynamics of laminar fractures. Upon successful validation of the method, DIC could be extended to the rest of the vertebra. However, it must be borne in mind that any imaging of the antero-lateral surface of the vertebra would require complete excision of the ligaments to expose the cortex. Thus, it would be advised to limit DIC investigation to the lamina and pedicles.

HR-pQCT scans taken in this study (pre- and post-fracture) were also used by Ilsoo Koh, a doctorate candidate within the SpineFX project at ETH (Zurich, Switzerland), for the development of an FE model of the fractured spine following cement augmentation. Results from this collaboration may help understanding better the behaviour of the bony fragments under load.

5.2.2 Biomechanics of spinal fixation

The first aim of the second part of the project was to develop a comprehensive protocol for the investigation of the biomechanics of SSPI/SSPI – KP in spinal burst fractures. However, due to the limited timeframe available some additional methodologies could not be implemented and should be included in the future to increase the completeness of the experiments. Firstly, accurate calibration of the fixator rods based on strain measures would enable quantifying load sharing between the implant and the vertebral body. A similar approach has been previously used by other authors in quasi-static conditions [213, 216, 232]. Combining such protocol with what developed in this study would enable continuous recording of the evolution of load sharing throughout fatigue loading. Therefore, it may be possible to define threshold values indicative of a high risk of implant failure, or inadequate load transmission through the vertebral body. In addition, the displacement measurements of the LVDTs could be integrated, or replaced, with an optoelectronic system to track the intervertebral motions [205, 301, 302], hence providing a 3D assessment of the relative motion of the bony fragments within the vertebra as well as with respect to the adjacent vertebrae.. Finally, a substantial improvement in the design of the testing apparatus would enable a more realistic replication of the *in vivo* biomechanics. In this work, the loading conditions were limited to axial compression, whilst shear was decoupled to avoid over-constraining the sample. This was done to create simple and controlled loading conditions, hence allowing a clearer interpretation of the results. On the other hand, a substantial improvement in the loading conditions would require including bending. This could be achieved by hinging the pots (i.e. allowing flexion/extension), as previously done by Kolb et al. [167]. In addition, encoders could be used to measure the induced rotation. Implementing all the above mentioned changes would provide a more comprehensive and realistic investigation, hence increasing its clinical relevance.

Eventually, different commercial implants, as well as augmentation solutions, could be tested using this experimental protocol, to aid surgeons choosing the best treatment or manufacturers developing new stabilisation strategies.

3D analysis enabled identifying differences that mechanical testing was not able to highlight, as well as providing insight on the changes that the vertebral anatomy undergoes throughout the fracture pathway. The method required only a CT scan of the vertebra, to extract its 3D surface, and thus it is suitable for *in vivo* applications. However, manual segmentation is time-consuming and requires an expert user. A clinical version of the tool might implement an automated segmentation algorithm (e.g. [303]), thus speeding the process, in spite of accuracy. Clinical methods conventionally use 2D views of the spine obtained from plain radiography, or reconstructed from CT scans, to assess relevant anatomical parameters [103]. Conversely, the methods developed were based on digital identification of marker sets on a 3D surface, which provides a more complete representation of the geometry, in contrast to the definition of a line passing through the endplate rim on a 2D view.

The image processing application quantified local and global curvature of the endplates, and such outputs could be used to design patient-specific intervertebral disc replacements or fusion cages. Therefore, the loading surfaces of the bespoke implant would be fully conforming to endplate geometry, whilst additive manufacturing could be used to produce it.

References

1. Brandolini, N., Kapur, N., and Hall, R.M. Dynamics of interpedicular widening in spinal burst fractures: an in vitro investigation. Spine J. 2014, **14**(9), pp.2164-71.
2. Roberts, N., Brandolini, N., Kapur, N., Whyne, C., and Hall, R.M. Finite element modelling of multiple myeloma infiltrated vertebrae using image based boundary conditions. *Comput Methods Biomech Biomed Engin.* 2015, **Submitted**.
3. Prakash, Prabhu, L.V., Saralaya, V.V., Pai, M.M., Ranade, A.V., Singh, G., and Madhyastha, S. Vertebral body integrity: a review of various anatomical factors involved in the lumbar region. *Osteoporos Int.* 2007, **18**(7), pp.891-903.
4. Khan, A.E., Gallo, V., Linseisen, J., Kaaks, R., Rohrmann, S., Raaschou-Nielsen, O., Tjonneland, A., Johnsen, H.E., Overvad, K., Bergmann, M.M., Boeing, H., Benetou, V., Psaltopoulou, T., Trichopoulou, A., Masala, G., Mattiello, A., Grioni, S., Tumino, R., Vermeulen, R.C., Peeters, P.H., Bueno-de-Mesquita, H.B., Ros, M.M., Lund, E., Ardanaz, E., Chirlaque, M.D., Jakszyn, P., Larranaga, N., Losada, A., Becker, N., Nieters, A., Martinez-Garcia, C., Agren, A., Hallmans, G., Berglund, G., Manjer, J., Allen, N.E., Key, T.J., Bingham, S., Khaw, K.T., Slimani, N., Ferrari, P., Boffetta, P., Norat, T., Vineis, P., and Riboli, E. Diabetes and the risk of non-Hodgkin's lymphoma and multiple myeloma in the European Prospective Investigation into Cancer and Nutrition. *Haematologica.* 2008, **93**(6), pp.842-50.
5. McDonnell, P., McHugh, P.E., and O'Mahoney, D. Vertebral osteoporosis and trabecular bone quality. *Ann Biomed Eng.* 2007, **35**(2), pp.170-89.
6. Kanis, J.A. *on behalf of the World Health Organization Scientific Group. Assessment of Osteoporosis at the Primary Health-Care Level.* University of Sheffield: World Health Organization Collaborating Centre for Metabolic Bone Diseases, 2007.
7. Klazen, C.A., Lohle, P.N., de Vries, J., Jansen, F.H., Tielbeek, A.V., Blonk, M.C., Venmans, A., van Rooij, W.J., Schoemaker, M.C., Juttmann, J.R., Lo, T.H., Verhaar, H.J., van der Graaf, Y., van Everdingen, K.J., Muller, A.F., Elgersma, O.E., Halkema, D.R., Fransen, H., Janssens, X., Buskens, E., and Mali, W.P. Vertebroplasty versus conservative treatment in acute osteoporotic vertebral compression fractures (Vertos II): an open-label randomised trial. *Lancet.* 2010, **376**(9746), pp.1085-92.
8. Pingali, S.R., Haddad, R.Y., and Saad, A. Current concepts of clinical management of multiple myeloma. *Dis Mon.* 2012, **58**(4), pp.195-207.
9. Whyne, C.M. Biomechanics of metastatic disease in the vertebral column. *Neurol Res.* 2014, **36**(6), pp.493-501.
10. Choi, D., Crockard, A., Bunger, C., Harms, J., Kawahara, N., Mazel, C., Melcher, R., and Tomita, K. Review of metastatic spine tumour classification and indications for surgery: the consensus statement of the Global Spine Tumour Study Group. *Eur Spine J.* 2009, **19**(2), pp.215-22.

11. Bataille, R., Chappard, D., Marcelli, C., Dessauw, P., Sany, J., Baldet, P., and Alexandre, C. Mechanisms of bone destruction in multiple myeloma: the importance of an unbalanced process in determining the severity of lytic bone disease. *J Clin Oncol.* 1989, **7**(12), pp.1909-14.

12. Kassamali, R.H., Ganeshan, A., Hoey, E.T., Crowe, P.M., Douis, H., and Henderson, J. Pain management in spinal metastases: the role of percutaneous vertebral augmentation. *Ann Oncol.* 2010, **22**(4), pp.782-6.

13. Pirouzmand, F. Epidemiological trends of spine and spinal cord injuries in the largest Canadian adult trauma center from 1986 to 2006. *J Neurosurg Spine.* 2010, **12**(2), pp.131-40.

14. Aebi, M. Classification of thoracolumbar fractures and dislocations. *Eur Spine J.* 2010, **19 Suppl 1**, pp.S2-7.

15. Denis, F. The three column spine and its significance in the classification of acute thoracolumbar spinal injuries. *Spine (Phila Pa 1976).* 1983, **8**(8), pp.817-31.

16. Smith, H.E., Anderson, D.G., Vaccaro, A.R., Albert, T.J., Hilibrand, A.S., Harrop, J.S., and Ratliff, J.K. Anatomy, Biomechanics, and Classification of Thoracolumbar Injuries. *Semin Spine Surg.* 2010, **22**(1), pp.2-7.

17. Shikata, J., Yamamuro, T., Iida, H., Shimizu, K., and Yoshikawa, J. Surgical treatment for paraplegia resulting from vertebral fractures in senile osteoporosis. *Spine (Phila Pa 1976).* 1990, **15**(6), pp.485-9.

18. Magerl, F., Aebi, M., Gertzbein, S.D., Harms, J., and Nazarian, S. A comprehensive classification of thoracic and lumbar injuries. *Eur Spine J.* 1994, **3**(4), pp.184-201.

19. Yugue, I., Aono, K., Shiba, K., Ueta, T., Maeda, T., Mori, E., and Kawano, O. Analysis of the risk factors for severity of neurologic status in 216 patients with thoracolumbar and lumbar burst fractures. *Spine (Phila Pa 1976).* 2011, **36**(19), pp.1563-9.

20. Vaccaro, A.R., Nachwalter, R.S., Klein, G.R., Sewards, J.M., Albert, T.J., and Garfin, S.R. The significance of thoracolumbar spinal canal size in spinal cord injury patients. *Spine (Phila Pa 1976).* 2001, **26**(4), pp.371-6.

21. Meves, R., and Avanzi, O. Correlation among canal compromise, neurologic deficit, and injury severity in thoracolumbar burst fractures. *Spine (Phila Pa 1976).* 2006, **31**(18), pp.2137-41.

22. Park, J.K., Park, J.W., Cho, D.C., and Sung, J.K. Predictable factors for dural tears in lumbar burst fractures with vertical laminar fractures. *J Korean Neurosurg Soc.* 2011, **50**(1), pp.11-6.

23. Caffaro, M.F., and Avanzi, O. Can the interpedicular distance reliably assess the severity of thoracolumbar burst fractures? *Spine (Phila Pa 1976).* 2012, **37**(4), pp.E231-6.

24. Kifune, M., Panjabi, M.M., Liu, W., Arand, M., Vasavada, A., and Oxland, T. Functional Morphology of the Spinal Canal After Endplate, Wedge, and Burst Fractures. *J Spinal Disord Tech.* 1997, **10**(6), pp.457-466.

25. Tran, N.T., Watson, N.A., Tencer, A.F., Ching, R.P., and Anderson, P.A. Mechanism of the burst fracture in the thoracolumbar spine. The effect of loading rate. *Spine (Phila Pa 1976).* 1995, **20**(18), pp.1984-8.

26. Wilcox, R.K., Boerger, T.O., Hall, R.M., Barton, D.C., Limb, D., and Dickson, R.A. Measurement of canal occlusion during the thoracolumbar burst fracture process. *J Biomech.* 2002, **35**(3), pp.381-4.

27. Van Toen, C., Melnyk, A.D., Street, J., Oxland, T.R., and Cripton, P.A. The effect of lateral eccentricity on failure loads, kinematics, and canal occlusions of the cervical spine in axial loading. *J Biomech.* 2014, **47**(5), pp.1164-72.

28. Panjabi, M.M., Kifune, M., Wen, L., Arand, M., Oxland, T.R., Lin, R.M., Yoon, W.S., and Vasavada, A. Dynamic canal encroachment during thoracolumbar burst fractures. *J Spinal Disord.* 1995, **8**(1), pp.39-48.

29. Abudou, M., Chen, X., Kong, X., and Wu, T. Surgical versus non-surgical treatment for thoracolumbar burst fractures without neurological deficit. *Cochrane Database Syst Rev.* 2013, **6**, p.CD005079.

30. Gnanenthiran, S.R., Adie, S., and Harris, I.A. Nonoperative versus operative treatment for thoracolumbar burst fractures without neurologic deficit: a meta-analysis. *Clin Orthop Relat Res.* 2012, **470**(2), pp.567-77.

31. Mumford, J., Weinstein, J.N., Spratt, K.F., and Goel, V.K. Thoracolumbar burst fractures. The clinical efficacy and outcome of nonoperative management. *Spine (Phila Pa 1976).* 1993, **18**(8), pp.955-70.

32. Reinhold, M., Knop, C., Beisse, R., Audige, L., Kandziora, F., Pizanis, A., Pranzl, R., Gercek, E., Schultheiss, M., Weckbach, A., Buhren, V., and Blauth, M. Operative treatment of 733 patients with acute thoracolumbar spinal injuries: comprehensive results from the second, prospective, Internet-based multicenter study of the Spine Study Group of the German Association of Trauma Surgery. *Eur Spine J.* 2010, **19**(10), pp.1657-76.

33. Parker, J.W., Lane, J.R., Karaikovic, E.E., and Gaines, R.W. Successful short-segment instrumentation and fusion for thoracolumbar spine fractures: a consecutive 4 1/2-year series. *Spine (Phila Pa 1976).* 2000, **25**(9), pp.1157-70.

34. Wood, K.B., Li, W., Lebl, D.S., and Ploumis, A. Management of thoracolumbar spine fractures. *Spine J.* 2014, **14**(1), pp.145-64.

35. McLain, R.F., Sparling, E., and Benson, D.R. Early failure of short-segment pedicle instrumentation for thoracolumbar fractures. A preliminary report. *J Bone Joint Surg Am.* 1993, **75**(2), pp.162-7.

36. Acosta, F.L., Jr., Aryan, H.E., Taylor, W.R., and Ames, C.P. Kyphoplasty-augmented short-segment pedicle screw fixation of traumatic lumbar burst fractures: initial clinical experience and literature review. *Neurosurg Focus.* 2005, **18**(3), p.e9.

37. Korovessis, P., Hadjipavlou, A., and Repantis, T. Minimal invasive short posterior instrumentation plus balloon kyphoplasty with calcium phosphate for burst and severe compression lumbar fractures. *Spine (Phila Pa 1976).* 2008, **33**(6), pp.658-67.

38. Blondel, B., Fuentes, S., Pech-Gourg, G., Adetchessi, T., Tropiano, P., and Dufour, H. Percutaneous management of thoracolumbar burst fractures:

Evolution of techniques and strategy. *Orthop Traumatol Surg Res.* 2011, **97**(5), pp.527-32.

39. Verlaan, J.J., Dhert, W.J., Verbout, A.J., and Oner, F.C. Balloon vertebroplasty in combination with pedicle screw instrumentation: a novel technique to treat thoracic and lumbar burst fractures. *Spine (Phila Pa 1976).* 2005, **30**(3), pp.E73-9.

40. Marco, R.A., Meyer, B.C., and Kushwaha, V.P. Thoracolumbar burst fractures treated with posterior decompression and pedicle screw instrumentation supplemented with balloon-assisted vertebroplasty and calcium phosphate reconstruction. Surgical technique. *J Bone Joint Surg Am.* 2010, **92 Suppl 1 Pt 1**, pp.67-76.

41. White, A.A., and Panjabi, M.M. *Clinical biomechanics of the spine.* 2nd ed. Philadelphia: Lippincott, 1990.

42. Stagnara, P., De Mauroy, J.C., Dran, G., Gonon, G.P., Costanzo, G., Dimnet, J., and Pasquet, A. Reciprocal angulation of vertebral bodies in a sagittal plane: approach to references for the evaluation of kyphosis and lordosis. *Spine (Phila Pa 1976).* 1982, **7**(4), pp.335-42.

43. Tabensky, A.D., Williams, J., DeLuca, V., Briganti, E., and Seeman, E. Bone mass, areal, and volumetric bone density are equally accurate, sensitive, and specific surrogates of the breaking strength of the vertebral body: an in vitro study. *J Bone Miner Res.* 1996, **11**(12), pp.1981-8.

44. Brinckmann, P., Biggemann, M., and Hilweg, D. Prediction of the compressive strength of human lumbar vertebrae. *Spine (Phila Pa 1976).* 1989, **14**(6), pp.606-10.

45. Bouxsein, M.L. Bone quality: where do we go from here? *Osteoporos Int.* 2003, **14 Suppl 5**, pp.S118-27.

46. Fields, A.J., Eswaran, S.K., Jekir, M.G., and Keaveny, T.M. Role of trabecular microarchitecture in whole-vertebral body biomechanical behavior. *J Bone Miner Res.* 2009, **24**(9), pp.1523-30.

47. Wegrzyn, J., Roux, J.P., Arlot, M.E., Boutroy, S., Vilayphiou, N., Guyen, O., Delmas, P.D., Chapurlat, R., and Bouxsein, M.L. Role of trabecular microarchitecture and its heterogeneity parameters in the mechanical behavior of ex vivo human L3 vertebrae. *J Bone Miner Res.* 2010, **25**(11), pp.2324-31.

48. Stauber, M., and Muller, R. Age-related changes in trabecular bone microstructures: global and local morphometry. *Osteoporos Int.* 2006, **17**(4), pp.616-26.

49. Wang, J., Zhou, B., Liu, X.S., Fields, A.J., Sanyal, A., Shi, X., Adams, M., Keaveny, T.M., and Guo, X.E. Trabecular Plates and Rods Determine Elastic Modulus and Yield Strength of Human Trabecular Bone. *Bone.* 2014.

50. Eswaran, S.K., Gupta, A., Adams, M.F., and Keaveny, T.M. Cortical and trabecular load sharing in the human vertebral body. *J Bone Miner Res.* 2006, **21**(2), pp.307-14.

51. Wegrzyn, J., Roux, J.P., Arlot, M.E., Boutroy, S., Vilayphiou, N., Guyen, O., Delmas, P.D., Chapurlat, R., and Bouxsein, M.L. Determinants of the

mechanical behavior of human lumbar vertebrae after simulated mild fracture. *J Bone Miner Res.* 2011, **26**(4), pp.739-46.

52. Roux, J.P., Wegrzyn, J., Arlot, M.E., Guyen, O., Delmas, P.D., Chapurlat, R., and Bouxsein, M.L. Contribution of trabecular and cortical components to biomechanical behavior of human vertebrae: an ex vivo study. *J Bone Miner Res.* 2010, **25**(2), pp.356-61.

53. Lochmuller, E.M., Poschl, K., Wurstlin, L., Matsuura, M., Muller, R., Link, T.M., and Eckstein, F. Does thoracic or lumbar spine bone architecture predict vertebral failure strength more accurately than density? *Osteoporos Int.* 2008, **19**(4), pp.537-45.

54. Hulme, P.A., Boyd, S.K., and Ferguson, S.J. Regional variation in vertebral bone morphology and its contribution to vertebral fracture strength. *Bone.* 2007, **41**(6), pp.946-57.

55. Cowin, S.C. Wolff's law of trabecular architecture at remodeling equilibrium. *J Biomech Eng.* 1986, **108**(1), pp.83-8.

56. Fields, A.J., Lee, G.L., Liu, X.S., Jekir, M.G., Guo, X.E., and Keaveny, T.M. Influence of vertical trabeculae on the compressive strength of the human vertebra. *J Bone Miner Res.* 2011, **26**(2), pp.263-9.

57. Bogduk, N. *Clinical anatomy of the lumbar spine and sacrum.* 4th ed. London: Elsevier Churchill Livingstone, 2005.

58. Panjabi, M.M., Goel, V., Oxland, T., Takata, K., Duranceau, J., Krag, M., and Price, M. Human lumbar vertebrae. Quantitative three-dimensional anatomy. *Spine (Phila Pa 1976).* 1992, **17**(3), pp.299-306.

59. Panjabi, M.M., Takata, K., Goel, V., Federico, D., Oxland, T., Duranceau, J., and Krag, M. Thoracic human vertebrae. Quantitative three-dimensional anatomy. *Spine (Phila Pa 1976).* 1991, **16**(8), pp.888-901.

60. Inceoglu, S., Burghardt, A., Akbay, A., Majumdar, S., and McLain, R.F. Trabecular architecture of lumbar vertebral pedicle. *Spine (Phila Pa 1976).* 2005, **30**(13), pp.1485-90.

61. Silva, M.J., Wang, C., Keaveny, T.M., and Hayes, W.C. Direct and computed tomography thickness measurements of the human, lumbar vertebral shell and endplate. *Bone.* 1994, **15**(4), pp.409-14.

62. Zindrick, M.R., Wiltse, L.L., Doornik, A., Widell, E.H., Knight, G.W., Patwardhan, A.G., Thomas, J.C., Rothman, S.L., and Fields, B.T. Analysis of the morphometric characteristics of the thoracic and lumbar pedicles. *Spine (Phila Pa 1976).* 1987, **12**(2), pp.160-6.

63. Cristofolini, L. In vitro evidence of the structural optimization of the human skeletal bones. *J Biomech.* 2014.

64. Raj, P.P. Intervertebral disc: anatomy-physiology-pathophysiology-treatment. *Pain Pract.* 2008, **8**(1), pp.18-44.

65. Moon, S.M., Yoder, J.H., Wright, A.C., Smith, L.J., Vresilovic, E.J., and Elliott, D.M. Evaluation of intervertebral disc cartilaginous endplate structure using magnetic resonance imaging. *Eur Spine J.* 2013, **22**(8), pp.1820-8.

66. Adams, M.A., Dolan, P., and McNally, D.S. The internal mechanical functioning of intervertebral discs and articular cartilage, and its relevance to matrix biology. *Matrix Biol.* 2009, **28**(7), pp.384-9.

67. Hulme, P.A., Ferguson, S.J., and Boyd, S.K. Determination of vertebral endplate deformation under load using micro-computed tomography. *J Biomech.* 2008, **41**(1), pp.78-85. Epub 2007 Oct 29.

68. Heuer, F., Schmidt, H., and Wilke, H.J. The relation between intervertebral disc bulging and annular fiber associated strains for simple and complex loading. *J Biomech.* 2008, **41**(5), pp.1086-94. Epub 2008 Jan 9.

69. Jaumard, N.V., Welch, W.C., and Winkelstein, B.A. Spinal facet joint biomechanics and mechanotransduction in normal, injury and degenerative conditions. *J Biomech Eng.* 2011, **133**(7), p.071010.

70. Ivicsics, M.F., Bishop, N.E., Puschel, K., Morlock, M.M., and Huber, G. Increase in facet joint loading after nucleotomy in the human lumbar spine. *J Biomech.* 2014, **47**(7), pp.1712-7.

71. Skrzypiec, D.M., Bishop, N.E., Klein, A., Puschel, K., Morlock, M.M., and Huber, G. Estimation of shear load sharing in moderately degenerated human lumbar spine. *J Biomech.* 2013, **46**(4), pp.651-7.

72. Izzo, R., Guarnieri, G., Guglielmi, G., and Muto, M. Biomechanics of the spine. Part I: spinal stability. *Eur J Radiol.* 2013, **82**(1), pp.118-26.

73. Datta, G., Gnanalingham, K.K., Peterson, D., Mendoza, N., O'Neill, K., Van Dellen, J., McGregor, A., and Hughes, S.P. Back pain and disability after lumbar laminectomy: is there a relationship to muscle retraction? *Neurosurgery.* 2004, **54**(6), pp.1413-20; discussion 1420.

74. Ebraheim, N.A., Hassan, A., Lee, M., and Xu, R. Functional anatomy of the lumbar spine. *Sem Pain Med.* 2004, **2**(3), pp.131-137.

75. Soyuncu, Y., Yildirim, F.B., Sekban, H., Ozdemir, H., Akyildiz, F., and Sindel, M. Anatomic evaluation and relationship between the lumbar pedicle and adjacent neural structures: an anatomic study. *J Spinal Disord Tech.* 2005, **18**(3), pp.243-6.

76. Johanson, C.E., Duncan, J.A., 3rd, Klinge, P.M., Brinker, T., Stopa, E.G., and Silverberg, G.D. Multiplicity of cerebrospinal fluid functions: New challenges in health and disease. *Cerebrospinal Fluid Res.* 2008, **5**, p.10.

77. Persson, C., Evans, S., Marsh, R., Summers, J.L., and Hall, R.M. Poisson's ratio and strain rate dependency of the constitutive behavior of spinal dura mater. *Ann Biomed Eng.* 2010, **38**(3), pp.975-83.

78. Brandolini, N., Cristofolini, L., and Viceconti, M. Experimental methods for the biomechanical characterization of the human spine: a review. *J Mech Med Biol.* 2013, **14**(1), p.1430002.

79. Bergmann, G. *OrthoLoad.* [Online]. 2014. [Accessed]. Available from: www.orthoload.com

80. Rohlmann, A., Dreischarf, M., Zander, T., Graichen, F., and Bergmann, G. Loads on a vertebral body replacement during locomotion measured in vivo. *Gait Posture.* 2014, **39**(2), pp.750-5.

81. Cristofolini, L., Brandolini, N., Danesi, V., Juszczyk, M.M., Erani, P., and Viceconti, M. Strain distribution in the lumbar vertebrae under different loading configurations. *Spine J.* 2013, **13**(10), pp.1281-92.

82. Rohlmann, A., Claes, L.E., Bergmannt, G., Graichen, F., Neef, P., and Wilke, H.J. Comparison of intradiscal pressures and spinal fixator loads for different body positions and exercises. *Ergonomics.* 2001, **44**(8), pp.781-94.

83. Rohlmann, A., Bergmann, G., Graichen, F., and Neff, G. Braces do not reduce loads on internal spinal fixation devices. *Clin Biomech (Bristol, Avon).* 1999, **14**(2), pp.97-102.

84. Wilke, H., Neef, P., Hinz, B., Seidel, H., and Claes, L. Intradiscal pressure together with anthropometric data--a data set for the validation of models. *Clin Biomech (Bristol, Avon).* 2001, **16 Suppl 1**, pp.S111-26.

85. McNally, D.S., and Adams, M.A. Internal intervertebral disc mechanics as revealed by stress profilometry. *Spine (Phila Pa 1976).* 1992, **17**(1), pp.66-73.

86. Skrzypiec, D.M., Pollintine, P., Przybyla, A., Dolan, P., and Adams, M.A. The internal mechanical properties of cervical intervertebral discs as revealed by stress profilometry. *Eur Spine J.* 2007, **16**(10), pp.1701-9. Epub 2007 Aug 2.

87. Pollintine, P., van Tunen, M.S., Luo, J., Brown, M.D., Dolan, P., and Adams, M.A. Time-dependent compressive deformation of the ageing spine: relevance to spinal stenosis. *Spine (Phila Pa 1976).* 2010, **35**(4), pp.386-94.

88. Adams, M.A., and Dolan, P. Spine biomechanics. *J Biomech.* 2005, **38**(10), pp.1972-83.

89. McMillan, D.W., McNally, D.S., Garbutt, G., and Adams, M.A. Stress distributions inside intervertebral discs: the validity of experimental "stress profilometry'. *Proc Inst Mech Eng H.* 1996, **210**(2), pp.81-7.

90. Dreischarf, M., Rohlmann, A., Zhu, R., Schmidt, H., and Zander, T. Is it possible to estimate the compressive force in the lumbar spine from intradiscal pressure measurements? A finite element evaluation. *Med Eng Phys.* 2013, **35**(9), pp.1385-90.

91. Nachemson, A.L. Disc pressure measurements. *Spine (Phila Pa 1976).* 1981, **6**(1), pp.93-7.

92. Sato, K., Kikuchi, S., and Yonezawa, T. In vivo intradiscal pressure measurement in healthy individuals and in patients with ongoing back problems. *Spine (Phila Pa 1976).* 1999, **24**(23), pp.2468-74.

93. Takahashi, I., Kikuchi, S., Sato, K., and Sato, N. Mechanical load of the lumbar spine during forward bending motion of the trunk-a biomechanical study. *Spine (Phila Pa 1976).* 2006, **31**(1), pp.18-23.

94. de Zee, M., Hansen, L., Wong, C., Rasmussen, J., and Simonsen, E.B. A generic detailed rigid-body lumbar spine model. *J Biomech.* 2007, **40**(6), pp.1219-27.

95. Zander, T., Dreischarf, M., Schmidt, H., Bergmann, G., and Rohlmann, A. Spinal loads as influenced by external loads: a combined in vivo and in silico investigation. *J Biomech.* 2015, **48**(4), pp.578-84.

96. Rohlmann, A., Consmuller, T., Dreischarf, M., Bashkuev, M., Disch, A., Pries, E., Duda, G.N., and Schmidt, H. Measurement of the number of lumbar spinal movements in the sagittal plane in a 24-hour period. *Eur Spine J.* 2014.

97. Hedman, T.P., Kostuik, J.P., Fernie, G.R., and Hellier, W.G. Design of an intervertebral disc prosthesis. *Spine (Phila Pa 1976).* 1991, **16**(6 Suppl), pp.S256-60.

98. Kopperdahl, D.L., Pearlman, J.L., and Keaveny, T.M. Biomechanical consequences of an isolated overload on the human vertebral body. *J Orthop Res.* 2000, **18**(5), pp.685-90.

99. Vaccaro, A.R., Oner, C., Kepler, C.K., Dvorak, M., Schnake, K., Bellabarba, C., Reinhold, M., Aarabi, B., Kandziora, F., Chapman, J., Shanmuganathan, R., Fehlings, M., Vialle, L., Injury, A.O.S.C., and Trauma Knowledge, F. AOSpine Thoracolumbar Spine Injury Classification System: Fracture Description, Neurological Status, and Key Modifiers. *Spine (Phila Pa 1976).* 2013, **38**(23), pp.2028-37.

100. Kepler, C.K., Felte, R.F., and Rihn, J.A. Current Concepts: Classification of Thoracolumbar Fractures. *Seminars in Spine Surgery.* 2012, (0).

101. Sethi, M.K., Schoenfeld, A.J., Bono, C.M., and Harris, M.B. The evolution of thoracolumbar injury classification systems. *Spine J.* 2009, **9**(9), pp.780-8.

102. Frankel, H.L., Hancock, D.O., Hyslop, G., Melzak, J., Michaelis, L.S., Ungar, G.H., Vernon, J.D., and Walsh, J.J. The value of postural reduction in the initial management of closed injuries of the spine with paraplegia and tetraplegia. I. *Paraplegia.* 1969, **7**(3), pp.179-92.

103. Keynan, O., Fisher, C.G., Vaccaro, A., Fehlings, M.G., Oner, F.C., Dietz, J., Kwon, B., Rampersaud, R., Bono, C., France, J., and Dvorak, M. Radiographic measurement parameters in thoracolumbar fractures: a systematic review and consensus statement of the spine trauma study group. *Spine (Phila Pa 1976).* 2006, **31**(5), pp.E156-65.

104. Bensch, F.V., Koivikko, M.P., Kiuru, M.J., and Koskinen, S.K. Measurement of spinal canal narrowing, interpedicular widening, and vertebral compression in spinal burst fractures: plain radiographs versus multidetector computed tomography. *Skeletal Radiol.* 2009, **38**(9), pp.887-93.

105. Saifuddin, A., Noordeen, H., Taylor, B.A., and Bayley, I. The role of imaging in the diagnosis and management of thoracolumbar burst fractures: current concepts and a review of the literature. *Skeletal Radiol.* 1996, **25**(7), pp.603-13.

106. Kuklo, T.R., Polly, D.W., Owens, B.D., Zeidman, S.M., Chang, A.S., and Klemme, W.R. Measurement of thoracic and lumbar fracture kyphosis: evaluation of intraobserver, interobserver, and technique variability. *Spine (Phila Pa 1976).* 2001, **26**(1), pp.61-5; discussion 66.

107. Takasu, M., Tani, C., Ishikawa, M., Date, S., Horiguchi, J., Kiguchi, M., Tamura, A., Sakai, A., Asaoku, H., Nango, N., and Awai, K. Multiple myeloma: microstructural analysis of lumbar trabecular bones in patients without visible bone lesions--preliminary results. *Radiology.* 2011, **260**(2), pp.472-9.

108. Oakland, R.J., Furtado, N.R., Timothy, J., and Hall, R.M. The biomechanics of vertebroplasty in multiple myeloma and metastatic bladder cancer: a preliminary cadaveric investigation. *J Neurosurg Spine.* 2008, **9**(5), pp.493-501.

109. Weber, M.H., Burch, S., Buckley, J., Schmidt, M.H., Fehlings, M.G., Vrionis, F.D., and Fisher, C.G. Instability and impending instability of the thoracolumbar spine in patients with spinal metastases: a systematic review. *Int J Oncol.* 2011, **38**(1), pp.5-12.

110. Sundaresan, N., Boriani, S., Rothman, A., and Holtzman, R. Tumors of the osseous spine. *J Neurooncol.* 2004, **69**(1-3), pp.273-90.

111. Nazarian, A., von Stechow, D., Zurakowski, D., Muller, R., and Snyder, B.D. Bone volume fraction explains the variation in strength and stiffness of cancellous bone affected by metastatic cancer and osteoporosis. *Calcif Tissue Int.* 2008, **83**(6), pp.368-79.

112. Kaufman, R.P., Ching, R.P., Willis, M.M., Mack, C.D., Gross, J.A., and Bulger, E.M. Burst fractures of the lumbar spine in frontal crashes. *Accid Anal Prev.* 2013, **59**, pp.153-63.

113. Petersilge, C.A., and Emery, S.E. Thoracolumbar burst fracture: evaluating stability. *Semin Ultrasound CT MR.* 1996, **17**(2), pp.105-13.

114. Yoganandan, N., Stemper, B.D., Baisden, J.L., Pintar, F.A., Paskoff, G.R., and Shender, B.S. Effects of acceleration level on lumbar spine injuries in military populations. *Spine J.* 2013.

115. Eardley, W.G., Bonner, T.J., Gibb, I.E., and Clasper, J.C. Spinal fractures in current military deployments. *J R Army Med Corps.* 2012, **158**(2), pp.101-5.

116. Lehman, R.A., Jr., Paik, H., Eckel, T.T., Helgeson, M.D., Cooper, P.B., and Bellabarba, C. Low lumbar burst fractures: a unique fracture mechanism sustained in our current overseas conflicts. *Spine J.* 2012, **12**(9), pp.784-90.

117. Dai, L.-Y., Jiang, S.-D., Wang, X.-Y., and Jiang, L.-S. A review of the management of thoracolumbar burst fractures. *Surg Neurol.* 2007, **67**(3), pp.221-231.

118. Oner, F.C., van der Rijt, R.R., Ramos, L.M., Dhert, W.J., and Verbout, A.J. Changes in the disc space after fractures of the thoracolumbar spine. *J Bone Joint Surg Br.* 1998, **80**(5), pp.833-9.

119. Heyde, C.E., Tschoeke, S.K., Hellmuth, M., Hostmann, A., Ertel, W., and Oberholzer, A. Trauma induces apoptosis in human thoracolumbar intervertebral discs. *BMC Clin Pathol.* 2006, **6**, p.5.

120. Dudli, S., Haschtmann, D., and Ferguson, S.J. Persistent degenerative changes in the intervertebral disc after burst fracture in an in vitro model mimicking physiological post-traumatic conditions. *Eur Spine J.* 2014.

121. Deng, Z., Zou, H., Cai, L., Ping, A., Wang, Y., and Ai, Q. The retrospective analysis of posterior short-segment pedicle instrumentation without fusion for thoracolumbar burst fracture with neurological deficit. *ScientificWorldJournal.* 2014, **2014**, p.457634.

122. Hashimoto, T., Kaneda, K., and Abumi, K. Relationship between traumatic spinal canal stenosis and neurologic deficits in thoracolumbar burst fractures. *Spine (Phila Pa 1976).* 1988, **13**(11), pp.1268-72.

123. Cammisa, F.P., Jr., Eismont, F.J., and Green, B.A. Dural laceration occurring with burst fractures and associated laminar fractures. *J Bone Joint Surg Am.* 1989, **71**(7), pp.1044-52.

124. Daffner, R.H., and Daffner, S.D. Vertebral injuries: detection and implications. *Eur J Radiol.* 2002, **42**(2), pp.100-16.

125. Lee, I.S., Kim, H.J., Lee, J.S., Kim, S.J., Jeong, Y.J., Kim, D.K., and Moon, T.Y. Dural tears in spinal burst fractures: predictable MR imaging findings. *AJNR Am J Neuroradiol.* 2009, **30**(1), pp.142-6.

126. Ozturk, C., Ersozlu, S., and Aydinli, U. Importance of greenstick lamina fractures in low lumbar burst fractures. *Int Orthop.* 2006, **30**(4), pp.295-8.

127. Tisot, R.A., and Avanzi, O. Laminar fractures as a severity marker in burst fractures of the thoracolumbar spine. *J Orthop Surg (Hong Kong).* 2009, **17**(3), pp.261-4.

128. Miller, C.A., Dewey, R.C., and Hunt, W.E. Impaction fracture of the lumbar vertebrae with dural tear. *J Neurosurg.* 1980, **53**(6), pp.765-71.

129. Harris, M.B. Commentary: Thoracolumbar spine fractures: is more knowledge better? *Spine J.* 2013, **13**(3), pp.222-3.

130. Bellabarba, C., Fisher, C., Chapman, J.R., Dettori, J.R., and Norvell, D.C. Does early fracture fixation of thoracolumbar spine fractures decrease morbidity or mortality? *Spine (Phila Pa 1976).* 2010, **35**(9 Suppl), pp.S138-45.

131. Rutges, J.P., Oner, F.C., and Leenen, L.P. Timing of thoracic and lumbar fracture fixation in spinal injuries: a systematic review of neurological and clinical outcome. *Eur Spine J.* 2007, **16**(5), pp.579-87.

132. McLain, R.F. Functional outcomes after surgery for spinal fractures: return to work and activity. *Spine (Phila Pa 1976).* 2004, **29**(4), pp.470-7; discussion Z6.

133. McLain, R.F. The biomechanics of long versus short fixation for thoracolumbar spine fractures. *Spine (Phila Pa 1976).* 2006, **31**(11 Suppl), pp.S70-9; discussion S104.

134. Cho, W., Cho, S.K., and Wu, C. The biomechanics of pedicle screw-based instrumentation. *J Bone Joint Surg Br.* 2010, **92**(8), pp.1061-5.

135. Erkan, S., Hsu, B., Wu, C., Mehbod, A.A., Perl, J., and Transfeldt, E.E. Alignment of pedicle screws with pilot holes: can tapping improve screw trajectory in thoracic spines? *Eur Spine J.* 2010, **19**(1), pp.71-7.

136. Pfeiffer, F.M., Abernathie, D.L., and Smith, D.E. A comparison of pullout strength for pedicle screws of different designs: a study using tapped and untapped pilot holes. *Spine (Phila Pa 1976).* 2006, **31**(23), pp.E867-70.

137. Sanden, B., Olerud, C., Larsson, S., and Robinson, Y. Insertion torque is not a good predictor of pedicle screw loosening after spinal instrumentation: a prospective study in 8 patients. *Patient Saf Surg.* 2010, **4**(1), p.14.

138. Sanden, B., Olerud, C., Petren-Mallmin, M., Johansson, C., and Larsson, S. The significance of radiolucent zones surrounding pedicle screws. Definition of

screw loosening in spinal instrumentation. *J Bone Joint Surg Br.* 2004, **86**(3), pp.457-61.

139. McLain, R.F., Burkus, J.K., and Benson, D.R. Segmental instrumentation for thoracic and thoracolumbar fractures: prospective analysis of construct survival and five-year follow-up. *Spine J.* 2001, **1**(5), pp.310-23.
140. Tezeren, G., and Kuru, I. Posterior fixation of thoracolumbar burst fracture: short-segment pedicle fixation versus long-segment instrumentation. *J Spinal Disord Tech.* 2005, **18**(6), pp.485-8.
141. Leferink, V.J., Nijboer, J.M., Zimmerman, K.W., Veldhuis, E.F., ten Vergert, E.M., and ten Duis, H.J. Burst fractures of the thoracolumbar spine: changes of the spinal canal during operative treatment and follow-up. *Eur Spine J.* 2003, **12**(3), pp.255-60.
142. Mohanty, S.P., Bhat, S.N., and Ishwara-Keerthi, C. The effect of posterior instrumentation of the spine on canal dimensions and neurological recovery in thoracolumbar and lumbar burst fractures. *Musculoskelet Surg.* 2011, **95**(2), pp.101-6.
143. Szivek, J.A., Roberto, R.F., and Margolis, D.S. In vivo strain measurements from hardware and lamina during spine fusion. *J Biomed Mater Res B Appl Biomater.* 2005, **75**(2), pp.243-50.
144. Cheng, L.M., Wang, J.J., Zeng, Z.L., Zhu, R., Yu, Y., Li, C., and Wu, Z.R. Pedicle screw fixation for traumatic fractures of the thoracic and lumbar spine. *Cochrane Database Syst Rev.* 2013, **5**, p.CD009073.
145. Shen, W.J., Liu, T.J., and Shen, Y.S. Nonoperative treatment versus posterior fixation for thoracolumbar junction burst fractures without neurologic deficit. *Spine (Phila Pa 1976).* 2001, **26**(9), pp.1038-45.
146. Wei, F.X., Liu, S.Y., Liang, C.X., Li, H.M., Long, H.Q., Yu, B.S., Chen, B.L., and Chen, K.B. Transpedicular fixation in management of thoracolumbar burst fractures: monosegmental fixation versus short-segment instrumentation. *Spine (Phila Pa 1976).* 2010, **35**(15), pp.E714-20.
147. Court, C., and Vincent, C. Percutaneous fixation of thoracolumbar fractures: current concepts. *Orthop Traumatol Surg Res.* 2012, **98**(8), pp.900-9.
148. Muralidhar, B.M., Hegde, D., and Hussain, P.S. Management of unstable thoracolumbar spinal fractures by pedicle screws and rods fixation. *J Clin Diagn Res.* 2014, **8**(2), pp.121-3.
149. Sanderson, P.L., Fraser, R.D., Hall, D.J., Cain, C.M., Osti, O.L., and Potter, G.R. Short segment fixation of thoracolumbar burst fractures without fusion. *Eur Spine J.* 1999, **8**(6), pp.495-500.
150. Wang, X.Y., Dai, L.Y., Xu, H.Z., and Chi, Y.L. Kyphosis recurrence after posterior short-segment fixation in thoracolumbar burst fractures. *J Neurosurg Spine.* 2008, **8**(3), pp.246-54.
151. Yang, H., Shi, J.H., Ebraheim, M., Liu, X., Konrad, J., Husain, I., Tang, T.S., and Liu, J. Outcome of thoracolumbar burst fractures treated with indirect reduction and fixation without fusion. *Eur Spine J.* 2011, **20**(3), pp.380-6.

152. Eckel, T.S., and Olan, W. Vertebroplasty and vertebral augmentation techniques. *Tech Vasc Interv Radiol.* 2009, **12**(1), pp.44-50.

153. Baroud, G., and Bohner, M. Biomechanical impact of vertebroplasty. Postoperative biomechanics of vertebroplasty. *Joint Bone Spine.* 2006, **73**(2), pp.144-50.

154. Maestretti, G., Sutter, P., Monnard, E., Ciarpaglini, R., Wahl, P., Hoogewoud, H., and Gautier, E. A prospective study of percutaneous balloon kyphoplasty with calcium phosphate cement in traumatic vertebral fractures: 10-year results. *Eur Spine J.* 2014, **23**(6), pp.1354-60.

155. Libicher, M., Hillmeier, J., Liegibel, U., Sommer, U., Pyerin, W., Vetter, M., Meinzer, H.P., Grafe, I., Meeder, P., Noldge, G., Nawroth, P., and Kasperk, C. Osseous integration of calcium phosphate in osteoporotic vertebral fractures after kyphoplasty: initial results from a clinical and experimental pilot study. *Osteoporos Int.* 2006, **17**(8), pp.1208-15.

156. Chen, C., Lv, G., Xu, B., Zhang, X., and Ma, X. Posterior short-segment instrumentation and limited segmental decompression supplemented with vertebroplasty with calcium sulphate and intermediate screws for thoracolumbar burst fractures. *Eur Spine J.* 2014, **23**(7), pp.1548-57.

157. Lewis, G. Injectable bone cements for use in vertebroplasty and kyphoplasty: state-of-the-art review. *J Biomed Mater Res B Appl Biomater.* 2006, **76**(2), pp.456-68.

158. Laredo, J.D., and Hamze, B. Complications of percutaneous vertebroplasty and their prevention. *Skeletal Radiol.* 2004, **33**(9), pp.493-505.

159. Grafe, I.A., Baier, M., Noldge, G., Weiss, C., Da Fonseca, K., Hillmeier, J., Libicher, M., Rudofsky, G., Metzner, C., Nawroth, P., Meeder, P.J., and Kasperk, C. Calcium-phosphate and polymethylmethacrylate cement in long-term outcome after kyphoplasty of painful osteoporotic vertebral fractures. *Spine (Phila Pa 1976).* 2008, **33**(11), pp.1284-90.

160. Gumpert, R., Bodo, K., Spuller, E., Poglitsch, T., Bindl, R., Ignatius, A., and Puchwein, P. Demineralization after balloon kyphoplasty with calcium phosphate cement: a histological evaluation in ten patients. *Eur Spine J.* 2014, **23**(6), pp.1361-8.

161. Verlaan, J.J., Oner, F.C., and Dhert, W.J. Anterior spinal column augmentation with injectable bone cements. *Biomaterials.* 2006, **27**(3), pp.290-301.

162. Limthongkul, W., Karaikovic, E.E., Savage, J.W., and Markovic, A. Volumetric analysis of thoracic and lumbar vertebral bodies. *Spine J.* 2010, **10**(2), pp.153-8.

163. Röder, C., Boszczyk, B., Perler, G., Aghayev, E., Kulling, F., and Maestretti, G. Cement volume is the most important modifiable predictor for pain relief in BKP: results from SWISSspine, a nationwide registry. *Eur Spine J.* 2013, **22**(10), pp.2241-8.

164. Frankel, B.M., Monroe, T., and Wang, C. Percutaneous vertebral augmentation: an elevation in adjacent-level fracture risk in kyphoplasty as compared with vertebroplasty. *Spine J.* 2007, **7**(5), pp.575-82.

165. Kayanja, M.M., Togawa, D., and Lieberman, I.H. Biomechanical changes after the augmentation of experimental osteoporotic vertebral compression fractures in the cadaveric thoracic spine. *Spine J.* 2005, **5**(1), pp.55-63.

166. Tzermiadianos, M.N., Renner, S.M., Phillips, F.M., Hadjipavlou, A.G., Zindrick, M.R., Havey, R.M., Voronov, M., and Patwardhan, A.G. Altered disc pressure profile after an osteoporotic vertebral fracture is a risk factor for adjacent vertebral body fracture. *Eur Spine J.* 2008, **17**(11), pp.1522-30.

167. Kolb, J.P., Kueny, R.A., Puschel, K., Boger, A., Rueger, J.M., Morlock, M.M., Huber, G., and Lehmann, W. Does the cement stiffness affect fatigue fracture strength of vertebrae after cement augmentation in osteoporotic patients? *Eur Spine J.* 2013, **22**(7), pp.1650-6.

168. Oakland, R.J., Furtado, N.R., Wilcox, R.K., Timothy, J., and Hall, R.M. Preliminary biomechanical evaluation of prophylactic vertebral reinforcement adjacent to vertebroplasty under cyclic loading. *Spine J.* 2009, **9**(2), pp.174-181.

169. Hulme, P.A., Boyd, S.K., Heini, P.F., and Ferguson, S.J. Differences in endplate deformation of the adjacent and augmented vertebra following cement augmentation. *Eur Spine J.* 2009, **18**(5), pp.614-23.

170. Nagaraja, S., Awada, H.K., Dreher, M.L., Gupta, S., and Miller, S.W. Vertebroplasty increases compression of adjacent IVDs and vertebrae in osteoporotic spines. *Spine J.* 2013, **12**(13), pp.1872-80.

171. Baroud, G., Heini, P., Nemes, J., Bohner, M., Ferguson, S., and Steffen, T. Biomechanical explanation of adjacent fractures following vertebroplasty. *Radiology.* 2003, **229**(2), pp.606-7; author reply 607-8.

172. Zhang, L., Zou, J., Gan, M., Shi, J., Li, J., and Yang, H. Treatment of thoracolumbar burst fractures: short-segment pedicle instrumentation versus kyphoplasty. *Acta Orthop Belg.* 2013, **79**, pp.718-725.

173. He, D., Wu, L., Sheng, X., Xiao, Q., Zhu, Y., Yu, W., Liu, F., and Zhu, K. Internal fixation with percutaneous kyphoplasty compared with simple percutaneous kyphoplasty for thoracolumbar burst fractures in elderly patients: a prospective randomized controlled trial. *Eur Spine J.* 2013, **22**(10), pp.2256-63.

174. Miyashita, T., Ataka, H., and Tanno, T. Clinical results of posterior stabilization without decompression for thoracolumbar burst fractures: is decompression necessary? *Neurosurg Rev.* 2012, **35**(3), pp.447-54; discussion 454-5.

175. Soultanis, K.C., Mavrogenis, A.F., Starantzis, K.A., Markopoulos, C., Stavropoulos, N.A., Mimidis, G., Kokkalis, Z.T., and Papagelopoulos, P.J. When and how to operate on thoracic and lumbar spine fractures? *Eur J Orthop Surg Traumatol.* 2013.

176. Verlaan, J.J., van de Kraats, E.B., Oner, F.C., van Walsum, T., Niessen, W.J., and Dhert, W.J. The reduction of endplate fractures during balloon vertebroplasty: a detailed radiological analysis of the treatment of burst fractures using pedicle screws, balloon vertebroplasty, and calcium phosphate cement. *Spine (Phila Pa 1976).* 2005, **30**(16), pp.1840-5.

177. Verlaan, J.J., Dhert, W.J., and Oner, F.C. Intervertebral disc viability after burst fractures of the thoracic and lumbar spine treated with pedicle screw fixation and direct end-plate restoration. *Spine J.* 2013, **13**(3), pp.217-21.

178. Wagner, S., Weckbach, A., and Muller-Gerbl, M. The influence of posterior instrumentation on adjacent and transfixed facet joints in patients with thoracolumbar spinal injuries: a morphological in vivo study using computerized tomography osteoabsorptiometry. *Spine (Phila Pa 1976).* 2005, **30**(7), pp.E169-78.

179. Bironneau, A., Bouquet, C., Millet-Barbe, B., Leclercq, N., Pries, P., and Gayet, L.E. Percutaneous internal fixation combined with kyphoplasty for neurologically intact thoracolumbar fractures: a prospective cohort study of 24 patients with one year of follow-up. *Orthop Traumatol Surg Res.* 2011, **97**(4), pp.389-95.

180. Afzal, S., Akbar, S., and Dhar, S.A. Short segment pedicle screw instrumentation and augmentation vertebroplasty in lumbar burst fractures: an experience. *Eur Spine J.* 2008, **17**(3), pp.336-41.

181. Fuentes, S., Blondel, B., Metellus, P., Gaudart, J., Adetchessi, T., and Dufour, H. Percutaneous kyphoplasty and pedicle screw fixation for the management of thoraco-lumbar burst fractures. *Eur Spine J.* 2010, **19**(8), pp.1281-7.

182. Korovessis, P., Repantis, T., Petsinis, G., Iliopoulos, P., and Hadjipavlou, A. Direct reduction of thoracolumbar burst fractures by means of balloon kyphoplasty with calcium phosphate and stabilization with pedicle-screw instrumentation and fusion. *Spine (Phila Pa 1976).* 2008, **33**(4), pp.E100-8.

183. Toyone, T., Tanaka, T., Kato, D., Kaneyama, R., and Otsuka, M. The treatment of acute thoracolumbar burst fractures with transpedicular intracorporeal hydroxyapatite grafting following indirect reduction and pedicle screw fixation: a prospective study. *Spine (Phila Pa 1976).* 2006, **31**(7), pp.E208-14.

184. Rajasekaran, S. Thoracolumbar burst fractures without neurological deficit: the role for conservative treatment. *Eur Spine J.* 2010, **19 Suppl 1**, pp.S40-7.

185. Ochia, R.S., and Ching, R.P. Rate dependence of hydraulic resistance in human lumbar vertebral bodies. *Spine (Phila Pa 1976).* 2006, **31**(22), pp.2569-74.

186. Shirado, O., Kaneda, K., Tadano, S., Ishikawa, H., McAfee, P.C., and Warden, K.E. Influence of disc degeneration on mechanism of thoracolumbar burst fractures. *Spine (Phila Pa 1976).* 1992, **17**(3), pp.286-92.

187. Ochia, R.S., Tencer, A.F., and Ching, R.P. Effect of loading rate on endplate and vertebral body strength in human lumbar vertebrae. *J Biomech.* 2003, **36**(12), pp.1875-81.

188. Stemper, B.D., Yoganandan, N., Baisden, J.L., Umale, S., Shah, A.S., Shender, B.S., and Paskoff, G.R. Rate-dependent fracture characteristics of lumbar vertebral bodies. *J Mech Behav Biomed Mater.* 2015, **41**, pp.271-79.

189. Hongo, M., Abe, E., Shimada, Y., Murai, H., Ishikawa, N., and Sato, K. Surface strain distribution on thoracic and lumbar vertebrae under axial compression. The role in burst fractures. *Spine (Phila Pa 1976).* 1999, **24**(12), pp.1197-202.

190. Wilcox, R.K., Allen, D.J., Hall, R.M., Limb, D., Barton, D.C., and Dickson, R.A. A dynamic investigation of the burst fracture process using a combined experimental and finite element approach. *Eur Spine J.* 2004, **13**(6), pp.481-8.

191. Langrana, N.A., Harten, R.R., Lin, D.C., Reiter, M.F., and Lee, C.K. Acute thoracolumbar burst fractures: a new view of loading mechanisms. *Spine (Phila Pa 1976).* 2002, **27**(5), pp.498-508.

192. Fakurnejad, S., Scheer, J.K., Patwardhan, A.G., Havey, R.M., Voronov, L.I., and Smith, Z.A. Biomechanics of thoracolumbar burst fractures: methods of induction and treatments. *J Clin Neurosci.* 2014, **21**(12), pp.2059-64.

193. Wang, X.Y., Dai, L.Y., Xu, H.Z., and Chi, Y.L. A comparison of single and incremental impact approaches for producing experimental thoracolumbar burst fractures. *J Neurosurg Spine.* 2007, **7**(2), pp.199-204.

194. Panjabi, M.M., Hoffman, H., Kato, Y., and Cholewicki, J. Superiority of incremental trauma approach in experimental burst fracture studies. *Clin Biomech (Bristol, Avon).* 2000, **15**(2), pp.73-8.

195. Kallemeier, P.M., Beaubien, B.P., Buttermann, G.R., Polga, D.J., and Wood, K.B. In vitro analysis of anterior and posterior fixation in an experimental unstable burst fracture model. *J Spinal Disord Tech.* 2008, **21**(3), pp.216-24.

196. Jones, H.L., Crawley, A.L., Noble, P.C., Schoenfeld, A.J., and Weiner, B.K. A novel method for the reproducible production of thoracolumbar burst fractures in human cadaveric specimens. *Spine J.* 2011, **11**(5), pp.447-51.

197. Carter, J.W., Mirza, S.K., Tencer, A.F., and Ching, R.P. Canal geometry changes associated with axial compressive cervical spine fracture. *Spine (Phila Pa 1976).* 2000, **25**(1), pp.46-54.

198. Zhu, Q., Lane, C., Ching, R.P., Gordon, J.D., Fisher, C.G., Dvorak, M.F., Cripton, P.A., and Oxland, T.R. Translational constraint influences dynamic spinal canal occlusion of the thoracic spine: an in vitro experimental study. *J Biomech.* 2008, **41**(1), pp.171-9.

199. Verlaan, J.J., van Helden, W.H., Oner, F.C., Verbout, A.J., and Dhert, W.J. Balloon vertebroplasty with calcium phosphate cement augmentation for direct restoration of traumatic thoracolumbar vertebral fractures. *Spine (Phila Pa 1976).* 2002, **27**(5), pp.543-8.

200. Verlaan, J.J., van de Kraats, E.B., Oner, F.C., van Walsum, T., Niessen, W.J., and Dhert, W.J. Bone displacement and the role of longitudinal ligaments during balloon vertebroplasty in traumatic thoracolumbar fractures. *Spine (Phila Pa 1976).* 2005, **30**(16), pp.1832-9.

201. Disch, A.C., and Schmoelz, W. Cement augmentation in a thoracolumbar fracture model: reduction and stability after balloon kyphoplasty versus vertebral body stenting. *Spine (Phila Pa 1976).* 2014, **39**(19), pp.E1147-53.

202. Kim, M.J., Lindsey, D.P., Hannibal, M., and Alamin, T.F. Vertebroplasty versus kyphoplasty: biomechanical behavior under repetitive loading conditions. *Spine (Phila Pa 1976).* 2006, **31**(18), pp.2079-84.

203. Wilke, H.J., Mehnert, U., Claes, L.E., Bierschneider, M.M., Jaksche, H., and Boszczyk, B.M. Biomechanical evaluation of vertebroplasty and kyphoplasty

with polymethyl methacrylate or calcium phosphate cement under cyclic loading. *Spine (Phila Pa 1976).* 2006, **31**(25), pp.2934-41.

204. Oakland, R.J., Furtado, N.R., Wilcox, R.K., Timothy, J., and Hall, R.M. The biomechanical effectiveness of prophylactic vertebroplasty: a dynamic cadaveric study. *J Neurosurg Spine.* 2008, **8**(5), pp.442-9.

205. Perry, T.G., Mageswaran, P., Colbrunn, R.W., Bonner, T.F., Francis, T., and McLain, R.F. Biomechanical evaluation of a simulated T-9 burst fracture of the thoracic spine with an intact rib cage. *J Neurosurg Spine.* 2014, **21**(3), pp.481-8.

206. Ponnappan, R.K., Serhan, H., Zarda, B., Patel, R., Albert, T., and Vaccaro, A.R. Biomechanical evaluation and comparison of polyetheretherketone rod system to traditional titanium rod fixation. *Spine J.* 2009, **9**(3), pp.263-7.

207. Doulgeris, J.J., Aghayev, K., Gonzalez-Blohm, S.A., Del Valle, M., Waddell, J., Lee, W.E., 3rd, and Vrionis, F.D. Comparative analysis of posterior fusion constructs as treatments for middle and posterior column injuries: an in vitro biomechanical investigation. *Clin Biomech (Bristol, Avon).* 2013, **28**(5), pp.483-9.

208. An, H.S., Singh, K., Vaccaro, A.R., Wang, G., Yoshida, H., Eck, J., McGrady, L., and Lim, T.H. Biomechanical evaluation of contemporary posterior spinal internal fixation configurations in an unstable burst-fracture calf spine model: special references of hook configurations and pedicle screws. *Spine (Phila Pa 1976).* 2004, **29**(3), pp.257-62.

209. Ma, J., Jia, H., Ma, X., Xu, W., Yu, J., Feng, R., Wang, J., Xing, D., Wang, Y., Zhu, S., Yang, Y., Chen, Y., and Ma, B. Evaluation of the stress distribution change at the adjacent facet joints after lumbar fusion surgery: A biomechanical study. *Proc Inst Mech Eng H.* 2014.

210. Hartensuer, R., Gehweiler, D., Schulze, M., Matuszewski, L., Raschke, M.J., and Vordemvenne, T. Biomechanical evaluation of combined short segment fixation and augmentation of incomplete osteoporotic burst fractures. *BMC Musculoskelet Disord.* 2013, **14**, p.360.

211. Bozkus, H., Senoglu, M., Baek, S., Sawa, A.G., Ozer, A.F., Sonntag, V.K., and Crawford, N.R. Dynamic lumbar pedicle screw-rod stabilization: in vitro biomechanical comparison with standard rigid pedicle screw-rod stabilization. *J Neurosurg Spine.* 2010, **12**(2), pp.183-9.

212. Meyers, K., Tauber, M., Sudin, Y., Fleischer, S., Arnin, U., Girardi, F., and Wright, T. Use of instrumented pedicle screws to evaluate load sharing in posterior dynamic stabilization systems. *Spine J.* 2008, **8**(6), pp.926-32.

213. Cripton, P.A., Jain, G.M., Wittenberg, R.H., and Nolte, L.P. Load-sharing characteristics of stabilized lumbar spine segments. *Spine (Phila Pa 1976).* 2000, **25**(2), pp.170-9.

214. Kettler, A., Niemeyer, T., Issler, L., Merk, U., Mahalingam, M., Werner, K., Claes, L., and Wilke, H.J. In vitro fixator rod loading after transforaminal compared to anterior lumbar interbody fusion. *Clin Biomech (Bristol, Avon).* 2006, **21**(5), pp.435-42.

215. Melnyk, A.D., Wen, T.L., Kingwell, S., Chak, J.D., Singh, V., Cripton, P.A., Fisher, C.G., Dvorak, M.F., and Oxland, T.R. Load transfer characteristics between posterior spinal implants and the lumbar spine under anterior shear loading: an in vitro investigation. *Spine (Phila Pa 1976).* 2012, **37**(18), pp.E1126-33.

216. Mermelstein, L.E., McLain, R.F., and Yerby, S.A. Reinforcement of thoracolumbar burst fractures with calcium phosphate cement. A biomechanical study. *Spine (Phila Pa 1976).* 1998, **23**(6), pp.664-70; discussion 670-1.

217. BS-ISO-12189:2008. *Implants for surgery - Mechanical testing of implantable spinal devices - Fatigue test method for spinal implant assemblies using an anterior support.* London: BSI Group, 2008.

218. ASTM-F1717-14. *Standard Test Methods for Spinal Implant Constructs in a Vertebrectomy Model.* West Conshohocken, PA: ASTM International, 2014.

219. Hahn, M., Nassutt, R., Delling, G., Mahrenholtz, O., Schneider, E., and Morlock, M. The influence of material and design features on the mechanical properties of transpedicular spinal fixation implants. *J Biomed Mater Res.* 2002, **63**(3), pp.354-62.

220. Lindsey, C., Deviren, V., Xu, Z., Yeh, R.F., and Puttlitz, C.M. The effects of rod contouring on spinal construct fatigue strength. *Spine (Phila Pa 1976).* 2006, **31**(15), pp.1680-7.

221. Nguyen, T.Q., Buckley, J.M., Ames, C., and Deviren, V. The fatigue life of contoured cobalt chrome posterior spinal fusion rods. *Proc Inst Mech Eng H.* 2011, **225**(2), pp.194-8.

222. Wilke, H.J., Jungkunz, B., Wenger, K., and Claes, L.E. Spinal segment range of motion as a function of in vitro test conditions: effects of exposure period, accumulated cycles, angular-deformation rate, and moisture condition. *Anat Rec.* 1998, **251**(1), pp.15-9.

223. Morgenstern, W., Ferguson, S.J., Berey, S., Orr, T.E., and Nolte, L.P. Posterior thoracic extrapedicular fixation: a biomechanical study. *Spine (Phila Pa 1976).* 2003, **28**(16), pp.1829-35.

224. Huber, G., Skrzypiec, D.M., Klein, A., Puschel, K., and Morlock, M.M. High cycle fatigue behaviour of functional spinal units. *Ind Health.* 2010, **48**(5), pp.550-6.

225. Muller, R., Gerber, S.C., and Hayes, W.C. Micro-compression: a novel technique for the nondestructive assessment of local bone failure. *Technol Health Care.* 1998, **6**(5-6), pp.433-44.

226. Christen, D., Levchuk, A., Schori, S., Schneider, P., Boyd, S.K., and Muller, R. Deformable image registration and 3D strain mapping for the quantitative assessment of cortical bone microdamage. *J Mech Behav Biomed Mater.* 2012, **8**, pp.184-93.

227. Thurner, P.J., Wyss, P., Voide, R., Stauber, M., Stampanoni, M., Sennhauser, U., and Muller, R. Time-lapsed investigation of three-dimensional failure and damage accumulation in trabecular bone using synchrotron light. *Bone.* 2006, **39**(2), pp.289-99.

228. Wu, G., Siegler, S., Allard, P., Kirtley, C., Leardini, A., Rosenbaum, D., Whittle, M., D'Lima, D.D., Cristofolini, L., Witte, H., Schmid, O., Stokes, I., Standardization, and Terminology Committee of the International Society of, B. ISB recommendation on definitions of joint coordinate system of various joints for the reporting of human joint motion--part I: ankle, hip, and spine. International Society of Biomechanics. *J Biomech.* 2002, **35**(4), pp.543-8.

229. Hazewinkel, M. *Encyclopedia of Mathematics.* [Online]. 2012. [Accessed]. Available from: http://www.encyclopediaofmath.org/

230. Lu, Y., Rosenau, E., Paetzold, H., Klein, A., Puschel, K., Morlock, M.M., and Huber, G. Strain changes on the cortical shell of vertebral bodies due to spine ageing: A parametric study using a finite element model evaluated by strain measurements. *Proc Inst Mech Eng H.* 2013.

231. Villa, T., La Barbera, L., and Galbusera, F. Comparative analysis of international standards for the fatigue testing of posterior spinal fixation systems. *Spine J.* 2013.

232. Melnyk, A.D., Chak, J.D., Cripton, P.A., Dvorak, M.F., and Oxland, T.R. Shear force measurements on low- and high-stiffness posterior fusion devices. *Med Eng Phys.* 2012, **34**(9), pp.1260-7.

233. Bergmann, G., Graichen, F., Rohlmann, A., Westerhoff, P., Heinlein, B., Bender, A., and Ehrig, R. Design and calibration of load sensing orthopaedic implants. *J Biomech Eng.* 2008, **130**(2), p.021009.

234. Hannah, R.L., and Reed, S.E. *Strain gage users' handbook.* Springer, 1992.

235. Zannoni, C., Mantovani, R., and Viceconti, M. Material properties assignment to finite element models of bone structures: a new method. *Med Eng Phys.* 1998, **20**(10), pp.735-40.

236. Hojjat, S.P., Beek, M., Akens, M.K., and Whyne, C.M. Can micro-imaging based analysis methods quantify structural integrity of rat vertebrae with and without metastatic involvement? *J Biomech.* 2012, **45**(14), pp.2342-8.

237. Herblum, R., Beek, M., and Whyne, C.M. muFEA successfully exhibits higher stresses and strains in microdamaged regions of whole vertebrae. *J Orthop Res.* 2013, **31**(10), pp.1653-60.

238. Roberts, N., Brandolini, N., Kapur, N., Whyne, C., and Hall, R.M. Using Micro-CT Derived Boundary Conditions to Evaluate Structural Stability of Multiple Myeloma Infiltrated Vertebrae. In: *WCB*, *Boston, USA*. 2014.

239. Tarsuslugil, S.M., O'Hara, R.M., Dunne, N.J., Buchanan, F.J., Orr, J.F., Barton, D.C., and Wilcox, R.K. Development of calcium phosphate cement for the augmentation of traumatically fractured porcine specimens using vertebroplasty. *J Biomech.* 2013, **46**(4), pp.711-5.

240. Schneider, C.A., Rasband, W.S., and Eliceiri, K.W. NIH Image to ImageJ: 25 years of image analysis. *Nat Methods.* 2012, **9**(7), pp.671-5.

241. Doube, M., Klosowski, M., Arganda-Carreras, I., Cordelieres, F., Dougherty, R., Jackson, J., Schmid, B., Hutchinson, J., and Shefelbine, S. BoneJ: Free and extensible bone image analysis in ImageJ. *Bone.* 2010, **47**(6), pp.1076-1079.

242. Furtado, N., Oakland, R.J., Wilcox, R.K., and Hall, R.M. A biomechanical investigation of vertebroplasty in osteoporotic compression fractures and in prophylactic vertebral reinforcement. *Spine (Phila Pa 1976).* 2007, **32**(17), pp.E480-7.

243. Duval-Beaupere, G., and Robain, G. Visualization on full spine radiographs of the anatomical connections of the centres of the segmental body mass supported by each vertebra and measured in vivo. *Int Orthop.* 1987, **11**(3), pp.261-9.

244. Fensky, F., Kueny, R.A., Sellenschloh, K., Puschel, K., Morlock, M.M., Rueger, J.M., Lehmann, W., Huber, G., and Hansen-Algenstaedt, N. Biomechanical advantage of C1 pedicle screws over C1 lateral mass screws: a cadaveric study. *Eur Spine J.* 2013.

245. Bland, J.M., and Altman, D.G. Statistical methods for assessing agreement between two methods of clinical measurement. *Lancet.* 1986, **1**(8476), pp.307-10.

246. Whyne, C.M., Hu, S.S., and Lotz, J.C. Burst fracture in the metastatically involved spine: development, validation, and parametric analysis of a three-dimensional poroelastic finite-element model. *Spine (Phila Pa 1976).* 2003, **28**(7), pp.652-60.

247. Grant, J.P., Oxland, T.R., and Dvorak, M.F. Mapping the structural properties of the lumbosacral vertebral endplates. *Spine (Phila Pa 1976).* 2001, **26**(8), pp.889-96.

248. Dall'Ara, E., Varga, P., Pahr, D., and Zysset, P. A calibration methodology of QCT BMD for human vertebral body with registered micro-CT images. *Med Phys.* 2011, **38**(5), pp.2602-8.

249. Jones, A.C., and Wilcox, R.K. Assessment of factors influencing finite element vertebral model predictions. *J Biomech Eng.* 2007, **129**(6), pp.898-903.

250. Chevalier, Y., Pahr, D., and Zysset, P.K. The role of cortical shell and trabecular fabric in finite element analysis of the human vertebral body. *J Biomech Eng.* 2009, **131**(11), p.111003.

251. Buckley, J.M., Loo, K., and Motherway, J. Comparison of quantitative computed tomography-based measures in predicting vertebral compressive strength. *Bone.* 2007, **40**(3), pp.767-74.

252. Christiansen, B.A., Kopperdahl, D.L., Kiel, D.P., Keaveny, T.M., and Bouxsein, M.L. Mechanical contributions of the cortical and trabecular compartments contribute to differences in age-related changes in vertebral body strength in men and women assessed by QCT-based finite element analysis. *J Bone Miner Res.* 2011, **26**(5), pp.974-83.

253. Dall'Ara, E., Schmidt, R., Pahr, D., Varga, P., Chevalier, Y., Patsch, J., Kainberger, F., and Zysset, P. A nonlinear finite element model validation study based on a novel experimental technique for inducing anterior wedge-shape fractures in human vertebral bodies in vitro. *J Biomech.* 2010, **43**(12), pp.2374-80.

254. Maquer, G., Dall'ara, E., and Zysset, P.K. Removal of the cortical endplates has little effect on ultimate load and damage distribution in QCT-based voxel

models of human lumbar vertebrae under axial compression. *J Biomech.* 2012, **45**(9), pp.1733-8.

255. El-Rich, M., Arnoux, P.J., Wagnac, E., Brunet, C., and Aubin, C.E. Finite element investigation of the loading rate effect on the spinal load-sharing changes under impact conditions. *J Biomech.* 2009, **42**(9), pp.1252-62.

256. Liebschner, M.A., Kopperdahl, D.L., Rosenberg, W.S., and Keaveny, T.M. Finite element modeling of the human thoracolumbar spine. *Spine (Phila Pa 1976).* 2003, **28**(6), pp.559-65.

257. Yoganandan, N., Arun, M.W., Stemper, B.D., Pintar, F.A., and Maiman, D.J. Biomechanics of human thoracolumbar spinal column trauma from vertical impact loading. *Ann Adv Automot Med.* 2013, **57**, pp.155-66.

258. Hall, R.M., Oakland, R.J., Wilcox, R.K., and Barton, D.C. Spinal cord-fragment interactions following burst fracture: an in vitro model. *J Neurosurg Spine.* 2006, **5**(3), pp.243-50.

259. Ohman, C., Baleani, M., Perilli, E., Dall'Ara, E., Tassani, S., Baruffaldi, F., and Viceconti, M. Mechanical testing of cancellous bone from the femoral head: experimental errors due to off-axis measurements. *J Biomech.* 2007, **40**(11), pp.2426-33.

260. Beckstein, J.C., Sen, S., Schaer, T.P., Vresilovic, E.J., and Elliott, D.M. Comparison of animal discs used in disc research to human lumbar disc: axial compression mechanics and glycosaminoglycan content. *Spine (Phila Pa 1976).* 2008, **33**(6), pp.E166-73.

261. Wang, Y., Liu, G., Li, T., Xiao, Y., Han, Q., Xu, R., and Li, Y. Morphometric comparison of the lumbar cancellous bone of sheep, deer, and humans. *Comp Med.* 2010, **60**(5), pp.374-9.

262. Bayraktar, H.H., Morgan, E.F., Niebur, G.L., Morris, G.E., Wong, E.K., and Keaveny, T.M. Comparison of the elastic and yield properties of human femoral trabecular and cortical bone tissue. *J Biomech.* 2004, **37**(1), pp.27-35.

263. Ivancic, P.C. Hybrid cadaveric/surrogate model of thoracolumbar spine injury due to simulated fall from height. *Accid Anal Prev.* 2013, **59C**, pp.185-191.

264. Figliola, R.S., and Beasley, D.E. *Theory and Design for Mechanical Measurements.* 6th ed. Wiley, 2015.

265. Mehta, J.S., Reed, M.R., McVie, J.L., and Sanderson, P.L. Weight-bearing radiographs in thoracolumbar fractures: do they influence management? *Spine (Phila Pa 1976).* 2004, **29**(5), pp.564-7.

266. Saari, A., Dennison, C.R., Zhu, Q., Nelson, T.S., Morley, P., Oxland, T.R., Cripton, P.A., and Itshayek, E. Compressive follower load influences cervical spine kinematics and kinetics during simulated head-first impact in an in vitro model. *J Biomech Eng.* 2013, **135**(11), p.111003.

267. Langrana, N.A., Kale, S.P., Edwards, W.T., Lee, C.K., and Kopacz, K.J. Measurement and analyses of the effects of adjacent end plate curvatures on vertebral stresses. *Spine J.* 2006, **6**(3), pp.267-78.

268. Heggeness, M.H., and Doherty, B.J. The trabecular anatomy of thoracolumbar vertebrae: implications for burst fractures. *J Anat.* 1997, **191 (Pt 2)**, pp.309-12.

269. Wilcox, R.K., Boerger, T.O., Allen, D.J., Barton, D.C., Limb, D., Dickson, R.A., and Hall, R.M. A dynamic study of thoracolumbar burst fractures. *J Bone Joint Surg Am.* 2003, **85-A**(11), pp.2184-9.

270. de Bakker, P.M., Manske, S.L., Ebacher, V., Oxland, T.R., Cripton, P.A., and Guy, P. During sideways falls proximal femur fractures initiate in the superolateral cortex: evidence from high-speed video of simulated fractures. *J Biomech.* 2009, **42**(12), pp.1917-25.

271. Ballock, R.T., Mackersie, R., Abitbol, J.J., Cervilla, V., Resnick, D., and Garfin, S.R. Can burst fractures be predicted from plain radiographs? *J Bone Joint Surg Br.* 1992, **74**(1), pp.147-50.

272. Martijn, A., and Veldhuis, E.F. The diagnostic value of interpediculate distance assessment on plain films in thoracic and lumbar spine injuries. *J Trauma.* 1991, **31**(10), pp.1393-5.

273. Quinn, K.P., and Winkelstein, B.A. Altered collagen fiber kinematics define the onset of localized ligament damage during loading. *J Appl Physiol (1985).* 2008, **105**(6), pp.1881-8.

274. Lakshmanan, P., Purushothaman, B., Dvorak, V., Schratt, W., Thambiraj, S., and Boszczyk, M. Sagittal endplate morphology of the lower lumbar spine. *Eur Spine J.* 2012, **21 Suppl 2**, pp.S160-4.

275. Wang, X.Y., Dai, L.Y., Xu, H.Z., and Chi, Y.L. The load-sharing classification of thoracolumbar fractures: an in vitro biomechanical validation. *Spine (Phila Pa 1976).* 2007, **32**(11), pp.1214-9.

276. Marini, G., and Ferguson, S.J. Nonlinear numerical analysis of the structural response of the intervertebral disc to impact loading. *Comput Methods Biomech Biomed Engin.* 2014, **17**(9), pp.1002-11.

277. Jackman, T.M., Hussein, A.I., Adams, A.M., Makhnejia, K.K., and Morgan, E.F. Endplate deflection is a defining feature of vertebral fracture and is associated with properties of the underlying trabecular bone. *J Orthop Res.* 2014, **32**(7), pp.880-6.

278. Zhao, F.D., Pollintine, P., Hole, B.D., Adams, M.A., and Dolan, P. Vertebral fractures usually affect the cranial endplate because it is thinner and supported by less-dense trabecular bone. *Bone.* 2009, **44**(2), pp.372-9.

279. Wang, Y., Battie, M.C., Boyd, S.K., and Videman, T. The osseous endplates in lumbar vertebrae: thickness, bone mineral density and their associations with age and disk degeneration. *Bone.* 2011, **48**(4), pp.804-9.

280. Deviren, V., Tang, J.A., Scheer, J.K., Buckley, J.M., Pekmezci, M., McClellan, R.T., and Ames, C.P. Construct Rigidity after Fatigue Loading in Pedicle Subtraction Osteotomy with or without Adjacent Interbody Structural Cages. *Global Spine J.* 2012, **2**(4), pp.213-20.

281. Lubelski, D., Healy, A.T., Mageswaran, P., Benzel, E.C., and Mroz, T.E. Biomechanics of the lower thoracic spine after decompression and fusion: a cadaveric analysis. *Spine J.* 2014.

282. Wang, J.L., Chiang, C.K., Kuo, Y.W., Chou, W.K., and Yang, B.D. Mechanism of fractures of adjacent and augmented vertebrae following simulated vertebroplasty. *J Biomech.* 2012, **45**(8), pp.1372-8.

283. Hulme, P.A., Krebs, J., Ferguson, S.J., and Berlemann, U. Vertebroplasty and kyphoplasty: a systematic review of 69 clinical studies. *Spine (Phila Pa 1976).* 2006, **31**(17), pp.1983-2001.

284. Nieuwenhuijse, M.J., Van Erkel, A.R., and Dijkstra, P.D. Cement leakage in percutaneous vertebroplasty for osteoporotic vertebral compression fractures: identification of risk factors. *Spine J.* 2011.

285. Lador, R., Dreiangel, N., Ben-Galim, P.J., and Hipp, J.A. A pictorial classification atlas of cement extravasation with vertebral augmentation. *Spine J.* 2010, **10**(12), pp.1118-27.

286. Rohlmann, A., Zander, T., and Bergmann, G. Spinal loads after osteoporotic vertebral fractures treated by vertebroplasty or kyphoplasty. *Eur Spine J.* 2006, **15**(8), pp.1255-64.

287. Oner, F.C., Verlaan, J.J., Verbout, A.J., and Dhert, W.J. Cement augmentation techniques in traumatic thoracolumbar spine fractures. *Spine (Phila Pa 1976).* 2006, **31**(11 Suppl), pp.S89-95; discussion S104.

288. Fribourg, D., Tang, C., Sra, P., Delamarter, R., and Bae, H. Incidence of subsequent vertebral fracture after kyphoplasty. *Spine (Phila Pa 1976).* 2004, **29**(20), pp.2270-6; discussion 2277.

289. Rahamimov, N., Mulla, H., Shani, A., and Freiman, S. Percutaneous augmented instrumentation of unstable thoracolumbar burst fractures. *Eur Spine J.* 2012, **21**(5), pp.850-4.

290. Yuan, H.A., Garfin, S.R., Dickman, C.A., and Mardjetko, S.M. A Historical Cohort Study of Pedicle Screw Fixation in Thoracic, Lumbar, and Sacral Spinal Fusions. *Spine (Phila Pa 1976).* 1994, **19**(20 Suppl), pp.2279S-2296S.

291. Hansson, T.H., Keller, T.S., and Spengler, D.M. Mechanical behavior of the human lumbar spine. II. Fatigue strength during dynamic compressive loading. *J Orthop Res.* 1987, **5**(4), pp.479-87.

292. Purcell, P., Tyndyk, M., McEvoy, F., Tiernan, S., and Morris, S. A parametric finite element analysis of the compacted bone-cement interface following balloon kyphoplasty. *Proc Inst Mech Eng H.* 2014, **228**(1), pp.89-97.

293. Evans, S.L. Fatigue crack propagation under variable amplitude loading in PMMA and bone cement. *J Mater Sci Mater Med.* 2007, **18**(9), pp.1711-7.

294. Kotani, Y., Cunningham, B.W., Cappuccino, A., Kaneda, K., and McAfee, P.C. The effects of spinal fixation and destabilization on the biomechanical and histologic properties of spinal ligaments. An in vivo study. *Spine (Phila Pa 1976).* 1998, **23**(6), pp.672-82; discussion 682-3.

295. Luo, J., Bertram, W., Sangar, D., Adams, M.A., Annesley-Williams, D.J., and Dolan, P. Is kyphoplasty better than vertebroplasty in restoring normal mechanical function to an injured spine? *Bone.* 2010, **46**(4), pp.1050-7.

296. Adams, M.A., Freeman, B.J., Morrison, H.P., Nelson, I.W., and Dolan, P. Mechanical initiation of intervertebral disc degeneration. *Spine (Phila Pa 1976).* 2000, **25**(13), pp.1625-36.

297. Luo, J., Daines, L., Charalambous, A., Adams, M.A., Annesley-Williams, D.J., and Dolan, P. Vertebroplasty: Only Small Cement Volumes Are Required to Normalize Stress Distributions on the Vertebral Bodies. *Spine (Phila Pa 1976).* 2009, **34**(26), pp.2865-73.

298. Xu, G., Fu, X., Du, C., Ma, J., Li, Z., and Ma, X. Biomechanical effects of vertebroplasty on thoracolumbar burst fracture with transpedicular fixation: a finite element model analysis. *Orthop Traumatol Surg Res.* 2014, **100**(4), pp.379-83.

299. Hedrick, T.L. Software techniques for two- and three-dimensional kinematic measurements of biological and biomimetic systems. *Bioinspir Biomim.* 2008, **3**(3), p.034001.

300. Grassi, L., Vaananen, S.P., Yavari, S.A., Jurvelin, J.S., Weinans, H., Ristinmaa, M., Zadpoor, A.A., and Isaksson, H. Full-field strain measurement during mechanical testing of the human femur at physiologically relevant strain rates. *J Biomech Eng.* 2014, **136**(11).

301. Holt, C.A., Evans, S.L., Dillon, D., and Ahuja, S. Three-dimensional measurement of intervertebral kinematics in vitro using optical motion analysis. *Proc Inst Mech Eng H.* 2005, **219**(6), pp.393-9.

302. Pollintine, P., Luo, J., Offa-Jones, B., Dolan, P., and Adams, M.A. Bone creep can cause progressive vertebral deformity. *Bone.* 2009, **45**(3), pp.466-72.

303. Korez, R., Ibragimov, B.A., Likar, B., Pernus, F., and Vrtovec, T. A Framework for Automated Spine and Vertebrae Interpolation-Based Detection and Model-Based Segmentation. *IEEE Trans Med Imaging.* 2015.

Appendix A

Details of the surgical procedure described in 2.2.3.1.

Details of SSPI procedure (carried out on all the samples).

Donor	Level	Group	Screw size		Pedicle breach		Loose screw	
			Length	Diameter	Left	Right	Left	Right
A	T9	SSPI	5.5	35	✗	✓	✗	✗
A	T11	SSPI	5.5	35	✗	✗	✗	✗
A	T12	SSPI – KP	5.5	40	✗	✗	✗	✗
A	L2	SSPI – KP	6.5	40	✗	✗	✗	✗
A	L3	SSPI	6.5	40	✓	✗	✗	✗
A	L5	SSPI	6.5	40	✗	✗	✗	✗
B	T9	SSPI	5.5	35	✗	✗	✗	✗
B	T11	SSPI	5.5	35	✗	✗	✗	✓
B	T12	SSPI	5.5	40	✗	✗	✓	✗
B	L2	SSPI	6.5	40	✗	✗	✗	✗
B	L3	SSPI – KP	6.5	35	✗	✗	✗	✗
B	L5	SSPI – KP	6.5	40	✗	✗	✓	✓
C	T9	SSPI – KP	5.5	40	✗	✗	✗	✗
C	T11	SSPI – KP	5.5	40	✗	✗	✓	✓
C	T12	SSPI – KP	6.5	35	✗	✗	✗	✗
C	L2	SSPI – KP	6.5	35	✗	✗	✗	✗
C	L3	SSPI	6.5	35	✗	✗	✓	✓
C	L5	SSPI	6.5	45	✗	✗	✗	✗
D	T9	SSPI – KP	5.5	35	✗	✓	✗	✗
D	T11	SSPI – KP	5.5	35	✗	✗	✗	✗
D	T12	SSPI	5.5	35	✓	✗	✗	✗
D	L2	SSPI	5.5	40	✗	✗	✗	✗
D	L3	SSPI – KP	6.5	35	✗	✗	✗	✗
D	L5	SSPI – KP	5.5	45	✗	✗	✗	✗

Screw was considered loose when extraction torque < 0.4 Nm.

Details of KP procedure (carried out on the SSPI – KP samples following SSPI).

Donor	Level	BIV	Max pressure		CV	Injected		CV_{exp}	Leakage
		(ml)	Left	Right	(ml)	Left	Right	(ml)	
A	L1	6.4	113	134	8.0	4	4	8	✓
B	L4	7.8	59†	51†	9.8	4.9	4.9	9.8	✓
C	L1	8.7	135	160	10.8	6	5.5	10.5	✓
C	T10	6	160	155	7.6	4	4	8	✗
D	T10	4.9	58	65	6.1	3	3	6	✓
D	L4	8	130	350‡	10.2	4	5	9	✗

BIV: total IBTs inflation volume; Max pressure: maximum pressure (psi) reached during the inflation of the IBT; CV: target cement volume; Injected: volume of cement (ml) injected per pedicle; CV_{exp}: total cement volume actually injected.

† Inflation was performed by placing two IBT, which were inflated by alternating one syringe (following previous breakage of the syringe nozzle, see below). ‡ The maximum pressure was exceeded at ~1.25 ml and the nozzle of the syringe broke. The balloon was removed and dedicated curette was inserted through the cannula to widen the initial cavity for the IBT (see figure below).

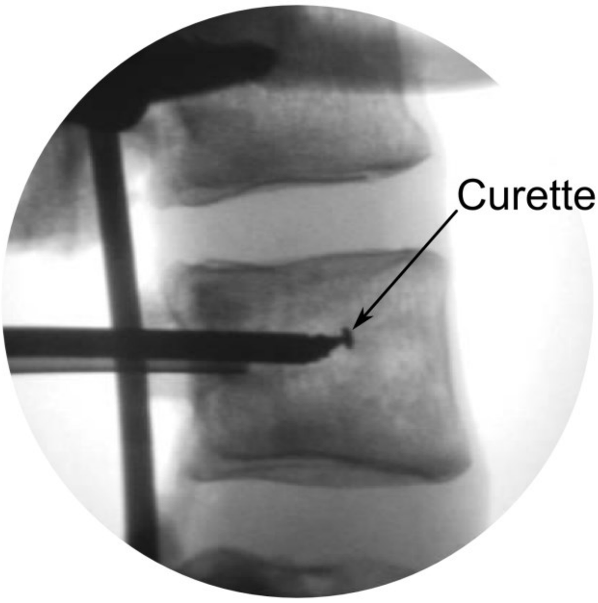

Transpedicular widening of the IBT cavity with specific instrumentation.

Appendix B

Summarised results and curves from fatigue testing of treated segments

Mean values calculated per each signal at the beginning of the test.

Donor	Level	Group	Load (N)	Axial displacement (mm)	Posterior displacement (mm)	Anterior displacement (mm)	Left strain gauge (με)	Right strain gauge (με)	Stiffness rising edge (N/mm)	Stiffness falling edge (N/mm)
A	T9-T10-T11	SSPI	-99.4	-0.32	-0.20	0.08	342	35	633	597
A	T12-L1-L2	SSPI – KP	-119.2	-0.30	-0.86	0.11	216	228	544	530
A	L3-L4-L5	SSPI	-139.0	-0.36	-0.25	0.14	292	257	621	603
B	T9-T10-T11	SSPI	-160.6	-1.74	-2.44	2.58	395	242	352	324
B	T12-L1-L2	SSPI	-197.1	-6.23	5.43	-0.91	756	169	130	113
B	L3-L4-L5	SSPI – KP	-229.0	-1.30	0.43	-0.81	552	333	488	461
C	T9-T10-T11	SSPI – KP	-124.2	-0.55	-0.29	0.18	223	147	666	617
C	T12-L1-L2	SSPI – KP	-149.1	-0.43	0.07	0.01	242	313	732	710
C	L3-L4-L5	SSPI	-179.2	-1.03	1.11	-0.64	304	348	426	406
D	T9-T10-T11	SSPI – KP	-149.2	-0.50	-0.58	0.51	214	254	482	463
D	T12-L1-L2	SSPI	-184.1	-1.12	-0.80	0.72	407	336	372	352
D	L3-L4-L5	SSPI – KP	-219.1	-1.04	0.00	0.17	308	487	479	453
Median			-155.9	-0.79	-0.23	0.13	306	255	485	462

Mean values calculated per each signal at the end of the test.

Donor	Level	Group	Load (N)	Axial displacement (mm)	Posterior displacement (mm)	Anterior displacement (mm)	Left strain gauge (με)	Right strain gauge (με)	Stiffness rising edge (N/mm)	Stiffness falling edge (N/mm)
A	T9-T10-T11	SSPI	-99.7	-0.47	-0.40	-0.04	439	64	632	577
A	T12-L1-L2	SSPI – KP	-119.1	-0.39	-1.23	0.08	233	228	535	518
A	L3-L4-L5	SSPI	-139.0	-0.49	-0.28	0.05	329	319	616	594
B	T9-T10-T11	SSPI	-161.5	-2.91	-4.45	4.79	379	264	365	324
B	T12-L1-L2	SSPI	-192.8	-11.02	-6.08	-5.66	342	368	139	125
B	L3-L4-L5	SSPI – KP	-231.6	-6.67	2.27	-2.01	195	347	421	377
C	T9-T10-T11	SSPI – KP	-124.3	-0.77	-0.39	0.08	209	230	682	646
C	T12-L1-L2	SSPI – KP	-149.0	-0.62	-0.20	-0.08	269	341	688	661
C	L3-L4-L5	SSPI	-179.7	-2.29	-0.78	-1.28	311	316	375	352
D	T9-T10-T11	SSPI – KP	-149.7	-0.94	-1.90	1.44	270	245	424	407
D	T12-L1-L2	SSPI	-186.0	-1.88	-2.01	1.26	396	345	342	315
D	L3-L4-L5	SSPI – KP	-220.3	-1.57	0.17	-0.06	285	612	402	373
Median			-155.6	-1.26	-0.59	0.00	298	317	423	392

Peak to peak values calculated per each signal at the beginning of the test.

Donor	Level	Group	Load (N)	Axial displacement (mm)	Posterior displacement (mm)	Anterior displacement (mm)	Left strain gauge (με)	Right strain gauge (με)
A	T9-T10-T11	SSPI	154.9	0.25	0.15	0.15	391	29
A	T12-L1-L2	SSPI – KP	195.3	0.36	0.25	0.15	393	449
A	L3-L4-L5	SSPI	224.8	0.36	0.21	0.20	560	366
B	T9-T10-T11	SSPI	250.8	0.72	0.57	0.99	512	407
B	T12-L1-L2	SSPI	302.1	2.40	2.46	0.20	880	311
B	L3-L4-L5	SSPI – KP	362.2	0.75	0.21	0.32	889	542
C	T9-T10-T11	SSPI – KP	194.9	0.31	0.17	0.19	360	305
C	T12-L1-L2	SSPI – KP	244.3	0.34	0.12	0.07	387	414
C	L3-L4-L5	SSPI	283.0	0.68	0.54	0.15	511	590
D	T9-T10-T11	SSPI – KP	232.4	0.49	0.03	0.30	475	574
D	T12-L1-L2	SSPI	292.9	0.79	0.58	0.61	551	596
D	L3-L4-L5	SSPI – KP	341.8	0.73	0.15	0.18	457	693
Median			247.5	0.58	0.21	0.19	493	431

Peak to peak values calculated per each signal at the end of the test.

Donor	Level	Group	Load (N)	Axial displacement (mm)	Posterior displacement (mm)	Anterior displacement (mm)	Left strain gauge (με)	Right strain Gauge (με)
A	T9-T10-T11	SSPI	155.7	0.26	0.14	0.14	400	98
A	T12-L1-L2	SSPI – KP	195.0	0.37	0.25	0.16	393	452
A	L3-L4-L5	SSPI	225.0	0.37	0.18	0.17	578	368
B	T9-T10-T11	SSPI	250.5	0.71	0.60	0.93	511	380
B	T12-L1-L2	SSPI	303.0	2.27	0.02	0.03	137	671
B	L3-L4-L5	SSPI – KP	361.7	0.88	0.33	0.10	489	459
C	T9-T10-T11	SSPI – KP	195.3	0.29	0.15	0.15	355	325
C	T12-L1-L2	SSPI – KP	244.4	0.36	0.06	0.08	437	446
C	L3-L4-L5	SSPI	282.7	0.77	0.20	0.04	488	546
D	T9-T10-T11	SSPI – KP	232.4	0.55	0.09	0.36	532	543
D	T12-L1-L2	SSPI	292.5	0.88	0.61	0.54	485	564
D	L3-L4-L5	SSPI – KP	342.1	0.86	0.16	0.21	423	744
Median			247.5	0.63	0.17	0.16	461	455

Curves for each signal throughout the test are presented below. Median among samples of each group is plotted within its minimum-maximum interval.

Axial displacement

SSPI

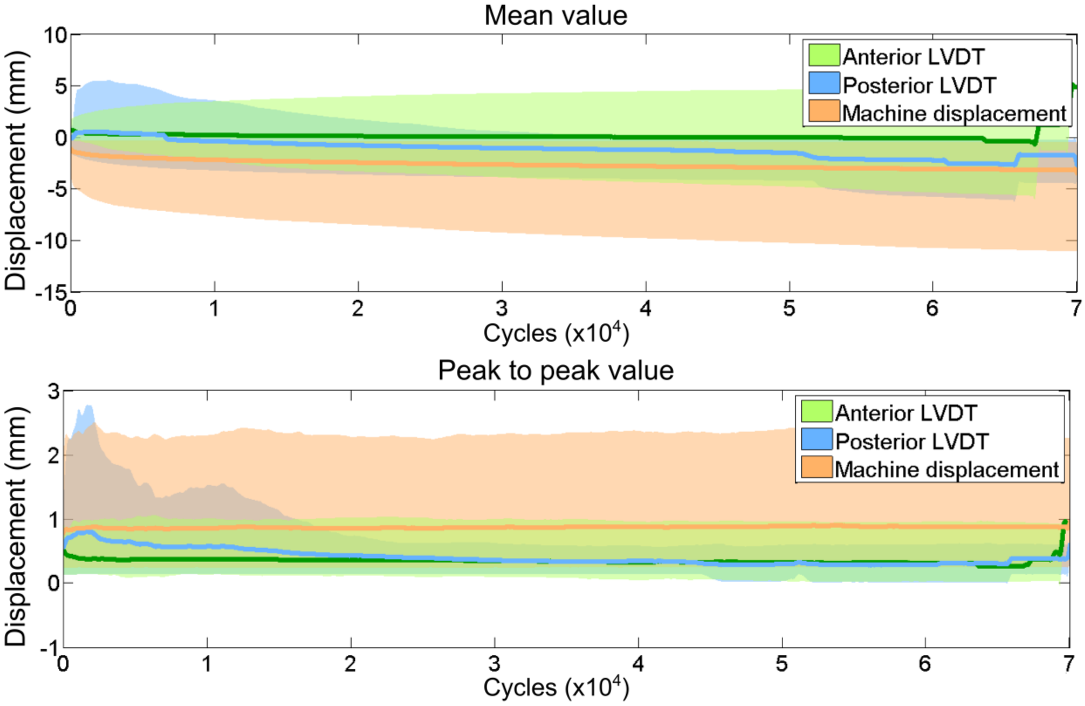

SSPI – KP

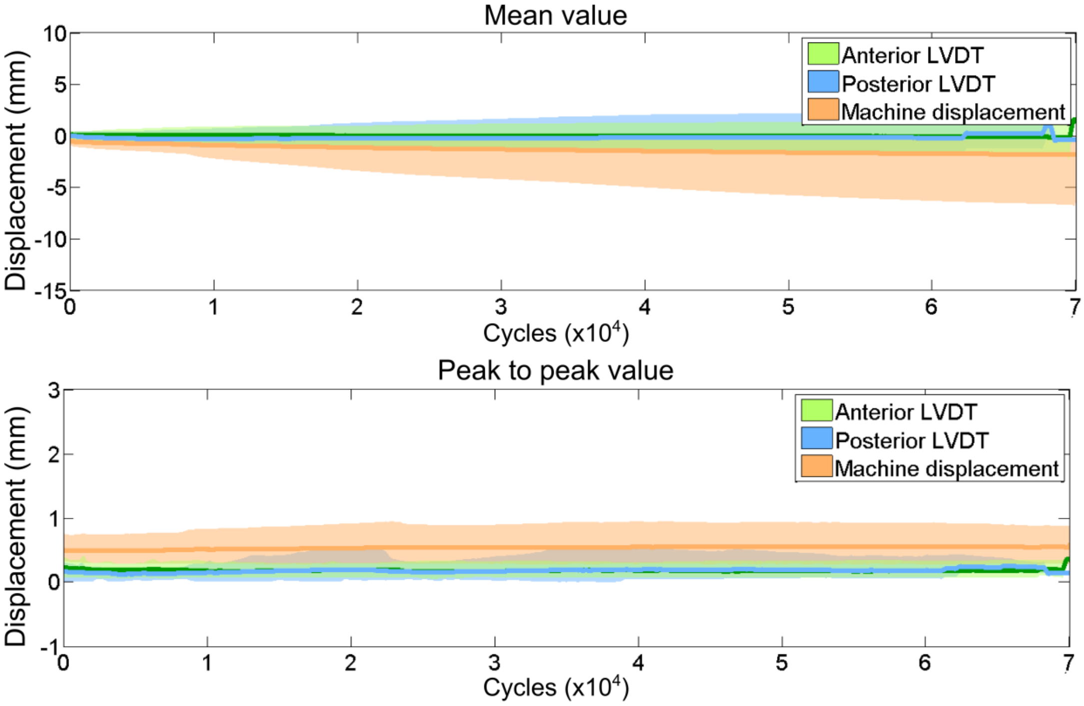

Strain on the fixator rods

SSPI

Mean value

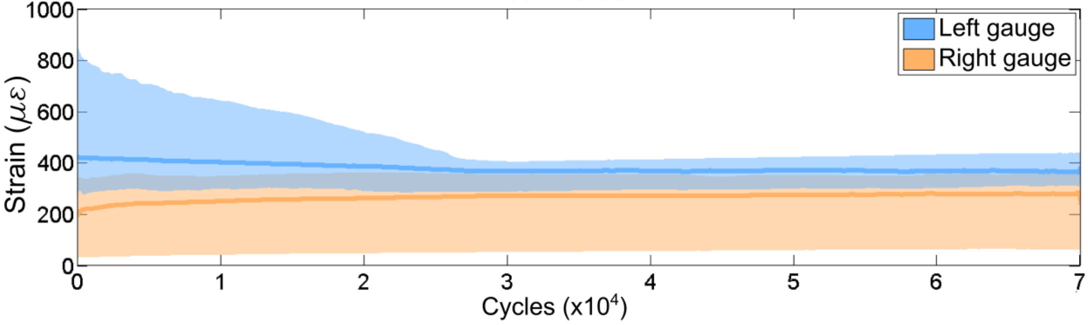

Peak to peak value

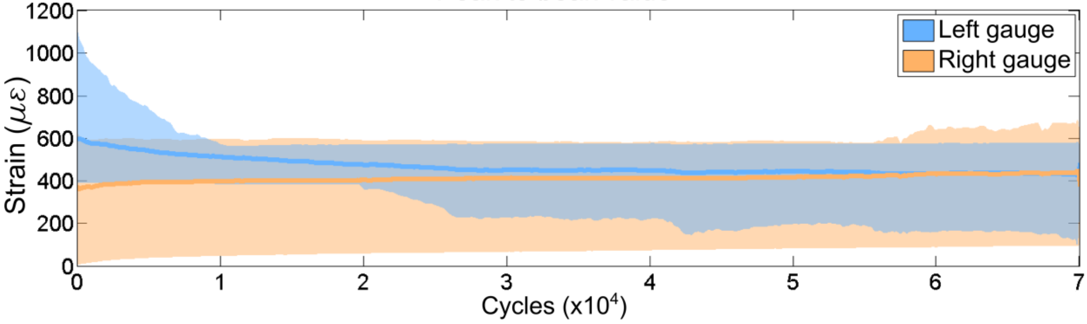

SSPI – KP

Mean value

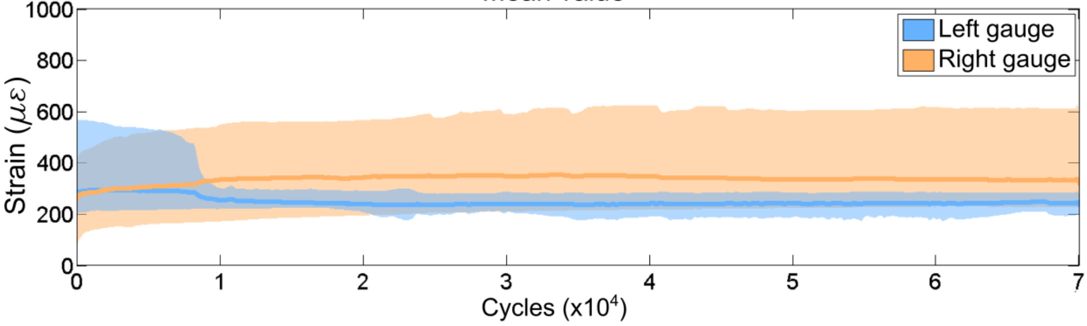

Peak to peak value

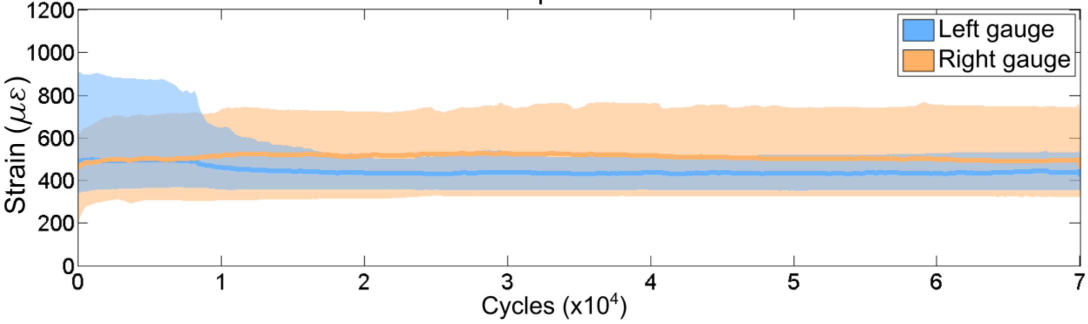

Stiffness

SSPI

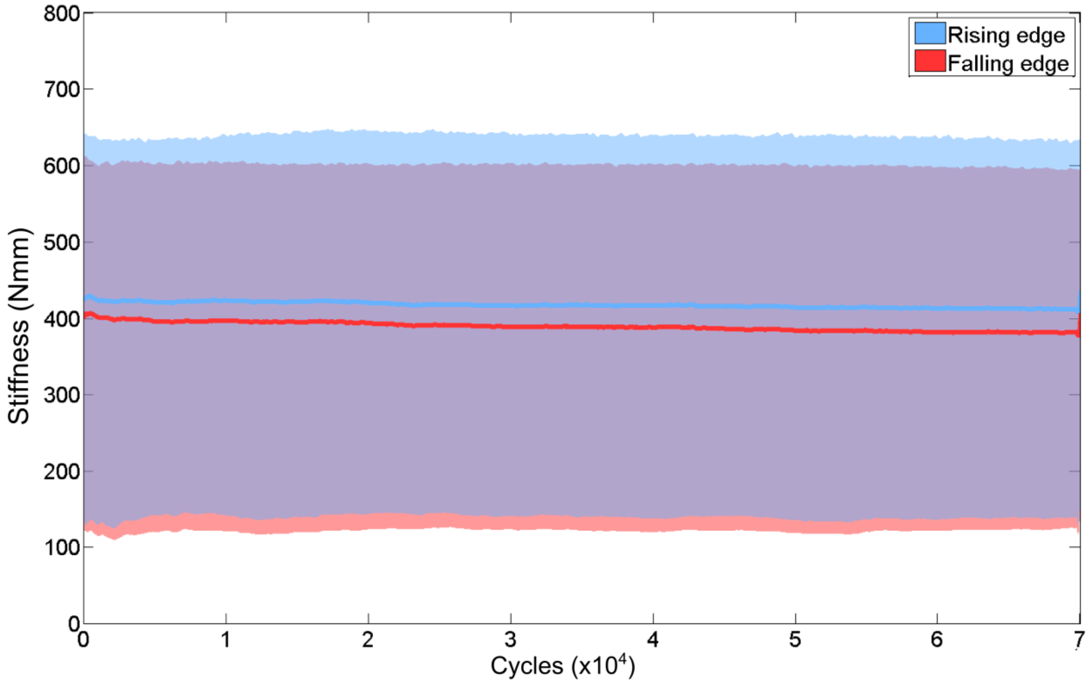

SSPI – KP

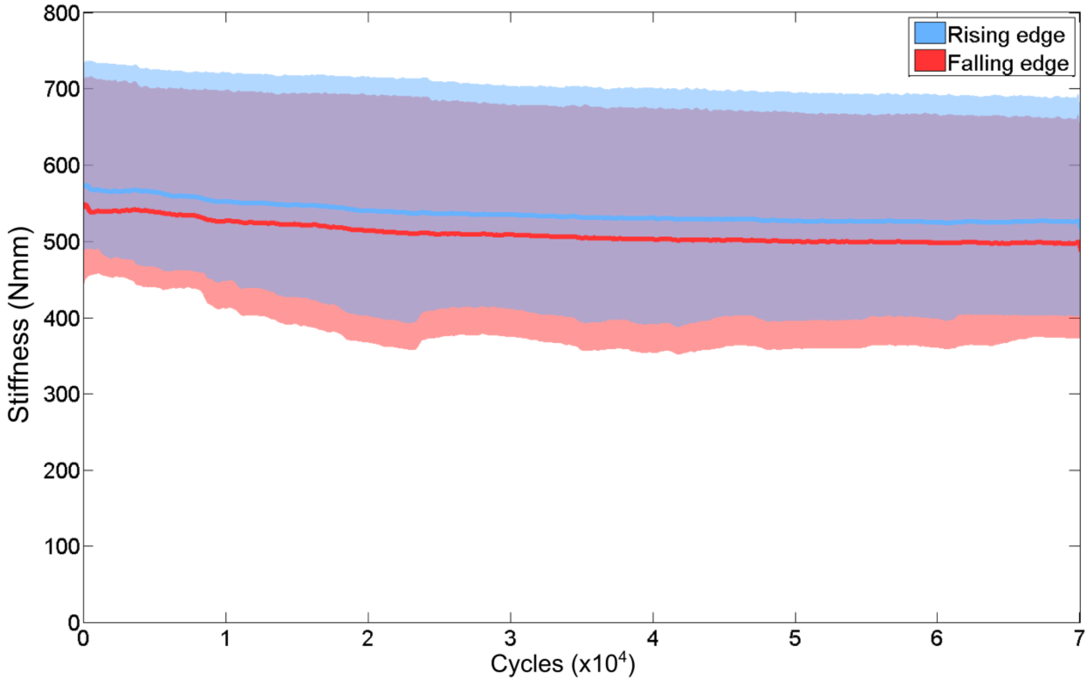

Appendix C

Deflection maps of the endplates adjacent to the treated vertebra following fatigue testing

Permanent deformation induced by fatigue loading was calculated for the endplates adjacent to the treated vertebra using the method described in 2.2.4.4. The following maps present the displacement (mm) along the cranio-caudal direction according to the anatomical reference frame. Therefore, it must be borne in mind that the sign of the displacement field depends on the side of adjacency to the treated vertebra. As shown in the figure below, inward displacement at the caudal endplate of the cranially adjacent vertebra will result in a positive value because aligned with the positive direction of the vertical axis. Conversely, the same displacement would have a negative sign if calculated at the cranial endplate of the caudally adjacent vertebra, because its direction would be opposite to that of the vertical axis.

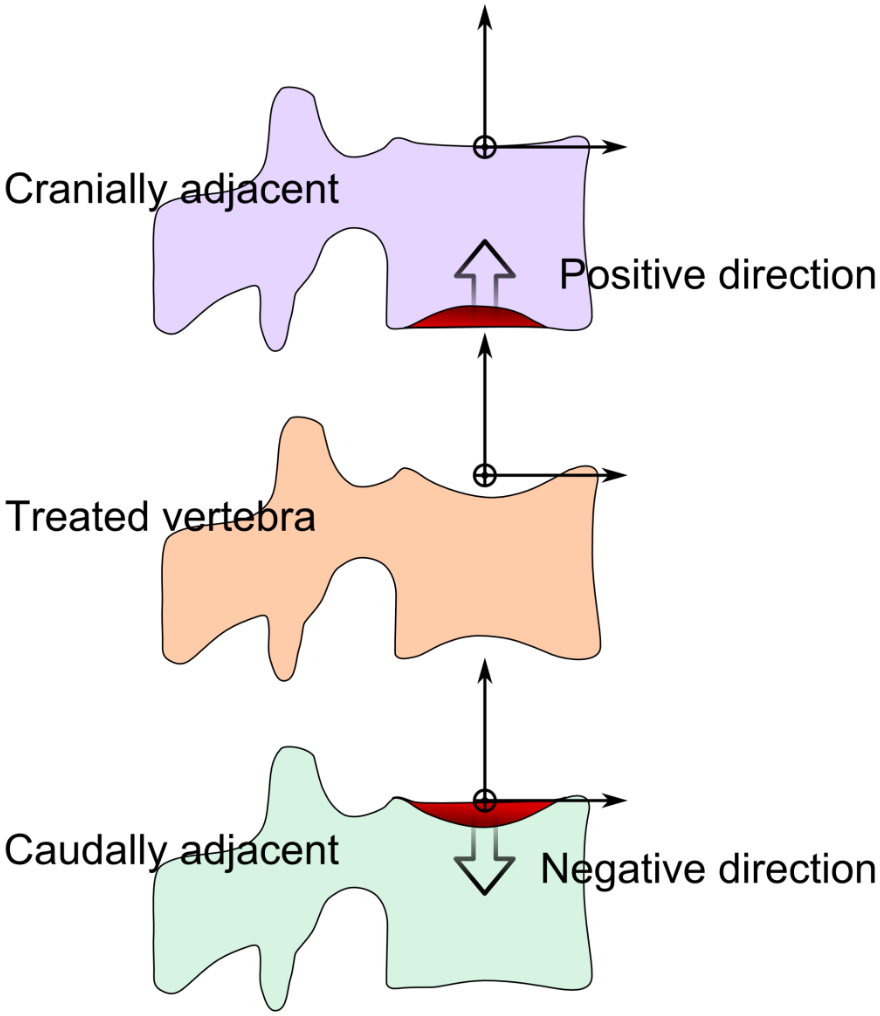

Donor A – T9-T10-T11

T9 caudal endplate

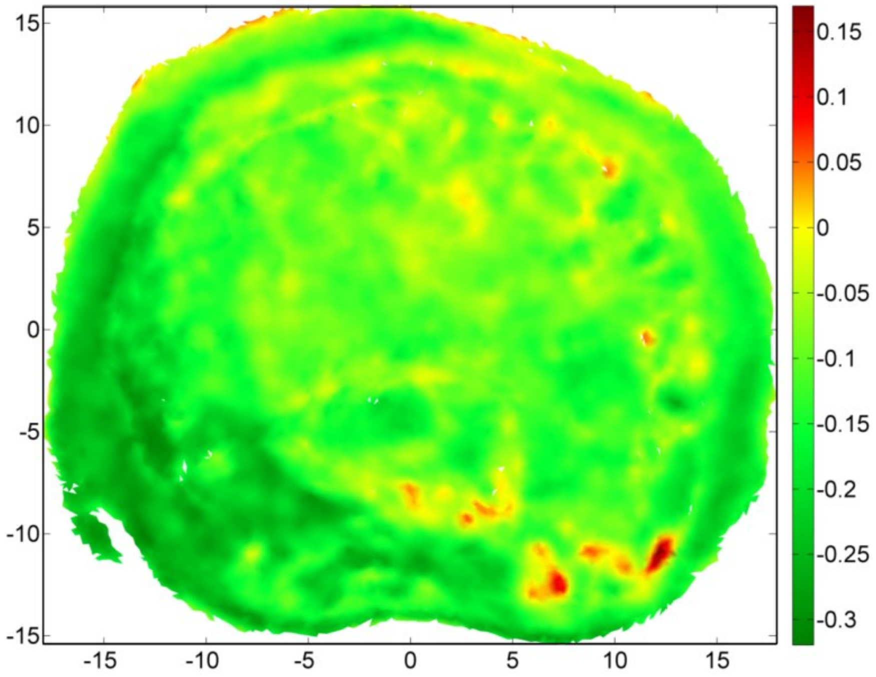

T11 cranial endplate

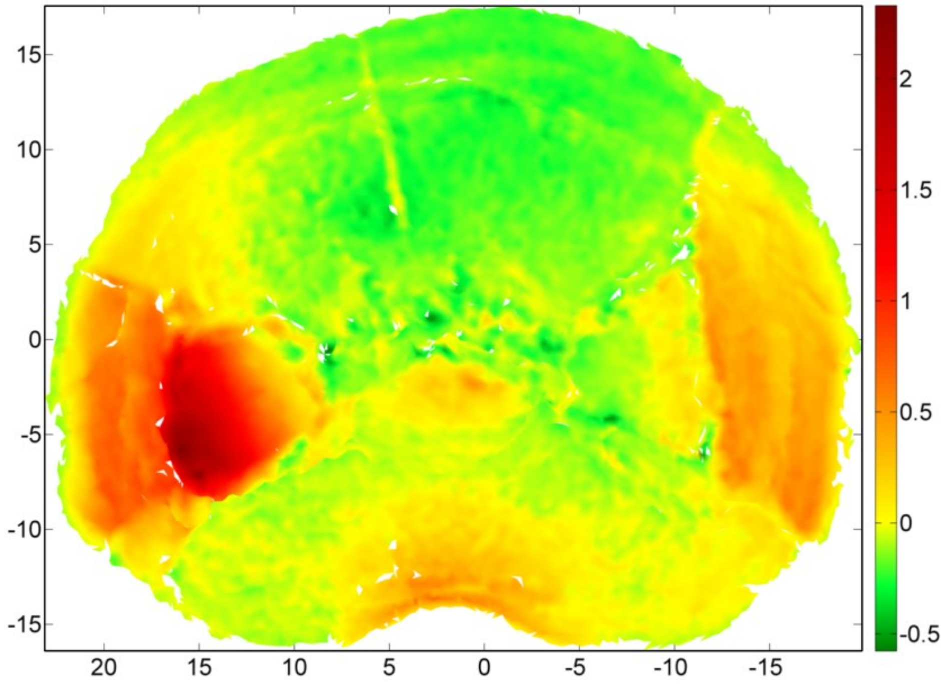

Donor A – T12-L1-L2

T12 caudal endplate

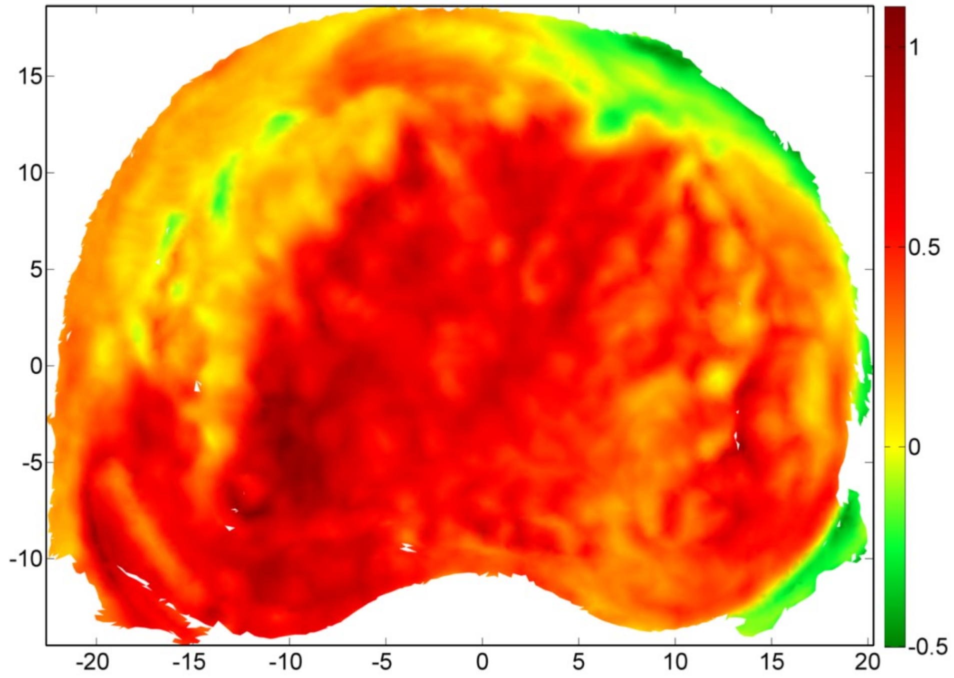

L2 cranial endplate

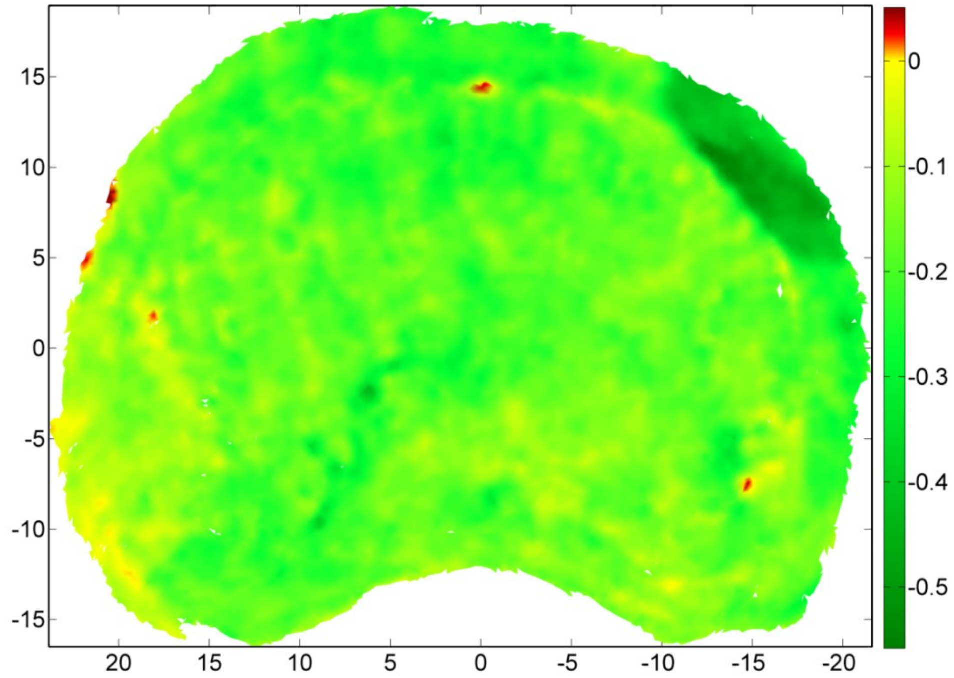

Donor A – L3-L4-L5

L3 caudal endplate

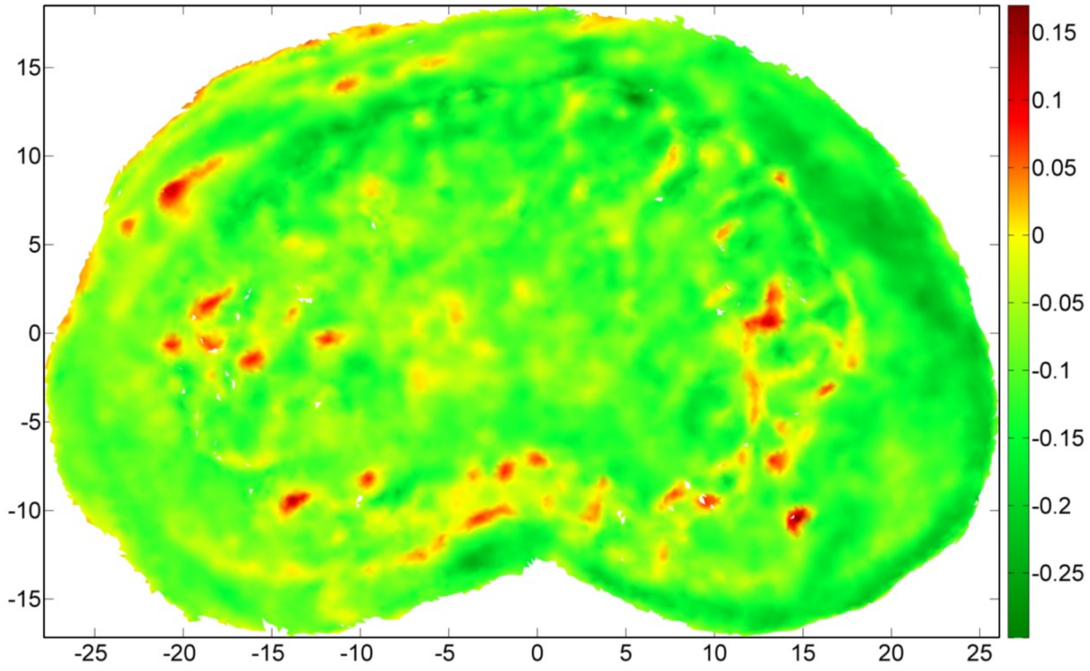

L5 cranial endplate

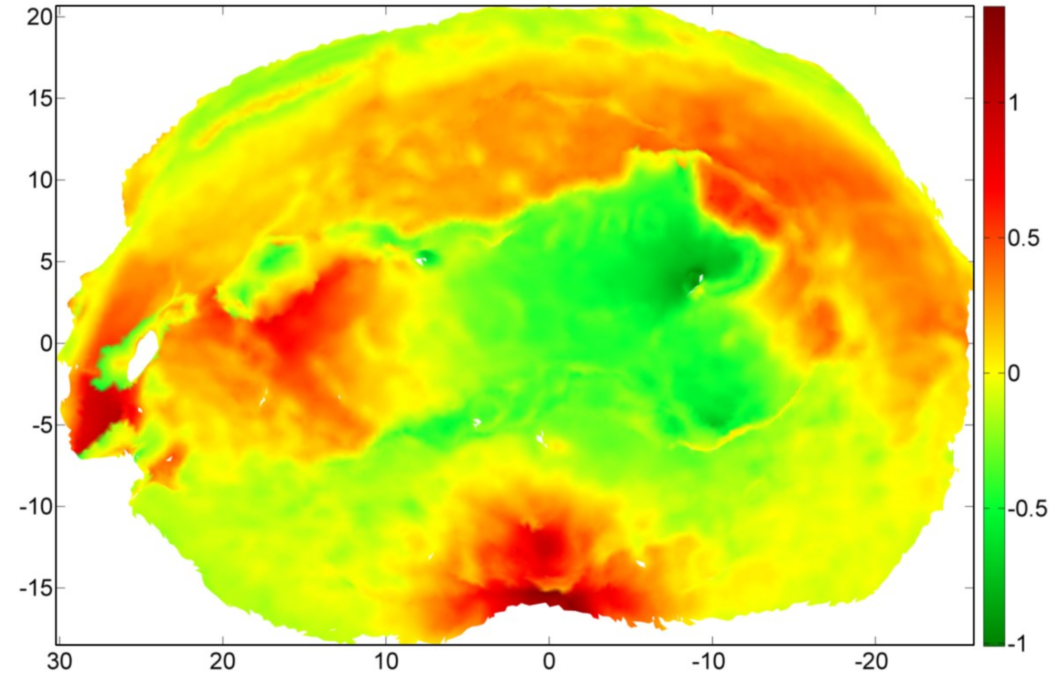

Donor B – T9-T10-T11

T9 caudal endplate

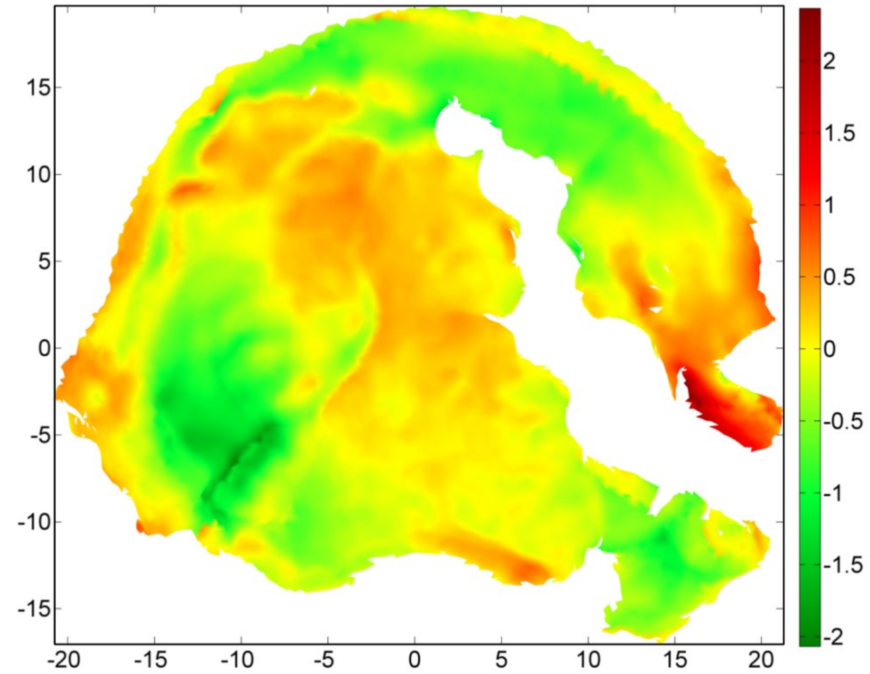

T11 cranial endplate

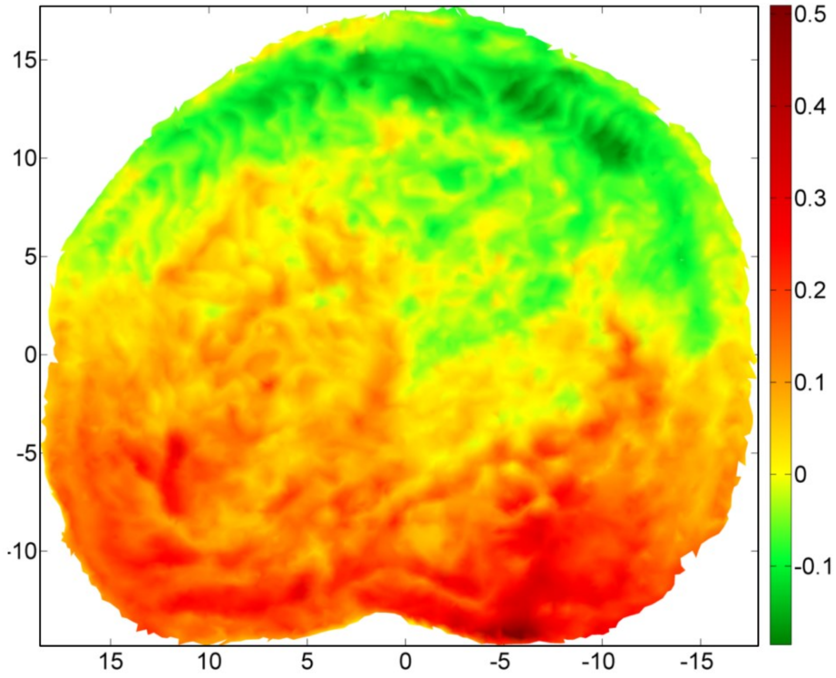

Donor B – T12-L1-L2

T12 caudal endplate

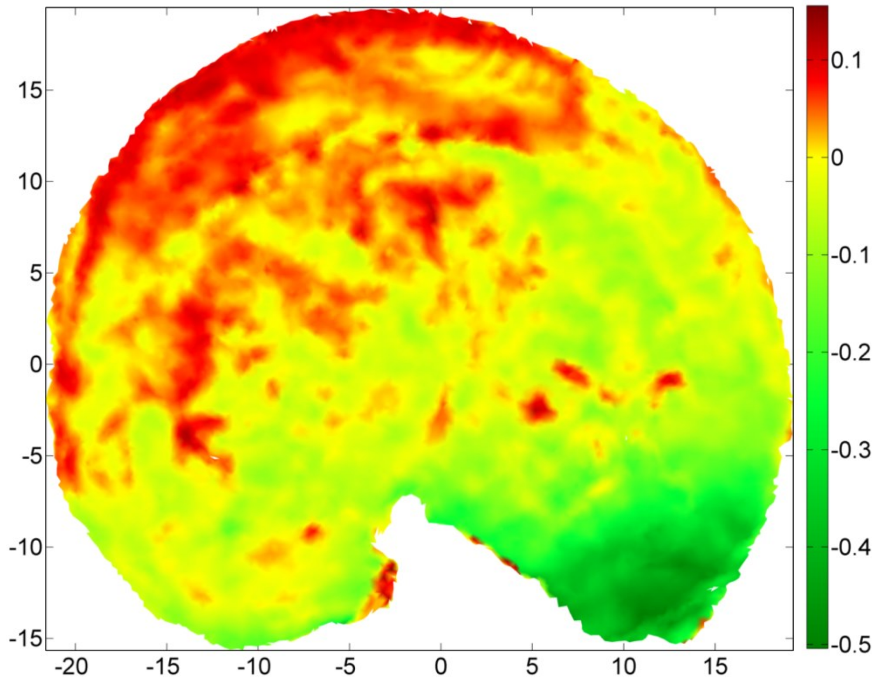

L2 cranial endplate

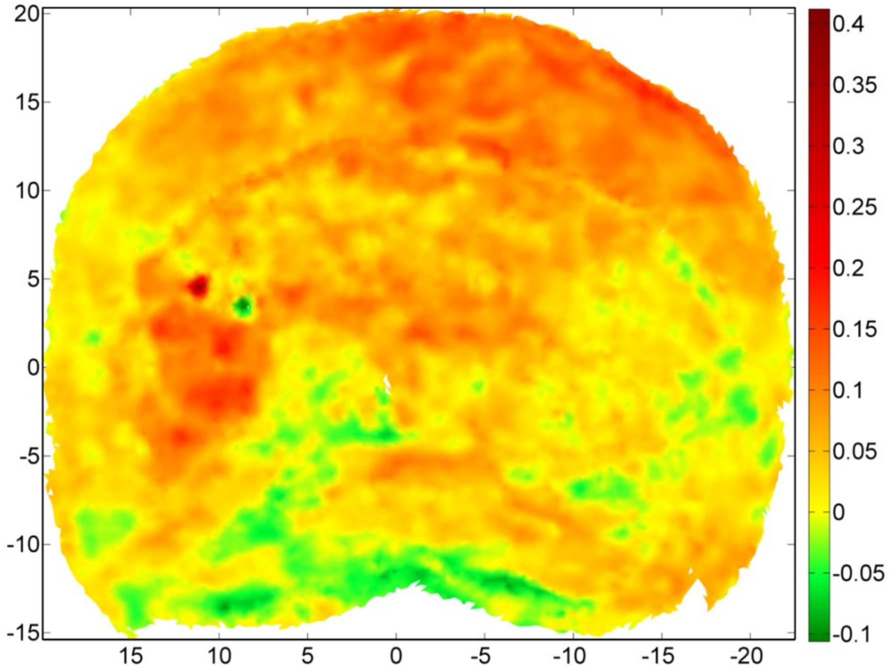

Donor B – L3-L4-L5

L3 caudal endplate

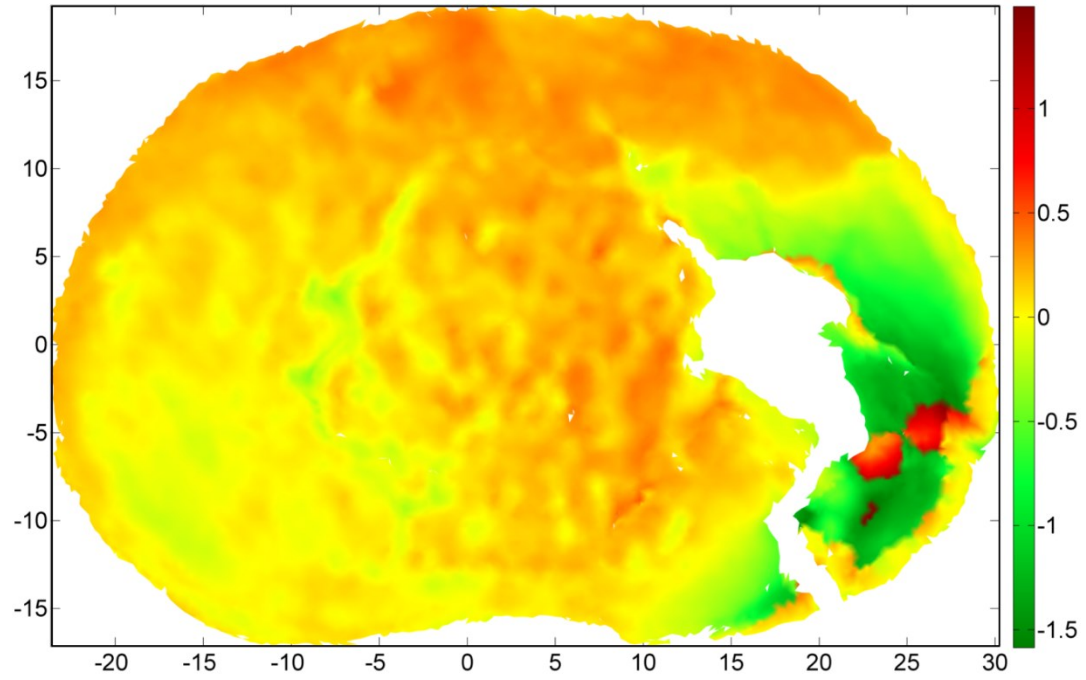

L5 cranial endplate

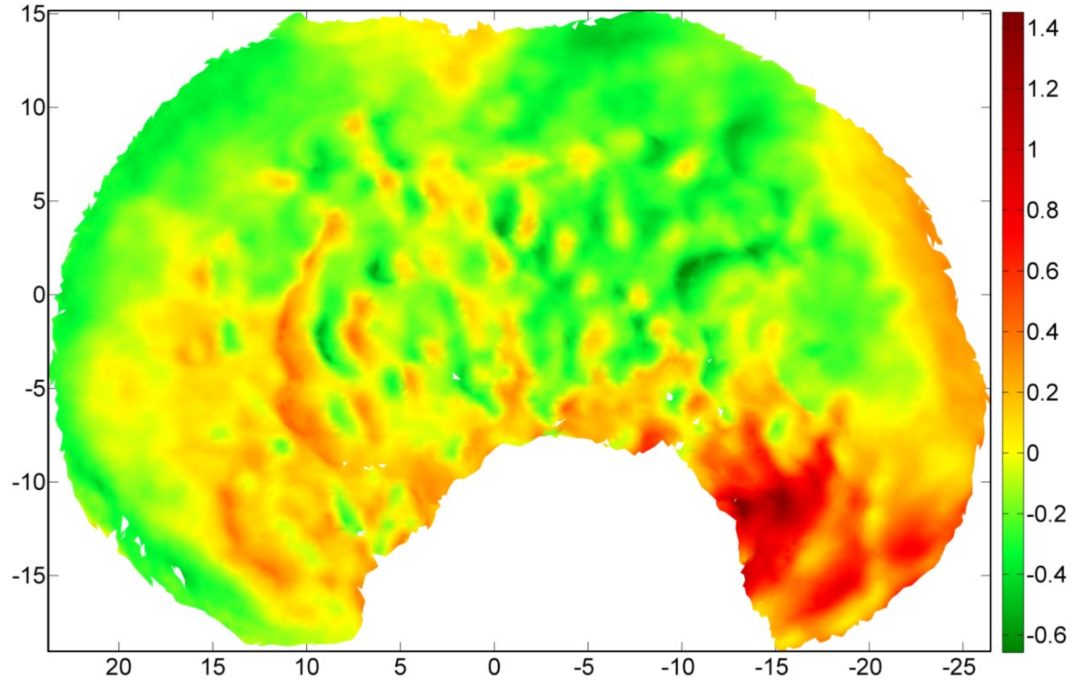

Donor C – T9-T10-T11

T9 caudal endplate

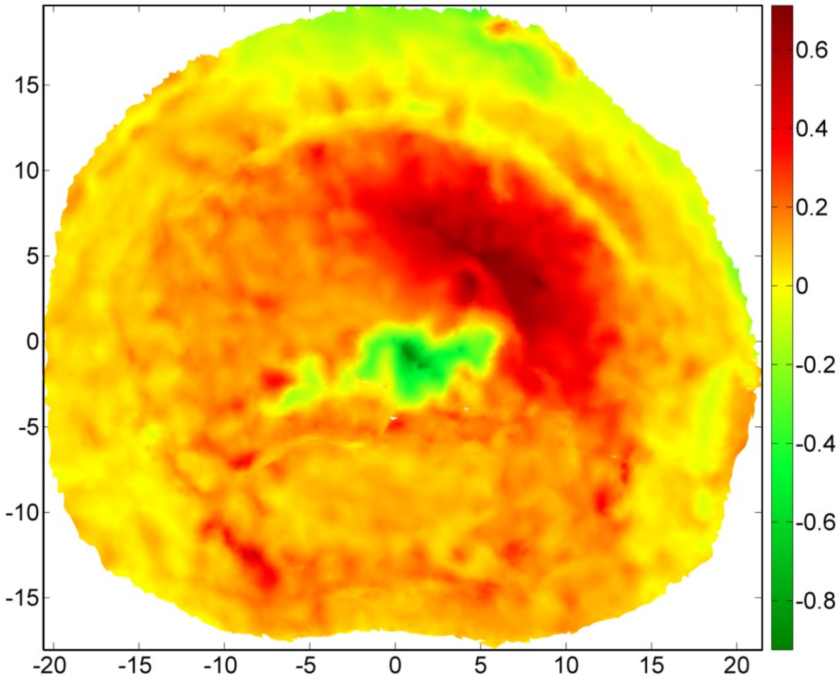

T11 cranial endplate

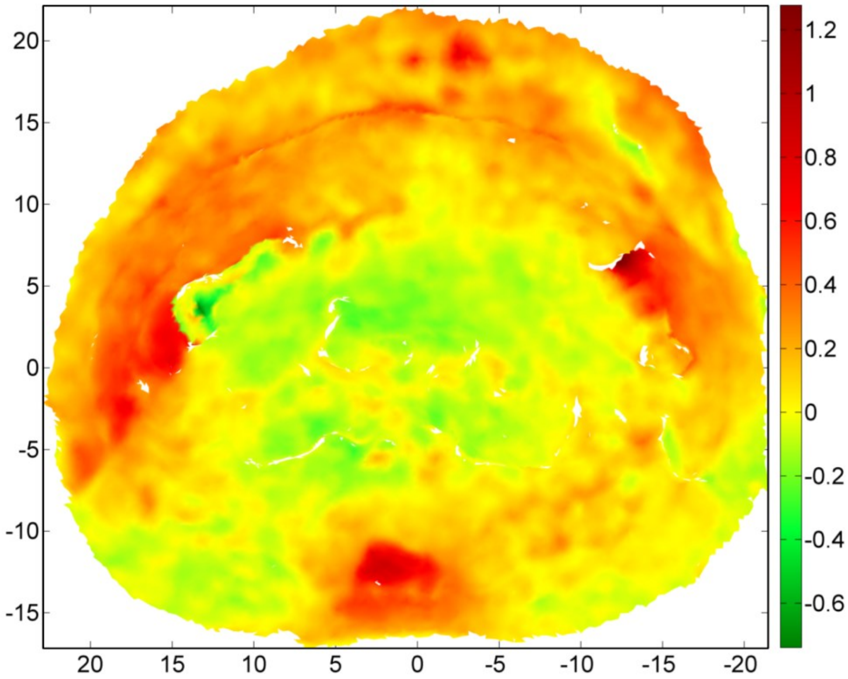

Donor C – T12-L1-L2

T12 caudal endplate

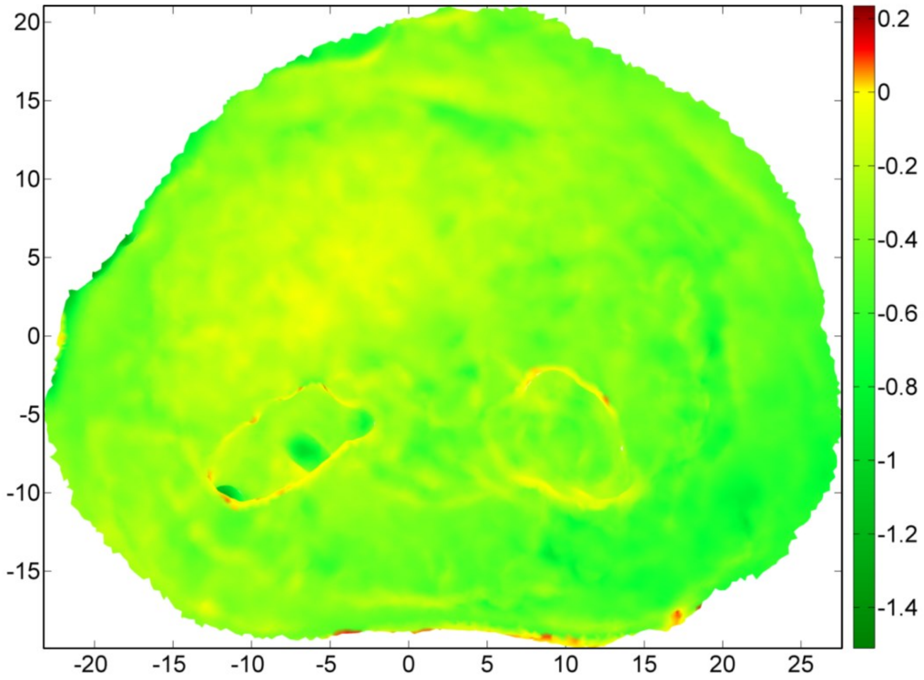

L2 cranial endplate

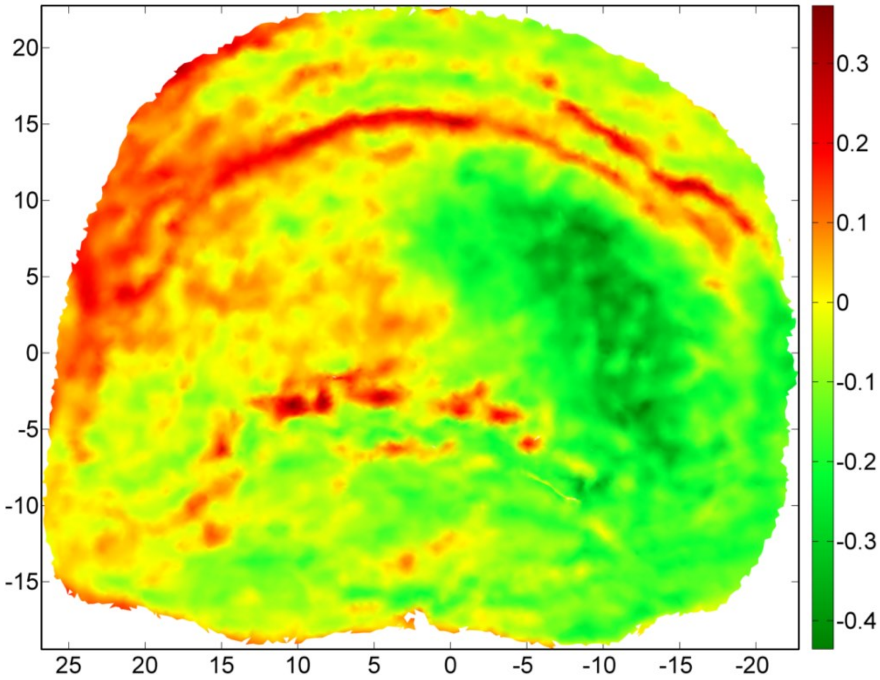

Donor C – L3-L4-L5

L3 caudal endplate

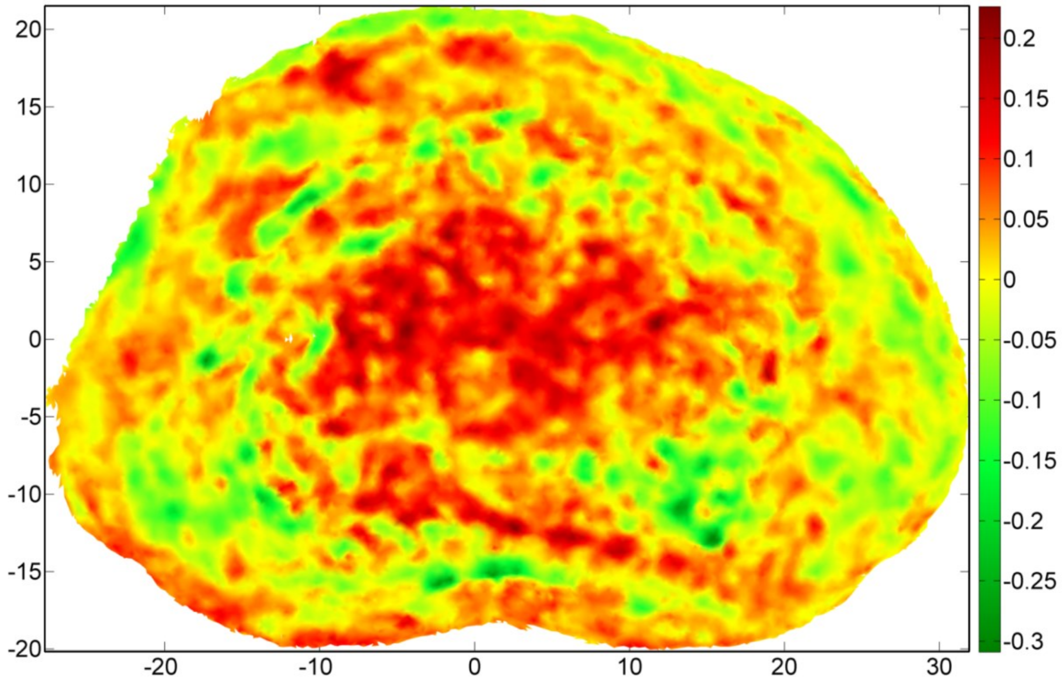

L5 cranial endplate

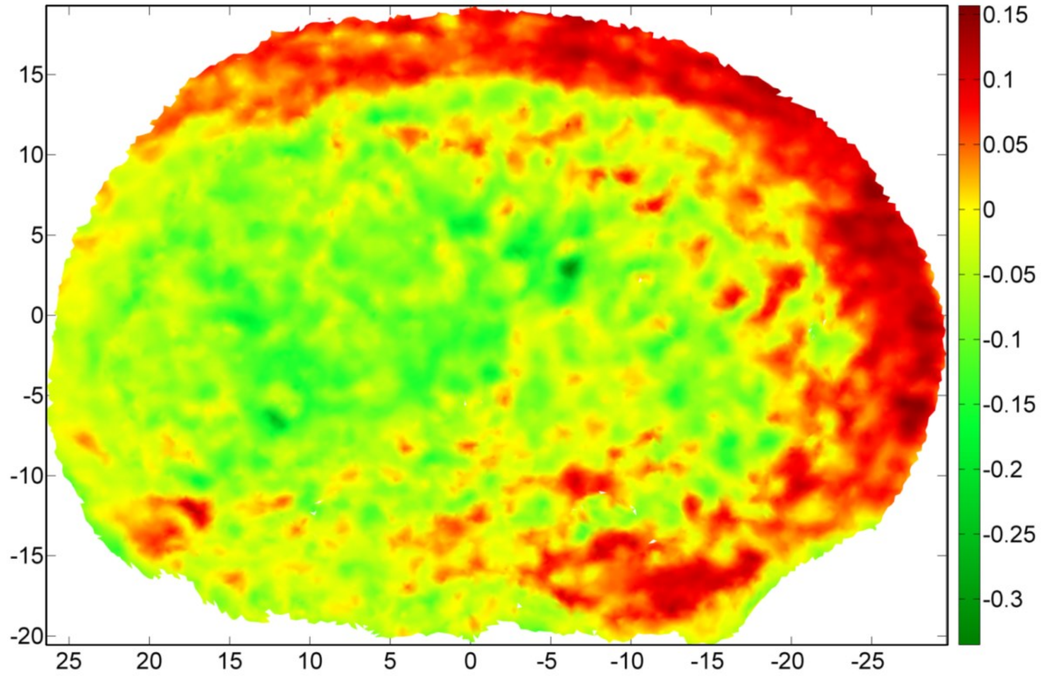

Donor D – T9-T10-T11

T9 caudal endplate

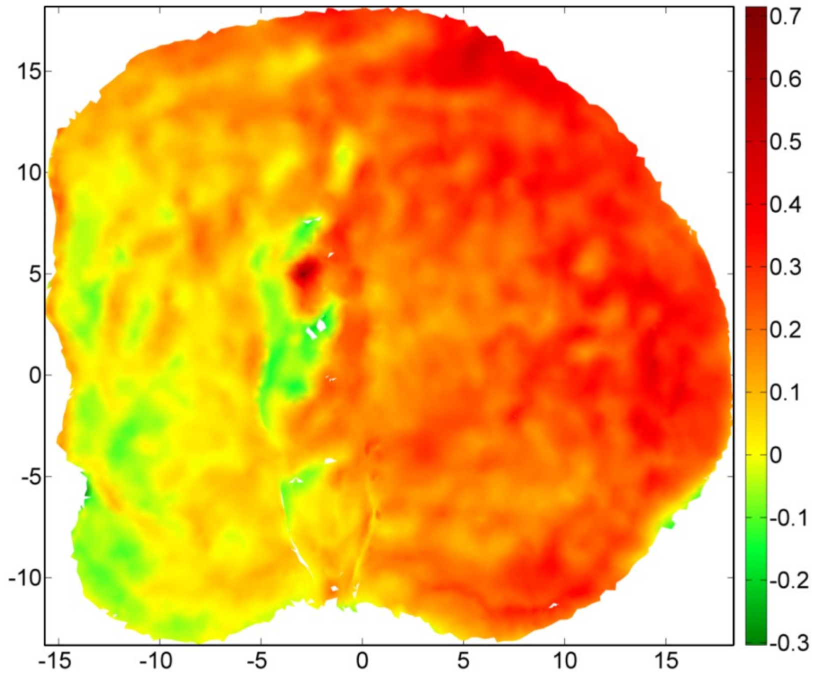

T11 cranial endplate

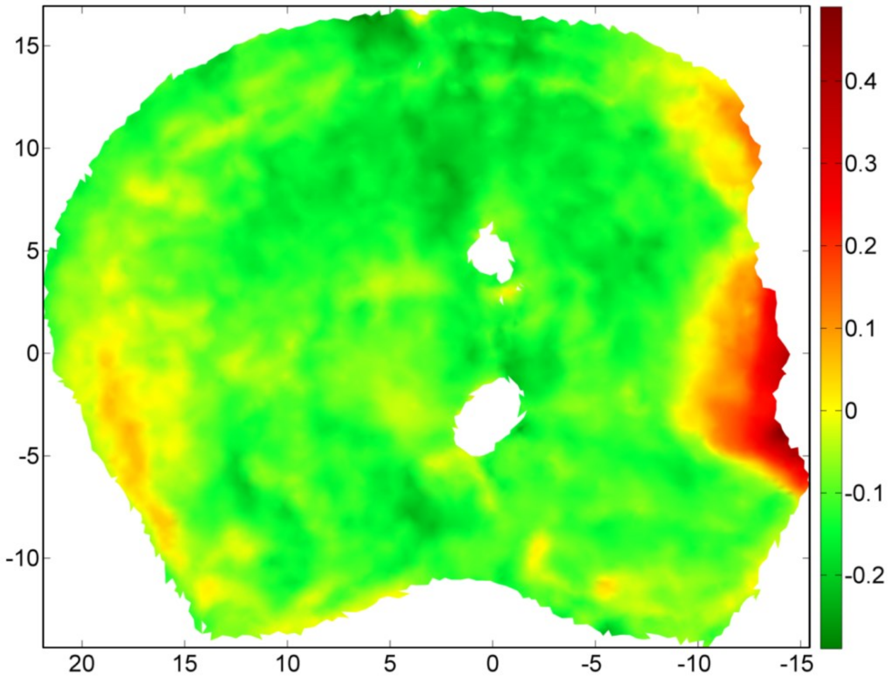

Donor D – T12-L1-L2

T12 caudal endplate

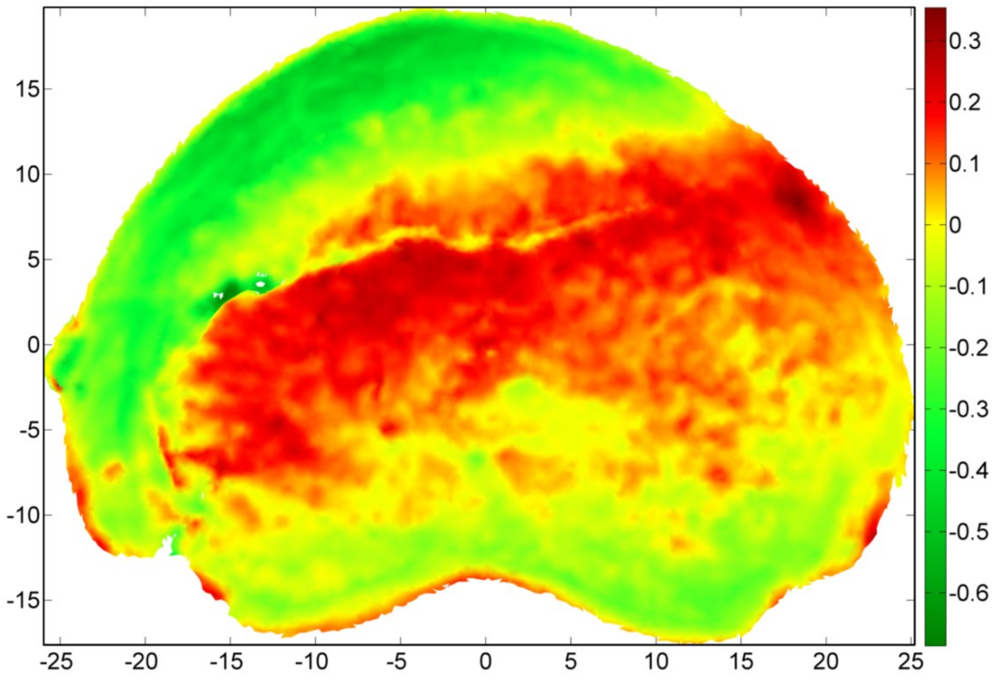

L2 cranial endplate

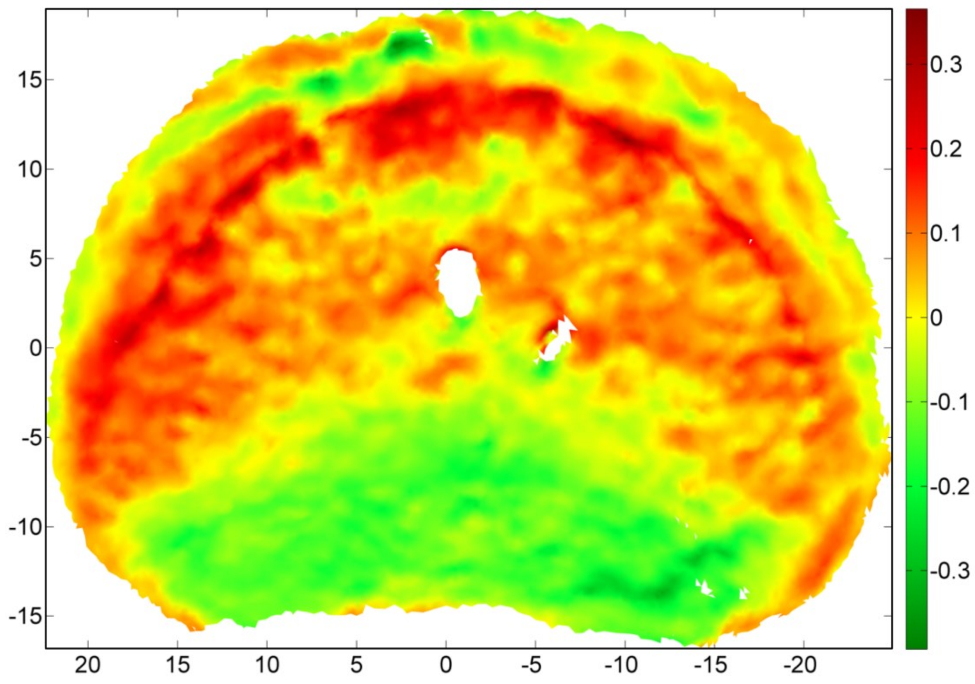

Donor D – L3-L4-L5

L3 caudal endplate

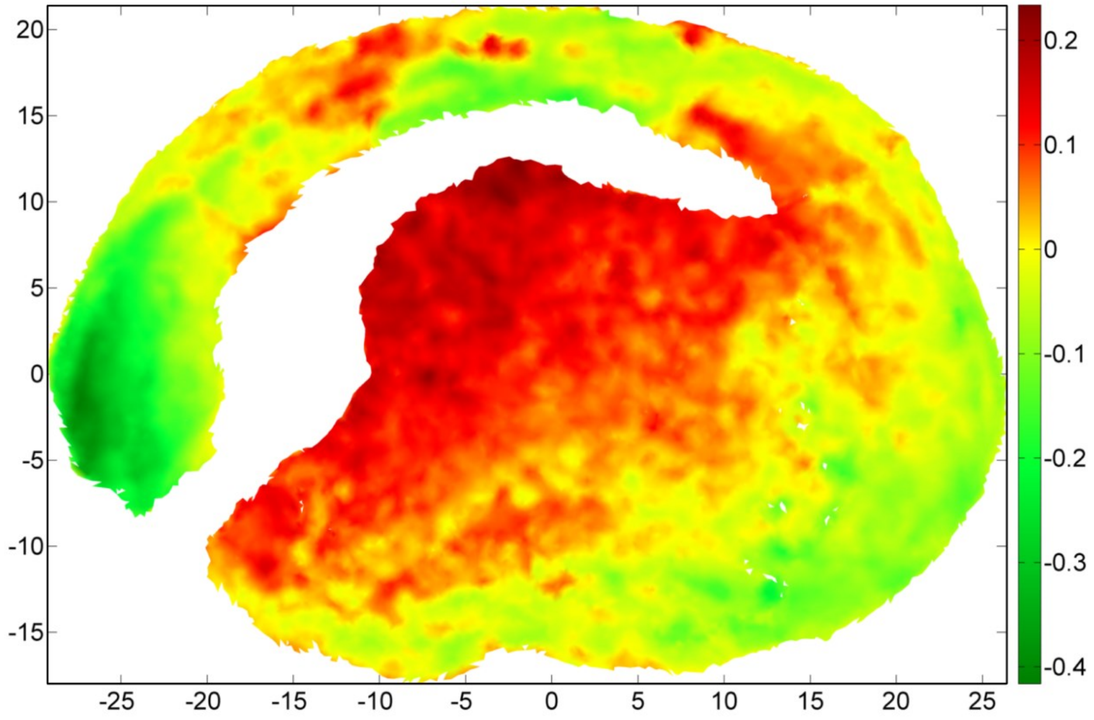

L5 cranial endplate

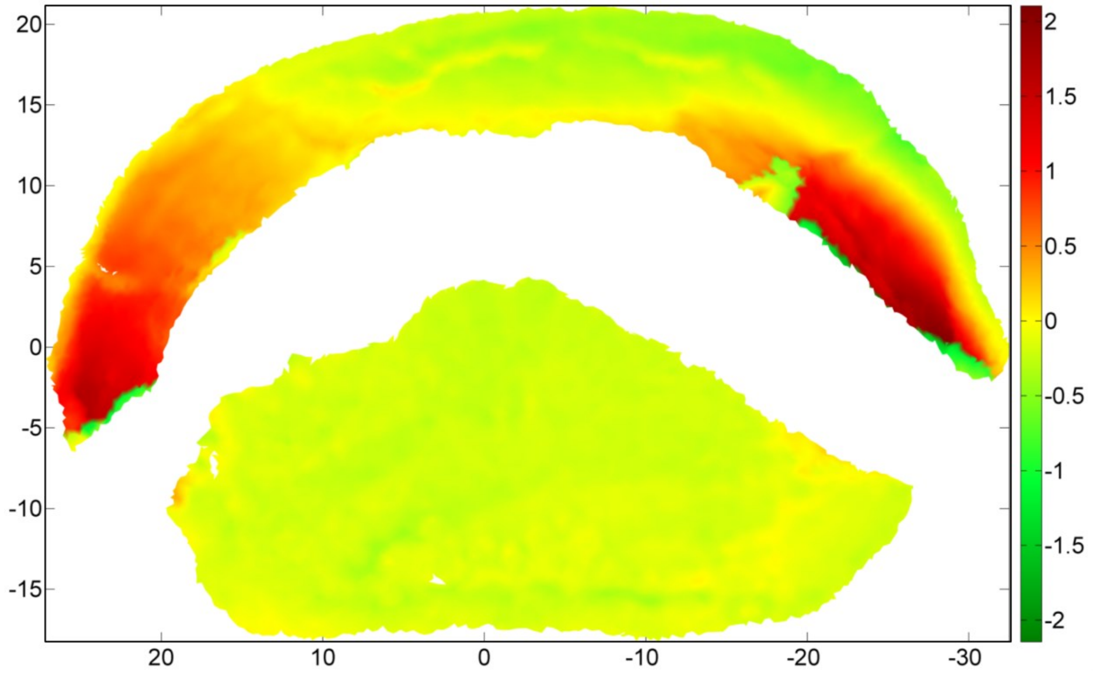

Cranially adjacent endplates: summarised results for 5th and 95th percentiles of displacement components according to the local anatomical reference frame.

	Level	Group	Cranio-caudal		Lateral		Antero-posterior	
			5th (mm)	95th (mm)	5th (mm)	95th (mm)	5th (mm)	95th (mm)
A	T9-T10-T11	SSPI	-0.25	-0.02	-0.06	0.06	-0.04	0.06
A	T12-L1-L2	SSPI – KP	-0.11	0.76	-0.20	0.14	-0.10	0.21
A	L3-L4-L5	SSPI	-0.19	0.00	-0.06	0.05	-0.03	0.06
B	T9-T10-T11	SSPI	-0.98	0.48	-0.45	0.23	-0.26	0.45
B	T12-L1-L2	SSPI	-0.33	0.08	-0.08	0.02	-0.03	0.05
B	L3-L4-L5	SSPI – KP	-0.92	0.33	-0.22	0.09	-0.27	0.15
C	T9-T10-T11	SSPI – KP	-0.09	0.39	-0.12	0.06	-0.09	0.06
C	T12-L1-L2	SSPI – KP	-0.66	-0.11	-0.16	0.22	-0.21	0.17
C	L3-L4-L5	SSPI	-0.09	0.11	-0.02	0.05	-0.02	0.03
D	T9-T10-T11	SSPI – KP	-0.04	0.34	-0.10	0.02	-0.03	0.12
D	T12-L1-L2	SSPI	-0.40	0.20	-0.04	0.14	-0.11	0.04
D	L3-L4-L5	SSPI – KP	-0.17	0.15	-0.03	0.03	-0.02	0.04
Median			-0.22	0.17	-0.09	0.06	-0.06	0.06

Caudally adjacent endplates: summarised results for 5th and 95th percentiles of displacement components according to the local anatomical reference frame.

	Level	Group	Cranio-caudal 5th (mm)	Cranio-caudal 95th (mm)	Lateral 5th (mm)	Lateral 95th (mm)	Antero-posterior 5th (mm)	Antero-posterior 95th (mm)
A	T9-T10-T11	SSPI	-0.24	0.70	-0.10	0.17	-0.34	0.21
A	T12-L1-L2	SSPI – KP	-0.30	-0.08	-0.08	0.05	-0.05	0.08
A	L3-L4-L5	SSPI	-0.43	0.44	-0.22	0.17	-0.13	0.16
B	T9-T10-T11	SSPI	-0.10	0.23	-0.02	0.07	-0.02	0.03
B	T12-L1-L2	SSPI	-0.03	0.12	-0.01	0.02	-0.01	0.01
B	L3-L4-L5	SSPI – KP	-0.36	0.45	-0.12	0.13	-0.20	0.13
C	T9-T10-T11	SSPI – KP	-0.12	0.41	-0.19	0.06	-0.18	0.09
C	T12-L1-L2	SSPI – KP	-0.27	0.12	-0.09	0.02	-0.03	0.07
C	L3-L4-L5	SSPI	-0.11	0.09	-0.02	0.03	-0.01	0.02
D	T9-T10-T11	SSPI – KP	-0.18	0.04	-0.04	0.03	-0.03	0.03
D	T12-L1-L2	SSPI	-0.16	0.16	-0.07	0.01	-0.03	0.03
D	L3-L4-L5	SSPI – KP	-0.39	1.06	-0.29	0.13	-0.20	0.37
Median			-0.21	0.20	-0.08	0.05	-0.04	0.07

Appendix D

Summarised results from 3D analysis of the vertebra

Anatomical parameters measured at intact conditions. Results refer to the central vertebra of the spinal segment.

Donor	Level	Group	Group	Vertebral body height (mm)	Angle on sagittal plane (°)	Angle on frontal plane (°)	Angle 3D (°)	Radius cranial endplate (mm)	Radius caudal endplate (mm)
A	T9-T10-T11	LE	SSPI	22.5	-1.6	0.3	1.6	81.1	89.9
A	T12-L1-L2	HE	SSPI – KP	27.7	3.8	0.3	3.8	99.5	55.9
A	L3-L4-L5	LE	SSPI	27.6	-7.8	1.1	7.8	1087.6	103.9
B	T9-T10-T11	HE	SSPI	23.3	-1.6	1.7	2.3	80.4	83.7
B	T12-L1-L2	HE	SSPI	28.2	2.8	0.7	2.9	268.8	163.0
B	L3-L4-L5	HE	SSPI – KP	27.5	-8.3	0.8	8.4	172.0	98.5
C	T9-T10-T11	LE	SSPI – KP	19.6	2.4	2.3	3.2	281.1	179.0
C	T12-L1-L2	LE	SSPI – KP	24.1	6.8	0.2	6.8	617.7	715.9
C	L3-L4-L5	HE	SSPI	25.4	-9.8	1.4	9.9	371.8	86.3
D	T9-T10-T11	HE	SSPI – KP	21.8	3.0	0.9	3.1	320.9	110.9
D	T12-L1-L2	LE	SSPI	25.9	3.1	0.7	3.1	269.5	191.8
D	L3-L4-L5	LE	SSPI – KP	27.1	-7.9	0.4	7.9	–	222.2
Median				25.7	0.4	0.8	3.5	269.5	107.4

Anatomical parameters measured at post-fracture. Results refer to the central vertebra of the spinal segment.

Donor	Level	Group	Group	Vertebral body height (mm)	Angle on sagittal plane (°)	Angle on frontal plane (°)	Angle 3D (°)	Radius cranial endplate (mm)	Radius caudal endplate (mm)
A	T9-T10-T11	LE	SSPI	21.4	-2.8	3.4	4.4	43.8	103.5
A	T12-L1-L2	HE	SSPI – KP	21.9	4.7	2.3	5.2	64.0	83.1
A	L3-L4-L5	LE	SSPI	27.7	-7.2	0.6	7.2	591.3	107.0
B	T9-T10-T11	HE	SSPI	15.6	-1.8	6.0	6.3	84.3	63.8
B	T12-L1-L2	HE	SSPI	16.5	-3.2	5.6	6.4	34.7	38.7
B	L3-L4-L5	HE	SSPI – KP	17.0	0.2	5.3	5.2	38.7	38.4
C	T9-T10-T11	LE	SSPI – KP	15.5	-2.4	2.7	3.6	76.9	108.0
C	T12-L1-L2	LE	SSPI – KP	18.8	-1.6	3.7	4.0	87.9	326.1
C	L3-L4-L5	HE	SSPI	18.3	-10.5	1.7	10.6	52.1	73.8
D	T9-T10-T11	HE	SSPI – KP	14.1	-5.2	0.8	5.2	45.8	43.7
D	T12-L1-L2	LE	SSPI	18.8	-5.7	3.4	6.7	78.5	78.1
D	L3-L4-L5	LE	SSPI – KP	26.6	-11.7	3.7	12.3	329.7	160.8
Median				18.5	-3.0	3.4	5.8	70.4	80.6

Anatomical parameters measured following surgical treatment. Results refer to the central vertebra of the spinal segment.

Donor	Level	Group	Group	Vertebral body height (mm)	Angle on sagittal plane (°)	Angle on frontal plane (°)	Angle 3D (°)	Radius cranial endplate (mm)	Radius caudal endplate (mm)
A	T9-T10-T11	LE	SSPI	21.7	-5.7	4.3	7.1	45.3	107.8
A	T12-L1-L2	HE	SSPI – KP	23.4	2.7	0.5	2.7	98.0	90.5
A	L3-L4-L5	LE	SSPI	27.9	-6.4	0.5	6.4	275.2	100.0
B	T9-T10-T11	HE	SSPI	18.7	-5.5	5.9	8.1	70.4	53.0
B	T12-L1-L2	HE	SSPI	19.8	-1.2	0.5	1.3	35.1	35.1
B	L3-L4-L5	HE	SSPI – KP	23.7	-6.1	0.2	6.1	47.9	45.9
C	T9-T10-T11	LE	SSPI – KP	17.4	-2.1	2.8	3.5	85.1	107.2
C	T12-L1-L2	LE	SSPI – KP	21.7	0.9	2.8	2.9	189.2	312.9
C	L3-L4-L5	HE	SSPI	20.5	-3.9	1.4	4.2	50.3	59.3
D	T9-T10-T11	HE	SSPI – KP	16.5	1.3	2.1	2.5	58.7	50.6
D	T12-L1-L2	LE	SSPI	21.1	-1.3	0.9	1.6	51.1	73.7
D	L3-L4-L5	LE	SSPI – KP	27.5	-8.5	0.1	8.5	576.2	352.5
Median				21.4	-3.0	1.2	3.8	64.5	82.1

Anatomical parameters measured after fatigue loading. Results refer to the central vertebra of the spinal segment.

Donor	Level	Group	Group	Vertebral body height (mm)	Angle on sagittal plane (°)	Angle on frontal plane (°)	Angle 3D (°)	Radius cranial endplate (mm)	Radius caudal endplate (mm)
A	T9-T10-T11	LE	SSPI	21.5	-6.0	4.1	7.2	47.7	113.9
A	T12-L1-L2	HE	SSPI – KP	22.4	3.4	2.0	3.9	88.2	86.8
A	L3-L4-L5	LE	SSPI	27.8	-7.9	0.2	7.9	273.4	103.4
B	T9-T10-T11	HE	SSPI	18.7	-4.0	6.2	7.4	–	58.5
B	T12-L1-L2	HE	SSPI	21.0	-2.9	3.0	4.2	32.5	37.6
B	L3-L4-L5	HE	SSPI – KP	24.6	-7.7	0.1	7.7	53.2	52.5
C	T9-T10-T11	LE	SSPI – KP	17.3	-3.9	2.6	4.7	78.4	116.5
C	T12-L1-L2	LE	SSPI – KP	21.3	-1.3	3.0	3.2	127.8	324.6
C	L3-L4-L5	HE	SSPI	20.4	-5.7	1.1	5.7	53.9	59.9
D	T9-T10-T11	HE	SSPI – KP	17.2	-6.0	2.1	6.4	71.2	46.5
D	T12-L1-L2	LE	SSPI	20.8	-3.5	1.0	3.6	53.3	64.5
D	L3-L4-L5	LE	SSPI – KP	27.4	-7.7	0.3	7.7	251.5	213.1
Median				21.1	-4.9	2.1	6.0	71.2	75.7

Appendix E

LVDT calibration

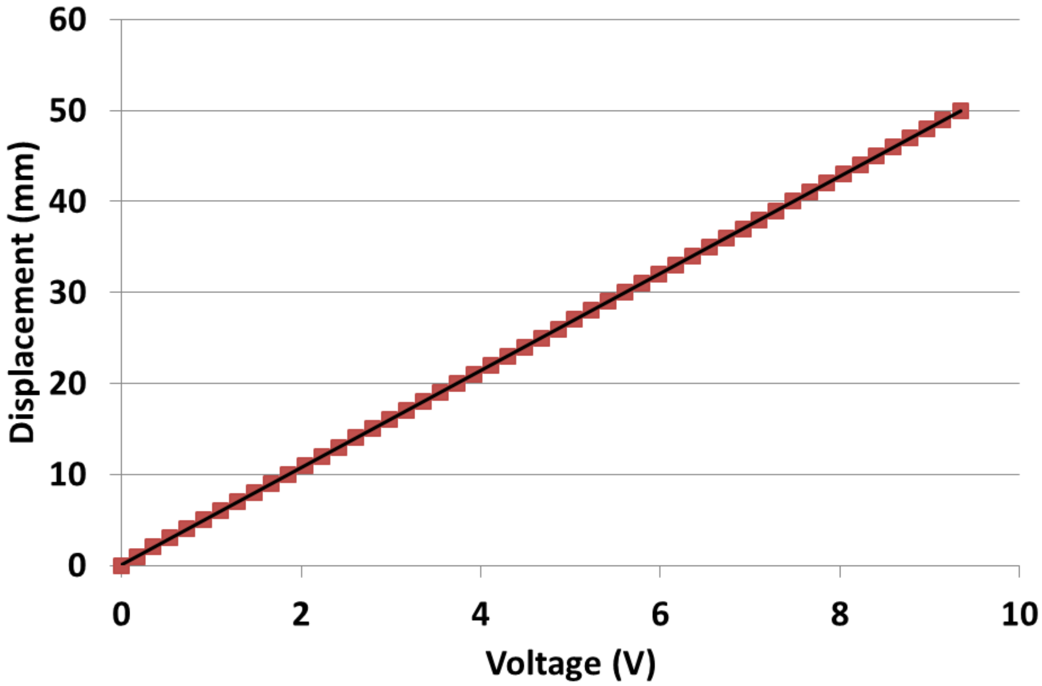

Calibration of the LVDT used in the experiments (serial number: 134470).

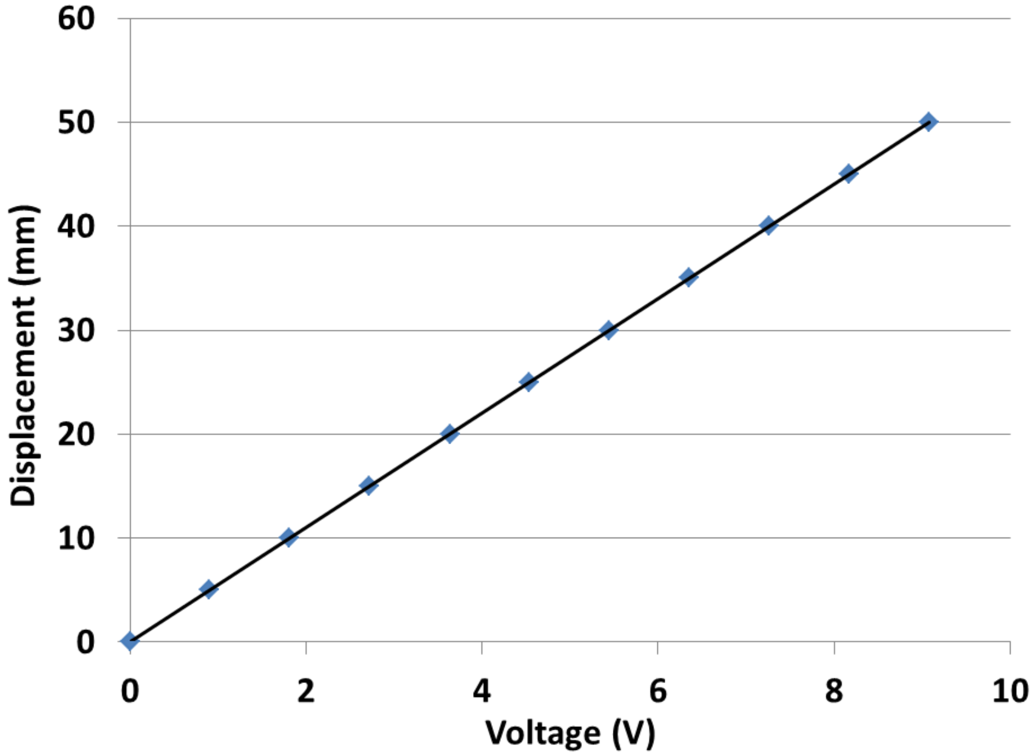

Calibration of LVDT used in the experiments (serial number: 133520).

Appendix F

Conference presentations

List of oral presentations (the presenting author is underlined):

Brandolini, N, Timothy, J, Kapur, N, Hall, RM. "Biomechanics of short segment pedicle instrumentation in conjunction with kyphoplasty for the treatment of spinal burst fractures". EANS, Madrid, October, 2015.

Brandolini, N, Kapur, N, Hall, RM. "An in vitro investigation on the relevance of interpedicular widening in the dynamics of spinal burst fractures". WCB, Boston, USA, July, 2014.

Brandolini, N, Kapur, N, Hall, RM. "A dynamic investigation on the behaviour of the pedicles and facets in spinal burst fractures". Bone & Joint Journal Orthopaedic Proceedings Supplement 96-B(Supp 11): 74. CORS, Venice, Italy, October, 2013.

Brandolini, N, Kapur, N, Hall, RM. "An *in vitro* investigation on the dynamics of spinal burst fractures". SpineFX Final conference at EUROSPINE, Liverpool, UK, October, 2013

Holub, O, Kasioptas, A, Brandolini, N, Kapur, N, Lidén E, Hall RM. "Augmentation of cadaveric vertebrae with an α−TCP/ α−CSH ceramic cement: A biomechanical study on the effect of injected volume". eCells & Materials Journal. 28(S1): 48. GRIBOI, Boston, USA, April, 2013.

List of poster presentations:

Roberts, NR, Brandolini, N, Kapur, N, Whyne, C, Hall, RM. "Using micro-CT derived boundary conditions to evaluate structural stability of multiple myeloma infiltrated vertebrae". WCB, Boston, USA, July, 2014.

Brandolini, N, Holub, O, Skrzypiec, DM, Roberts, NR, Kapur, N, Hall, RM. "On the design of an *in situ* testing protocol for the structural characterization of the multiple myeloma affected vertebra". Leeds Oncological Engineering Conference, Leeds, UK, September, 2012.